Laser Induced Incandescence Imaging for the Investigation of Soot Formation in Laminar Flames

Robert Gray Roy

A thesis submitted to the Department of Chemical and Process Engineering, University of Strathclyde in fulfilment of the requirements for the degree of Doctor of Philosophy

Department of Chemical and Process Engineering
University of Strathclyde

This thesis is the result of the author's original research. It has been composed by the author and has not been previously submitted for examination which has led to the award of a degree.

Signed: Date:

Abstract

This work has been aimed at applying laser induced incandescence imaging for the measurement of soot concentration within a variety of novel flame sources and setups. Laser induced incandescence (LII) is an optical technique used in laser diagnostics to measure soot volume fraction and estimate particle size *in-situ*. Using imaging to measure LII allows for a range of combustion environments to be investigated and soot volume fractions to be measured. An experimental methodology had to be setup to measure the LII signal using a Nd:YAG laser, ICCD camera and flat flame burner and calibrated along with another optical technique known as extinction. This allowed for the soot volume fraction to be calibrated and measured and this gives the standard case for calibrating other measurements in different flames.

From burner setup it is possible to change the boundary temperature of the flame. It was thought that by changing this temperature it would be possible to change the soot concentration within the flame. However, using LII imaging it was shown that despite this change in temperature the soot volume fraction remains the same, this was also eventually found to be the case when modelling these types of flames. This gives confidence in different experimental setups between groups can be used for comparison.

The burner being characterised by a standard setup allows for comparison when using a different excitation source, a long-pulsed fibre laser. Using a long pulse fibre laser has benefits and it is shown in this work that it is possible to get a comparable result with LII centre line height above burner (HAB) profiles matching. Modelling also allows for comparisons and understanding on how the laser temporal and spatial profile can affect the LII signal.

The rise of the interest in sustainable energy generation has led to the increase of using alternative fuel sources such as biofuels. Using the method developed it was possible to record soot volume fraction images within a wick diffusion flame which used a selection of biofuels and show improvement on previously published temporal profiles produced in these flames. The sooting propensity of each fuel was able to be characterised more accurately using spatially resolved profiles over temporally measured profile.

Conferences attended:

- International Combustion Institute Winter School on Combustion in Eindhoven (Poster Presented) (2015)
- IOP Combustion Physics Group Current Research in Combustion: A Forum for Research Students and Early Career Researchers in London(Poster Presented) (2017)
- 8th International Workshop on LII (2018) in Tutzing. (Oral Presentation on Laser Induced Incandescence using a Long-pulsed fibre laser for the *in-situ* study of flames, and poster presentation of Laser induced incandescence imaging in diffusion flames of liquid fuels relevant to biomass combustion)

Submitted for publication:

- In-situ photoacoustic measurement of soot profiles in laminar flames using a high repetition-rate pulsed fibre laser

  Gordon S. Humphries[1,2,*] , Robert Roy , John D. Black[1] , Michael Lengden[2] Iain S. Burns[1]

  [1]*Department of Chemical and Process Engineering, University of Strathclyde,*

  [2]*Centre for Microsystems and Photonics, Department of Electronic and Electrical Engineering, University of Strathclyde,*

Manuscripts in preparation:

- Laser induced incandescence (LII) using a long-pulsed fibre laser for in-situ study of soot in flames.

  R.Roy[1], G.Humphries[1,2], A. Mawbey[1], J.D. Black[1], I.S. Burns[1]

  [1] *Department of Chemical and Process Engineering, University of Strathclyde,,Glasgow*

  [2] *Department of Electronic and Electrical Engineering, University of Strathclyde, Glasgow*

- Laser induced incandescence imaging in diffusion flames of liquid fuels relevant to biomass combustion

  R.Roy[1], I.S. Burns[1]

  Department of Chemical and Process Engineering, University of Strathclyde, Glasgow

‘*Never fear, inevitably we shall have our years of failure, and when they arrive, we must reveal tolerance and sanity. No matter the days of anxiety that come our way, we shall emerge stronger because of the trials to be overcome’*

Bill Struth

Acknowledgements

I would like to thank my supervisor Dr Iain Burns for all the help and support he has provided me over the years to help get me to where I am today. I would also like to extend thanks to Dr Gordon Humphries, Dr John Black, Dr Moinul Hossain, Precious Otti and Andrew Mawbey for all their help throughout this project. I would also like to extend thanks to the technical staffs that have helped throughout the years as well as many others within the chemical engineering department. I would also like to thank the University of Strathclyde, it has been a quick ten years.

I would also like to thank fellow PhDers for their help, support and laughter over the years; the originals Scott, David, the Javelin, Herroca, Alessia, Paul and Carlota, Chris, Joy, Craig, Dorin, Maryam, Costa and Evan and the many more who helped over the years. I would like to thank the Ark crew for their good times and banter; Daria for her support when using MATLAB and having the most hilarious nickname, Andrew, Big head Dave, Carla Ferrari, Georgia, Baige, Ruben, Jose and Martin for cracking Andrew and anyone else who I might have forgotten about.

I would also like to thank the old uni boys for all the laughs and travels abroad whilst doing my PhD. Josh, Martin, Lewis, Ciaran, Kev, Kenny, Dale, the Clark bros and Billy. Some days out we had.

I also need to give a special thanks to Carla Santos for all the hard work and effort she put in helping me complete, soon, it will be my turn to help you.

I would also show gratitude all my family for everything they have done for me and put up with over the years, Mum and Dad, Darren, Jennifer, Alfie the spaniel and Aunt Cath. Finally, I would also like to thank a person whose help and support over the years that had a massive impact on my life: William Roy. I hope and I’m sure you would have been proud.

Table of contents

Table of figures

Nomenclature and glossary

Symbol	Definition	Unit
B_λ	Spectral Radiance	W sr^{-1} m^{-2} Hz^{-1}
C	Absolute intensity calibration	
c_p	Specific Heat Capacity	J/kg K
c	Speed of Light	m/s
CMD	Count mean diameter	nm
C_{Abs}	Absorbance Cross Section	m
c_v	Specific Heat Capacity at constant Volume	J/kg K
$\bar{c}$	Average Gas molecule Speed	m/s
D_{ab}	Diffusion Coefficient	m^2/s
d_p	Diameter of Particle	m
d	Focal Spot Size	mm
$E(m)$	Refractive Index Function for Absorption	-
ELS	Elastic Light Scattering	
$F(t)$	Laser Temporal Profile	
F	Laser Fluence	J/m^2
f_v	Soot Volume Fraction	ppm
$G(x)$	Gaussian Function Equation	
G	Geometry heat transfer factor	
h	Planck's Constant	$6.6262*10^{-34}$ J s
Kn	Knudsen Number	-
I_o	Light intensity with no extinction	
I_T	Transmitted light intensity	
k_B	Boltzmann's Constant	$1.3806*10^{-34}$ (m^2 kg)/(s^2 K)
k_g	Gas heat transfer coefficient	

k_a	Rate Constant for oxidation at A sites on the particle surface	(1/ s cm^2 atm)
k_b	Rate Constant for oxidation at B sites on the particle surface	(1/ s cm^2 atm)
k_{Ox}	Overall Rate constant for Oxidation	(1/s cm^2)
k_z	Rate constant for surface oxide formation at A sites	(1/atm)
M	Mass of primary soot particle	kg
M_{sv}	Molecular Weight Of Soot Vapour	kg/mole
LPLII	Long pulsed laser induced incandescence	
N_A	Avogadro's constant	$6.022*10^{-23}$ $mole^{-1}$
Np	Number of density of aggregates per unit volume	
N_2	Number density of atoms in excited state for fluorescence	
N_{SV}	Mole number of soot vapour	
n_p	Average number of primary particles per aggregate	
Q_f	Heat Transfer Rate	W
Q_{Vap}	Vaporisation Heat Transfer Rate	W
Q_{Cond}	Conduction Heat Transfer Rate	W
Q_{Rad}	Radiation Heat Transfer Rate	W
Q_{Abs}	Absorbance Heat Transfer	W

	Rate	
PAH	Polycyclic Aromatic Hydrocarbon	-
P	Pressure	Pa
P_{o2}	Partial Pressure of Oxygen	0.209 atm
R_O	Universal Gas constant	J/ mol K
T_p	Temperature of Particle	K
T_g	Temperature of Gas	K
S	LII Signal	W/m
P_{VS}	Pressure of Soot Vapour	
S_2	Fluorescence Magnitude	
$FWHM$	Full Width Height Maximum	S
W_1	Average Molecular weight of air	g/mole
α	Thermal Accommodation Factor	-
$\propto$	Fraction of area of annulus	
σ	Variance in Gaussian Function	
σ_g	Variance of Geometric width of the particles	
μ	Expected Value in Gaussian Function	S
ε	Emissivity Coefficient	-
ϕ	Equivalence Ratio	
β	Vaporisation Coefficient	
$\propto$	Decay Rate	s^{-1}
ρ_p	Density of Particle	kg/m^3
λ_{mfp}	Mean Free Path	m
τ	Decay Time	S
Σ_{VS}	Macroscopic Cross Section	m

ΔH_{vap}	Heat of Vaporisation of Soot	J/mole
ΔH_{ox}	Enthalpy of Oxidation reaction	J/mole
χ_A	Mass Fraction Annealed	-
γ^*	Heat Capacity Ratio for gas surrounding the particle	-
λ_S	Excitation Wavelength	nm

1 Introduction

1.1 Combustion in today's world and thesis outline

Energy consumption in the world is rising every year.[1] The EIA in 2017 predicts 28 % increase in the world energy use by 2040 and that fossil fuels will still account for more than three quarters of the world energy consumption by then.[2]

A number of sources have produced an outlook of scenarios for the primary energy consumption by fuel and even in the best case scenarios, the outlook still has oil and gas to be very significant energy providers.[3,4,5] This demonstrates that even the most environmental friendly resources state even with a best case scenario; they will still be far from enough to producing enough energy to meet the world's energy supply. This means that oil and gas will still be a main source of energy production. In other words combustion will still be the main way of providing energy however combustion poses a problem in the pollutants that it creates.[6]

The main pollutants from combustion are typically carbon monoxide, nitrogen oxides and particulates also known as soot. These emissions are damaging to the environment and health. It is well reported in media outlets such as the BBC, in the UK, cities such as London and Glasgow rank below average in the soot pollution league in the European city ranking.[7] Soot pollution causes damaging effects on the public health.[8] It was the 1920's was when the impact of soot was first studied, showing the impact of the inhalation of soot and the link to lung cancer. Along with damaging effects to human health, the release of pollutants into the atmosphere is a larger problem. Highwood and Kinnersley[9] state that the effects soot has on the climate are multiple. One of effects is the breakdown of soot changing the properties of the solar radiation at the Earth's surface. Importantly, soot pollution accounts for over one quarter of the total pollution in the air. Numerous legal regulations have been enforced for combustion processes releasing pollutants into the atmosphere such as the Air quality Control Act,[10] but is necessary to understand of combustion processes in order to better understand combustion. The development and improvement of accurate measurement techniques during combustion is important to better understand combustion processes and reduce the damaging effects of soot pollution. Combustion process details could only be assumed before laser-based diagnostics.[11] At that time, researcher's hypothesis on combustion and pollutants were proved wrong by the results gathered by laser diagnostics. Emissions numbers and particle sizes from engines to be regulated better since improvements would lead to better instrumentation to identify key health hazards commercially by improvements in measurement using laser diagnostic techniques.[12,13] One of the key diagnostics used to measure soot within flame is laser induced incandescence (LII). LII can give information on the soot concentration and the primary particle size. The bulk of this work has been focussed on using this technique of laser induced

incandescence (LII) in flames and is concerned with the measurement and characterisation of a variety of flames under a variety of conditions as well as novel methods on how the LII measurement was done.

Chapter 2 discusses elements of soot formation and provides a short overview of the techniques used to acquire information about pollution formation going into detail about laser induced incandescence (LII), the technique that was used throughout this project.

Chapter 3 goes into detail about the laser induced incandescence modelling. The chapter shows details into the heat transfer components and how coupled equations can show the process behind LII. Production of a standard more allows for further development of the model which is used in chapter 7.

Chapter 4 describes the methodology behind using the laser induced incandescence technique. It goes into detail about how the equipment utilised and why certain pieces of equipment were suitable for laser induced incandescence imaging.

Chapter 5 shows the validation and characterisation of the methodology and the standard flat-flame burner used for soot calibration. Chapter 5 shows the results of measuring soot concentration within a flame using laser induced incandescence. The results will show the characterisation and comparison of a sooting flame. There is also an investigation into this flame into using a way to measure soot precursors using subtraction from two different signals. This was done in a standard laboratory flame since it is allows for more control of the flame and allow for measurements to be stable and reproducible.

Chapter 6 is an investigation into the heat transfer effects of the burner setup. It was hypothesised the temperature of the flame could be changed by varying the temperature of the stabilisation plate and the effect on soot formation was studied.

Chapter 7 uses the technique developed in the previous chapter but with a different excitation laser source. By changing the laser source it allows for another level of flexibility in being able to use this technique to measure soot pollution in a range of circumstances using a different type of laser. However, there are difficulties of using this laser and the chapter will discuss these downsides and the best ways to overcome them.

The increase in the need for sustainable energy using biofuels has become more evident. It is important to understand pollutant formation and combustion associated with using these types of fuels. Chapter 8 uses the techniques detailed in the previous chapters to then measure the soot volume fraction within a set of biofuel flames stabilised on a wick burner. These fuels are chosen to mimic wood combustion and were previously measured using LII and point measurement; imaging methods were used to overcome the disadvantages associated with point measurements.

The results produced throughout this thesis may in the future be used to as input for various combustion models for validation purposes. This thesis has a mix of experimental and some modelling results throughout.

2 Background on soot formation and detection

Over the last 50 or so years there has been much work done in the study of soot formation such as the developments and established pathways for soot formation.[14,15]

This chapter gives a brief overview into soot formation in the combustion process, the current accepted routes of soot formation. The chapter will also discuss the diagnostic techniques used to determine soot structures and properties and the advantages and disadvantages of these techniques.

2.1 Combustion and soot formation

2.1.1 Types of flames

Combustion involves two reactive components: the fuel and the oxidiser. The fuel contains the chemical energy which is liberated through oxidation. The exothermic reactions involved are complex even with a simple fuel. [16]

Combustion can either be premixed or non-premixed. Premixed is where the oxidiser is mixed before ignition of the flame. Non-premixed is where the fuel and oxidiser mix at the boundary layer. The advantage of premixed combustion is that there is much greater control of combustion. Non- premixed flames are more complex since the fuel to oxidiser ratio covers the range of rich combustion on the fuel side and lean combustion of the air side.[16]

In diffusion flames the oxidiser mixes with the fuel by diffusion. Therefore, the rate of reaction is limited by the rate of diffusion because of changes the structure of the flame when compared to the premixed flame. The work within this thesis has measurements of soot within a premixed laminar flame and non-premixed diffusion flames.

2.1.2 Equivalence ratios

In LII the most common fuel used is ethylene. Ethylene is commonly used in combustion research for its ability to produce controllable sooting flames as well as its availability of pure ethylene. The ethylene-oxygen complete combustion reaction is defined as:

$$C_2H_4 + 3\,O_2 + N_2 \rightarrow 2\,H_2O + 2\,CO_2 + N_2 \qquad \textbf{Equation 2-1}$$

One way of describing the fuel to oxidiser mixture is with the equivalence ratio (ϕ). If the fuel and oxidiser are burned completely it is said that the flame is stoichiometric. If there's an excess of fuel ϕ >1 it is said to be fuel-rich and if there's more oxidiser than fuel it is said to be fuel-lean ϕ <1.

$$\Phi = \frac{(\frac{n_{fuel}}{n_{oxidiser}})_{gas\ mixture}}{(\frac{n_{fuel}}{n_{oxidiser}})_{stochiometric}}$$ **Equation 2-2**

Where:

n_{fuel} and $n_{oxidiser}$ are the number of moles measured in the gas mixture of the stoichiometric conditions

The larger the equivalence ratio the higher the sooting propensity due to higher fuel to oxidiser ratio which causes more incomplete combustion to take place which causes unburnt fuel to become pollutants such as soot and produce more carbon monoxide. For this work it is important to understand how the equivalence ratio changes the sooting propensity changes.

2.1.3 Growth of soot within a flame

While there have been well-established chemical reaction pathways and physical processes for soot formation further investigation is needed for a better understanding and production of optimum combustion conditions within different fuels, burner types and the respective applications.[17]

The laser diagnostic technique LII used throughout this thesis is independent of the process of soot formation and depends solely on the concentration and particle size that is produced.

Soot formation and growth

The simple stages of soot formation and growth start with the molecular zone, particle nucleation, surface growth and coagulation and, finally aggregation which causes agglomerate formation. Soot goes through these stages along with reaction time. The soot formation starts with the pyrolysis of the fuel. The high temperature of the reaction zone breaks the fuel into smaller hydrocarbons.[18] There is an abundance of Acetylene in rich flames. Acetylene is a building precursor for polycyclic aromatic hydrocarbons, known as PAHs, which make soot particles. The next step is the production of aromatic hydrocarbons which grow with the addition of other aromatic hydrocarbons and other smaller hydrocarbons.[14] There are several different potential pathways from PAHs to nascent soot, which is typically around 1-6 nm though they aren't defined by their size. These particles typically have significantly more aromatic character than aliphatic and can maybe contain oxygenated species. [19] The soot particles then grow by addition of smaller hydrocarbon molecules in a process known as surface growth. Coagulation also occurs with surface growth and it is the reason why surface growth causes the particle to form in non-spherical shapes. The larger soot particles can then aggregate. Mature soot tends to be composed of primary particle sizes ranging from 10-50 nm with high levels of Carbon to Hydrogen, C/H ratios. One likely pathway for this is known as the HACA method.[17,20]

HACA

In the process known as the HACA method, which stands for Hydrogen abstraction carbon addition, these PAHs get larger with time combining with other PAHs or the other radicals present.[21] Figure 2-1 shows the mechanism of the PAH growth. Particle formation occurs and because of surface growth and coagulation the soot grows. However, over time, the growth on the surface of the soot will be less because of the reduction in Hydrogen atom concentration. The particles join together through aggregation which is where the soot particles form aggregates of smaller soot particles to form larger particles which are approximately several hundred of nanometres in size and not spherically shaped. Soon the soot particles oxidise which can reduce the particles mass and size.[17,18,22]

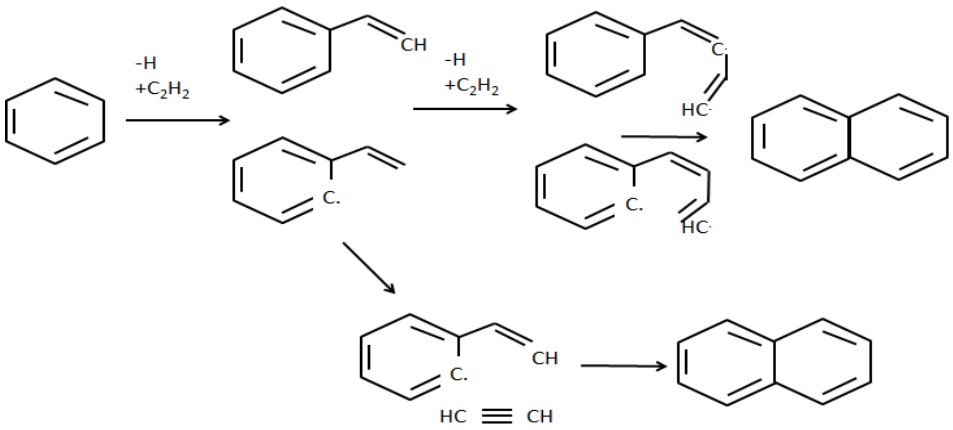

Figure 2-1: PAH growth with the HACA mechanism adapted from Davis et al.[23]

Nascent soot

Nascent soot is soot which has just been freshly nucleated. Nascent soot has typically lower C/H ratio and can be potentially liquid. It is important for soot formation because it represents the area of the growth phase where the products are between gas molecules and particulate matter. It was discovered that this area has what is called a 'dark zone' where optical technique measurements show a signal meaning that the soot particles are not at a large enough mass to measure by typical LII. These particles tend to be below 10 nm and absorb light differently when compared to larger particles.[18,24] When measuring nascent soot particles using laser diagnostics a wavelength longer than 700 nm should be used due to the stronger wavelength dependence on absorption. The formation of nascent soot is an important step in soot formation. Modelling and other studies focussed in this region show the need for improved experimental techniques to help develop these models.[25] Premixed flames have given and continue to give a lot of data on nascent soot formation and with the improvement of certain in-situ

techniques this area of soot formation can be studied more accurately and improved models could maybe be produced.[26]

2.1.4 Soot diagnostics

Soot produced in a flame can be characterised using two categories of technique, probe and optical methods. Discussed here is a quick overview of some techniques used in the field of soot diagnostics, followed by a more extensive discussion on laser-induced incandescence.

Probe techniques

Using probe techniques over optical techniques is useful for gathering data sensitively and selectively. Transmission electron microscopy uses a sample of soot from a flame to gather information. Typically for this technique is to use a wire mesh is inserted into the flame which captures soot thermophoretically. The mesh can be removed and the soot stuck on the mesh can be imaged using transmission electron microscopy (TEM). TEM typically uses beams of electrons transmitted through the soot sample. This method typically gives information about primary particles sizes as well as aggregates. Using bright and dark field TEM Vander Wal[27] was able to show the crystalline structure of soot produced from a flame. Dark field is when the image in the field is literally dark, and bright field is when there is a light background. Dark field is when the image in the field is literally dark, and bright field is when there is a light background and a schematic diagram of each setup can be seen in Vander Wal.[28] Results showed that the two TEM methods appear to complement each other for qualitative measurements. Vander Wal[28] also compared optical results of LII and LIF using Bright and Dark field TEM. Using TEM Vander Wal was able to show clear and similar trends of the soot particle sizes when compared with LII and LIF optical technique measurements.

Scanning Mobility Particle Sizing (SMPS) was first described by Wang and Flagan[29] for aerosol analysis. SMPS cam measure the particle distribution of particles from 5 nm to 1 μm with concentrations between 10^6 and 10^{14} particles per m^3. Kruger et al[30] has carried out studies comparing Laser Induced Incandescence results with SMPS. These results show that laser heating during LII has an influence on the soot particle size distribution.[30] SMPS measures the particle size when moving in air which is affected by an electric field and provides a measurement on the total size of the particles whereas LII is related by the primary particle diameters meaning that when comparing SMPS and LII the particles are best not to be aggregated.[30]

Probe techniques results can give interesting information on the soot morphology however the main problems with probe techniques are the flame may be disturbed when sampling, thus interfering with the recorded data as well as the time it takes to produce and analyse the results is much longer than optical techniques.[11]

Optical techniques

Non-invasive optical techniques have been used in the investigation into soot formation. These techniques typically consist of various spectroscopy methods and light scattering techniques. Optical techniques have advantage over probe techniques as typically, measurements can be taken instantaneous. On the other hand, probe techniques have a lag between removing the sample and analysis and are invasive to the flame, which may perturb combustion and risk uncertainty of the sample not being representative of the measured flame. [31]

For LII there is a critical need for supplementary diagnostics to relate to unanswered questions related to soot formation as well as important LII parameters such as temperature and pressure, and gas phase combustion constituents.[17]

One method used to study particulate matter is light scattering methods. Scattering techniques typically work by having a fraction of laser light scattered by hitting the soot particle. Elastic Light Scattering (ELS) has been used combined with Laser Induced Incandescence to allow for a quantitative two-dimensional determination of morphological characteristic properties such as aggregates of the soot as shown in Reimann et al.[32] Reimann et al.[32] used a combination of light scattering and LII to measure two-dimensionally soot properties such as aggregates along with soot volume fraction. This setup used 532 nm laser light and a typical LII setup for LII measurements and for ELS measurements a similar setup was used except a continuous laser Nd:YAG beam was used as this provided a better laser beam profile. The results show successful 2-D measurements with some overlaying assumptions about the particles measured. This technique showed the results agreed with microscopy results .Typically elastic light scattering works by measuring the scattered laser light from a soot particle with the detector placed at an angle to the measurement plane, the intensity of the Rayleigh scattering can then be measured. Lee et al.[33] used a combination of LII and Laser Induced Scattering with previous calibration methods to find the soot volume fraction, mean diameter size and number density in a laminar diffusion flame. [32,34,35,36]

Photoacoustic techniques have been shown to be capable of measuring soot volume fraction across a range of conditions. These are line of sight techniques where the signal is path integrated across the flame. Photoacoustic detection works by the absorption of laser energy leading to change in the heat transfer, this produces an acoustic pressure wave and using laser modulation the intensity can be measured. Humphries et al.[37] show the intensity of the photoacoustic signal has been calibrated and compared with LII signals to produce a reliable height above burner (HAB) profile.[37]

2.2 Laser Induced Incandescence (LII)

2.2.1 History of LII and development of LII

For the study of soot volume fraction and particle sizing laser induced incandescence (LII) has become widely used. Detection of soot by LII requires that the soot is able to absorb the laser at the specific wavelength and the particles are mature enough to be heated without vaporising or undergo photolysis therefore incipient soot is difficult to measure by LII.[17] Advances in LII have led to particles as small as 2.5nm and possibly 2nm being detected with changes in soot primary particle size and concentration being resolved till about 10 nm. [24 25] Once the mature soot particles have been heated up to a hot enough temperature to emit broadband light. The intensity of this light can then be used to determine soot volume fraction.

The formation of soot has been studied using laser induced incandescence since the mid 1970's. The technique allows for soot volume fraction to be determined and particle sizing to be carried out subject to various assumptions about the soot properties (further discussed in this chapter). LII is a laser diagnostic technique that works by using light energy produced by a laser, either pulsed or continuous, to heat particulate matter (mainly soot) to heat up and the incandescent light produced from this heating can be measured.

Previous work focussed on the development and application on LII has led to temporally as well as spatially resolved data to be gathered when measuring LII within a flame. This has led to multiple research groups measuring a variety of these flames and conditions using LII.

Eckbreth[11] first discovered LII when carrying out Raman spectroscopy diagnostic experiments, a source of important interference, this lead to particle size being related to the decay of incandescence through time. Melton then presented a heat transfer model supporting subsequent work to measure soot volume fraction and investigate soot formation using LII experimentally.[11]

To ensure that modelling data as well as experimental data was comparable between groups several conditions when making standard measurements was set out. These conditions set known as 'target flames' which have a well-defined set of conditions to allow for comparison and modelling. Even with these set conditions there still is some choice in parameters in models such as refractive index, soot density etc. which can lead to massive differences and large error margins so this is why it is important when modelling and calculating results from experiments to wisely choose these factors. There have been efforts within the LII research community to improve comparisons between lab models and experiments.[38]

LII has been carried out in a number of different conditions and environments. Hofmann et al.[39] have demonstrated using LII at higher pressure. The investigation was to find the influence of pressure on

factors such as laser fluence and time resolved detection. This investigation found that the pressure only has a minor influence on two key components of LII heat transfer components (vapourisation and conduction). This was inconsistent with expectations and so this shows the need for modelling as well as experimental investigations to truly understand the soot behaviour.

Current research and future directions of LII includes research such as the determination of detection limits for volume-fractions as well looking to narrow the uncertainties associated with LII.[40]

2.2.2 LII theory

Described as the *'workhorse for soot volume fraction and mass concertation determination in combustion'* [40] Laser induced Incandescence works by using a pulsed laser which heats the soot particle up to near sublimation temperatures. When the soot particle heats up it emits more intense visible light spectra over a short period of time, the soot particle then cools down using key cooling mechanisms changes the signal over this short period of time. Since the soot acts as a near blackbody the spectrum of wavelength of light emitted is dependent on the temperature although since the soot doesn't explicitly behave like a blackbody there is an emissivity coefficient associated (ε). The intensity of light emitted by these particles is proportional to the volume fraction of particles and the time it takes for the light to decay is related to the primary size of the soot particles. This is based on the fact that the soot particles are all heated to the same temperature and the prompt detection for the measurement of the soot volume fraction. Since the soot particle diameter(d_p) is smaller than the wavelength it follows the Rayleigh approximation where $\pi d_p / \lambda << 1$ meaning it absorbs the laser energy,where d_p is the primary particle diameter.[39,41,42]

The emitted light follows Planck's law:

$$B_\lambda(T_S) = \frac{2hv}{\lambda^5} \frac{1}{e^{-\frac{hv}{k_B T_S}} - 1}$$ **Equation 2-3**

Where:

B_λ is the Spectral Radiance (W sr^{-1} m^{-2} Hz^{-1})
h is Planck Constant (J s)
c is the speed of light (m/s)
λ is the Wavelength (m)
k_b is the Boltzmann Constant((m^2 kg)/(s^2 K))
T_s is the Temperature of the Soot Particle (K)

Soot volume fraction can be described by:

$$f_V = \frac{\pi}{6} Npn_p d_p^3$$ **Equation 2-4**

Where:

f_V= Soot Volume Fraction (ppm)

Np=Number of density of aggregates per unit volume

n_p= average number of particles per aggregate

d_p= particle diameter (m)

Since there is a close linear relationship between the peak LII signal and the soot volume fraction since it is a near blackbody, it can be useful in finding out the soot volume fraction within a flame. This shows that larger particles have a much stronger effect on the resulting signal than the smaller particles Equation 2-5 shows an early approximation of the LII signal by Melton.

$$S_{LII} \propto Nd^{3+\frac{0.154}{\lambda_{det}}}$$ **Equation 2-5**

Heat transfer from the soot to the surrounding gas such as conduction and evaporation as seen in Figure 2-2 and by using the decay in signal, it is possible to find a time decay for the particle which can then be used to infer particle size. Since smaller particles have higher surface to volume ratio, the smaller particles cool faster than the larger particles and the relative signal of smaller particles compared to larger decreases faster with time which could be a problem when using a gated measurement system for soot volume fraction measurements.[43]

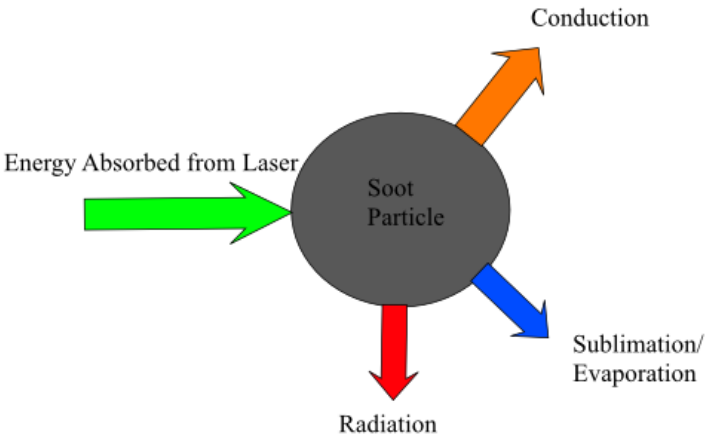

Figure 2-2: Typical heat transfer components of LII in soot

An example of a typical model of the signal the soot produces can be seen in Figure 2-3 with individual heat transfer component rates shown in Figure 2-4. More information on how the model was generated is given in chapter 3.

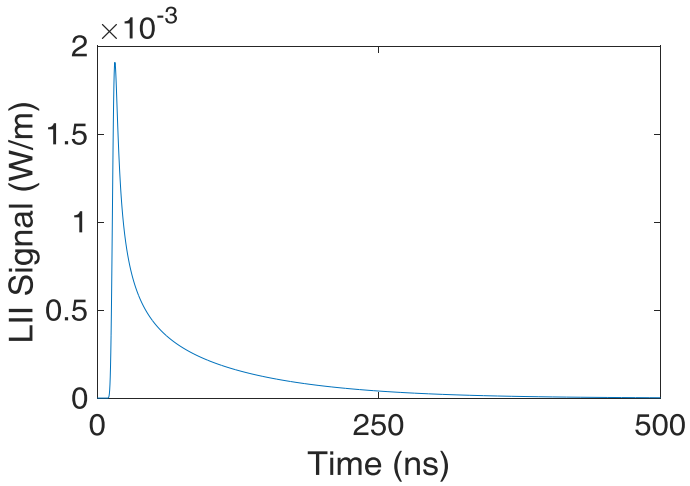

Figure 2-3: Example of modelled LII signal over time[44]

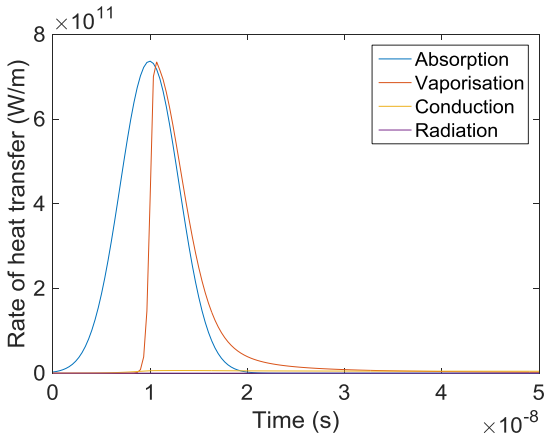

Figure 2-4: Modelled heat transfer rates

One problem of LII measurements is that there is possible interference from PAH's. These PAHs typically fluoresce when using 532 nm excitation wavelength.[45] One way around this is to use an appropriate detection filter which in the work done throughout this thesis uses a 450 nm since this is a lower wavelength than the excitation wavelength and since the fluorescence is red shifted meaning the signal produced will be usually higher in wavelength will cause a reduction in interference. Using 1064nm Nd: YAG laser for excitation source reduces fluorescence interference since using this laser

wavelength means that there is likely no interference from fluorescence from other species since the PAH species don't absorb at this wavelength.

Using a different excitation wavelength can affect at how the particle absorbs light energy and therefore this can give a different fluence curve. A fluence curve is the response of LII signal to change in energy per unit area and helps describe the relation of signal to soot volume fraction. Another issue is that the signal changes with detection wavelength. Therefore care has to be taken in experiments to make sure that the signal being measured is comparable.[46]

Particle sizing using time resolved LII (TiRe-LII)

The rate of cooling of the soot particle is related to the size. By finding time resolved (TiRe-LII) profiles of the LII signal can be analysed to find a decay time which theoretically is related to particle diameter. [44] The larger the soot particle the longer the temporal decay time meaning that they cool slower. Smaller particles shorter temporal decay time meaning that they cool faster. The larger particles cool slower than the smaller ones due to a smaller surface area-to-volume ratio. Since conduction typically is the main heat transfer mechanism the conduction is modelled to fit the decay time[47,48,49] To find the decay time an exponential decay can be fitted to the natural log of the LII profile. The fit is done at around 100ns after the peak signal so that the main method of heat transfer between the soot particles is conduction and effects such as vapourisation can be neglected. These results can then be used to help model particle sizing, however the model in use could be more complicated as well as inaccurate due to parameters such as particle density, refractive index etc.

$$\tau = A\exp(-\propto t) \qquad \textbf{Equation 2-6}$$

Where:

A is a constant

$\propto$ is the decay rate(s^{-1})

τ is the decay time(s)

The decay time τ can be used to infer information about the particle size. For premixed flames the decay time is lower as examples presented by Axelsson et al. [50] Axelsson et al.[50] demonstrated using a PMT time resolved profile in a premixed laminar flame to produce a technique for soot particle size measurements. To experimentally find primary particle sizes, a line was fitted to a log decay of the LII signal 150 ns after the peak LII signals. Results show decay times produced for two different heights of stabilisation plates. These decay times can then be used to estimate particle size. Particle size was compared with scattering results and it was found that at lower heights there was good agreement between the two techniques however at larger HABs where the soot particle was larger there was a

disagreement of around 18 %. This has been put down to aggregation as well as an uncertainty in the flame temperature.

2.2.3 Absorption function E(m)

For LII measurements there is a need to know and understand the optical properties of the soot. One of these optical properties is the widely debated absorption function- E (m). There has been shown to be a high variability between LII groups chosen value of E (m). The E (m) factor depends on many things such as soot maturity and spectral dependence. E (m) describes the efficiency of light absorption of the soot particle. Schulz et al.[51] shows the variability of different groups derived absorption functions and how the differ between wavelengths. For the work presented here the E (m) value used was the 0.3 +/- 0.06 was deemed to be acceptable since it is approximately constant from the visible to near-IR region.[52]

Recent discussion at an LII workshop[53] has suggested 0.36 or 0.38 an acceptable value for mature soot. Mature soot is composed of small primary particles around 10-50 nm in diameter which can be bound in aggregates of different size.[54]

2.2.4 Fluence curve

The fluence curve is important to laser induced incandescence as it describes the signal to the energy per unit area of the laser pulse. Depending on the flame and how the signal is collected this can have a dramatic effect on the fluence curve. The collection of signal depending on the measurement such as measuring the curve using prompt or gated signal. With gated signal the influence of fluence on the gated signal is more severe. [55] [56] [24] Modelling shows this in chapter 3.

Bladh et al.[24] shows a change in the fluence curve where the leaner flames don't reach a plateau region whereas the more fuel rich flame does reach a plateau. This is believed to be because the particles are more nascent and just produced and that the optical properties and physical properties of this type of soot is different from mature soot.

2.2.5 Calibration of LII signal into soot volume fraction

Extinction

In this thesis when extinction is mentioned, it is solely a process which uses absorption of light by soot particles and by using the beer lambert law is able to calibrate into a soot volume fraction. The calibration relies on the absorption function which as discussed previously has a large uncertainty attached to the value around 20 % in the absorption function. Since this is such a large uncertainty it is the main source of uncertainty in extinction.

When doing extinction measurements it is important to avoid scattering so that the only loss of intensity is caused by extinction. Scattering is where the light is displaced in different directions instead of being

absorbed. To avoid scattering the wavelength of light used should be chosen to avoid scattering regimes. For soot using an infrared wavelength will typically avoid most scattering. Using this wavelength will also avoid absorption from PAH interference.

Extinction works by measuring the laser intensity (I_0) without the flame and then measuring the power after the beam has been through the flame (I_T) and seeing a decrease in the power due to soot absorbing some of the laser energy.

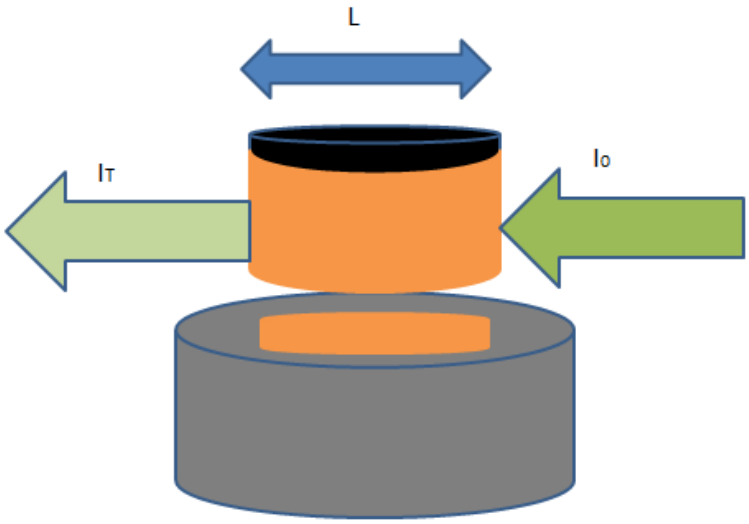

Figure 2-5: Extinction measurement, Beer-Lambert law example showing the laser propagating through the flame and decreasing in output power due to extinction

Figure 2-5 shows an example of how the extinction measurement works. The Beer-Lambert law uses the relationship of the amount of substance to the amount of light attenuated by absorption. Using the Beer-Lambert law the soot volume fraction can be calculated for soot volume fraction:

$$\ln\frac{I_T}{I_0} = -K_e\frac{f_v}{\lambda}L$$ **Equation 2-7**

Where:

λ is the wavelength,
K_e the dimensionless extinction coefficient
L the length of the absorbing medium (the diameter of the flame).

The soot concentration along the optical path is assumed to be constant and assumed no scattering of the light takes place. [50,57]

K_e can be estimated to be:

$$K_e = -6\,\pi\,E(m) = 6\,\pi\,Im(\frac{m^2-1}{m^2+2}) \quad \textbf{Equation 2-8}$$

$$K_e = \frac{36\,\pi\,n_\lambda\,k_\lambda}{(n_\lambda^2 - k_\lambda^2 + 2)^2 + 4\,n_\lambda^2\,k_\lambda^2} \quad \textbf{Equation 2-9}$$

Where n_λ and k_λ are the real and the imaginary parts of the complex soot refractive index m, respectively.The absorption function E(m) has been discussed earlier and is dependant on wavelength and the properties of the soot.

Overall, when combining equation for extinction and absorption, since it is assumed there is no scattering, the equation can be given as:

$$f_v = \frac{\lambda}{6\,\pi\,L\,E(m)}\ln(\frac{I_0}{I_T}) \quad \textbf{Equation 2-10}$$

Overall the accuracy of LII calibration based on extinction is limited by uncertainties related to the soot extinction coefficient (the absorption function) and by uncertainties in the soot optical property variation within a given combustion or flame system such as the soot index of refraction.[58, 57]

While extinction is commonly used, the technique is has disadvantages because the calibration occurs not simultaneous with the LII signal recorded, meaning that the flame may change if unstable or if there is any changes in the conditions However, because of the simplicity and easy-to-use nature, there have been multiple experimental setups that have been used for this technique[57]. Correlating the relative soot volume fractions, i.e. LII intensities, with the average soot volume fraction of the integral extinction provides the following expression for the calibration constant:[59]

$$C_{Cal} = \frac{\lambda \ln\left(\frac{I_T}{I_0}\right)}{6\,\pi\;E\,(m)\int_0^L S_{LII}(x)dx} \quad \textbf{Equation 2-11}$$

This technique is discussed more in the methodology and section, where it has been implemented to calibrate soot volume fraction throughout this project. Extinction is a simple process that has been demonstrated useful in many studies. Unlike natural luminosity measurements extinction does not rely upon the temperature of the soot involved.[60]

Many studies have decided to use extinction methods and incorporate them further into the LII setup. Quay et al.[35] used extinction and scattering to find an agreement in profiles of soot volume fraction which negates the need for the conventional line of sight extinction method. Axelsson et al.[58] have demonstrated a novel measurement technique for two-dimensional measurements of soot volume fraction and particle size by using a combined method of simultaneous LII and extinction. The LII signal is collected by using a 1064 nm excitation wavelength where extinction uses a 532 nm wavelength. This method worked on stable flames successfully however with turbulent flames, the particle sizing must use either of two different cameras or a fast enough camera to execute two images within a time of a few hundred nanoseconds.

Two-colour LII

There has been multiple ways of measuring the peak soot temperature. The main way of measuring this is to use a form of thermometry known as 2-Colour LII. Unlike standard pyrometry, as shown by Cignoli et al.[61], there is no need for abel inversion and corrections based on position. Two-colour LII soot volume fraction calibration is advantageous as it reduces the error in soot refractive index E(m).[62,63]

Since with a near-blackbody the light emitted has a more dominant wavelength caused by the temperature by being able to take a ratio of the signal at 2 different detection wavelengths at their temporal peak, indicating that the peak temperature of incandescent soot particles is almost constant if the index of refraction is assumed not to vary significantly.[64] By using two different detection wavelengths using the expression: [63]

$$T_p = \frac{hc}{k_B}\left(\frac{1}{\lambda_2} - \frac{1}{\lambda_1}\right)\left[ln\left(\frac{S_1 C_2 \lambda_1^6}{S_2 C_1 \lambda_2^6}\right)\right]^{-1} \quad \textbf{Equation 2-12}$$

Where:

λ_2 is the detection wavelength of the second detector (m)
λ_1 is the detection wavelength of the first detector (m)
C_1 is the calibration constant of the detector for the first wavelength
C_2 is the calibration constant of the detector for the second wavelength
S_1 is the LII signal at the first wavelength
S_2 is the LII signal at the second wavelength

Knowing the flame temperature, the soot volume fraction at a local point can then be obtained without the need for correlation to another measurement of soot like extinction, by:

$$f_v = \frac{S}{C\ \lambda w_b} \frac{(\lambda^6 \left(\exp\left(\frac{hc}{k_b\ \lambda\ T}\right) - 1\right)}{12\ \pi\ c^2 h\ E(m)}$$

Equation 2-13

S is the LII signal at the wavelength measured

C is absolute intensity calibration

w_b is the width of the laser beam

This method for calibration could be used either for point measurements and imaging measurements. De Iuliis et al.[65] demonstrated a method for 2-colour LII for measurement of absolute volume fraction within a flame. They use a PMT to produce a spatial profile of an ethylene diffusion flame. They used a tungsten ribbon lamp for temperature calibration. Potenza et al.[64] used two-dimensional two-colour LII in a laminar diffusion flame to find the primary particle size from the temperature decrease. 50 images for each point were deemed as acceptable to provide enough images to find reliable results.

However, because of the complexity in calibration such as having to use 2 expensive intensified CCD (ICCD) cameras and temperature calibration with tungsten lamp as well as the uncertainty of the wavelength dependence of the absorption function is not well known this technique hasn't been used in this project so far.

2.2.6 Methods of LII signal detection

The way the signal is measured can affect the outcome of data that can be found using LII. Typically the signal is measured by imaging or point measurements.

Imaging

LII signal can be collected using imaging techniques. This mainly involves uses a gated intensified CCD (ICCD) camera.

Using an intensifier to amplify the amount of light collected by a CCD chip, which is placed behind the intensifier allows for low levels of light signal to be collected. The function of the image intensifier is the multiplication of the incoming photons allow for measurement of single photons .The intensifier is typically consists of a photocathode, micro channel plate (MCP) and a phosphor screen. The photocathode converts the photons to electrons, these electrons then are guided through the MCP, the MCP multiples the electrons which uses the phosphor screen to convert the electrons produced back to photons. The intensifier has a controllable gain which determines how much the photon signal is increased; this enables the ICCD camera to take images at extremely low light conditions. The photons can then be guided to the CCD, which corresponds to the pixels shown in the readout. The chip is then

able to convert the number of photons to a single digital value by creating electron-hole pairs on the CCD and creating a charge that can be accumulated and converted to the digital value.[66]

The intensifier also allows for short time integrals of signal to be collected and the amount of time that the intensifier is open to collect signal is known as the gate. The relatively short gate is able to be achieved as a quick change in voltage in and across the photocathode allows the electrons to escape. For low gain levels the signal will not be amplified enough and no signal would be shown on the digital readout. [67]

An advantage of an ICCD camera over normal CCD is the ability to capture signal over a short period of time. The ability to use short gate using an ICCD camera allows for critical discrimination of the background luminosity of the flame. Once the signal is collected with respect to the gate time, the signal is then released to the CCD surface by phosphor decay and then imaged onto the surface.[68, 69]

Sun et al. [70] use an experimental setup where 4 ICCD cameras are setup to take a simultaneous single shot and find the time resolved profile of the flame using just a single laser shot. The information from this experiment can then be used to calculate soot particle size and soot volume fraction. Tian et al [71] show an example of two-dimensional , two colour time resolved LII(2D-2C-TiRe-LII). They were able to produce soot temperature and soot primary particle sizes. They achieve temporal resolution by shifting the gate of the ICCD camera by 20 ns for each individual measurement.

Point measurements

Another way to measure the time resolved profile of LII is through the use of a Photomultiplier Tube (PMT). The PMT works by the photons emitted from LII causing an emission of electrons caused by the photoelectric effect. The PMT is able to then amplify and cause an electric current which can then be measured and examined using an oscilloscope. The PMT allows for temporally resolved measurements of the LII signal to be taken with relatively low signal to noise ratio.[72,35]

2.3 Laser induced fluorescence (LIF) signals from LII images

2.3.1 Introduction

Laser Induced Fluorescence is a laser diagnostic technique that is commonly used in combustion for the quantitative measurement of specific species. LIF has the ability to identify small molecules within the flame as well as being able to determine a temperature of the flame, without the need to be invasive to the flame using a probe.[16]

Being able to monitor these smaller molecules is useful for the understanding of flame chemistry including through their role as precursors to PAH formation. The size of aromatic structures increases the wavelength of emitted light increases. Therefore LIF can be used to identify where larger molecules

are and the development of soot formation, it is expected that larger PAH will be found at larger HABs and smaller PAHs will be found at lower in the flame.[73,74]

2.3.2 Laser induced fluorescence theory

Fluorescence emission is achieved by a specific molecule absorbing energy which causes it to be excited to a higher energy level. The molecule will then have some energy loss through non radiative transitions, and then then the fluorescence light emission brings the molecule back to a ground state. The energy emitted from fluorescence is lower than what is absorbed and this causes the wavelength emitted to be 'red-shifted' as the wavelength is longer. An example of these transitions can be seen in Figure 2-6.[75]

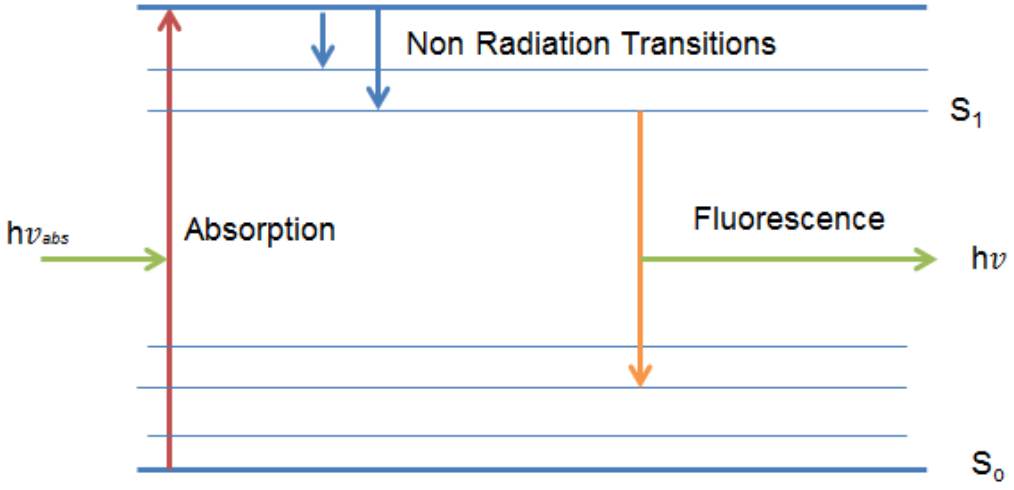

Figure 2-6: Energy level diagram, fluorescence emission description

The problems which are evident during fluorescence may be contributions to the relaxation of the molecule by processes such as quenching and when trying to produce a quantitative signal must be taken account for. It is found is that PAH concentration is found to not be proportional to the LIF signal because of the temperature dependence of quenching as well as having signal from multiple species. The LIF signal consists of multiple signals from different PAH molecules so it can't be used to identify specific molecules however it can be used to identify a group of molecules through size. Fluorescence measurements overcome the disadvantages of absorption spectroscopy methods by imaging the light emission rather than the transmitted light, fluorescence is a zero base line technique, meaning that it does not measure the fractional change-which measures small change in a large value meaning that fluorescence is more precise and not being a line of sight technique which means that with fluorescence spatial inhomogeneity can be resolved. [73]

2.3.3 Fluorescence from subtracted LII signal

It would be advantageous to imply fluorescence signal from an LII signal. Previous work within the group have used signal from incandescence and fluorescence at two different wavelengths. Since fluorescence isn't expected to occur at 1064nm 1st Harmonic of the Nd: YAG laser and expected to occur in 532nm 2nd harmonic of the Nd: YAG laser, the temporal signal was gathered and the peak values can be subtracted to give the fluorescence signal produced. It is indicative that it is the fluorescence contribution to the signal other than the laser pulse because the FWHM of the fluorescence signal is around 16ns whereas the laser FWHM is about 5-7 ns. This shows the importance of being able to use other wavelengths to give information of fluorescence in flames may be difficult to measure fluorescence due to the larger soot volume fraction. For this type of experiments to work the fluence has to be matched to ensure empirically the same signal is produced after the fluorescence lifetime since because the fluorescence lifetime is short it only affects the point of peak signal in the LII+LIF signal. Advantage of this optical technique is the ability to measure the whole soot formation process.

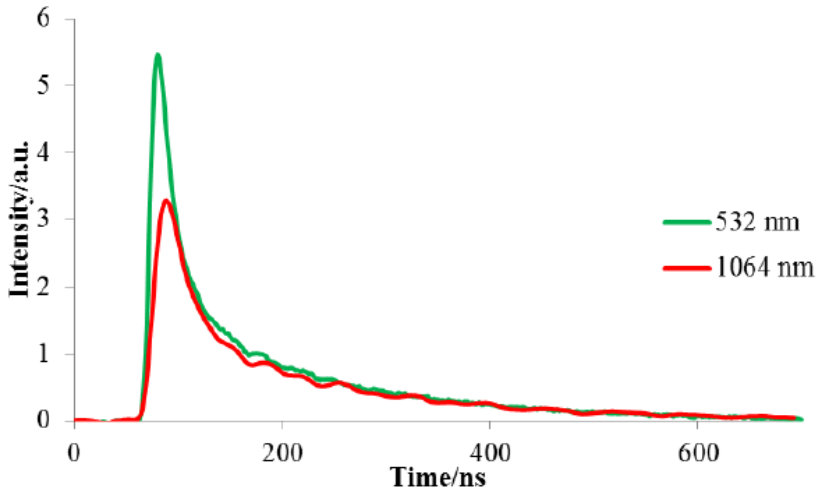

Figure 2-7: Comparison of Signal at 2 different wavelengths for the same equivalence ratio copied from Dunn[72]

Vander Wal has shown 2-D images by simultaneous combined LIF-LII signal from 266 nm and 1064 nm excitation wavelengths.[76] Smyth et al.[77] state that it was difficult to visualise PAH fluorescence measurements only using standard one colour. While this group had previously only done point measurement some other groups have used imaging to subtract LII to infer LIF signal. These signals can be used to infer the size of the fluorescing particles. Schoemaecker et al.[68] was able to use the differences in LII signals from two images with two different excitation wavelengths and produce and image of the PAH fluorescence within a diffusion flame. Quantitative values were found for soot volume fraction as well as PAH concentration in a 2-D resolved flame. These results show that the PAH

concentration occurs at lower points within the flame Shaddix et al.[78] also took simultaneous PAH PLIF and planar LII measurements. They showed in a turbulent flame that near the top of the flame where there is a strong LII there is a low PAH LIF signal with a larger PAH LIF signal lower down in the flame.

Meyer et al.[79] has a setup which allows for simultaneous planar LII, OH PLIF and Mie-Scattering in a swirl-stabilised combustor. The setup consists of splitting a 532 nm Nd:YAG laser pulse into two separate beams. One laser is used for exciting the LII and the other to send to a dye laser to produce a laser beam wavelength at 308 nm that will cause OH fluorescence.

3 Description of modelling laser induced incandescence

3.1 Introduction to LII heat transfer modelling

By being able to model LII signal it gives the chance to compare to results and improve data sets and test hypothesis about soot formation. Considerable effort has gone into modelling laser induced incandescence because by being able to accurately model LII can give information on primary particle size and even soot volume fraction. Most LII models work by accounting for heat and mass balance equations. Michelsen et al[43]. shows a comparison of many different models and shows how the difference in how some variables and assumptions such as the method of calculating vapourisation or how the density of the soot particle changes with temperature, can lead to large differences in the final signal generation output.

In MATLAB been developed and further implemented for LII. This model was found to be like other models in with it follows the main components of heat transfer with the ability to add or reduce the amount of heat transfer components depending on the assumptions that is made. With the purpose of a creating a standard working model, this can then be developed to produce a model comparing long-pulsed LII modelling as discussed further in the long-pulsed LII chapter.

3.1.1 Assumptions

For the standard version of the LII model used a few assumptions would have to be in place to start with[44]:

- All primary particles are spherical
- The primary particles are monodisperse, meaning they are all the same size.
- No chemical changes to the particle as a result of laser heating
- Energy is equally distributed throughout the particle, meaning that it is the same temperature at every position in the particle.
- The particles surface is stationary and vapour is carried away by diffusion.
- Vaporisation is from the entire surface of the particle.
- Any vapour produce does not affect the signal received from the particle.
- Carbon Soot assumed to consist of C_1-C_{10} carbon chains
- The gas temperature of the flame was assumed to be constant and not change over time

3.2 Heat transfer components

LII models are based on the consideration of various models of heat transfer. This section will discuss the standard implementation of this model of these heat transfer components and how they are quantified, what they mean and their effect on the overall model. The typical method is to solve heat balance equation using the Runge-Kutta 4th order method.

3.2.1 Overall

The overall heat transfer components of LII can be described [56,51,43]:

$$Q_{int} = Q_{abs} - Q_{sub} + Q_{ox} - Q_{con} - Q_{rad} \quad \textbf{Equation 3-1}$$

Where:

Q_{int} is the rate of change of internal energy of the soot particle being heated (W)
Q_{abs} is the rate of change energy of absorption of the laser to the soot particle being heated
Q_{sub} is the rate of change of energy lost through the effect of vapourisation/sublimation
Q_{con} is the rate of change of energy lost from conduction from the soot particle to the surrounding gas
$Q_{ox}$is the rate of change of energy caused by the oxidation of the soot particle
Q_{rad} is the rate of change of energy lost from radiation of the soot particle

3.2.2 Internal energy

The energy of the particle is often termed as the internal energy. The rate of change of internal energy rate depends on the specific heat, density, volume, and rate of change of the temperature of the particle.

$$Q_{int} = c_{p\,s}\,\rho_s \left(\pi \frac{d_p^3}{6}\right)\frac{dT}{dt} \quad \textbf{Equation 3-2}$$

$$C_p = 1878 + (0.1082\,T) - \left(\frac{(1.5149E8)}{T^2}\right) \quad \textbf{Equation 3-3}$$

Where:

Q_{Imt} is the interal energy of the soot particle
ρ_s is the density of soot (kg/m^3)
C_p is the heat capacity of the soot particle (J/ kg K)

d_p is the particle diameter (m)

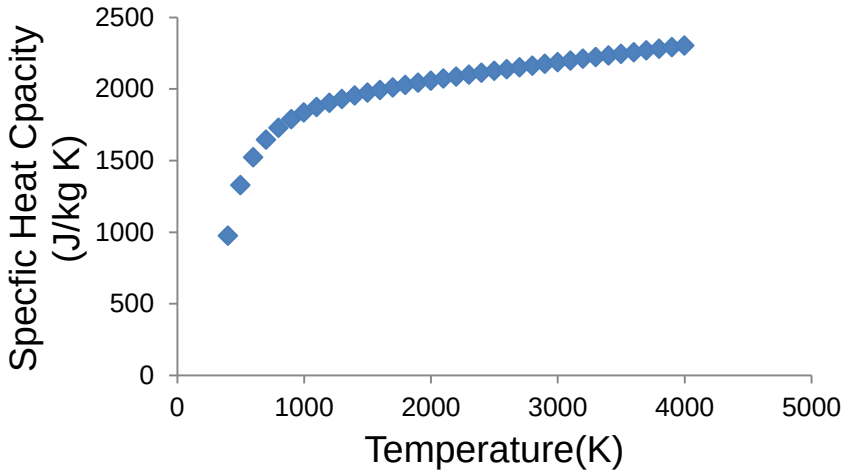

Figure 3-1: Model graph showing the change of heat capacity with temperature

Figure 3-1 shows the change on specific heat capacity of soot has with temperature according to Equation 3-3 showing that a use of a single heat capacity can't be used when modelling would lead to errors.

$$\rho_s = 23031.1 - ((7310.6 \text{ x}10^{-5})\, T_p) \qquad \textbf{Equation 3-4}$$

Where:

ρ_s is the density of the soot particle in kg/m^3.

3.2.3 Absorption

One of the most important aspects of the model is to try and model the absorption of laser light from the soot particle

$$Q_{abs} = C_{abs}\, F(t) \qquad \textbf{Equation 3-5}$$

The rate of absorption Q_{abs} depends on the absorption cross section C_{abs} and the fluence F(t) as well as temporal profile of the laser. Therefore Equation 3-6describes how the energy changes over time:

$$F(t) = F\ g(t)$$ **Equation 3-6**

Where

g(t) is the normalised laser temporal profile
F(t) is the energy per unit time over time
F is the overall fluence (J/m^2)

The laser temporal profile for a pulsed laser is assumed to be Gaussian and therefore follows Equation 3-7 as to ensure the normal Gaussian distribution:

$$g(t) = \frac{1}{\sigma\sqrt{2\,\pi}}\exp(-\frac{1}{2}\left(\frac{(t-\mu)}{\sigma}\right)^2)$$ **Equation 3-7**

$$\sigma = \frac{FWHM}{2\sqrt{2\,ln2}}$$ **Equation 3-8**

The absorption cross section is given by:

$$C_{abs} = \frac{\pi^2 d_p^3}{\lambda_{Exct}} E(m)$$ **Equation 3-9**

This relies on the soot absorption function E(m) which indicates how much light is lost through absorption as discussed in chapter 2.2.3. Equation 3-10 and Equation 3-11 show how this value is related to the complex refractive index of soot:

$$E(m) = -Im\frac{m^2-1}{m^2+2} = \frac{6n_m k_m}{(n_m^2 - k_m^2 + 2)^2 + 4n_m^2 k_m^2}$$ **Equation 3-10**

$$m = n_m - k_m i$$ **Equation 3-11**

Where:

E(m) is the absorption coefficient

m is the refractive index

n_m is the real part of the soot refractive index

k_m is the imaginary part of the soot refraction index

3.2.4 Conduction

One of the main methods for heat transfer from the particle is conduction. This section of the model aims to build a model of heat transfer of conduction that is reasonable and can be used to calculate the amount of heat lost by conduction reliably. Conduction occurs through caused by energy being lost at the particle surface due to collisions with gas molecules. There are two distinct regimes in conduction free molecular and continuum.[41] The influence these regimes have on the heat transfer by conduction is determined by the Knudsen number. The Knudsen number is determined by the ratio of the mean free path of molecules to the diameter of the soot primary particle and is seen in Equation 3-12:

$$Kn = \frac{\lambda_{mfp}}{d_p}$$ **Equation 3-12**

Where:

Kn is the Knudsen number

λ_{mfp} is the mean free path (m)

If the Knudsen number ratio is high (approx.. *Kn*>1) then this means that the main method of heat transfer is in the Free Molecular Regime and the mean free path of the molecule is comparable to the length scale which means that the soot particles behave like the gas molecules. if the Knudsen number Iis low (approx. *Kn*<0.1) this means that the most heat transfer occurs in the Continuum regime which means that the particles are big compared to the mean free path meaning that the surrounding gas is a continuous fluid flowing around the soot particle. If the ratio is neither explicitly high nor low then that means that a transition regime may be used to account for the effect both regimes have on the loss of heat due to conduction.[80, 40]

The free molecular regime is where particle-molecule collisions are the main source of heat transfer. This is described here since this is usually the main mode of conduction when using the model. The free molecular regime is described by the Equation 3-13 to Equation 3-16:

$$Q_{Conduction,FM} = \propto \pi\, d_p^2\, \frac{p_g \bar{c}}{2}\, \frac{y^* + 1}{y^* - 1} \left(\frac{T_p}{T_g} - 1 \right) \quad \textbf{Equation 3-13}$$

Where

y^* is the heat capacity ratio for air

$\propto$ is the thermal accommodation factor

$\bar{c}$ is the average molecule speed (m/s)

T_p is the particle temperature (K)

T_g is the gas temperature (K)

The average molecule speed is given by:

$$\bar{c} = \sqrt{\frac{8 k_B T_g}{\pi M_g}} \quad \textbf{Equation 3-14}$$

This then can be related by:

$$q_f = \propto \frac{\pi d_p^2}{8}\, \frac{P_g}{k_B T_g} \sqrt{8 \frac{k_B T_g}{\pi M_g}}\, \frac{y^* + 1}{y^* - 1}\, \left(\frac{T_p}{T_g} - 1 \right) \quad \textbf{Equation 3-15}$$

$$Q_{Conduction,FM} = \propto \pi\, d_p^2\, \frac{P}{8} \sqrt{\frac{8 Ro\, T_g}{\pi\, M_g}}\, \frac{y^* + 1}{y^* - 1} \left(\frac{T_p}{T_g} - 1 \right) \quad \textbf{Equation 3-16}$$

Where

k_B is the Boltzmann constant (m^2 kg)/ (s^2 K)

R_O is the Universal Heat constant (J/ mol K)

In the continuum regime the main method of heat transfer is the molecule-molecule interactions rather the particle-molecule interactions, however it will have a larger amount of particle-molecule

interactions than the free molecular phase, because of this the rate of conduction of heat is strongly increased compared to the free molecular regime. This is a much more standard way of heat transfer since it only considers the bulk of the gas component and depends mainly on the thermal conductivity of bulk. The continuum regime exists when the Knudsen number is low, this allows for the molecules to directly collide rapidly and energy will be dissipated through these collisions rather than direct molecular contact between surfaces. In the continuum regime, heat transfer is independent of pressure since increasing the pressure affects the number of gas molecules but also reduces the distance of the molecular collisions and these two essentially cancel each other out.

Overall the McCoy and Cha equation describes transition regime between the two distinct regimes and is the typically used heat transfer equation for the model. It can be seen that if the Knudsen number is high it tends towards the free molecular regime and if it is low it only takes into account the continuum regime. Equation 3-17 shows the overall equation for conduction:

$$Q_{Conduction,McCoy} = \frac{\left(2\pi\, d_p^2\, k_g\, \left(T_p - T_g\right)\right)}{(d_p + G\, \lambda_{mfp})} \qquad \textbf{Equation 3-17}$$

Where G is the geometry heat transfer factor

3.2.5 Vapourisation / Sublimation

At higher fluences the particles reach temperatures so high that they are enough to cause evaporation. Evaporation not only causes energy loss it also causes the mass loss and thus the diameter of the particle to change. The energy lost through evaporation is dependent on the enthalpy of evaporation of soot and the rate at which the mass is lost. The energy lost by evaporation per particle is shown below in Equation 3-18:

$$Q_{Vap} = \frac{\Delta H_{Vap}}{M_{SV}} \frac{dm_p}{dt} \qquad \textbf{Equation 3-18}$$

Where

ΔH_{Vap} is the enthalpy of vapourisation for soot (J/kg)

M_{sv} is the molecular weight of soot vapour (kg/mole)

m_p is the mass of the soot particle (kg)

The term M_{SV} is the mean molecular weight of the soot vapour, not the solid Carbon, because the heat of evaporation is the energy required to evaporate one mole of solid into gaseous Carbon species. C_3 is the most abundant species produced in the vapour. The mean molecular weight of the soot vapour is temperature dependant meaning that if the temperature is increased to 2000 K then the mean molecular weight is increased by a factor of 2 and if to 4000 K then it is increased by a factor of 4, this wouldn't be accounted for if a value was used that wasn't temperature dependant.[81]

Mass change during evaporation can be described by a mass balance using the equations from Equation 3-19 to Equation 3-20 :

$$\frac{dm_p}{dt} = -\pi\, d_p^2\, N_{SV}\, \frac{M_{SV}}{N_A}$$ **Equation 3-19**

$$\frac{dm_p}{dt} = \frac{d(\rho_p\, \frac{\pi d_p^3}{6})}{dt} = \frac{d(\rho_p\, \frac{\pi d_p^3}{6})}{dd_p}\frac{dd_p}{dt}$$ **Equation 3-20**

Where

N_A is the Avogadro number

N_{SV} is the molecular molar transfer

Equation 3-21 to Equation 3-23 shows the derivation of mass change in the particle over time and how it can be related to the soot flux from soot evaporation.

$$\frac{d(\rho_p\, \frac{\pi d_p^3}{6})}{dt} = 0.5\, \rho_p\, \pi\, d_p^2 \frac{dd_p}{dt}$$ **Equation 3-21**

$$\text{Since } \frac{dm_p}{dt} = -\pi\, d_p^2\, N_{SV}\, \frac{M_{SV}}{N_A}$$ **Equation 3-22**

$$\frac{dd_p}{dt} = \frac{-\,2\, N_{SV}\, M_{VS}}{\rho_p\, N_A}$$ **Equation 3-23**

This flux N_{sv} is a transitional flux since that neither flux regime can be discounted. The Continuum flow regime is when there is a short mean free path and there are a lot of molecule-molecule collisions. The

Free Molecular flux is the regime where there is a long mean free path and no molecule-molecule collisions take place. The molecular flux in the two regimes can be described by Equation 3-24:

$$N_{SV} = \left(\frac{1}{N_{FM}} + \frac{1}{N_C}\right)^{-1} \quad \textbf{Equation 3-24}$$

$$\text{with } N_{FM} = \beta \frac{P}{k_B T_p}\sqrt{\frac{R T_p}{2 \pi M_{SV}}} \quad \textbf{Equation 3-25}$$

$$\text{and } N_C = 2\frac{P_{VS}}{k_B T_p}\frac{D_{ab}}{d_p} \quad \textbf{Equation 3-26}$$

$$D_{ab} = \frac{f\ k_B T_p}{4\ \Sigma_{SV}\ P}\sqrt{\frac{R_O T_p}{\pi\ M_{SV}}} \quad \textbf{Equation 3-27}$$

Where

N_{SV} is the overall mass transfer
N_{Fm} is the free molecular molar mass transfer regime (s^{-1} m^{-2})
N_C is the continuum regime molar mass transfer regime (s^{-1} m^{-2})
D_{ab} is diffusion coefficient (m^2/s)
Σ_{SV} is macroscopic cross section (m^{-1})

As the temperature increases the vapour pressure of the soot increase since there will be a larger volume of soot vaporised, the average molecular weight increases as larger Carbon molecules in the soot will be vaporised increasing the molecular weight thus the macroscopic cross section of the molecules because of this effect the model has to account for it using the equations below from Equation 3-28 to Equation 3-31. The polynomial coefficients for the following equations can be found in Table **3-1**. [41] [56]

$$P_{VS} = \exp(\sum_{i=0}^{5}(P_i T_p^i)) \quad \textbf{Equation 3-28}$$

$$M_{Vs} = \sum_{i=0}^{5} m_i T_p^i \quad \textbf{Equation 3-29}$$

$$\Delta H_{Vap} = \sum_{i=0}^{5} h_i T_p^i \quad \textbf{Equation 3-30}$$

$$\Sigma_{SV} = \sum_{i=0}^{5} \sigma_i M_{Vs}^i \quad \textbf{Equation 3-31}$$

Table 3-1: Evaporation heat transfer coefficients[82]

i	**p_i**	**m_i**	**h_i**	σ_i
0	-111.4	0.01718	205398	1.8×10^{-19}
1	0.0906	6.865×10^{-7}	736.6	-1.857×10^{-17}
2	-2.764×10^{-5}	2.996×10^{-9}	-0.4071	1.404×10^{-15}
3	4.175×10^{-9}	-8.595×10^{-13}	1.199×10^{-4}	-2.593×10^{-14}
4	-2.488×10^{-13}	1.049×10^{-16}	-1.795×10^{-8}	2.075×10^{-13}
5	0	0	1.072×10^{-12}	-6.667×10^{-13}

Equation 3-32 describes how the diameter changes with mass it is assumed that the particle is still spherical:

$$d_p = \left(\frac{6 * m}{\pi * \rho_p}\right)^{\frac{1}{3}} \quad \textbf{Equation 3-32}$$

3.2.6 Radiation

Planck' Function allows the energy of the radiation given off at a specific temperature for a perfect blackbody. To account for the fact that the Carbon soot is not a perfect Blackbody an emissivity term is applied. ε_λ is known as the emissivity factor. This is the consistant approximation of the relative ability of a component to emit energy by radiation compared to that of a blackbody i.e. if it was a perfect Blackbody, emissivity=1. The emissivity is dependent on the wavelength in the visible and infrared regions. [83] This equation gives the amount of radiation coming from the whole particle.

Radiation is independent of pressure compared to other methods of heat transfer and is typically much slower method of heat loss compared to heating and vaporisation; however at lower pressures it becomes a larger factor in the overall heat transfer and has to be taken into account. To account for loss by radiation the model started off using Planck's function and integrating it over all solid angles and wavelengths:

$$Q_{Rad} = \pi\, d_p^2 \int_0^\infty (\varepsilon_\lambda) \frac{2\,\pi\, c^2}{\lambda^5((\exp\left(\frac{h\,c}{\lambda\, k_B T_p}\right)) - 1)}\, d\lambda \qquad \textbf{Equation 3-33}$$

If the model is integrated and the wavelength is converted to an energy it gives:

$$Q_{Rad} = \frac{\left(199\,\pi^3 d_p^3\right)\left(k_B\, T_p\right)^5\, E(m)}{h\,(h\,c)^3} \qquad \textbf{Equation 3-34}$$

3.2.7 Oxidation

The effect of oxidation was added to the model since some researchers[55,84] have suggested its influence may be more significant for long-pulse excitation, which is subject of a later chapter.

When the particle is heated by a laser pulse, it reaches temperatures high enough such that the carbon reacts with any oxygen in the surrounding gas through oxidation. As this is an exothermic reaction, it increases the temperature of the particle.

At atmospheric conditions, the reaction of carbon and oxygen typically produces both CO and CO_2 in almost equal amounts. As temperature increases, however, as does the ratio of CO to CO_2 and for the temperatures involved in LII the reaction produces almost entirely CO. [83]

The reaction used is:

$$C + \frac{1}{2}O_2 \rightarrow CO$$ **Equation 3-35**

The increase in the amount of energy of the particle can be estimated by [85]:

$$Q_{Ox} = \left(-\Delta H_{Ox} - 2\alpha_T C_p^{CO} T\right)\frac{\pi d^2 k_{Ox}}{N_a}$$ **Equation 3-36**

Where $Cpco$ is the specific heat capacity of carbon monoxide, N_a is Avogadro's number, αT is the thermal accommodation factor, ΔH_{ox} is the heat of reaction and k_{ox} is the rate constant in 1(scm^2).Within this model, it is assumed that the reaction is not dependent on the diffusion of oxygen to the particle surface, i.e. the surface is continuously exposed.

The rate constant is expressed as:

$$k_{Ox} = 12\ P_{O_2}\ [\frac{k_a \chi_A}{1 + \ k_z P_{O_2}} + k_b(1 - \chi_A)]$$ **Equation 3-37**

Where

P_{o2} is the partial pressure of Oxygen

k_{Ox} is the overall rate constant for Oxidation (1/s cm^2)

k_a is the rate constant for oxidation at site A on the particle surface (1/ s cm^2 atm)

k_b is the rate constant for oxidation at site B on the particle surface (1/ s cm^2 atm)

k_z is the Rate constant for surface oxide formation at A sites (1/atm)

χ_A is the mass fraction of soot annealed

Equation 3-37 takes into account or the existence of two different types of active site upon which oxidation can occur. These are type A and a less active type B and which have been denoted with rate constants of k_a and k_b respectively. According to Strickland-Constable, that A sites can change to form B sites due to annealing at a rate kT.[86] For typical experiments the partial pressure of O_2 is taken to be 0.209 atm however Michelsen et al.[83] have stated that using a lower value may give better agreement between experimental results and modelled.

The fraction of available sites that are type A is:

$$k_a = 5 * 10^{23} \exp(\frac{-1.255 * 10^5}{RT}) \quad \textbf{Equation 3-38}$$

$$k_b = 5 * 10^{21} \exp(\frac{-6.352 * 10^4}{RT}) \quad \textbf{Equation 3-39}$$

$$k_T = 3.79 * 10^{27} \exp\left(\frac{-4.06 * 10^3}{RT}\right) \quad \textbf{Equation 3-40}$$

Where

k_T is the total rate constant

Another important factor in the role of oxidation is the relationship between chemisorption and desorption, which can also be described as the rate at which solid oxides form on the surface of the particle itself. This is denoted as k_Z and expressed as follows:

$$k_z = 21.3 \exp(\frac{1.713E4}{RT}) \quad \textbf{Equation 3-41}$$

When incorporating the energy loss due to oxidation, one must also include the mass that is lost expressed as:

$$(\frac{dm}{dt})_{ox} = -\frac{2\pi d^2 W_1 k_{ox}}{N_a} \quad \textbf{Equation 3-42}$$

Where

W_1 is the Average Molecular weight of air

If this model were to take into account the effects of the annealing of particles, there would have to be an inclusion of an annealed surface rate of oxidation. This is due to the difference in active site density that occurs in carbon materials that have more order than soot

3.2.8 Signal modelling

The signal is produced from radiation from a single particle, so the signal is related to Planck's law integrated over all solid angles. The difference between radiation and the signal is the radiation is

integrated over all wavelengths while the signal is just integrated from the collection wavelength as shown in Equation 3-43. The effect temperature and particle diameter which is time dependant has on the signal and explains how the signal evolves over time can be seen.

By integrating over all wavelengths and including an emissivity term Equation 3-45 can be produced:

$$S = \pi\, d_p^2(t) \int_{\lambda_1}^{\lambda_2} \varepsilon_\lambda \frac{(2\,\pi\,h\,c^2)}{\lambda^5(\exp\left(\frac{(h\,c)}{k_B\,T_p(t)}\right) - 1)} d\lambda$$

Equation 3-43

The emissivity is given by:

$$\varepsilon_\lambda = \frac{4\pi\, d_p}{\lambda} E(m)$$

Equation 3-44

$$S = \frac{8\,\pi\, d_p^3(t)\, h\, c^2\, E(m)}{\lambda_s^6(\left(\exp\left(\frac{h\,c}{\lambda_s\, k_B\, T_p(t)}\right)\right) - 1)}$$

Equation 3-45

Where:

ε_λ is the emissivity factor

The signals at certain wavelengths can then be subtracted to give a total relative signal. This depends on the band pass wavelengths setup in experiments. To gain an overall empirical model the spectral response of the detector has to be taken into account as well as the solid angle of the detection source. This model also only shows the results if the fluence of the particles is one value, if for instance the beam shape was non-uniform the signal would have to be weighted. This can be seen in the later long-pulsed LII chapter.

3.3 Modelling results

3.3.1 Validation of implemented model

Figure 3-2 shows the model with the simple components of vapourisation, conduction, absorption and radiation included. It is compared with a similar model the LII SIM program, a common and well referenced model within the LII community and ran with the similar input values. The signal plotted is based off of Equation 3-45

This shows the model is working as expected differences are put down to the different assumptions such as the equation for density. Individual heat transfer components have been checked and made sure they are producing reasonable values as seen in Michelsen et al. [41,43] For standard LII measurements the model is shown to behave well. Results indicate trends and values when compared to literature such as Schulz et al.[51] give similar values on the same scale. Validation of the model has been done at the early stages of use and found to match other modelling software such as LIISIM.

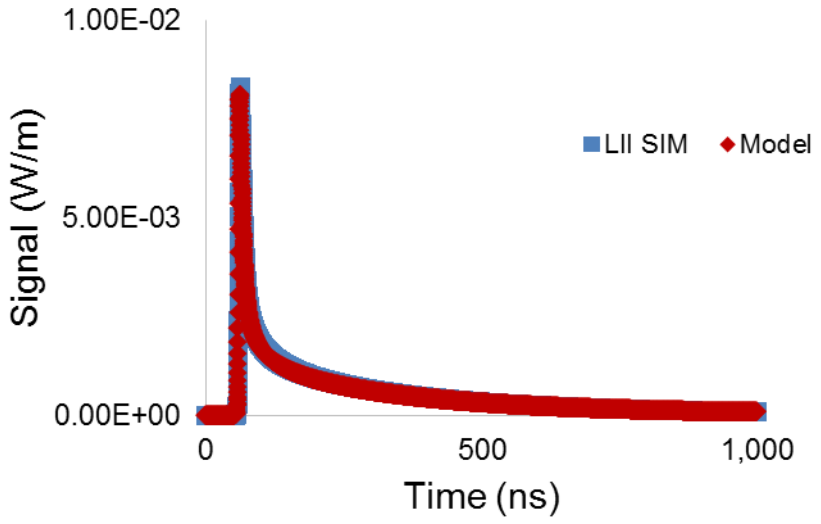

Figure 3-2: LII model comparison with LII SIM Program matching fluences between models.

This model comparison has the primary particle diameter set to 30 nm, the absorption function of 0.36 and a detection wavelength of 450 nm, an initial gas temperature of 1700 K and a fluence of 220 mJ/cm^2. The model value is found from Equation 3-34

3.3.2 Fluence curve

The model is able to be adapted to account for differences in how the measurement is taken through the form of gating. Typically when using PMT measurements the max signal is possible to use whereas with the camera it has to be gated over the time-resolved profile. One of the main changes this can cause is the difference in the fluence curves.

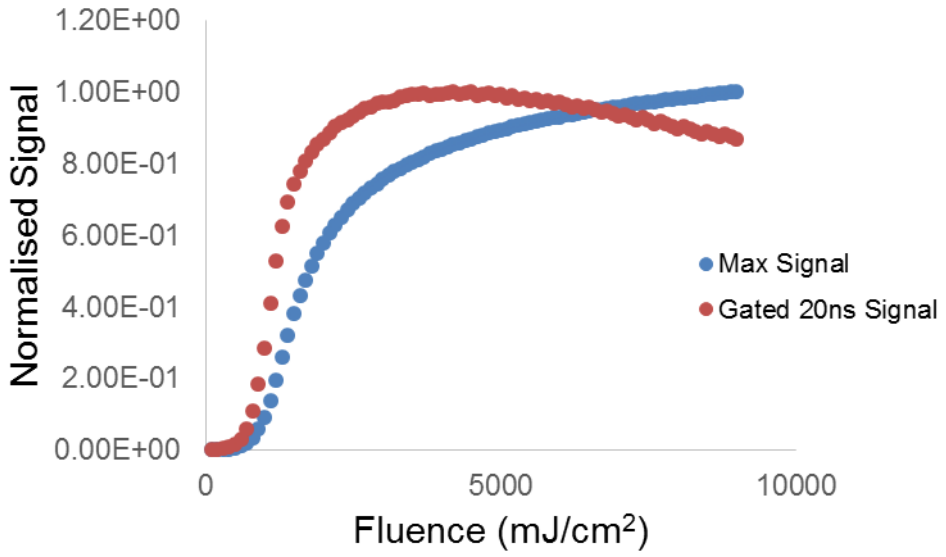

Figure 3-3: Modelled fluence curves using results from peak signal as well as signal integrated over 20 ns

Figure 3-3 shows modelled fluence curves with two different methods of detection measurement. One measurement uses the peak signal often used when measuring with a photomultiplier and the other is using a integrated signal over a gate of 20 ns over the peak of the signal which is how an intensified CCD camera measures the LII signal.

These results show the influence vapourisation has on the soot particle. Whereas the peak maximum signal increases the effect which causes mass loss is decreased at higher fluences which when measured over a gate causes a decrease in the signal measured. When compared to literature such as Bladh et al.[56] it shows a similar trend to what is expected. This model comparison has the primary particle diameter set to 30 nm, the absorption function of 0.36 and a detection wavelength of 450 nm, gas temperature of 1700 K. The model value is found from Equation 3-34

3.3.3 Soot particle diameter comparison

Figure 3-4 shows the model with different particle sizes which have been normalised to each particles largest size. This shows the difference in decays between the different particle sizes. This result shows the fact that the model correctly predicts the smaller particles cool faster due to their larger surface area to volume ratio. What this demonstrates is that the model can produce the trend that is expected for increasing the particle size as demonstrated by Leipertz et al.[87]

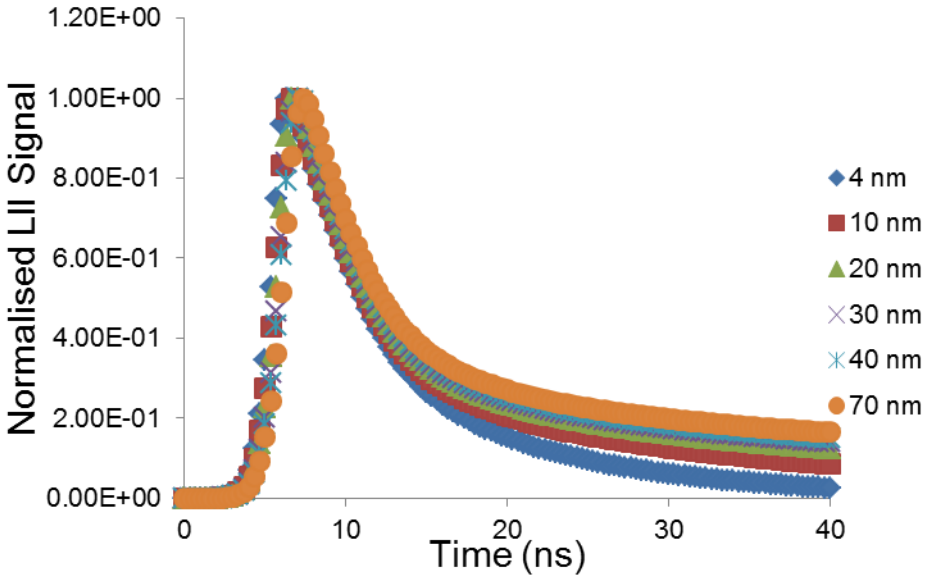

Figure 3-4: Model Results for normalised LII signal decay from different sized particles by a 220 mJ/cm^2 at 1064 nm excitation and 450 nm detection and gas temperature of 1700 K

3.5 Potential for further developments

3.5.1 Potential for further developments and improvements in the model

Future work and expansion of this model is being carried out into the development of this model and should be used for comparison of data in the near future.

The physical properties of soot can also be further developed to accurately model by including the polydispersity of primary particle size as well as the formation of aggregates. Each of these factors will affect the rate at which the particles cool, as well as their ability to absorb energy from the laser. The particle size distribution of primary particles follows a lognormal distribution, in that it is slightly more probable to find a particle larger than the median size than it is to find one smaller than the median.

$$d_f = \frac{1}{\sqrt{2\,\pi} d_p\, ln\sigma_g} \exp(-\frac{1}{2}\frac{\left(\ln(d_p) - \ln(CMD)\right)^2}{\ln \sigma_g^2}) d\, d_p$$ **Equation 3-46**

$$S_{Polydisperse} = \sum_{i=1}^{n} S_{Mono}(d_P)\, d_f(d_p)\ \Delta d$$ **Equation 3-47**

Where:

CMD is the count median diameter

σ_g is the variance in the geometric width of the particles/

$S_{Polydisperse}$ is the signal from the polydisperse particles

Another source of uncertainty in modelling is due to the high temperatures involved with LII the carbon particle can restructure to a more ordered configuration such as a carbon onion through both melting of the particle to then recrystallize, as well as through the curvature of the graphite layers due to oxidation and sublimation. This will likely affect the refractive index of the particle, the rate at which the particle vaporises and the rate at which the particle is able to conduct heat to the surrounding gas (the thermal accommodation coefficient). This is something that could be very difficult to model therefore it could be important not to have the particles at a high temperature over a longer period of time, something which may affect the long-pulse results as discussed in chapter 6.

Aggregation of the soot particle is another factor which could be added but hasn't been implemented. Aggregation can affect the soot particle temperature because of a shielding effect which may change the heat of conduction thus affecting the temperature.

Other components such as thermionic emissions could also be modelled and is the process in which electrons are thermally ejected from the particle.[40] Another process which could be modelled is the effect of annealing however for modelling standard behaviours the components used are typically accepted. However because of the dominant components such as absorption and conduction , it is thought these factors won't change the overall signal significantly. [88]

4 LII experimental set-up, measurement and data processing methodology and development for conventional experiments

4.1 Introduction to experimental approach for LII measurements

This chapter describes in detail the set-up and approach to make LII imaging reliable and repeatable. The equipment used is described in substantial detail and justification is provided for the methodology adopted. The equipment can be split up into different sections including the sooting flame, the excitation source (pulsed laser) and the detection measurement. The way the data is processed is discussed showing how the data recorded can be used to provide a soot volume fraction image, HAB profile, radial profile and temporal signal profiles. This includes a description into a flat field correction that may have to be applied depending on the experimental circumstances.

Details about the fluence of the laser as well as comparisons of fluence matching between the 1^{st} harmonic (1064 nm light) and 2^{nd} harmonic frequency (532 nm) of the laser excitation source are also provided. This helps to ensure that, with experiments involving two different excitation wavelengths, the particles are being heated to the same temperature.

4.2 Conventional LII methodology

4.2.1 LII experimental apparatus for imaging and point measurements

LII imaging measurement set-up

The schematic diagram for a typical LII imaging experiment used throughout this thesis is shown in Figure 4-1. A Nd:YAG 1064 nm laser produces a Gaussian beam which is approximately 7 mm ($1/e^2$) in diameter, at a frequency of 10Hz. If the Nd:YAG has the doubling crystal attached and to produce 532 nm light this can be separated from the fundamental using two dichroic mirrors and a beam dump . This beam is positioned using specific Nd:YAG 532/1064 nm mirrors. The beam is then expanded by negative cylindrical lens of f = -100 mm and allowed to expand for 30 cm where it is collimated in one direction by a cylindrical lens of focal length f = 400 mm. This then passes through a slit of 1 cm in height and either 1 or 2 mm in width. This slit is to shape the sheet to try to make it as close to a top hat profile as possible. The slit is placed as close to the burner as reasonably possible to avoid diffraction effects.

For experiments requiring accurate control of the power, the pulse energy of the laser is controlled and can be adjusted by a half-waveplate and a polariser and the power is measured using a thermophile Coherent PV10-1 power meter.

The signal is then collected on a perpendicular axis through the ICCD camera, lens and filters. The front of the collection lens is typically placed 50 cm away from the centre of the burner and from the front of the lens. An object of known size is used to help focus and scale the camera for taking measurements and is always perpendicular to the flame. [40, 89]

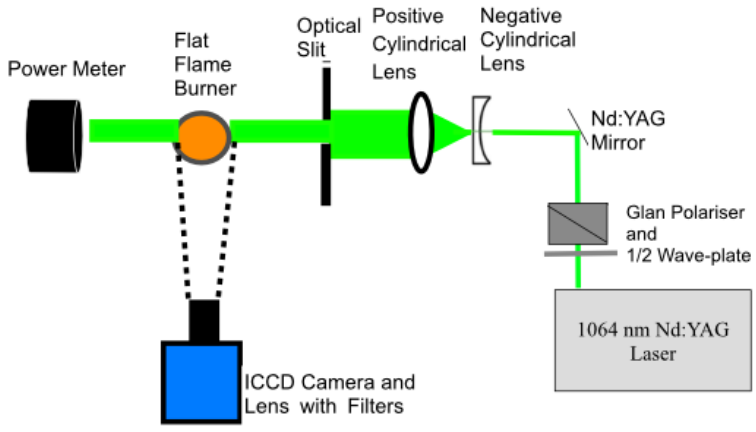

Figure 4-1: LII Laser sheet methodology setup

The camera has typically three settings which have to be input into the software: the gate duration, the gate timing and the intensifier gain setting. The gate time delay is the time the gate is opened at with respect to the trigger into the camera. The gate duration is the amount of time the camera is recording an image for. The intensifier gain is a factor of how much the signal is intensified by. For LII the gate duration is set to either 20 ns or 50 ns depending on the application.

Point measurement set-up

The other detection setup, used for point imaging is shown in Figure 4-2. This set-up includes a Photomultiplier Tube (PMT), which can temporally resolve of the LII signal. The PMT has a 1 mm pinhole placed in front of the entrance of the PMT housing and the image is formed and focused at this point by using a spherical focusing lens of f = 50 cm. *2-f* imaging results in a magnification of unity. The PMT is attached to an x-y translation stage to allow for the precise movement of the pinhole especially in the vertical direction to maximise the signal level.

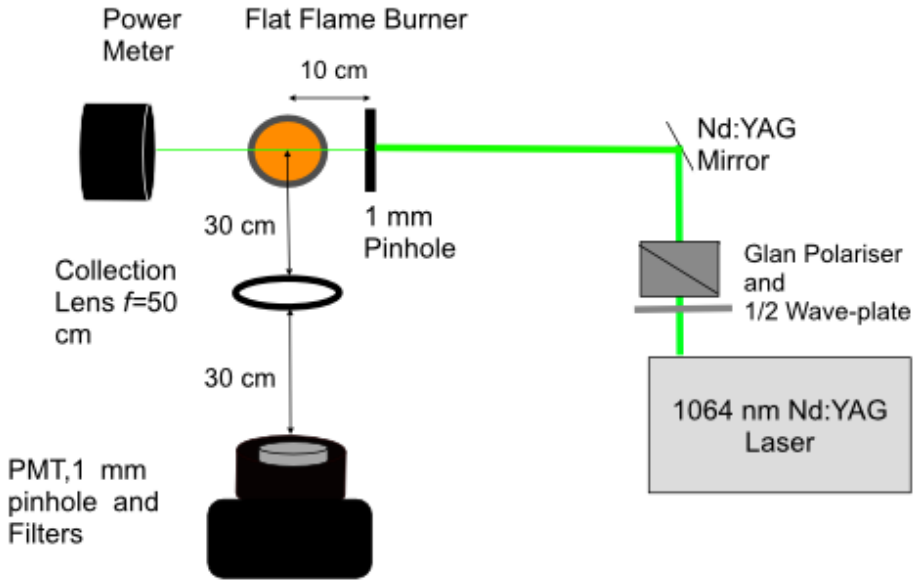

Figure 4-2: PMT detection setup

4.3 Equipment description used in LII

4.3.1 LII excitation source equipment

Nd:YAG 1064nm 1st harmonic laser

For typical LII experiments, the excitation source used was a 1064 nm Nd: YAG (neodymium-doped yttrium aluminium garnet) laser is used for the excitation source. This laser generates short pulses of 1064 nm Gaussian beam light at a repetition rate of 10 Hz, which is used to heat up soot particulate matter within the flame. This laser allows for high energy pulses of a short amount of time meaning that it is ideal for LII since it provides enough energy for the soot particles to absorb the light in a short enough time to heat the soot hot enough to induce incandescence to a point where the signal can be measured. Using 1064 nm light also avoids exciting PAHs and other molecules, causing the generation of a fluorescence signal and interference with the LII signal.[45,54] The laser used is a *Surelite Continuum II SLII-10*.[90] The laser was found to have maximum pulse energy of 560 mJ at 10 Hz (flashlamp voltage of 1.44 kHz Q-switch delay of 180 μs at 1064 nm). The fundamental frequency has pulse duration of 5-7 ns (FWHM). It was found to have a 200 mJ maximum pulse energy at the 2nd harmonic 532 nm under the same conditions with a similar pulse duration.[90]

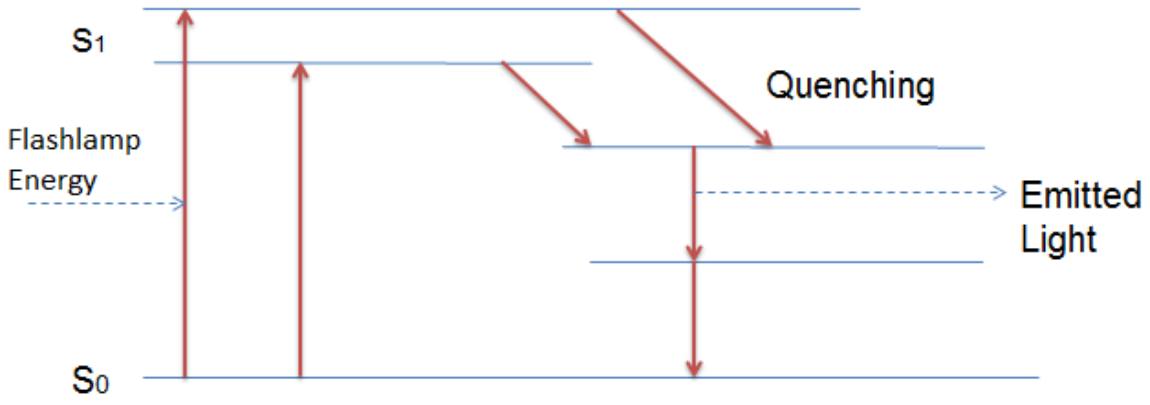

Figure 4-3: Excitation of laser neodymium Ions

The Nd:YAG is a solid state laser which uses a YAG crystal doped with Neodymium ions. The YAG crystal is excited when optically pumped by the flashlamp as seen in Figure 4-3. This crystal is the active gain medium which is placed between two mirrors (optical resonators). One mirror is fully reflective and the other mirror is an optical switch which waits for a maximum population inversion in the ions before being opened and when opened allows coherent light to escape the cavity. This is known as Q-switching and the time when Q-switching happens with respect to the optical resonation can affect

the pulse energy though to control the pulse energy this way isn't preferred due to issues such as beam profile etc.. Q-switching allows for high intensity pulses at a pulse profile of nanoseconds, while Nd:YAG lasers can emit a range of wavelengths depending on the transition levels. The typical emission is the 1064 nm fundamental frequency.

The light can then be frequency doubled to emit 532 nm light using a 2nd harmonic Crystal installed in front of the laser cavity before the beam fully exits the housing. Frequency doubling essentially works by the 1064 nm laser light being effectively combined through non-linear optical interaction to generate photons of double the frequency, thus half the wavelength of the initial photons. This light can be then used to perform LII measurements after separation from the residual light at the fundamental wavelength.[90] This could be then doubled again using 3rd harmonic crystal to give 355 nm wavelengths, however this was used in the present work.

Figure 4-4 shows the laser pulse shape of the Nd:YAG laser measured by directing a weak reflection of the beam(so to avoid saturation of the diode) onto a fast Si photodiode(Thorlabs PDF10A, the spec sheet can be found in the appendix). The data sheet can be found in the appendices for further information.[91] An estimated FWHM of 7.5 ns is shown which similar to the stated value in the laser manual as seen in the spec sheet in the appendix. This could then be used for modelling purposes.

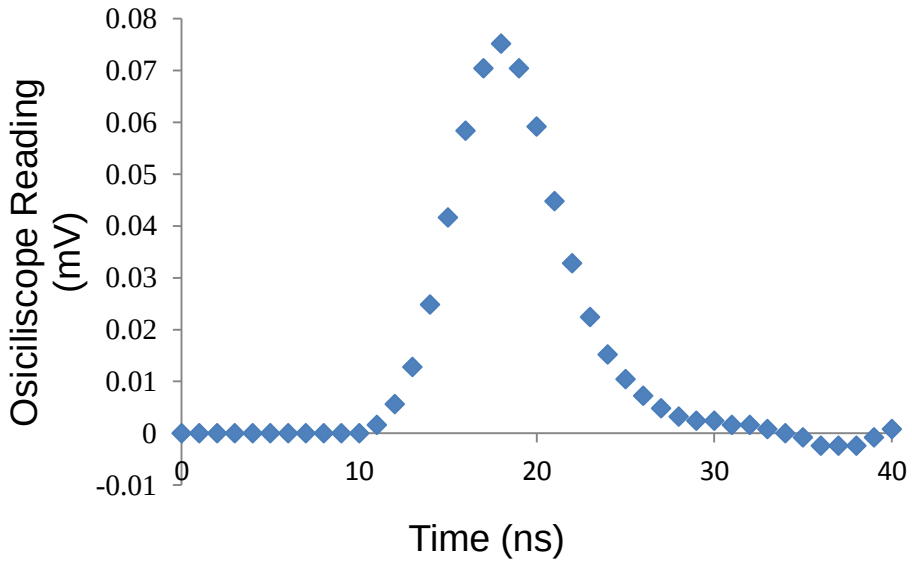

Figure 4-4: Nd:YAG laser pulse shape measured using Si photodiode

Beam shaping optics

For these experiments of planar imaging, a laser sheet had to be made. To do this the beam from the laser was expanded using a cylindrical lens of focal length f = -100 mm and then collimated using a

positive cylindrical lens of focal length f = 400 mm, as mentioned previously. Cylindrical lenses were used over a positive spherical lens because the spherical lens focuses the beam tightly in all directions. When attempting to use a spherical lens, it was found that the sheet spatial profile increased the fluence of the laser at the focus so much to the point where it affected the uniformity of the images and extreme vapourisation of the soot particle at the centre of the focus of the sheet. It has also been stated that when using imaging techniques it is simpler not to have vast changes in the shape of the laser profile which as discussed in the long-pulsed LII chapter can be a bit of an issue.

To ensure uniformity of the laser profile an optical slit was employed, as represented in Figure 4-5. For these experiments a 2 mm or 1 mm slit were used depending on the demands of the experiments with a trade-off between spatial resolution and signal to noise.

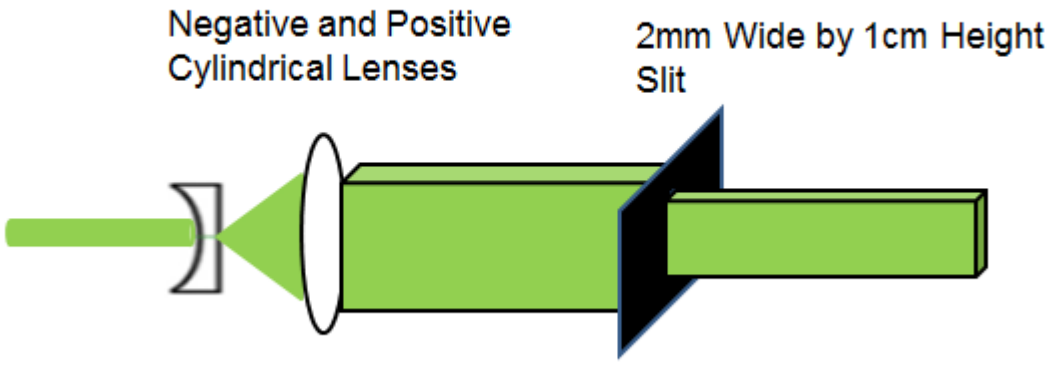

Figure 4-5: Optical lenses (negative cylindrical f = -100 mm and positive cylindrical f = 400 mm and slit for laser sheet shaping

In other experiments, point measurements were performed using a top-hat beam. Figure 4-6 shows what happens when the beam it is reduced from around 7 mm to 1mm using the pinhole. The size of the pinhole or slit determines the divergence of the laser, so the burner is placed as close to the slit as possible. Diffraction occurs after a certain distance after the pinhole related to the beam width. This affects the profile of the laser and can change dramatically if the distance of the beam is large enough.

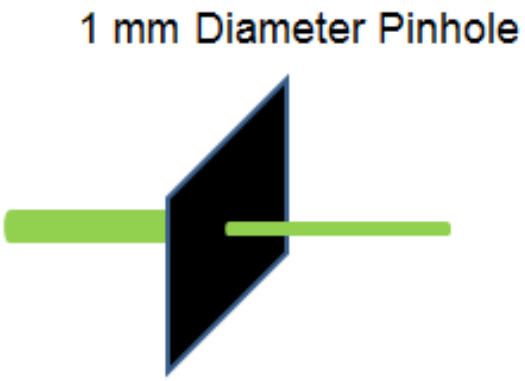

Figure 4-6: 1mm pinhole used for shaping laser beam from Gaussian spatial profile to top-hat [72]

The reason for the use of the slits and pinhole is that when the beam source exits the laser it is collimated and has a Gaussian spatial profile. Since the Gaussian profile results in different fluences at different radial positions within the measurement volume, it means that some particles would not be heated to the same temperature within the measurement volume. Therefore to heat the particles to the same temperature a top-hat spatial profile and slit/pinhole is used to select a near portion of the beam at the centre of the Gaussian profile. The principle is shown in Figure 4-7, with the shaded area representing the energy that is lost by the shaping of the beam using the pinhole/slit.

Figure 4-7: The change in shape from Gaussian to top hat and the cutting of beam intensity using pinhole/slit [72]

Beam attenuator

For experiments requiring precise control of power a variable beam attenuator set-up of a half-waveplate and Glan-polariser (Thorlab's *GL10*) was used in a setup as seen in Figure 4-8. By modifying the position of the waveplate, when the light passes through the beam polarisation direction is changed. The polariser is able to attenuate the beam transmitted depending on the plane of polarisation with the

other part of the polarised light being reflected into a beam dump. The polariser only transmits one component of polarisation to pass through. This is a common way to have precise control of the power necessary for some experiments.[92,93]

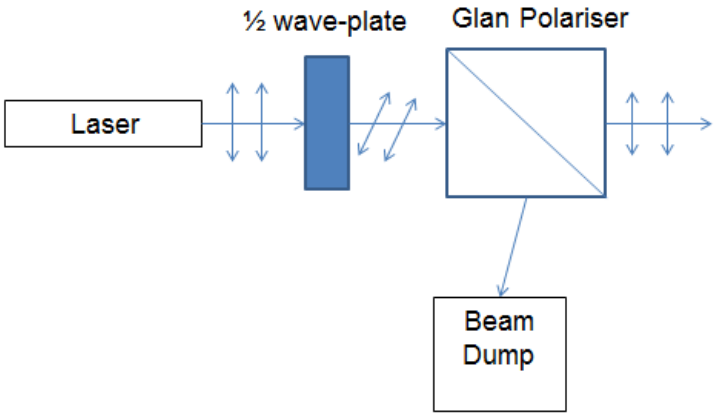

Figure 4-8: Schematic of the variable attenuator setup

4.3.2 Detection equipment

ICCD camera, lens and filters

For imaging experiments a LaVision ICCD Nanostar camera was used. A general description of how an ICCD camera works can be found in the previous background chapter in section 2.2. The camera is controlled and parameters set using LaVison *DaVis* software. The camera can be triggered externally by connecting the BNC connector from the Laser to the pulse triggering unit in the programmable timing unit (PTU) computer, which is attached and used to control the camera. The camera can be triggered to match the 10 Hz output from the laser. The timing of this trigger can be adjusted with relation to the laser pulse and the camera can also be set as to when take a recording known as gate delay. The camera can be set to trigger when the external trigger either rising edge or falling edge depending on the circumstances. Therefore, a wide range of trigger inputs can be used for the camera. When the PTU receives this trigger, the image can then be taken with the camera. The camera has a minimum temporal resolution of 20 ns which makes it the smallest gate that can be used. A short gate dramatically increases the chances of a larger signal to the background as discussed previously, which is important for LII imaging experiments. The camera has a high gain setting to increase the LII signal when there is a low light level. Throughout this thesis the largest gain of arbitrary setting on the camera of 99 was used to produce the best signal to noise possible and this is linear with signal.

The camera was focused using an image in the object plane to produce the best spatial resolution. It was assumed that no distortion occurred in the collection of images.

The camera has a chip of 1024x1280 pixels therefore if a known sized object such as a resolution test card is imaged it can be found what length scale one pixel relates to and a scaling factor can be found.

An object of known size, such as a ruler, was imaged to allow for scaling of the image. The camera lens is a Nikkon UV-105 f/4.5 multispectral imaging lens. It is useful in applications requiring imaging in the ultraviolet, visible and infrared spectral regions as it is free of chromatic aberrations across this wavelength region.

To supress background radiation from the flame a 450 nm (10 nm FWHM) bandpass filter was used. This filter also has the advantage of avoiding interference signal from C_2 Swann bands.[40,94,68] From Thorlab's data Figure 4-9 shows the optical transmission of the 1" diameter filter where the transmission width has a small FWHM.

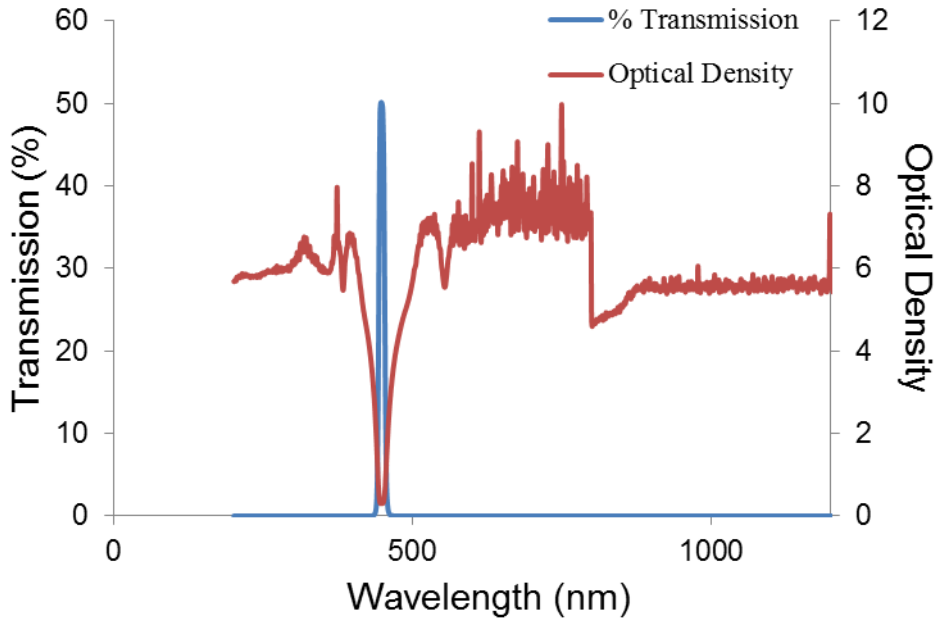

Figure 4-9: 450nm Bandpass Filter information from Thorlabs Manufacturing

Photomultiplier tube (PMT)

For point measurements throughout this thesis a photomultiplier tube (PMT) Hamamatsu R636-10[95] was used. Photons emitted from the soot particle due to LII causes an emission of electrons (through the photoelectric effect) when focussed in the PMT. The PMT is able to amplify and cause an electric

current which can then be measured and examined using an oscilloscope. A PMT allows for temporal measurement of the LII signal to be recorded with a favourable signal to noise ratio.

For experiments using PMT measurements, the PMT replaced the camera and a separate collection lens was added. A 1 mm pinhole was used to select the centre part of the beam. A focusing lens was used in front of the PMT pinhole with a focal length of 15 cm. This was used in a *2-f* setup giving 30 cm between the centre of the flame and the detector. The signal from the PMT was analysed using a Tetronix DPO 2024 oscilloscope and triggered from the laser pulse just like the camera. By using an oscilloscope it allows for averages to be taken and the typical average taken was 64 shots. The same 1" diameter 450 nm bandpass and 532 nm notch filters to avoid interference from the laser can be used in a way similar to the camera set-up.

Power meter

Throughout experiments accurate power measurements are important to know the fluence curve as discussed in previous background on LII. A *Coherent PM10V1* thermophile power meter was used for the calculation of the fluence. This power meter uses a sensor which is specially designed for high power, low repetition Q-switched conventional Nd:YAG lasers. It works by having the volume absorbing substrate in front of the detector which uses the heat production to give a power reading. Therefore for accurate readings the power has to be measured in the absence of a heat source like a flame

4.3.3 Sooting source equipment- porous plug burner setup

Mass flow controllers

To ensure the correct mass flow of gases to the burner a *Cole Palmer MC Series* mass flow controller was used for air and fuel gas (ethylene). The accuracy for each of these mass flow controllers was +/-0.8% of reading and +0.2% of full scale. [96] These mass flow controllers were checked against manual volumetric bubble flowmeters to ensure the correct output flow for air and ethylene. This is done by using a tube of known length and volume; the gas from the flow meters is passed through the tube with a soap bubble, which then rises between two known length points, the time taken to reach this volume can be measured and thus a volumetric flowrate can be found. The flow meters were originally calibrated for air so therefore it was crucial to also test for ethylene. These measurements agree within to their expected error limits. The flowrates were set using Standard Litres per minute which is 1 atm and 20 ^{O}C.

Burners

A flat flame burner was used for standard experiments and calibration images. It is a stainless steel porous plug burner. This burner is used to produce a one dimensional flame. The flame used throughout this thesis is not strictly a standard McKenna burner because it lacks an air co-flow from the sides. The

burner is also smaller than typical McKenna burners and thus the flow rates have to be accounted for exit velocity and mass flux. By using a flat flame burner it is possible to have a 1-dimensional flame in the centre-line. By using this type of burner focuses on the chemical reactions relevant to on the production of pollutants by simplifying the fluid mechanics of the system.[97]

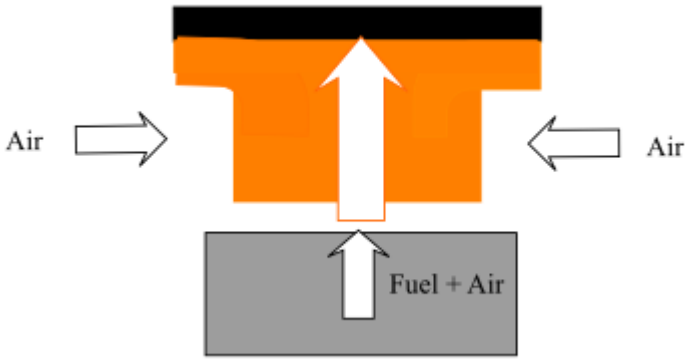

Figure 4-10: Diagram of Burner showing the effect of no coflow

Figure 4-11 shows the burner at a flame condition which is moderately sooting at an equivalence ratio of 2.2. The area of soot can be seen in the middle whereas moving along the width of the flame can be seen to be blue area where there is less soot, if any produced. For standard experiments, the porous plug diameter is 33 mm whereas the stabilisation plate is 38 mm wide and 30 mm thick.

Figure 4-11: Porous Plug Burner @ ϕ = 2.2

The stabilisation plate stabilises the flow, and is of much interest later in this thesis, in the heat transfer effects chapter, by theoretically acting like a heat sink. The separation between the stabilisation plate and the burner is set at 21 mm.[51]

Initially, a procedure was followed whereby measurements were started about 5 minutes after the flame has been ignited to allow for thermal stabilisation. After roughly 25 minutes measurements are usually stopped and the flame is turned off and the stabilisation plate left to cool and be cleaned due to a build-up of soot which can interfere with data collection. However as seen later in the heat transfer effects chapter 6.2.3, it was found that the time when the image is taken it can be seen it has no effect on the soot signal.

Target flames

The International LII workshop and International Sooting flame workshop[98] have set rules for a standard flame in keeping with similar soot-forming flat-flames studied by others; notwithstanding the narrow burner dimensions already noted. In the LII chapter 4 it can be seen that the porous plug burner can be seen to be comparable with a flat-flame McKenna burner. The standard fuel used for this burner is ethylene. The ratio of fuel to air is described as the equivalence ratio seen in Equation 3-1.

$$\phi = \frac{(\frac{x_{fuel}}{x_{air}})}{(\frac{x_{fuel,stoic}}{x_{air,stoic}})}$$

Equation 4-1

The target flames for experiments using this porous plug flat flame burner are shown in Table 4-1. A wide range of equivalence ratios was used to demonstrate the changes in sooting propensity and are typically used values when measuring soot in a flat flame burner. The volumetric flowrates are stated based on the standard temperature of 20 ^{o}C and standard pressure of 1 atm.

Table 4-1: Fuel and Oxidiser Flows and Equivalence Ratios

Fuel Setting (SLPM)	Air Setting (SLPM)	Total (SLPM)	X_{fuel}	X_{air}	ϕ	m flux	exit velocity
0.377	2.663	3.04	0.124	0.876	2.03	0.063	0.059
0.387	2.643	3.03	0.128	0.872	2.10	0.063	0.059
0.407	2.623	3.03	0.134	0.866	2.22	0.063	0.059
0.417	2.613	3.03	0.138	0.862	2.29	0.063	0.059
0.428	2.593	3.02	0.142	0.858	2.36	0.063	0.059
0.448	2.583	3.03	0.148	0.852	2.48	0.063	0.059

One chapter focuses on the heat transfer effects and involves a comparison using a larger capillary-hole burner, which was used in group members previous studies such a direct flame fuel cell.[99] The burner

was 64 mm in diameter just under double the size of the porous plug burner. The stabilisation plate, which was used for this burner, was still placed the standard 21 mm away from the burner and the size of the plate was 35 mm thick and 64 mm in diameter. The LII signal was compared between these two burners and for a comparable measurement the equivalence ratio had to be the same. Table 4-2 show the flowrates used for this larger burner. Figure shows an example of this burner in use with Figure 4-12 showing the larger burner at an equivalence ratio of 2.2.

Table 4-2: Fuel and Oxidiser flows and Equivalence Ratios for the Larger Burner

Fuel Setting (SLPM)	Air Setting (SLPM)	Total (SLPM)	X_{fuel}	X_{air}	ϕ	m flux	exit velocity
1.52	9.87	11.39	0.133	0.867	2.20	0.063	0.059
1.49	9.89	11.39	0.138	0.862	2.30	0.063	0.059

Figure 4-12: Image of larger burner @ ϕ =2.2

4.4 Data processing

4.4.1 MATLAB code for image processing

The camera produces a series of IM7 images, which is LaVision's file format which contains the full information of the experimental setup. An illustration of the blocks the data is processed through and the results produced can be found in Figure 4-13. The main key points needed from the images are a soot volume fraction image, centre line HAB profiles as well as radial profiles at different HABs. To average and process this data, a MATLAB program has been written where the data can be extracted

averaged and filtered using a median filter which helps reduce noise and is a reliable way to smooth the image as seen in Figure 4-14. A median filter is widely used in image processing as it removes noise while also preserving the edges of the focussed image.[100,101,102]

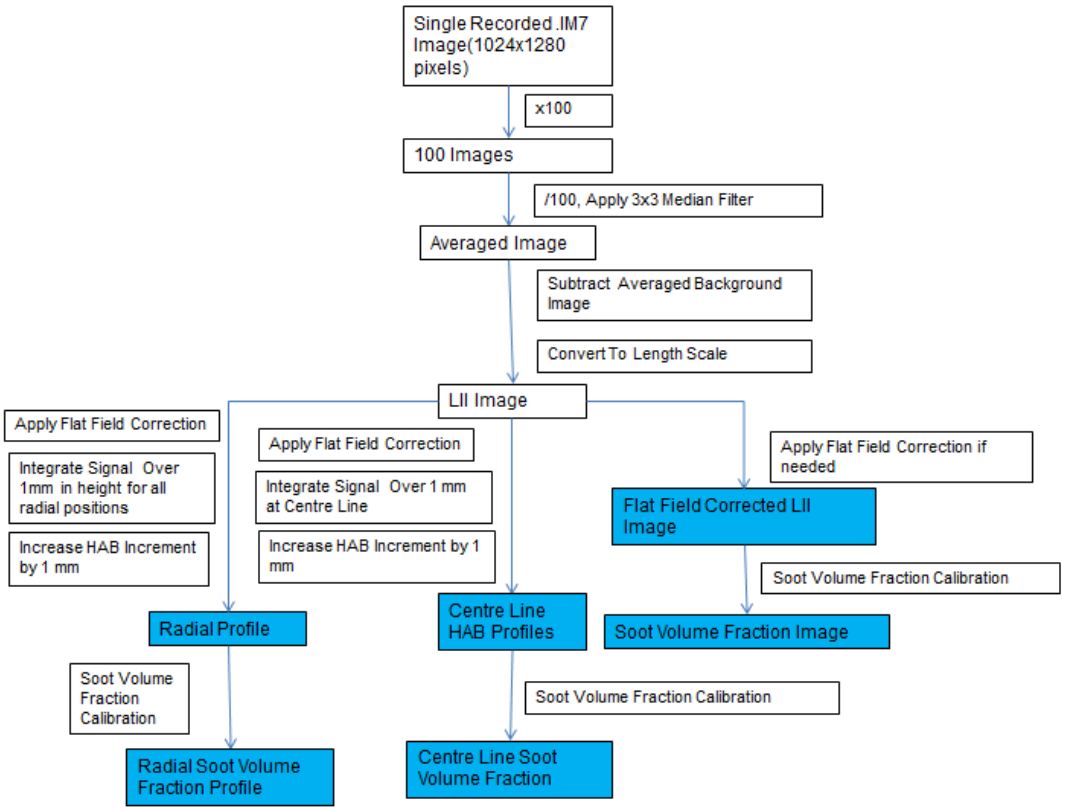

Figure 4-13: Data processing flowchart for producing an average LII image from 100 images (Blue shows important outputs)

The code works by first using a FOR loop to read in the IM7 images, where each pixel has an associated value of signal. The background can be subtracted by reading in an image of the background with no laser irradiation of the same number of averages and subtracting it from the LII image giving the overall image. The background does not vary much across the images and is around 90 counts maximum. The camera dynamic range is 16 bit, which means signal can vary from 0 to 2^{16}. The image can then be averaged and a standard deviation of the signal can also be produced. A small median filter of 3 by 3 pixels is applied as this is more accurate than a mean filter and helps smooth the image while preserving the sharp gradients in the images. The scale can be found by recording a corresponding known size object and finding the amount of pixels that are the length of the object. This can then allow for a scaling factor by knowing the pixels per unit length. By having a scaling factor which scales the pixels into length values which can be overlapped onto the LII image to show the length scales of the

LII emissions. The position HAB=0 mm can be determined by comparing the burner and object and a scale can be applied for all of the measurement area. The code is then set up in a FOR loop so that for every increase in HAB by 1mm the signal is integrated over which region this gives a vertical profile as seen in Figure 4-16. An increase in the loop by 1 mm for measurements was chosen since this is what is commonly measured in LII and keeps the code to a reasonable time. It was also used because this was the measurement of spatial resolution of the comparative PMT measurements. The standard error between all of the images is also calculated for this set of results and can be plotted with them.

Another loop is setup so it produces a horizontal radial profile across the flame for each HAB as seen in Figure 4-15 and with the standard error of all images included in Figure 4-18. These results can be then normalised as well as scaled using a calibration based on extinction measurements to give a soot volume fraction as seen in Figure 4-19, Figure 4-17. For the calibration an image is taken in a flame with known soot concentration by extinction in a ϕ = 2.48 flame with a HAB of 15 mm, it can then be used to provide a factor relating a signal count to soot volume fraction constant. It was found that the number of images needed to be at least 50 to ensure correct averaging.

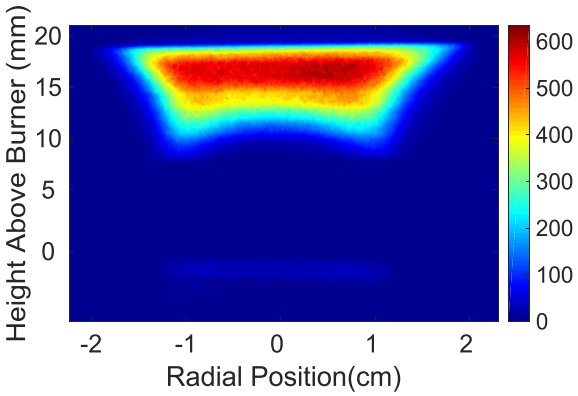

Figure 4-14: LII signal image for ϕ = 2.3 at gate of 50 ns

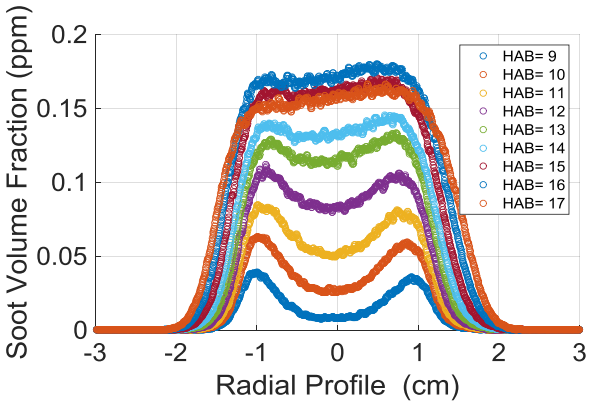

Figure 4-15: Soot volume fraction across image integrated over a height of 1 mm for each HAB for ϕ =2.3.

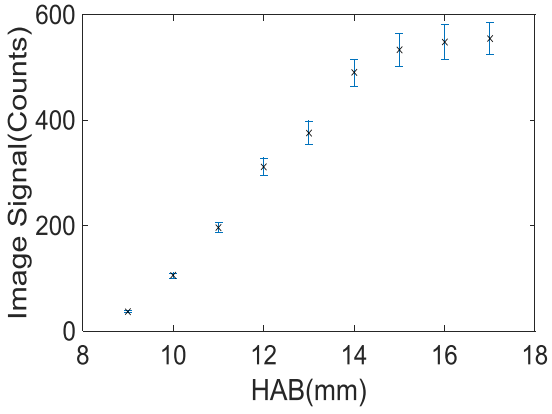

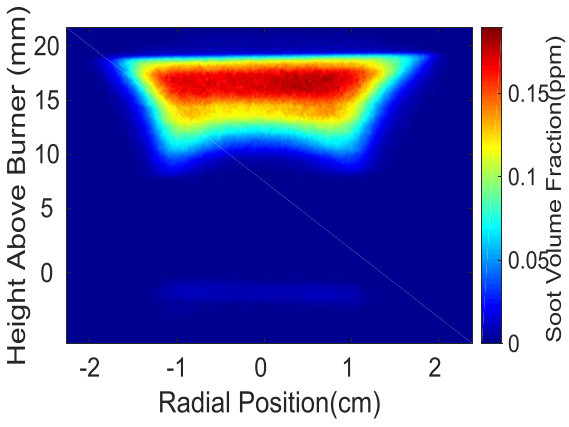

Figure 4-16: HAB centre line signal profile measured over 1mm Width for ϕ =2.3 for gate of 50 ns. The error bars represent the standard error between all images

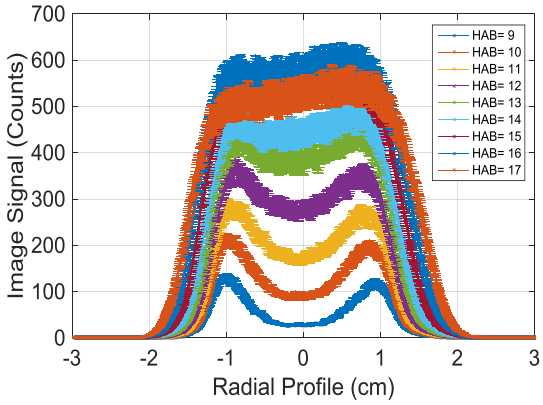

Figure 4-17: LII soot volume fraction Image for ϕ = 2.3

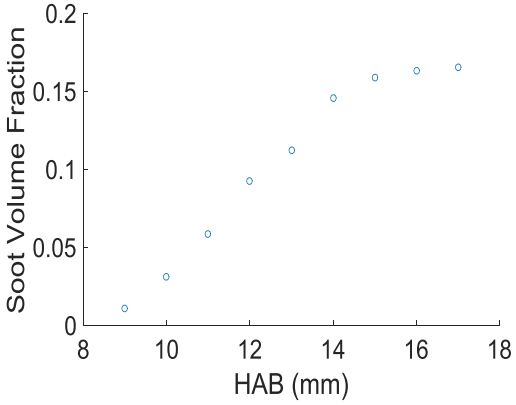

Figure 4-18: Horizontal profile across image at different HAB integrated over a height of 1 mm with error bars represent the standard error between all images

Figure 4-19: Soot volume fraction in ppm at Centre Line HAB for ϕ = 2.3

Flat-field correction

There is the rare occasion when there are spatial non-uniformities in the laser, this can lead to errors in the LII signal profile to correct for this a flat-field correction can be applied. The flat field correction works by comparing the results of an image set against a known profile of soot volume fraction profile and finding a correction factor for each vertical position in the beam. This correction factor can then be applied to other flames for each HAB of the beam. Previous experiments from other groups have shown flat field being reproducible.[103] For most cases the flat field correction was not need to be applied since there were no larger vertical non-uniformities in the laser sheet. The correction is based on a PMT measurement and the HAB can be compared.

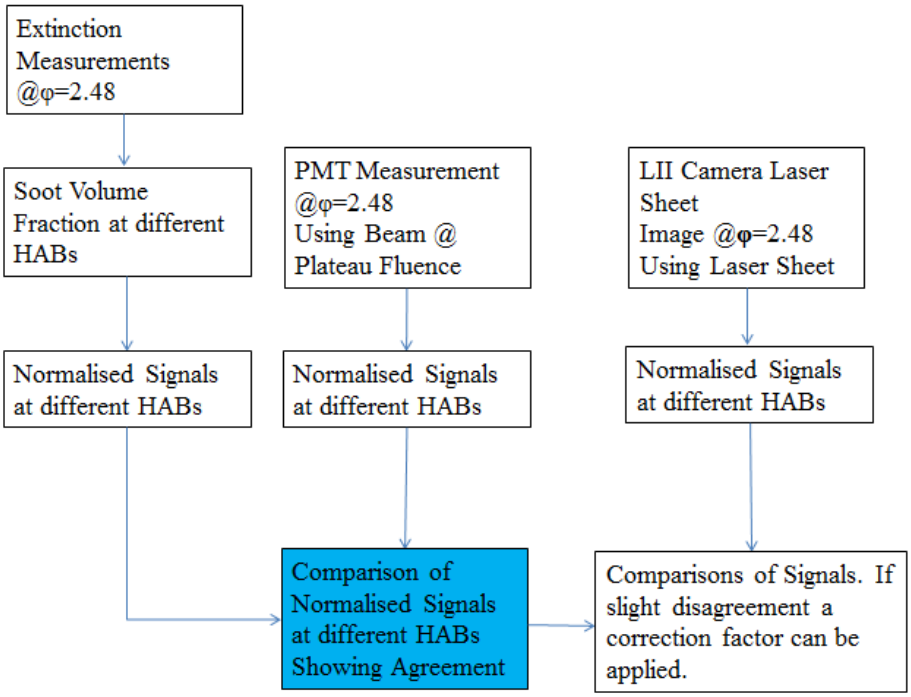

Figure 4-20: Flat-field correction (FFC) block diagram showing how the FFC was produced

Another way of performing a correction without a calibration image is to translate the burner by one mm. The correction should be the same at each translation +1 mm. Therefore there should be overlap and a correction can be made. This method is particularly useful when using the 532 nm laser light because the impact fluorescence may have at this wavelength. The next chapter will demonstrate this.

4.4.2 Data processing for PMT measurements

Using an oscilloscope, it is possible to record the LII temporally using a photomultiplier tube (PMT). It records an average of shots/LII results in increments from 8, 16, 32 64, 125,252. The standard number used for most experiments is the 64. An example of recorded results is shown in Figure 4-21. The temporal signal can be recorded and a MATLAB code is used to processes the signal.

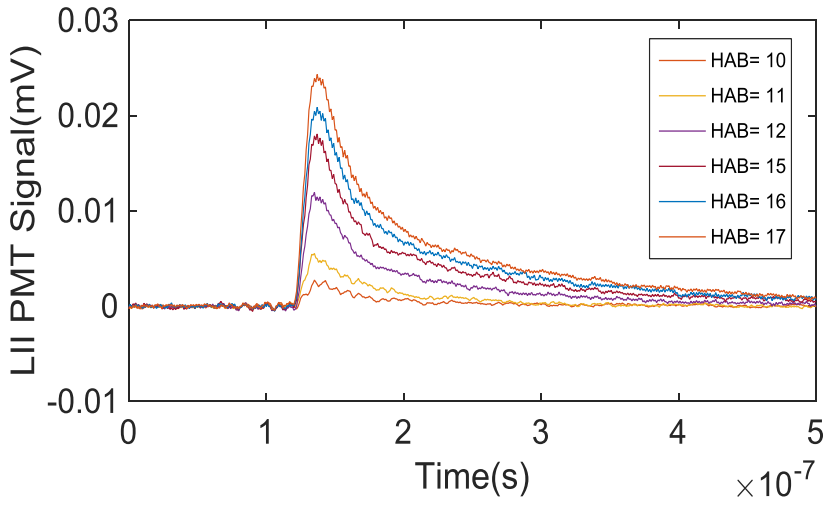

Figure 4-21: Example PMT signal result at different HABs for ϕ = 2.3 PMT Gain=600

By finding the temporal profile, the peak signal which is related to soot volume fraction and the decay which is related to particle size can be found. The code records the value of the peak signal and can then be used to produce a log signal at around 120 ns after the peak ensuring that the decay is in the heat conduction regime allowing an exponential fit. A line can then be fitted to the log to produce a decay time.[50] The fit is produced using MATLABs *nlinfit* fitting function to the model function which fits a non-linear regression fit. Care has to be taken when producing a fitted curve as it is important to start the curve in the heat conduction regime as well as the signal being large enough signal to reduce the noise to get a good fit. Using LII modelling techniques it could be possible for modelling data to be fitted to the data.

4.4.3 Time resolved LII (TiRe LII) imaging

Gate timing with relation to LII signal

Figure 4-22 shows the camera using two different gate lengths with relation to the peak signal. The gating causes integration over signal within this period. 50 ns is a common gate time used for experiments.[64] Since camera images are gated if vapourisation was to occur this could cause a difference in LII signal therefore it is important to know in relation to the signal where is being measured.[33]

These gates were lengths of 20 ns and 50 ns both deemed to be prompt enough as seen in the next chapter, when compared to other literature such as Hadef et al.[59] The PMT was found to have a time response transit time of 20 ns so therefore when comparing the gate to signal this needs to be taken into

account and the best way to produce a peak signal image is to do a temporal profile. This was found by to be the case by camera imaging[95,104]

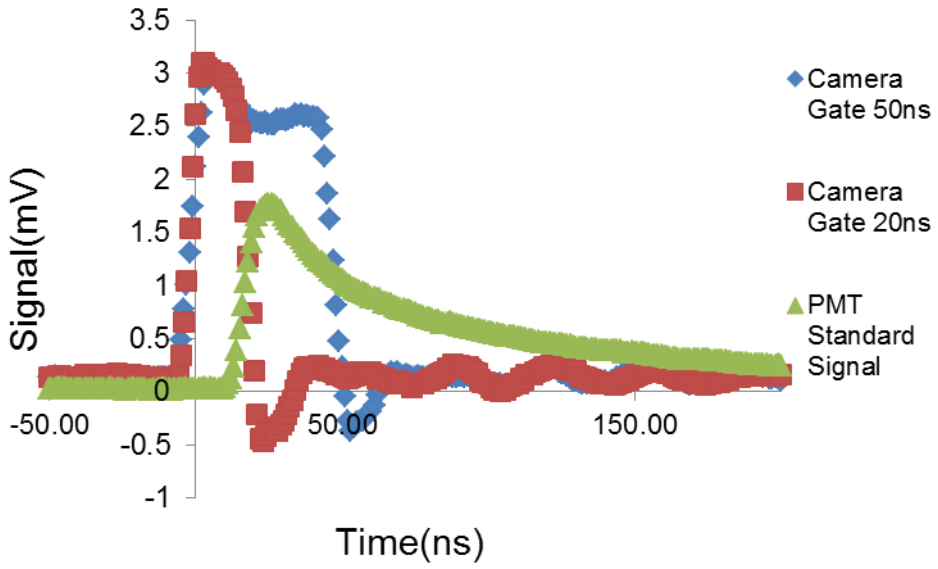

Figure 4-22: Graph showing different gates @ peak signal collection without correction for LII PMT signal transit time. 0s is arbitrary

Time Resolved Imaging

To produce a time resolved LII (TiRe) profile from LII imaging, these experiments used a short prompt gate of 20 ns, by using a short prompt gate allows for a maximum temporal resolution to be achieved, and when the gate is opened can then delayed with respect to the laser pulse to measure the signal of the LII signal forward in time. Each image can be processed at each time delay and then a HAB profile for each time delay can then be plotted to give a temporal signal over time using imaging technique. Using time resolved imaging works best in stable one-dimensional flames however this technique is expected to be applied to more complex flames such as the biofuel burner. [70, 105] Decay Times can then be found by fitting a linear fit though a log signal, after 120ns so to ensure the fit is to the heat conduction regime.

4.4.4 Choice of laser fluence

The fluence regime plays an important part in the absolute soot volume fraction measurement as well as the spatial distribution of laser light fluence can have a significant effect on measured LII signal. Zerbs et al.[57] show that there will be an optimum choice of fluence depending on the optical and detection setup. It is well stated that the spatial distribution of the laser can have an effect upon the LII measured signal such as a top-hat beam will show a different fluence curve when compared to a top-hat beam.

Figure 4-23 shows the fluence when measured with a camera and using a laser sheet profile at measured at the same gate position each time with Table 4-3 showing some detection parameters. When using the laser sheet, the highest fluence available is when it is starting to enter a plateau regime. This is similar to where the plateau occurs in other fluence curves of around 200 mJ/ cm^2. The results also show similar fluence curves indicating similar soot properties.[50,69,106]

The fluence curve has an underestimation of signal at lower fluences because the maximum signal occurs at different times as the fluence decreases whereas the camera gate remained fixed in relation to the laser trigger, this is a particularly relevant point in the long-pulsed LII chapter and can be demonstrated even through modelling. This is quite a subtle point but shows that for measurements using camera detection method the position of the gate with respect to the peak signal has to be known to get comparable results. For all these measurements used in this thesis the highest fluence achieved for a beam sheet was used and the position of the gate is known and covers the peak signal as known by recording the temporal profile of the LII signal.

Camera sheet profile

Table 4-3: Detection set up for fluence measurements using the camera

Intensifier Gain Setting	99 (maximum value)
Number of Images used to average	200
Gate	20 ns
Filters	450nm Bandpass 532nm Notch

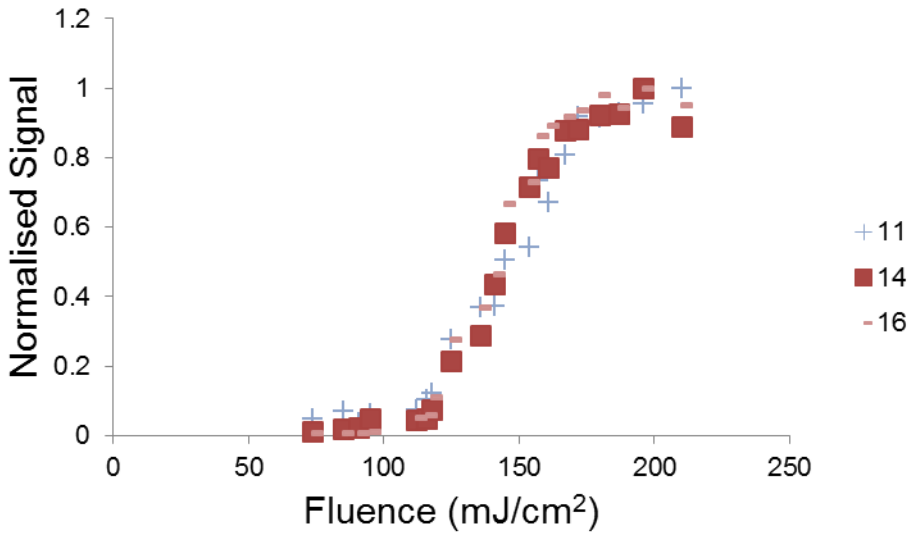

Figure 4-23: Sheet fluence measured by Camera 20ns gate to produce maximum signal @ ϕ = 2.3 at different HAB normalised to the same point

For soot volume fraction measurements in highly sooting environments higher fluences are preferred due to wanting to overcome extinction. However, because it is important in imaging to not cause perturbing the flame in not as extremely sooting environment a lower fluence was used to reduce the effects of vapourisation, an effect which when using imaging has a large effect on the signal.

4.5 Excitation with 532 nm experiments

For experiments where the fluorescence signal is implied from the subtraction of the LII signals form two different excitation wavelengths, (532 nm – 1064 nm), using a process discussed in the previous theory chapter, the fluence curve has to be compared and overlapped so that the amount of laser energy absorbed by the soot particles can be estimated and is the same for each excitation wavelength. The fluences must be matched to ensure the temperatures the soot particles reach are the same and the signal matches. For 532 nm excitation wavelength the setup is similar to the 1064 nm excitation wavelength except in this case the output of the laser is frequency double and the residual 1064nm light is discarded .[107]

The fluence was chosen for 1064 nm based on maximum possible so there being a good signal to noise ratio therefore a corresponding fluence has to be used for the 532 nm wavelength to ensure the particles absorb the same amount of laser energy and reach the same temperature. The fluence curve was done by plotting the LII centre line signal after 160 ns seen in Figure 4-24. By measuring the fluence with delayed detection, when the signal is at delay of 160 ns, ensures no interference from fluorescence which when the signal is measured over the peak signal because of the fast lifetime of fluorescence will interfere with the LII signal.[68]

It was found that to match the fluences the 532nm wavelength is around 1.9-2.1 times the 1064 nm wavelength fluence. The fluences used for this investigation were 210 and 105 mJ/cm^2 for 1064 nm and 532 nm respectively. There may be a small mismatch in the fluences however a small correction can be applied which doesn't affect the peak signal too much. The fluence curves could be better if a polarizer and half-waveplate was used and more discrete points were used but since the doubling crystal was in place the polariser was removed as it was only coated for a wavelength of 1064 nm causing a hazard if it was to be used.

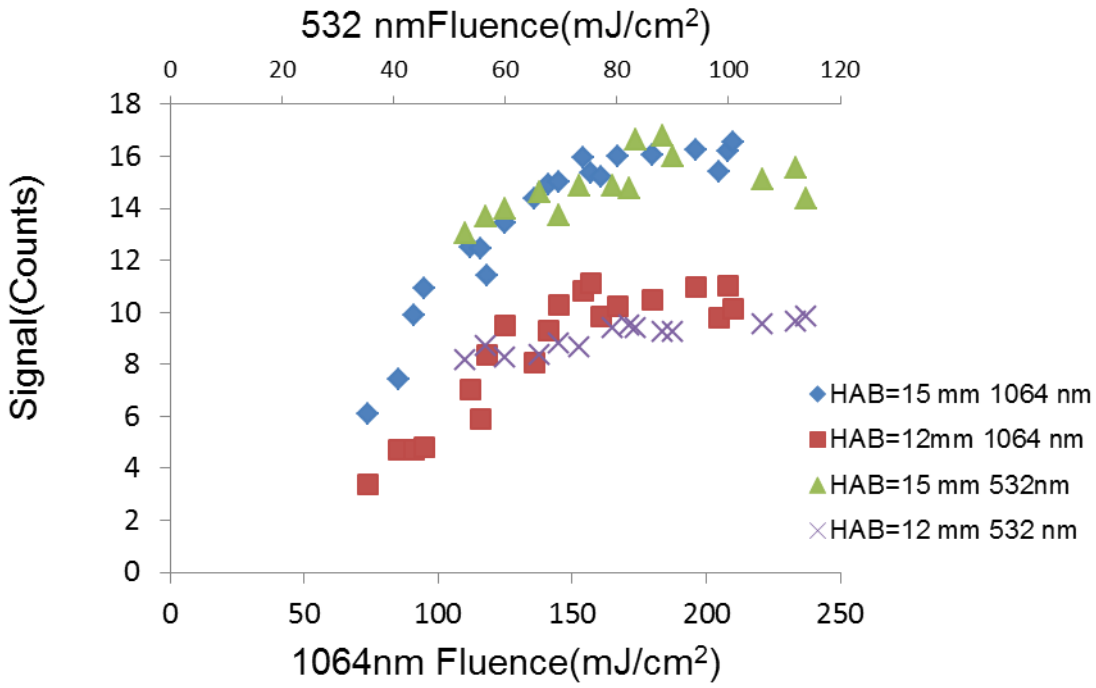

Figure 4-24: Fluence comparison between 532 nm and 1064 nm. Excitation wavelengths @ ϕ = 2.3 at a delay detection of 160 ns as to avoid interference of Fluorescence. The 532 nm wavelength fluence in measured in the top x-axis whereas the 1064 nm fluence was measured on the bottom

4.6 LII methodology summary

This methodology will be used in the next chapter to measure and characterise the flat flame burner that has been discussed in this chapter. The way the data is processed is described and allows for a comparable dataset of soot volume fractions at different equivalence ratios. After this burner has been characterised it also allows for other burners such as the capillary burner (comparing against the same equivalence ratio) and the biofuel diffusion wick flame (which uses the porous plug burner for calibration into soot concentration).

The fluence has been characterised as to relate to soot volume fraction as well as fluence curves between two wavelengths have been matched at delayed detection as to allow for comparison of the inferred LIF signal in the next chapter.

5 Validation of LII imaging methodology and characterisation of a flat flame burner

5.1 Introduction

This chapter shows how the soot LII image is calibrated to a soot volume fraction. This chapter also demonstrates how the methodology discussed in the previous chapter may be changed in ways to accommodate different requirements for experiments and validates any changes made to the methodology.

For validation LII imaging results are compared against different techniques (both extinction and LII point measurements) to ensure reliability in the procedure. This then allows for an accurate soot volume fraction calibration to be used to give soot profiles within the flame and burner being measured. LII using the camera produces a signal which is proportional to light intensity. By using extinction measurements a calibration between signal and soot volume fraction can be performed. Characterisation of the burner using LII can be done in multiple different ways such as HAB profiles of soot volume fraction and radial profiles across the burner at specific heights. These results can be used in a variety of flames with different equivalence ratios.

These results are taken in the water cooled porous plug burner as discussed in the methodology chapter. Measurements take place in a flame of ethylene fuel and air oxidiser flame over a wide range of stoichiometries from slightly to more substantially sooting. The range of height measurements vary from experiment to experiment, because the height of the stabilisation plate is 21 mm this range was chosen because it allows for a wide range of measurements without the laser sheet clipping the stabilisation plate with the light sheet covering 1 cm in height. Typically soot volume fraction profiles can be measured from 7 to around 18 mm. This is typical standard height measurements used in LII experiments.[108, 109]

This chapter shows results of different LII images at different equivalence ratios. This chapter shows the extinction measurement results used to produce a soot volume fraction. The calibration is then used to produce images of the soot volume fraction of the flame as well as soot volume fraction profiles.

Temporal profile measurements using the camera and PMT can be taken and decay times can be produced. This is useful especially for the camera as it allows for incandescence lifetime measurements to be taken at each individual point within the flame.

For verification that the methodology and technique is characterising the flame property results show comparisons to other techniques and include comparisons between collection methods such as

comparison between point measurements using a photomultiplier tube and imaging measurements using an ICCD camera. These include HAB profiles as well as radial profile measurements. They may also include comparisons between temporal profiles produced.

For validation and to allow for changes in the methodology, this chapter includes a detailed investigation of the effect of parameters including gate timing, filter type and size and slit size. The comparison between these factors allows for flexibility in the experimental set up so if the need for a slight change to the procedure to allow for better measurement conditions for a specific flame. For example by changing this slit size width from 2 mm to 1 mm it is possible to measure more precise positions which is especially useful in the case of the diffusion wick burner used in the biofuel chapter later on in the thesis.

After characterising the burner using the 1st Harmonic 1064 nm excitation wavelength of the Nd:YAG laser, the 2nd Harmonic 532 nm was used to induce incandescence as well. A comparison could take place to infer fluorescence signal from the subtraction of the two signals as discussed in the previous chapter. Previous research has shown that with an increased equivalence ratio there is an increase in the fluorescing species.[68]

5.1.1 Experimental factors and conditions

Table 5-1 shows the experimental factors used within this set of experiments. It shows the range of stoichiometries used, the excitation wavelengths and fluences used which was the largest capable using this methodology for the 1064nm light. As previously discussed the flames were of premixed ethylene and air and a detection wavelength of 450 nm used.

Table 5-2 shows some information on the detection settings typically employed and some information on the data processing used.

Table 5-1: Conditions and information relating to the experiments

Stoichiometry	2.05, 2.1, 2.2 , 2.3 ,2.4,2.5
Excitation wavelength/ fluence	532 nm 105 mJ/cm^2 1064 nm 220 mJ/cm^2
Fuel	Ethylene
Oxidiser	Air
Detection wavelength	450 nm +/- 10 mm

Table 5-2: Detection settings and data processing factors

Number of images	300
Camera gate	20 ns 50 ns
Camera gain	99
Camera delay	20 ns for prompt signal
Median filter applied to images	3x3

5.2 Laser induced incandescence results in a premixed flat flame burner

5.2.1 Images of LII signals in a flame

Figure 5-1 to Figure 5-6 show the LII signal measured in counts at different equivalence ratios when measured using a 50 ns gate and a 99 intensifier gain setting. These are produced by the data processing discussed in the previous chapter. These images are used to create radial and vertical profiles. The results shown have no flat field correction after comparison to reference measurements show that there was not one needed and not included even at the edges.

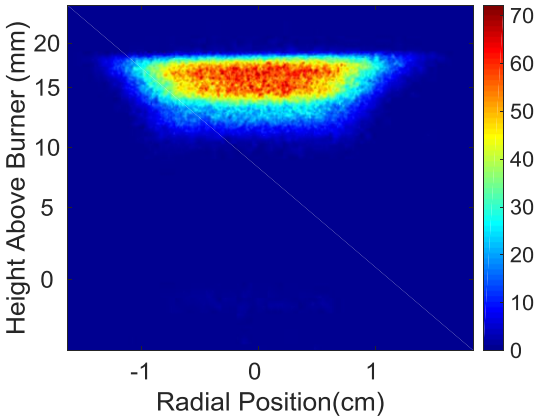

Figure 5-1: Image @Φ = 2.05 at 50 ns gate

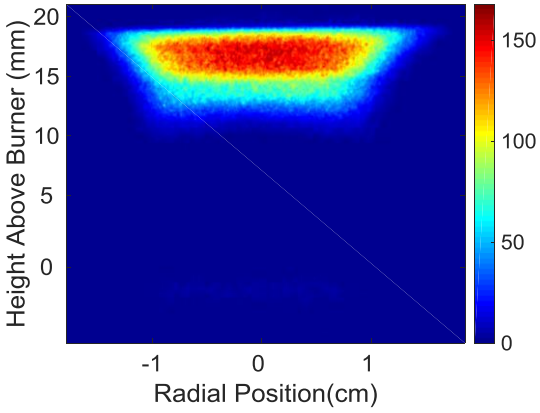

Figure 5-2: Image @ Φ = 2.1 at 50 ns gate

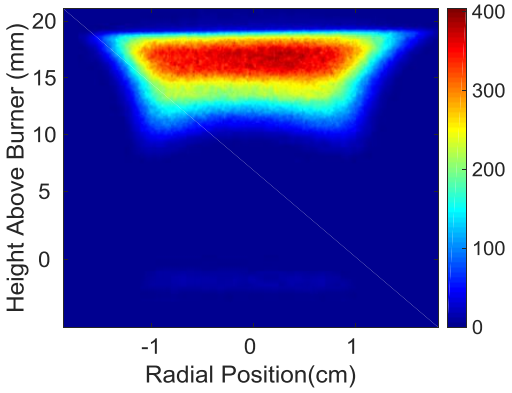

Figure 5-3: Image @ Φ = 2.2 at 50 ns gate

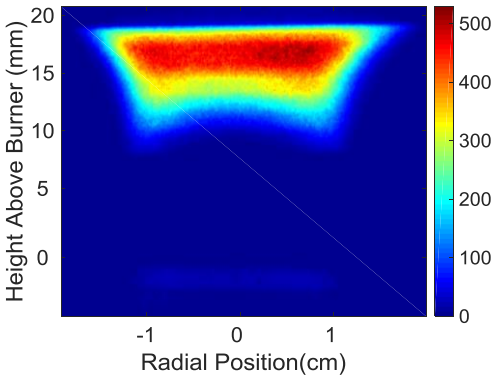

Figure 5-4: Image @ Φ = 2.3 at 50 ns gate

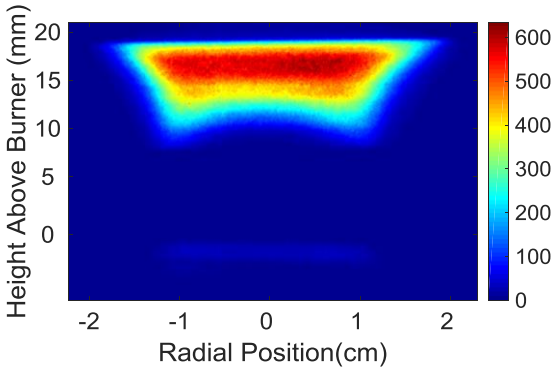

Figure 5-5: Image @ Φ = 2.4 at 50 ns gate

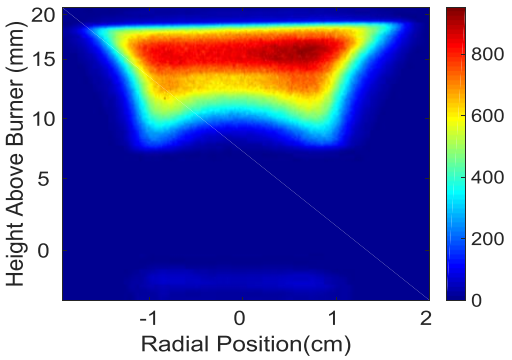

Figure 5-6: Image @ Φ = 2.5 at 50 ns gate

5.2.2 Centre-line profiles measured using camera and laser sheet

Figure 5-7 shows the centre line HAB profiles measured and average over 1 mm by 1 mm of pixel over the burner centre for different equivalence ratios. This is a common way of characterising the burner. Results show that with HAB burner measurements show what is as expected with this type of flame, when a flat field correction is applied. Soot formation occurs at around HAB=7mm and has a steady

rise and growth which typically levels out and forms a plateau region. Around this point particle growth ceases since there is a decrease in soot particle interaction since there is decreasing hydrogen content and decreasing particle surface caused by coagulation.[37]

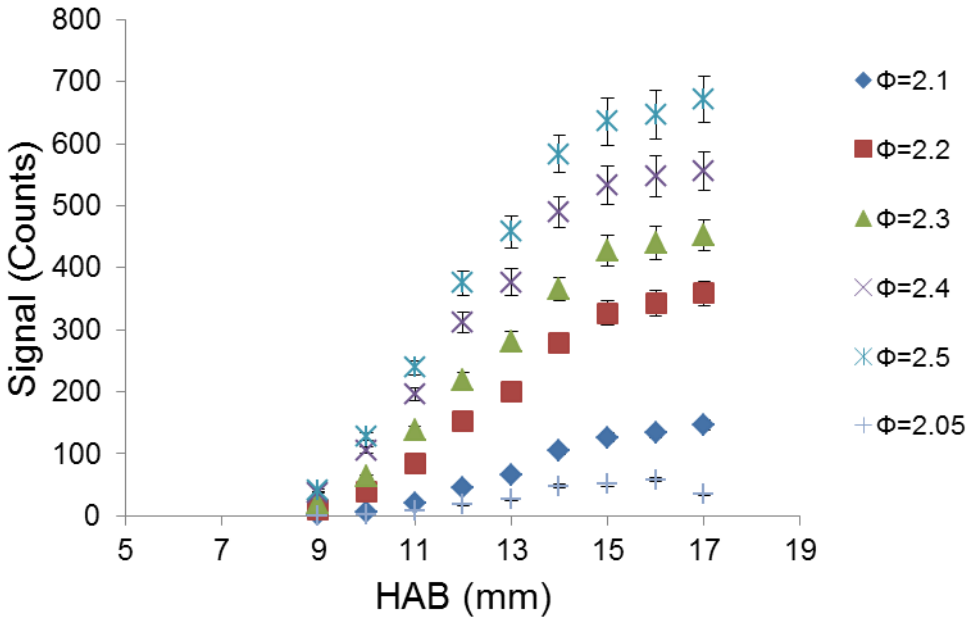

Figure 5-7: Centre line signal measured over width of 1 mm at different HABs at different equivalence ratios at 50ns Camera Gate averaged over 200 images. The error bars represent the standard error taken over all the images

5.2.3 Radial profiles measured using camera and laser sheet

Figure 5-8 to Figure 5-14 show the radial profiles measured and averaged over by 1 mm. for different equivalence ratios.

For profiles up until ϕ = 2.4 the profile at HAB = 15 mm is uniform however above this equivalence ratio there is a large dip in the centre. This is believed to be caused by signal trapping. The width of the soot forming area is also seen to increase with the increase in equivalence ratio as expected.

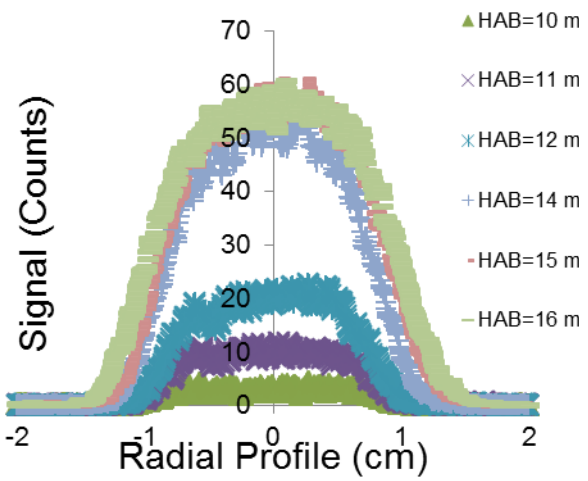

Figure 5-8: Radial profiles at different HABs for ϕ = 2.05

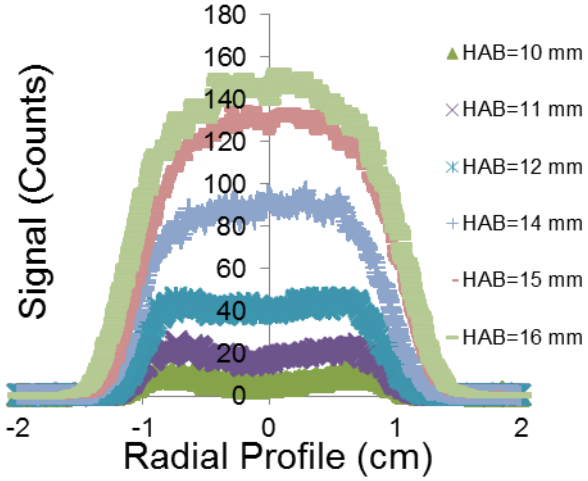

Figure 5-9: Radial profiles at different HABs for ϕ = 2.1

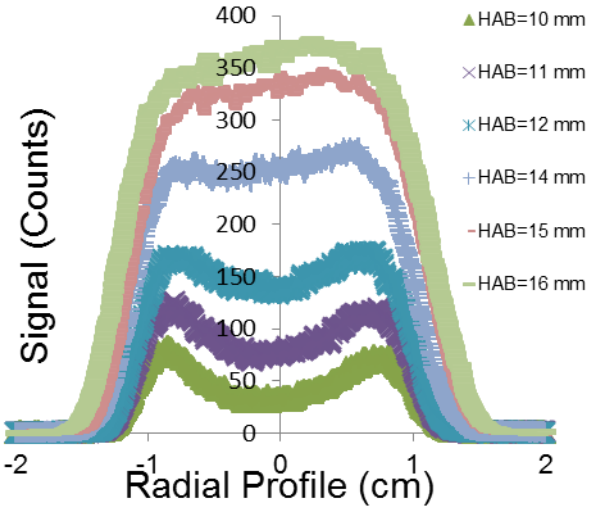

Figure 5-10:Radial profiles at different HABs for ϕ = 2.2

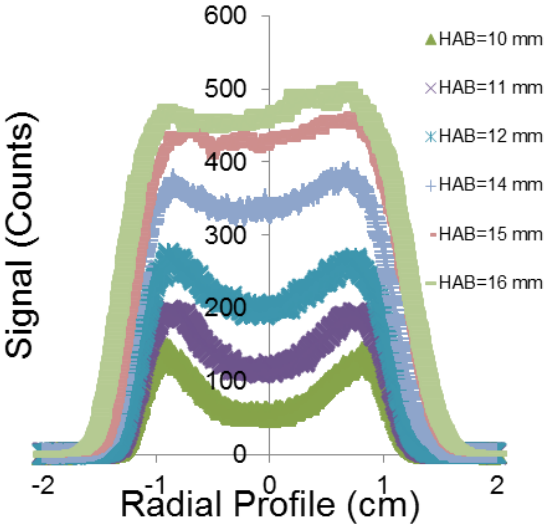

Figure 5-11: Radial profiles at different HABs for ϕ = 2.3

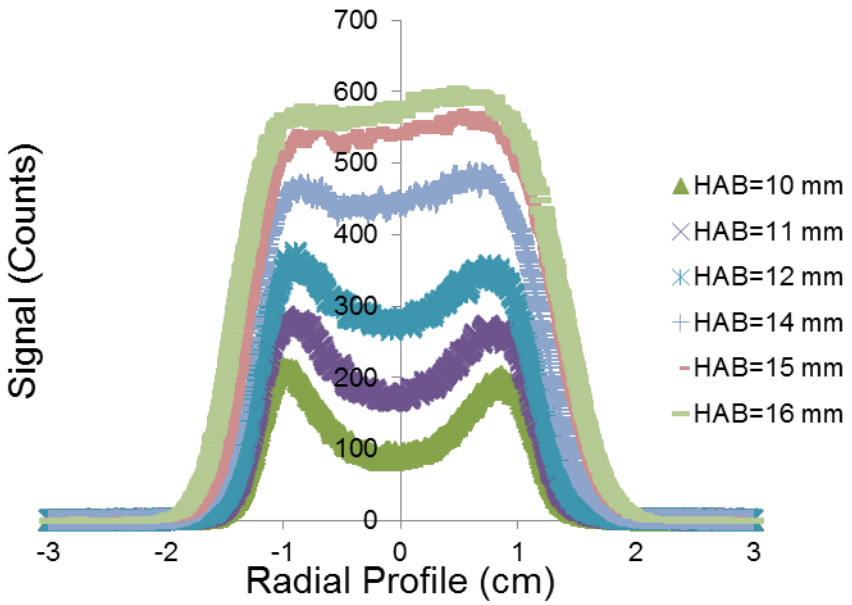

Figure 5-12: Radial profiles at different HABs for ϕ = 2.4

At lower heights for flames above ϕ = 2.2, the profile is axisymmetric for these heights until at higher positions above the burner they typically become uniform.[110] Figure 5-13 shows the start of the dip in the centre for when the equivalence ratio increases particularly the ϕ = 2.5 flame. This is where the extinction within the flame can be clearly seen with extinction measurements so it makes sense that some signal trapping would happen at the equivalence ratio. Care has to be taken when using any equivalence ratio above the 2.5 flame.

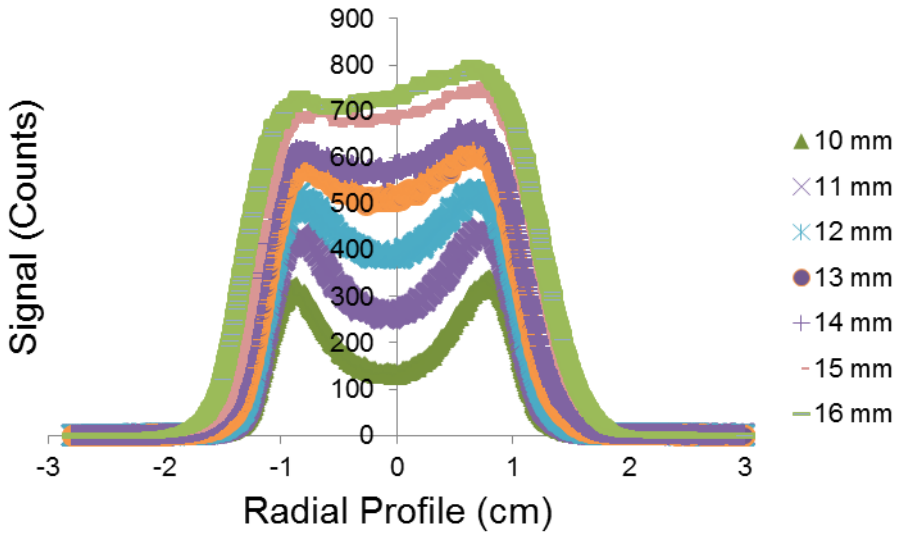

Figure 5-13: Radial profiles at different HABs for ϕ = 2.5

Signal trapping at larger equivalence ratios

Signal trapping is believed to exist in sheet imaging because when the equivalence ratio increases to ϕ = 2.6 and above there is a dip in signal in the centre of the flame. Figure 5-14 shows the radial profile for the ϕ = 2.6 profile.

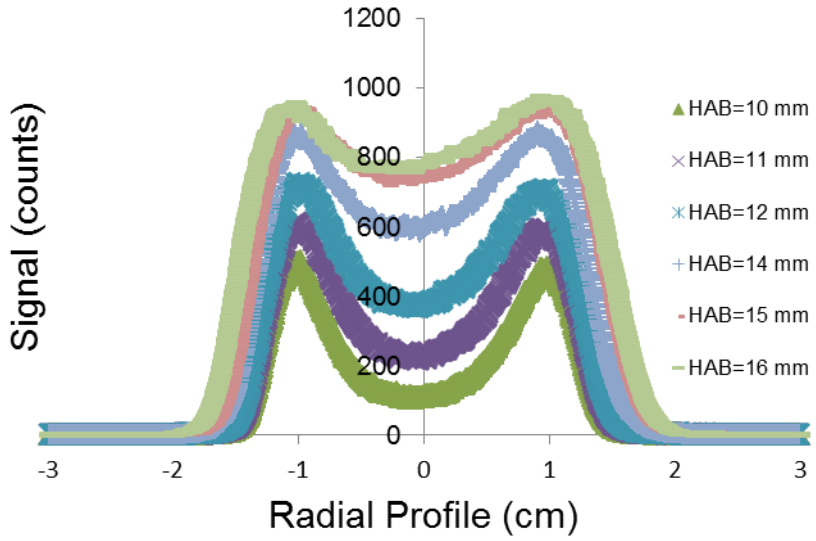

Figure 5-14: Radial profiles at different HABs for ϕ = 2.6

At larger equivalence ratios φ =2.6 and above the radial PMT measurements indicate that it is a uniform centre lime profile as measured in Figure 5-15

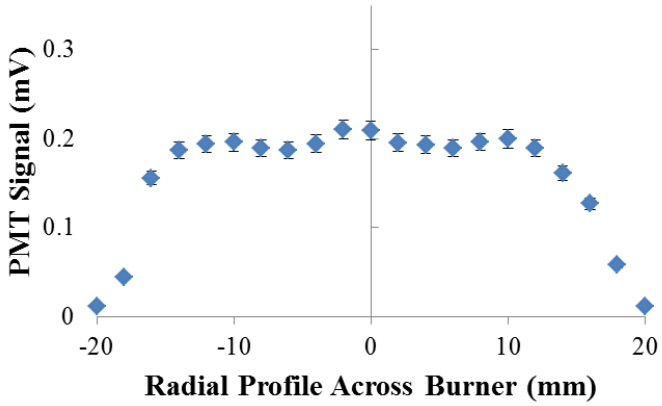

Figure 5-15: Radial Profile across burner at HAB of 15 mm at approx. ϕ = 2.9

It is believed that this is caused by the detection aperture heightens this effect. Whereas with the PMT the limiting aperture is the collection lens-a large aperture whereas the limiting factor for the camera is the different sized lens assumed to be smaller lens. Signal trapping may be overcome by using an onion like correction technique.[93] However, because of the scope of the work and the fact it doesn't happen until high, unrealistic equivalence ratios therefore a correction technique was mot developed. Boufflers et al.[111] show the radial effects that signal trapping has on the LII signal. Beam steering also becomes a problem in more sooting environments which also may contribute to this effect as seen in Liu et al.[112]

5.3 Validation of LII methodology

5.3.1 LII of laser beam Measured by camera, with comparison to measurements made with laser sheet

By comparing with other methods of LII excitation, it is possible to see if the results produced by each method compare and confirm that the methodology is working. The local fluences of the sheet and beam will be different with the beam having higher fluences meaning it should be suitable to use to help generate a profile for flat field correction. While the fluence may change the results, a larger fluence of 480 mJ /cm^2 was used for the beam to ensure the beam has entered the plateau region of the fluence curve and previous work carried out in this burner also deemed this level of fluence acceptable.

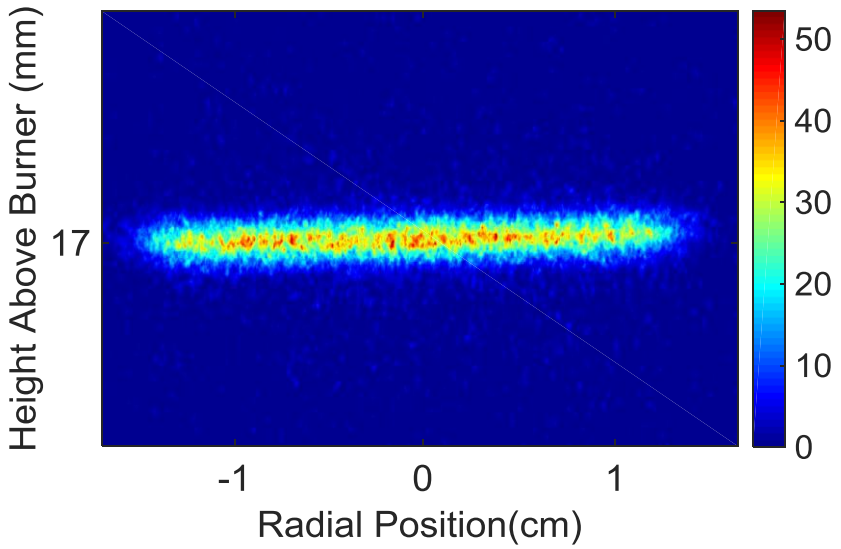

Figure 5-16: Example Image of LII using laser beam @480mJ/cm^2. Measured using ICCD Camera @ ϕ = 2.3

Figure 5-16 shows an image of LII in an ϕ =2.3 flame at HAB =15mm. The laser beam profile can also be assumed to be relatively top-hat but taking a vertical profile of the image could give more information. The gate was 20 ns so that it could be compared against the laser sheet value.

Radial Profile of the laser beam

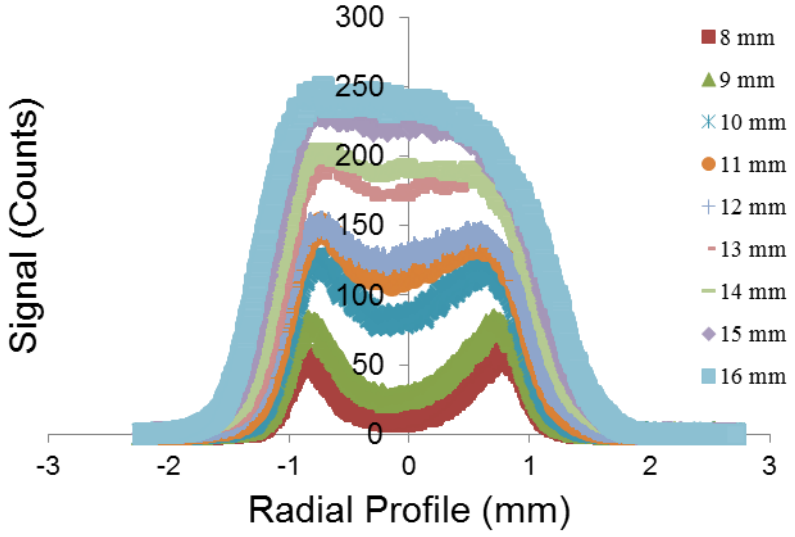

Figure 5-17: Radial profiles of beam measured using ICCD camera for ϕ = 2.3 at a gate of 20 ns

Figure 5-17 shows the profile using laser beam measured with the ICCD camera. This is what is expected from previous results since it exhibits the behaviour of soot formation to be axisymmetric at lower height above burners and at larger heights the soot profile is much more uniform similar as to what is seen when measured with the laser sheet. Overall they give agreement in normalised signal even though the comparisons between the beam and sheet have different fluences.

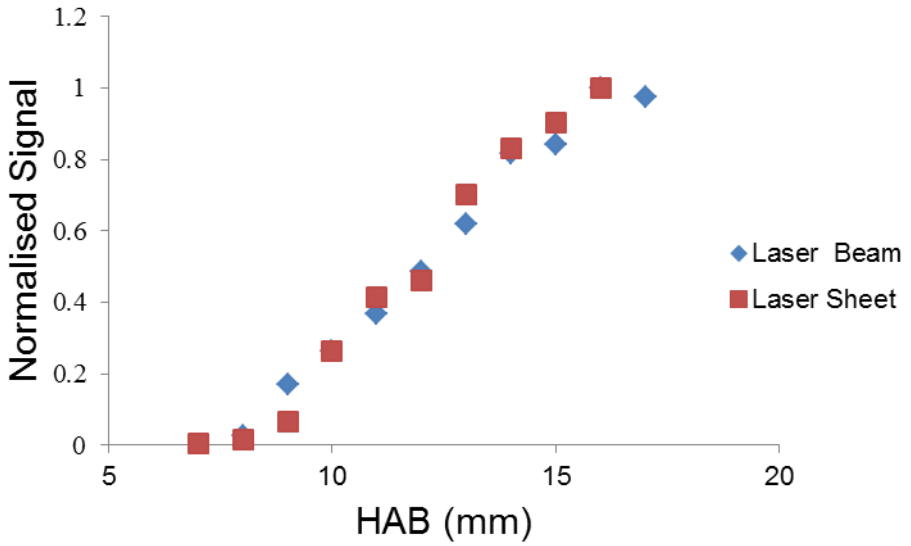

Figure 5-18: Comparison between laser beam and laser sheet @ ϕ = 2.3 using the same camera gate both normalised to their respective largest signal

Figure 5-18 shows a comparison between the normalised signal for the laser sheet and beam, where both data sets have been normalised to each their largest value. Results show good agreement and the profiles are similar and uniform indicating the imaging technique could also work with a beam if 1-dimensional measurements were needed.

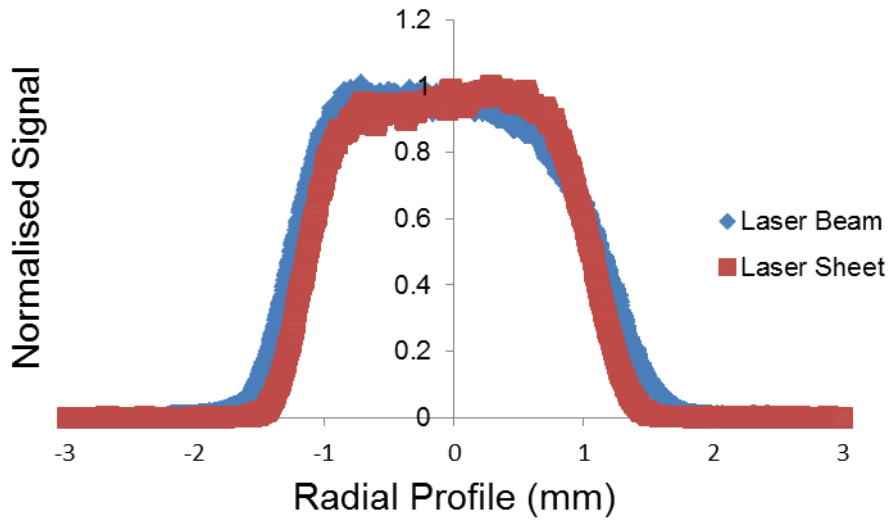

Figure 5-19: Radial profile Comparison of the laser sheet and beam at HAB=15 mm for ϕ = 2.3. Both normalised to each their own largest signal

5.3.2 LII signal measured with photomultiplier tube (PMT)

To compare against results for the beam sheet a PMT comparison had to be made. This was done in similar way to measuring the LII beam signal using the camera except with a PMT- HAB profiles and Radial profiles. More information can be found in the methodology section. For the radial profiles the burner was moved 1 mm perpendicular for each measurement into the beams path and a recording was taken. This was done for two different HABs for comparison.

For the HAB profiles the laser was placed in the centre through the burner, then translated by 1mm and then a recording was taken. This was done for two different heights above burners (15 mm and 10 mm).

To make sure that camera imaging measurements are properly measured, results can be measured against point measurements using a laser beam. The flame is moved with respect to the laser along the radial axis to measure at each radial point. A PMT recording of an average of 64 shots was recorded on an oscilloscope for each radial position.

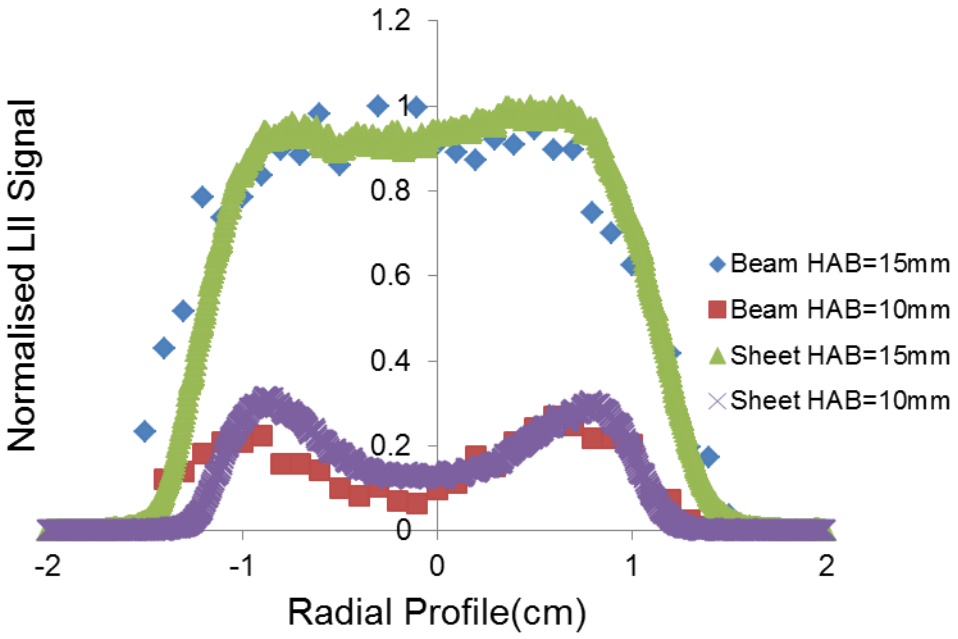

Figure 5-20: PMT beam and camera sheet comparison at 2 different HABs at ϕ = 2.3. Normalised to each respective beam and sheet measurements largest value

Figure 5-20 shows a comparison between the beam and sheet, measured using the PMT and camera comparison taken at Φ =2.3 at two different HABs of 10 mm and 15 mm. PMT measurements were taken by moving the burner 1 mm perpendicular to the PMT, parallel to the laser beam. The profile also shows the extinction profile in the next section. The results shows good agreement for the profiles are 2 different heights where the largest signal has been normalised indicating the profiles are similar so is the relative signal compared to both HAB.[65] These results also help explain the extinction profiles where the centre line of the lower heights is overestimated by extinction because of the larger soot signal at the edges.

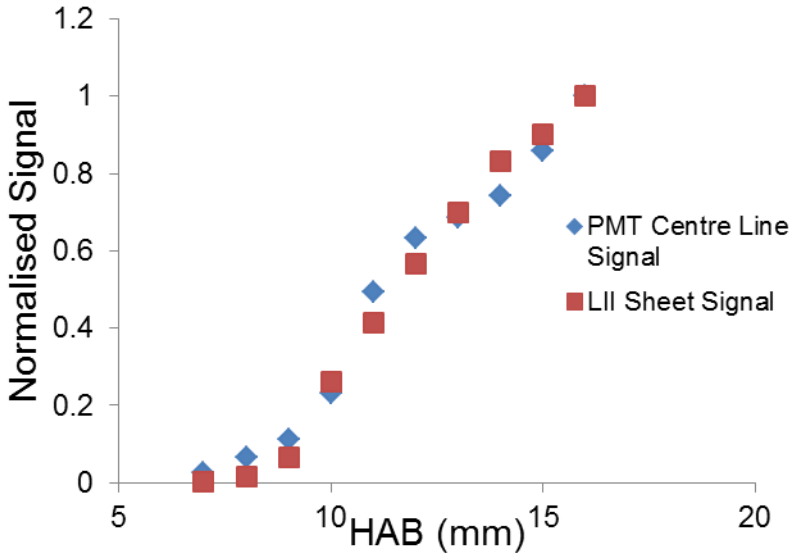

Figure 5-21: Camera image signal and peak PMT measurement centre line comparison at ϕ = 2.3 with normalisation occurring at largest value

Figure 5-21 shows the comparison when measuring the HAB with the PMT and laser sheet camera imaging. It shows good agreement indicating that the technique when applied with a flat field correction is suitable to use. They have both been normalised to their own maximum for comparison. Overall this result is important as the PMT beam is used to help create the flat field correction and show that the soot volume fraction calibration can be used.

5.4 Soot volume fraction calibration and calculation

5.4.1 LII signal profiles used for calibration

Figure 5-22 shows the profiles used for the soot volume fraction calibration and calculation that are shown later in Figure 5-32. Figure 5-22 is shown earlier but is shown again to show the calculation for soot volume fraction. Results show that with HAB burner measurements show what is as expected with this type of flame, when a flat field correction is applied. Soot formation occurs at around HAB=7mm and has a steady rise and growth which typically levels out and forms a plateau region. Around this point particle growth ceases since there is a decrease in soot particle interaction since there is decreasing hydrogen content and decreasing particle surface caused by coagulation.[37]

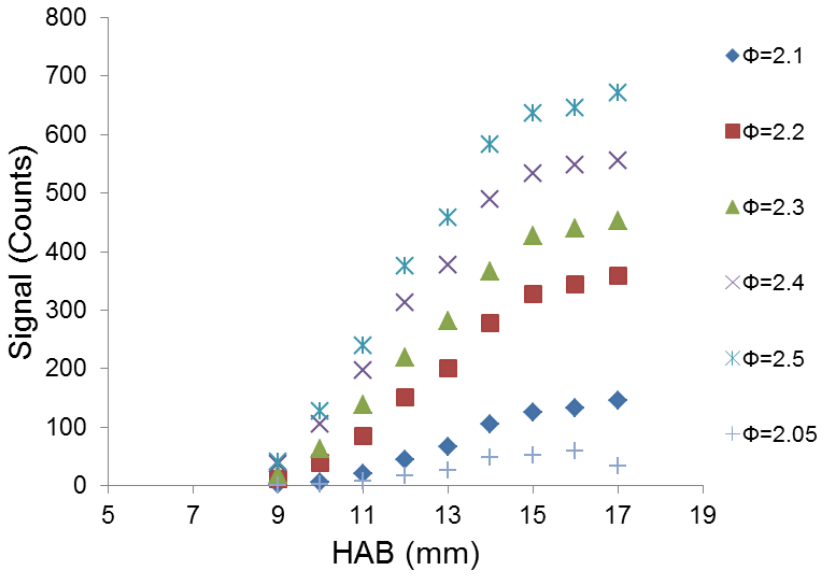

Figure 5-22: Centre-line profile for different HABs at different equivalence ratios used for soot volume calibration

.

5.4.2 Extinction measurements

Extinction Measurements were carried out and calculated in the same way as the method discussed in chapter 2.2.5 using a 1060 nm continuous fibre laser and measuring the change in intensity using a diode and lock in amplifier as seen in Figure 5-23. A lock in amplifier was used to improve accuracy by only registering the change in the 1060 nm wavelength. This wavelength was used as it is similar to the wavelength of the Nd:YAG laser meaning the E(m) value which is wavelength dependant is the same. It is also assumed that at this higher wavelength no scattering takes place due to the size, which might not be the case if a shorter wavelength was used.[40]

Measurements were taken at ϕ = 2.48 as this was the lowest equivalence ratio that gave a reliable reading. The soot volume fraction was then calculated using the extinction coefficient measured. E(m)

was taken to be 0.3 +/ 20 %[51] as well as 32mm diameter for path length. These measurements were repeated twice.

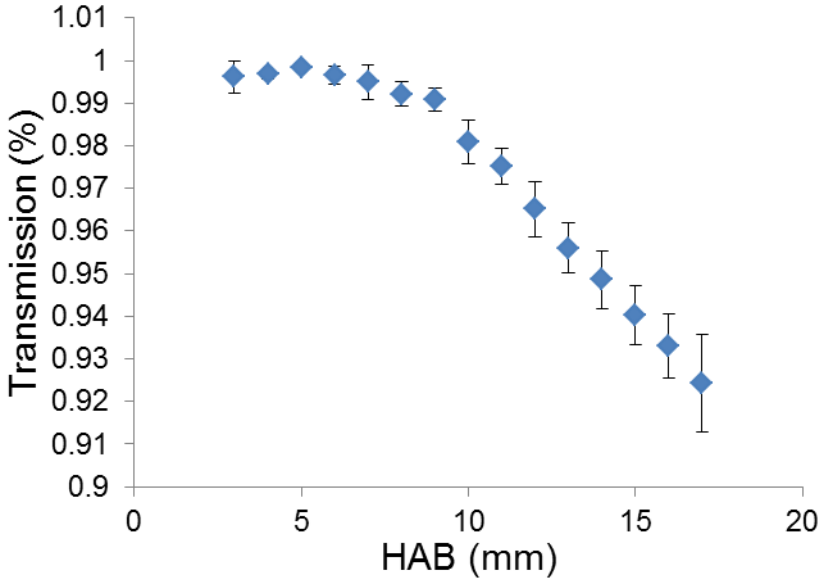

Figure 5-23: Extinction measurements using 1060nm DFB. Transmission at different HAB @ ϕ =2.48 in a premixed ethylene flame. Standard error based on 3 measurements

Figure 5-23 shows the transmission of the results from extinction measurements and as the HAB the transmission decreases indicating to results similar to ICCD camera measured soot volume fraction profiles. It can be seen that at larger HABs the error becomes larger. This is probably due to the fact it is a line of sight technique. The error bars show the standard error between three different measurements.

Figure 5-24 shows the overall soot volume calibration and at is expected and compared to other soot volume fraction from literature such as Hadef et al.[59] Soot formation starts at around 7 mm HAB which is consistent with previous results.

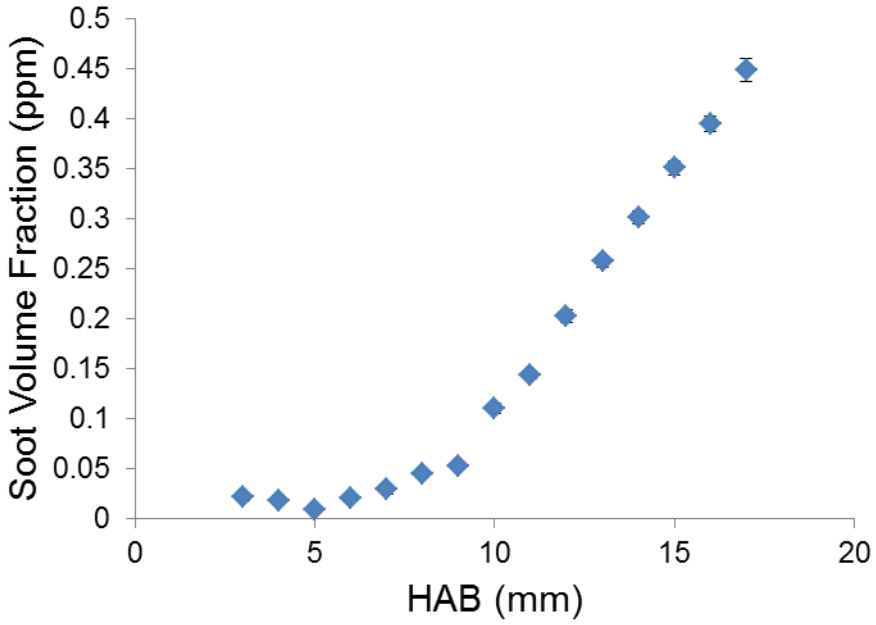

Figure 5-24: Soot Volume Fraction Calculated from Extinction Measurements @ ϕ = 2.48

Figure 5-25 shows the normalised to the value at 17 mm from extinction measurements and the results from the LII sheet imaging experiments at ϕ = 2.3. They show similarities except at lower heights this is probably due to the fact extinction is a line of sight technique whereas the imaging is a centre line measurement; therefore at points where the profile is axisymmetric the extinction will be overestimated. Since the calibration only needs to be dependent on one point this is not much of an issue.

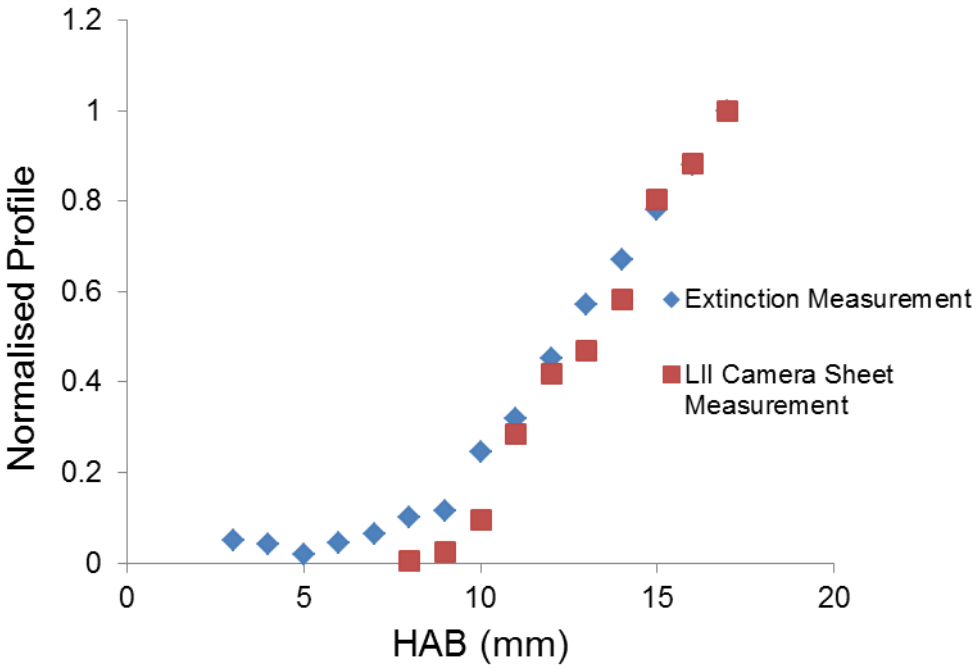

Figure 5-25: Extinction and LII comparisons of burner at ϕ = 2.48

5.4.3 Soot volume fraction results calibrated from extinction measurements

Soot Volume Fraction Calibrated Images

Figure 5-26 to Figure 5-31 show the colour map of soot volume fraction for flames where from ϕ = 2.05 to 2.5 using a camera gate of 20 ns and measured at the peak signal. These are a set of images averaged over 300 images. The variation in these images is typically 5% or below. These are the calibrated images shown previously. The soot volume calibration works by finding a soot concentration to pixel calibration constant for the ϕ = 2.5 flame from extinction measurements. This value can then be used to find the full soot volume fraction profile of each image.

The images give reasonable results and show what would be expected in this burner up until above ϕ = 2.5 where a large dip in signal occurs in the centre of the flame. This is believed to be caused by mainly signal trapping as discussed previously. An interesting side note is that as the signal from the flame increases the signal from the burner can be seen in the images; therefore care must be taken when using measurements in high equivalence ratios flames to avoid interference from the burner plate.

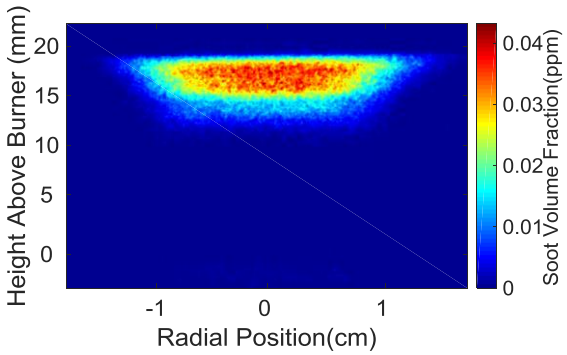

Figure 5-26: Image of soot volume fraction @ ϕ = 2.05

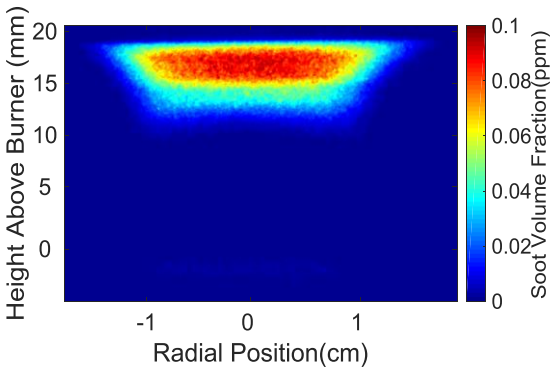

Figure 5-27: Image of soot volume fraction @ ϕ = 2.1

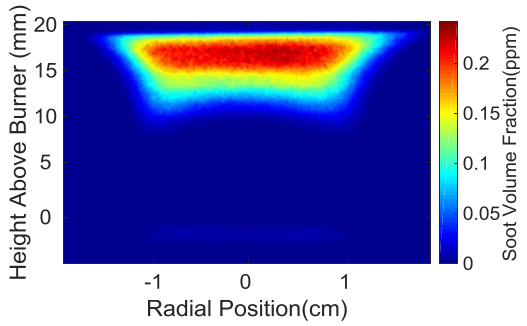

Figure 5-28: Image of soot volume fraction @ ϕ = 2.2

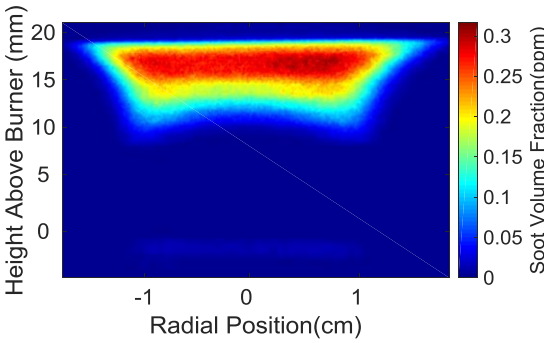

Figure 5-29: Image of soot volume fraction@ ϕ = 2.3

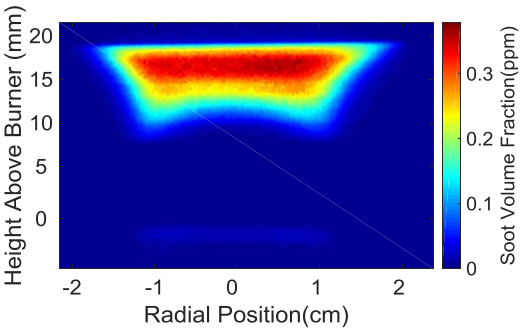

Figure 5-30: Image of soot volume fraction@ ϕ = 2.4

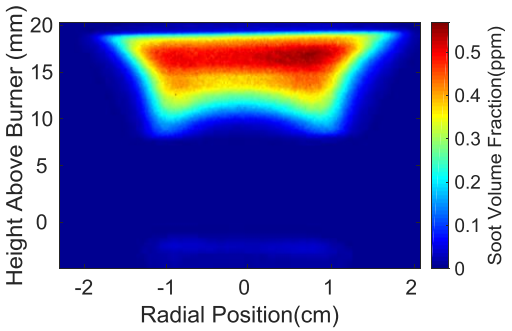

Figure 5-31: Image of soot volume fraction @ ϕ = 2.5

Soot volume fraction centre line profiles

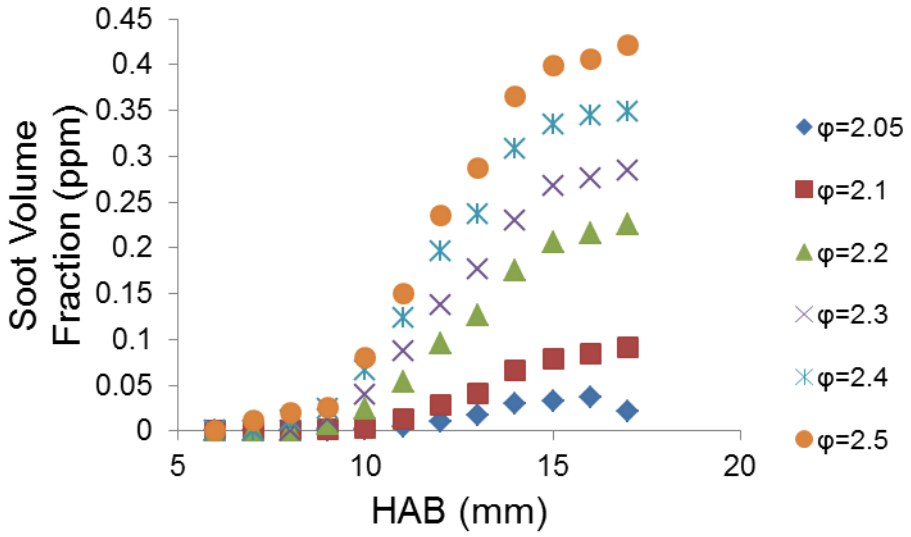

Figure 5-32: Soot volume fraction centre line profiles at different equivalence ratios

Figure 5-32 shows the soot volume fraction calculated using the extinction measurements for calibration. This was measured using a measurement of different images to produce a full soot profile. It gives results similar to what was expected. The largest error is assumed to be in the E(m) calculation which is around 20 %, whereas the standard error of results of signal is always below about 5 %. Therefore no error bars have been attached to the figure.

The results are what were expected as they show soot formation at similar HABs as well as being reasonable when comparing to other similar burners. The results show a good similarity to the results shown in Hadef et al.[59] With the increase in equivalence ratio there is an increase in signal thus soot volume fraction, this can typically even be seen by eye with the flame glowing brighter with larger equivalence ratios. This is expected as it indicates that with less fuel there will be a decrease in particle or the amount of soot particulates.[113]

The overall images show reliable images up until a point where an equivalence ratio that wouldn't typically be used in typical experiments. For all flame conditions there was no detected signal below 7 mm implying that there is no matter that can be large enough to incandescence there such as soot and because it is assumed the 1064nm does not induce fluorescence in the PAHs or that the detector isn't sensitive enough to measure LII at these positions. Even when visually looking at the flame, there appears to be no orange glow at these heights which is characteristic.

The profiles exhibit typical behaviour where soot formation occurs around 8-9 mm and rise steady due to surface and coalescence growth and reaches a plateau region. This has been accredited due to the

decrease in soot particle activity caused by decreasing number of hydrogen atoms or the decrease in particle surface caused by coagulation. [25,50,59]

The shape of the profiles is also similar to aromatic compounds previously stated by Melton et al.[114]

5.4.4 Temporal profile of LII measured using an ICCD camera in a flat flame burner

As discussed in the methodology section it was possible to move the camera gate with respect to the signal, allowing the measurement of temporal profiles. Temporal profiles from images were able to be produced by moving the gate forward 20 ns with two examples of temporal profiles with different equivalence ratios seen in Figure 5-33 and Figure 5-34. The gate was kept as prompt as possible to 20 ns which ensure a more reliable profile. Temporal profiles show good agreement with what is to be expected for conventional LII signals. These results consist of an average of 50 images. This was chosen since De Risi et al.[64] used the same amount of images for time resolved profile in a diffusion flame and showed that this was enough averages to reduce the standard error to around 3.5%. There was only one position of the centre line that was measured. However, it is possible to measure the decay at different positions. The decay time gives an indication of the particle size and by using a model and assumptions it is possible to estimate the particle size. The larger the particles the larger the decay time.

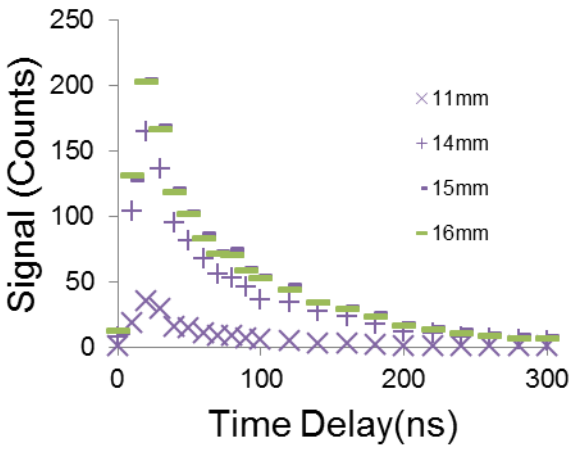

Figure 5-33: Camera temporal profile for ϕ = 2.3 with 20ns Gate

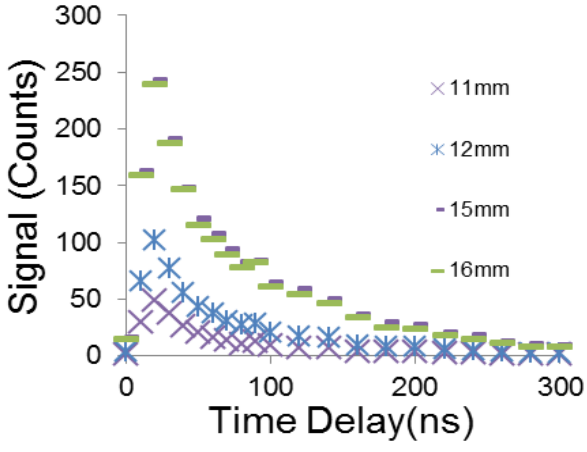

Figure 5-34: Camera temporal profile for ϕ= 2.4 with 20ns Gate

Results show that the higher the sooting propensity the higher the signal is produced. One main advantages of being able to use 2-dimensional images is being able to take LII images and produce temporal images within stable flames for stable flames.[72] Further work in modelling may allow for a model LII signal to be fitted on to the experimental curve allowing for a primary particle diameter to be estimated. As discussed previously a decay curve is able to be produced by taking the relevant part of

the curve after 120 ns where conduction is the main regime for heat transfer, and by plotting the log of the curve, the curve can then have a fit applied to it:

$$Decay = A\exp(-\frac{t}{\tau}) \quad \textbf{Equation 5-1}$$

Where A is a constant

Where τ is the decay time.

The decay time is related to the decay rate by:

$$decayrate = \frac{1}{\tau} \quad \textbf{Equation 5-2}$$

As discussed previously larger particles will have longer decay times due to smaller surface to volume ratio than smaller particles so the particle size can be estimated.

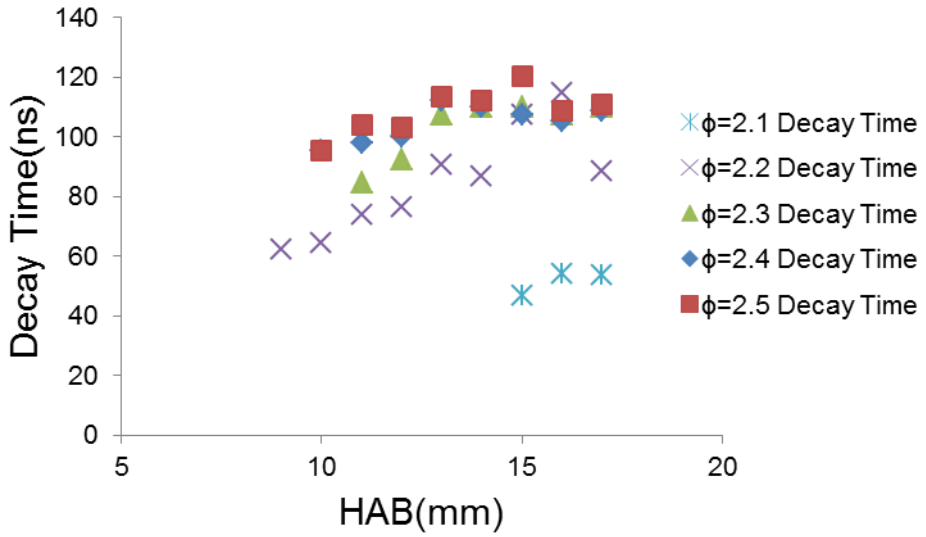

Figure 5-35: Decay times taken from 120 ns delay

A natural log curve was produced and a fit was taken at 120 ns after to the curves to produce a straight line equation and using the technique discussed before in the theory chapter, to produce a decay time. Decay profiles at the equivalence ratio of 2.05 could not be used because of the very weak signal when

fitting the decay. Bladh et al.[24] demonstrated time resolved profiles in low sooting so-called nucleation flame with the extremely low sooting flames and to overcome low signal had to use broadband detection.

Figure 5-35 shows the decay times calculated from the temporal profiles. This time was chosen to avoid the heat transfer components other than the conduction regime. The decay times are in the same magnitude as other decay time measurements from other groups such as Axelsson et al. [50] There are slight differences which are possibly caused by differences in calculation of decay time. Examples are differences in fluence which can cause change in particle size and consequently changes the decay time.

There is an issue with a fit at lower point in the flame where the signal to noise ratio and the fit is not as reliable-around HAB=10 mm depending on the equivalence ratio.

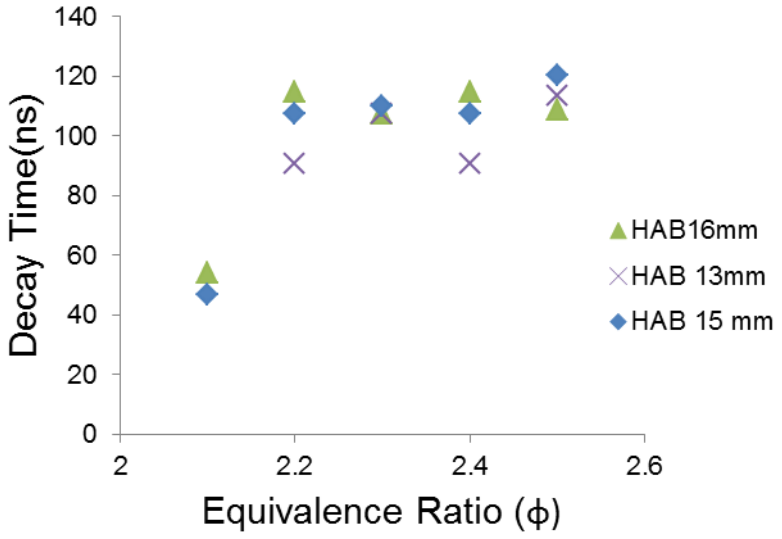

Figure 5-36: Different decay times for different HABs at increasing equivalence ratio

Figure 5-36 shows the difference in decay time with equivalence ratio at different height above burners. The results show similarities to results shown in Hadef et al.[59] Desgroux et al.[115] also show that with lower equivalence ratios there is also a lower decay rate in low pressure methane flames. Figure 5-36 shows that with all HABs the decay time increases however it seems to level off more with each increase in equivalence ratio. For the lowest equivalence ratio, the only HAB that could be roughly calculated was 16 mm as the rest showed results which were not applicable. Overall these results show that being able to take a reliable temporal LII profile is possible and at different heights the temporal signals can be simultaneously collected which is one advantage over using a PMT.

5.5 Imaging results characterising the effect of various measurement parameters on experimental performance

This section of the thesis investigates the effects of changing some parts of the methodology that would be useful in other types of environments. These changes include changing the camera gate length, changing from a 2 mm wide slit to a 1 mm wide slit which would be useful in thinner flame fronts, and changing the filter size from a 2" dimeter filter to a 1" diameter filter. By ensuring that changing these experimental parameters doesn't affect the empirical trends and data that the set up can be interchangeable and therefore can be used for when an experiment requires the use of a certain setup.

Having demonstrated that the default procedure gives reliable results and generated images of soot volume fraction, we now address some experimental situations where modifications to the methodology are needed such as the need to increase the gate time or change the imaging slit size. These changes are needed dependant on signal level, geometry of the flamer and other factors that need to be taken into account to allow changes when the experimental work requires slight changes to the methodology.

5.5.1 LII signal comparison using different gate lengths

For some types of flames the signal to noise ratio may be so low that a longer gate may have to be employed. However, this can lead to differences in expected signal and radial profiles since the signal collection isn't as prompt, and therefore for this burner the effect of gate length on signal was compared. So when doing a calibration image the same gate should be used therefore it is important to test the differences in gate for this flat flame burner.[56]

This is particularly important for comparison to the long-pulsed laser excitation source chapter where the gate has to be 50 ns as the signal to noise ratio was too low for the 20 ns prompt gate. This is also important for the biofuel chapter where the large amount of signal requires a smaller gate which helps distinguish between the movements within the flame that occur as well as improving the resolution of the signal.

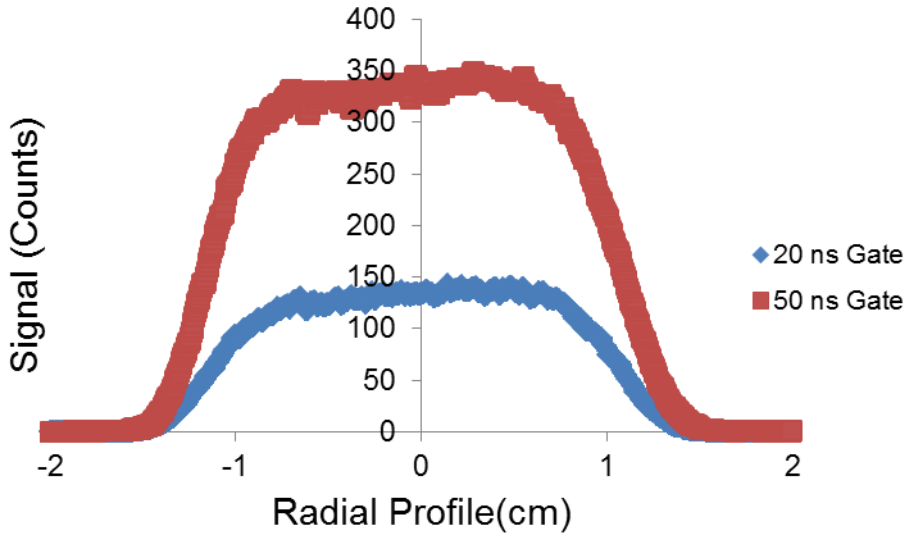

Figure 5-37: Comparison between 50 ns and 20 ns Gate @ HAB=15 mm @ ϕ = 2.3

Figure 5-37 and Figure 5-38 shows the radial profile at one HAB (15mm, a commonly measured HAB) with Figure 5-38 showing the normalised comparison showing overlap and the same profile.

Stirn et al.[116] found no influence of the stabilisation plate on the decay curve at this height giving good indication it provides a reasonable position to measure the radial profile. A normalised comparison where each gate profile was normalised to their highest value can be found in Figure 5-38 showing good agreement indicating that the particle size profile is uniform across the burner.

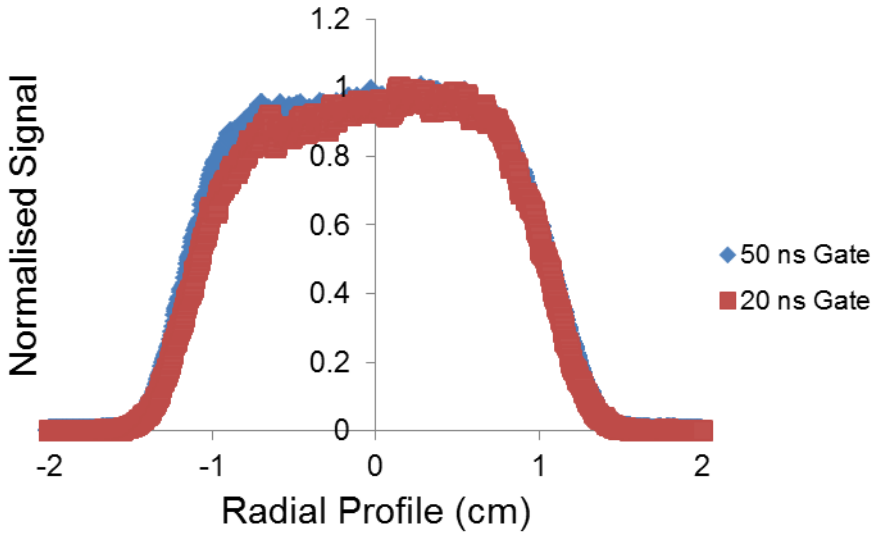

Figure 5-38: Normalised Signal Comparison between Camera Gates @ ϕ = 2.3 @ HAB=15mm

Figure 5-39 shows the normalised profile centre line signals of these two different gate lengths. Both gates are normalised to their largest value. The results show good agreement indicating that for this type of flat flame burner the gate length does not have a considerable difference between the points so it makes no difference to the profile. This means that if a case occurs where a longer gate has to be used the calibration image will still be reliable. The normalised signal does not depend on the soot concentration but rather the particle size, therefore this trend will not change over equivalence ratios.

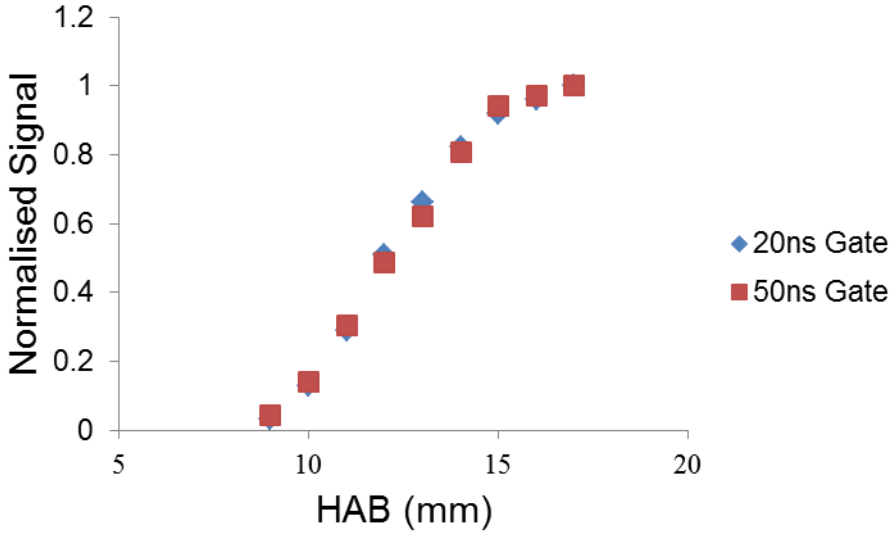

Figure 5-39: Normalised Centre Line between 20 ns and 50 ns @HAB=15 mm @ ϕ = 2.3

Figure 5-40 and Figure 5-41 shows the overall signals for 2 different gates at the same HABs and equivalence ratios for just one set of images of 300 images. The signal was integrated over a height of 1 mm and a width of 1 mm. This is a standard length measurement for HAB profiles and a similar size measured by the photomultiplier tube.

They both show similar profiles as well as similar profiles to literature.[50,117,118] It was found that soot growth mainly starts at around 8-9mm however starts even lower for more sooting flames as expected.[24]

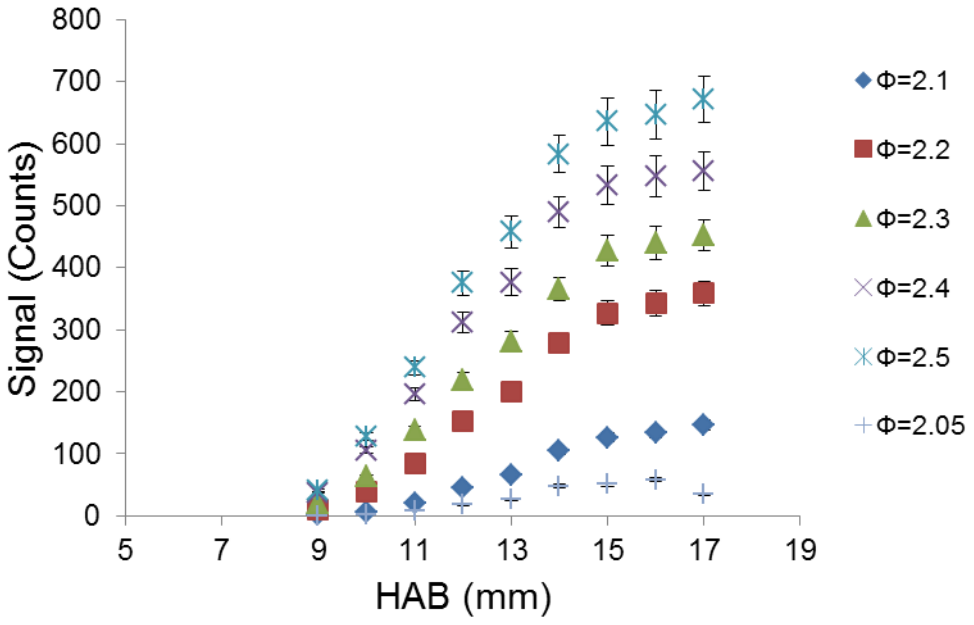

Figure 5-40: Centre line signal measured over width of 1 mm at different HABs at different equivalence ratios at 50ns camera gate averaged over 300 images

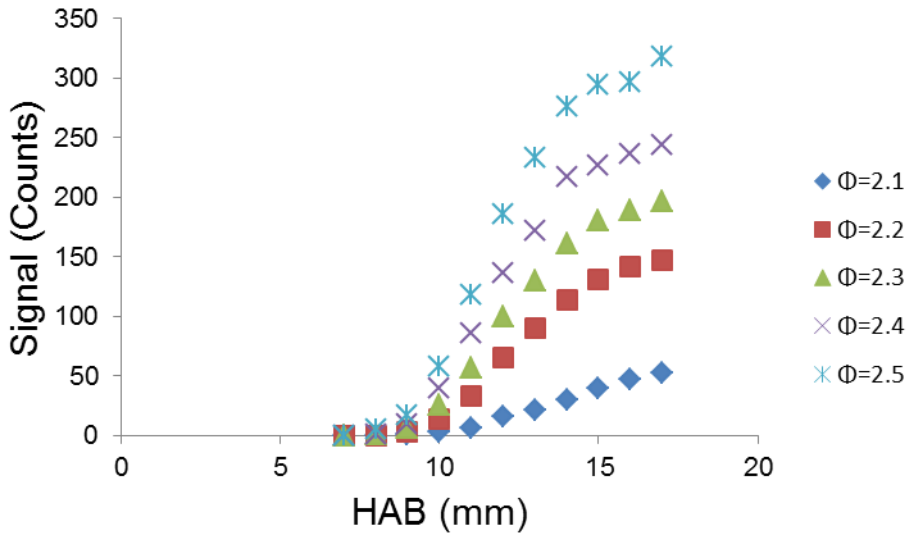

Figure 5-41: Centre line signal measured over a width of 1 mm at different HABs at different equivalence ratios measured at 20ns gate averaged over 200 images

5.5.2 LII signal comparison using different slit sizes

For these experiments the experimental procedure is kept the same as the set-up explained in the methodology except a slit size of 1 mm was used for shaping the laser sheet was used instead of the 2 mm slit, which has been used throughout this chapter. By using a finer slit the measurement volume becomes more fine which allows for smaller diameter burners to be measured accurately, in particular the biofuel wick diffusion burner which is the subject in a later chapter. To ensure that when using the narrower slit, signal remained acceptable. The profiles using these two slits were measured and a comparison was produced. With a narrower slit from experiments the vertical profile was seen to be less precise with a flat field correction needed more when the narrow 1-mm width slit was in use.

Figure 5-42 shows a comparison of the normalised signal differences between using a 1 mm slit or 2 mm slit. This shows no real difference between the slit profiles, therefore for experiments it makes no real difference whether a 1 mm slit or 2 mm slit is in use.

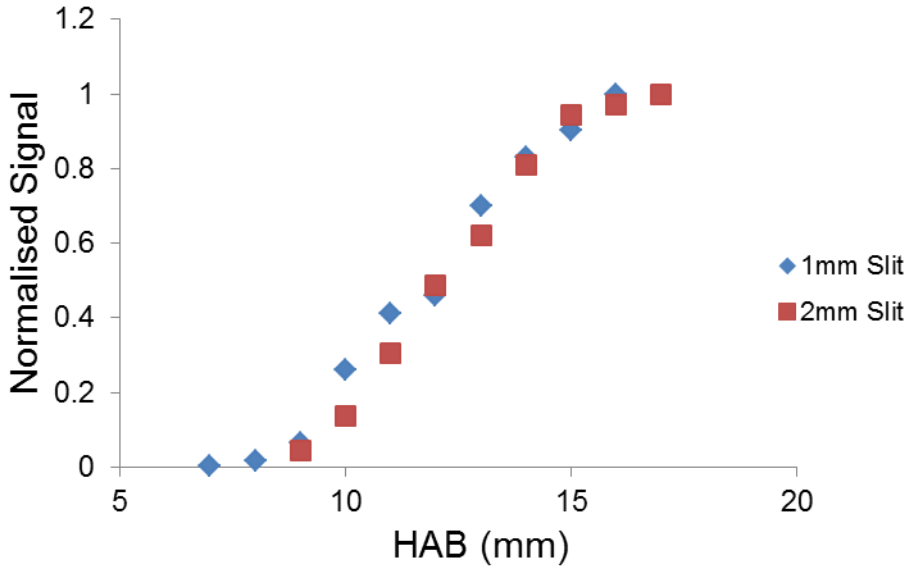

Figure 5-42: Slit size comparison @φ = 2.3 at a gate of 50 ns

The overall resultant signals when using a smaller width slit are shown in Figure 5-43.

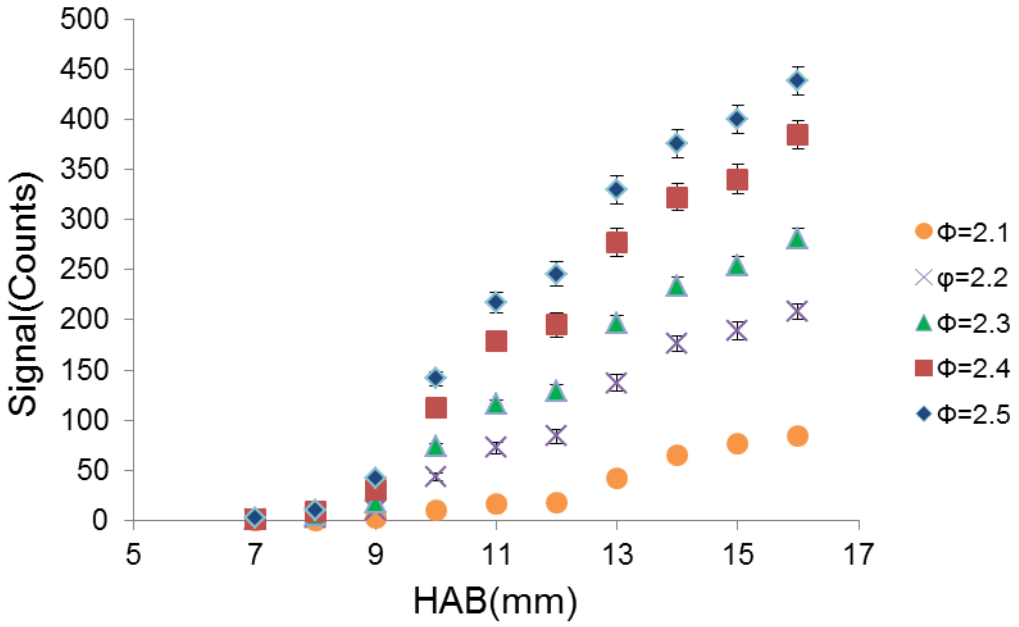

Figure 5-43: Centre line signals measured over 1 mm width at Different HABs at different equivalence ratios @ 50 ns for 1 mm slit

5.5.3 LII signal comparison using different filter sizes on the detection lens

For experiments when using the 2nd harmonic of the laser a smaller 1"filter instead of the standard 2" would have to be used in conjunction with a 532 nm notch filter lens to make sure no stray 2nd harmonic light from the laser could strike the camera. Therefore, a different size of filter would have to be used to make sure that the signals are comparable. A comparison had to be made between different filter sizes to make sure that nothing unexpected happens with this change. For these experiments the experimental procedure is kept the same as the set-up explained in the methodology except the filter attached to the camera that was changed. A comparison on filter size was used to ensure the collection solid angle change didn't affect the profiles of the two measurements.

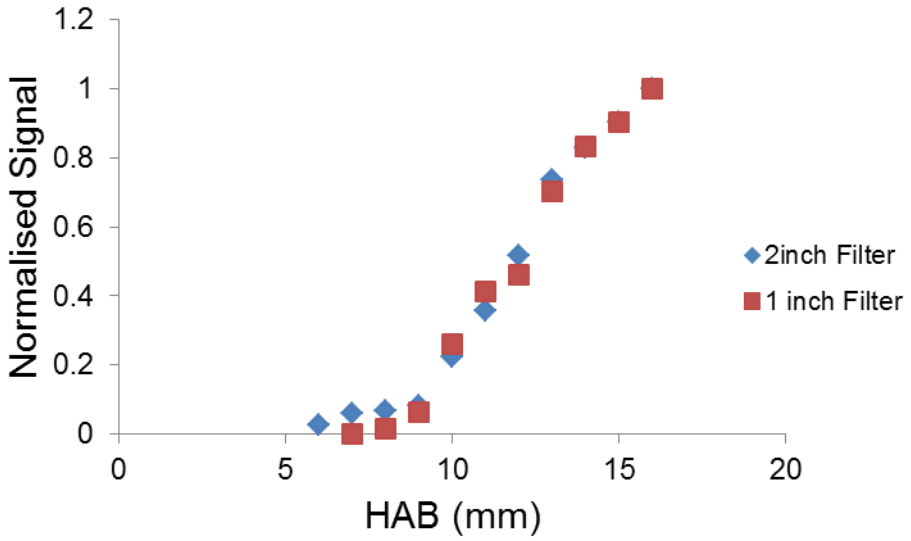

Figure 5-44: Size of filter comparison @ ϕ = 2.3

Figure 5-44 shows the comparison of the normalised centre line signal with the two different filters. It shows good agreement and therefore it does not matter to the profile. The 1" filter also uses a 532nm notch filter however as seen it does not change the overall LII profiles of the flame while it will cause a slight change in the empirical signal. Overall it can be seen that the change in filter size does not change the profile and using the smaller filter only decreases the signal to noise ratio but is suitable to use for experiments.

5.5.4 Overall conclusions on adapting the methodology

Overall we can see that the changes in setup do not change the normalised laser induced incandescence signal meaning that for different burner and setup needs the methodology can be adapted.

5.6 Excitation with 532 nm with comparison and subtraction of 1064 nm excitation signals to produce fluorescence profile

The flat flame burner has been characterised with the 1064 nm laser light and imaging, it is now possible to characterise fluorescence in the same flame by comparing 1064 nm and 532 nm results and using subtraction to infer Laser induced fluorescence of certain PAHs species. As discussed previously in the background and methodology chapters, the fluences between the 1064 and 532 nm have to match to the same signal after delayed detection (160 ns) so that the signal is able to be comparatively similar. The detection wavelength is shorter than the excitation wavelength at 532 nm; this may indicate that no fluorescence will contribute to signal due to red shift nature of fluorescence. However, for some sized PAHs the energy levels are closely spaced, the thermal population is higher than the ground state making it possible that excited particles fall to the ground state losing larger amounts of energy than was induced through excitation indicating it is possible to occur.[68,119]

No decay times were taken with the lower excitation wavelength as it was assumed to not make a difference and has been seen in the past to have no effect.

Results show as expected that when imaging with 532 nm excitation wavelength it is better to use delayed detection (signal obtained at a time past the peak signal, since interference can affect the prompt signal (the peak of the LII signal).

5.6.1 LII temporal comparisons between 1064 nm and 542 nm excitation

Figure 5-45 shows an example of the temporal profile comparison between 1064nm and 532nm taken using the camera. Overall the results show that the peak signal is not the same, which can be attributed to the fluorescence of species included in the result. This is a good indication that the difference in signals can be attributable to fluorescence due to its much shorter lifetime causing the peak signals to be different however after the peak they have the same signal over the temporal profile. This is what is believed to be expected when comparing to other previous measurements of temporal measurements of excitation by different wavelengths done by previous members of this group. A shorter gate and larger collection angle would also help increase the LIF to LII ratio.

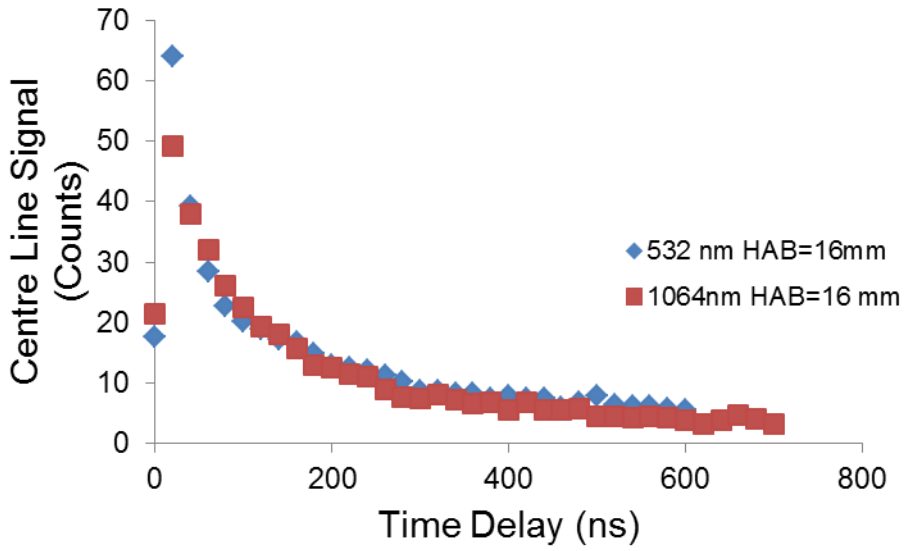

Figure 5-45: Timing comparison between 532 and 1064 nm excitation at ϕ = 2.2 using 20 ns gate at a HAB of 15 mm

These results indicate that delayed detection should be used if wanting to calculate the soot volume fraction when using 532 nm.

5.6.2 LII images with 532 nm laser excitation

Figure 5-46 shows the image taken with the 532 nm excitation wavelength. The gate time for measurement of 532 nm light was 20 ns. The signal was measured at the peak signal to ensure that a subtraction of the 1064 nm excitation wavelength could take place. The detection filter is measured at 450 nm as discussed previously with a camera gate of 20 ns which is over the peak signal to ensure the maximum signal where fluorescence occurs.

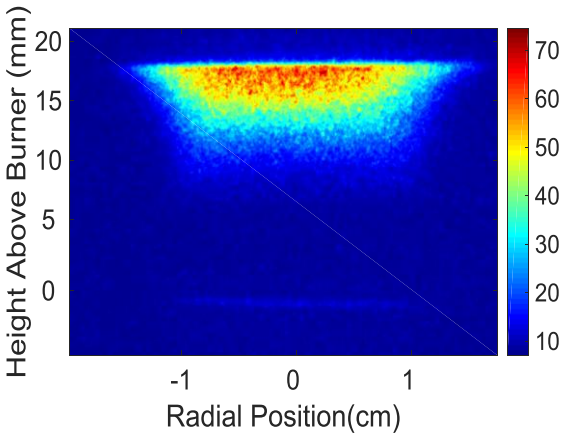

Figure 5-46: LII Imaging using 532 nm laser excitation @ ϕ = 2.3 using 20 ns at a delay of 20ns to ensure peak signal

To make sure that no flat field correction is needed to take place, the sheet can be translated and at different HABs there should be overlap. Figure 5-47 shows these profiles taken with translation of 1 mm to ensure that the correct signal can take place. A good overlap is visible in the HAB profile meaning that there is not a large need for a flat field correction.

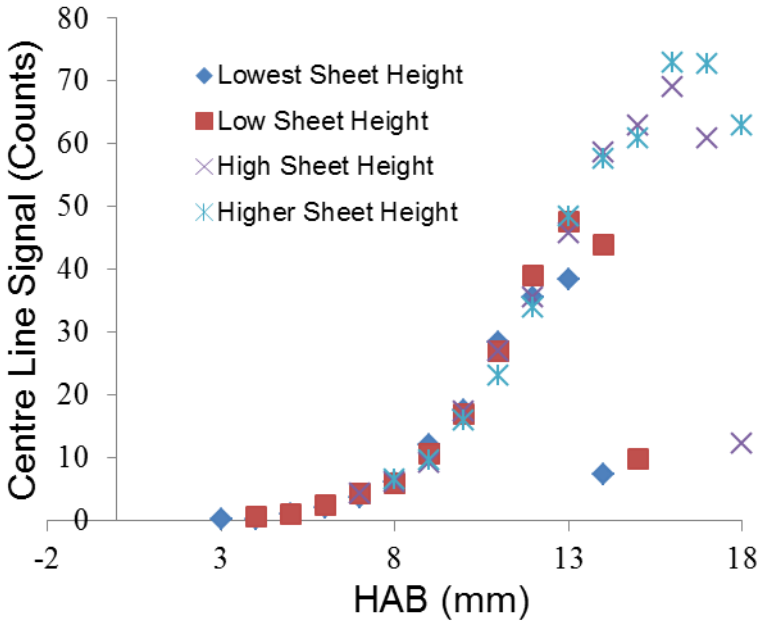

Figure 5-47: 532nm centre line signal with 1mm Translations measured over 1 mm width and 20 ns camera gate length @ ϕ = 2.3

5.6.3 Comparison between 2 laser excitation wavelengths at 2 different equivalence ratios

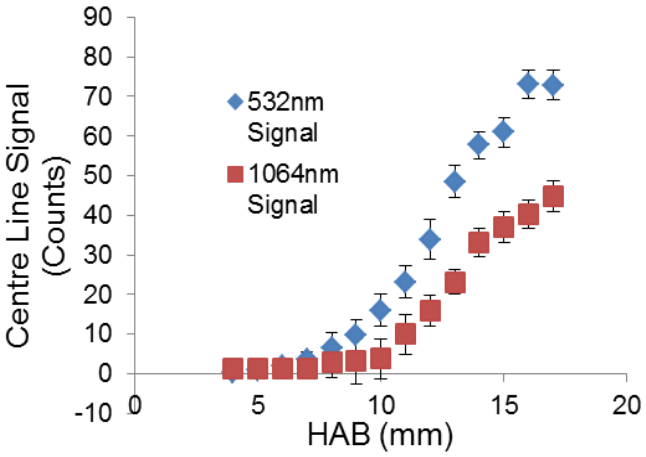

Figure 5-48:Comparison of HAB centre line profiles with 1064nm and 532nm excitation wavelength at peak signal @ ϕ =2.3 camera gate @ 20ns

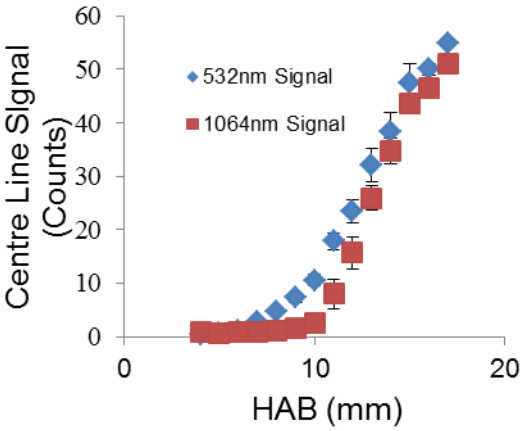

Figure 5-49: Comparison of HAB centre line profiles with 1064nm and 532nm excitation wavelength at peak signal @ ϕ =2.2 camera gate @20ns

The results show in that at much lower heights the signal is higher in the 532nm results than excitation with 1064 nm. This indicates interference from fluorescence of nascent soot and other interfering particles at this height. Figure 5-50 shows the fully subtracted signal and shows some interesting characteristics. These results are non-simultaneous. For where ϕ =2.3 it seems there is a steady increase in fluorescence at around 5 mm until 11 mm then a drop till 14 mm and then a plateau onwards. Whereas for the ϕ =2.3 flame a steady increase can be seen until around 12 where it decreases slightly and then rises up again. This could be because while it is expected that lower down in the flame there will be more but smaller PAHs which is what is assumed to be contributing to the fluorescence. The signal increases because the larger PAHs and have a larger florescence signal. The section where the signal decreases could maybe be attributed to oxidation as a heat mechanism. Oxidation causes the breakdown of some soot molecules back to PAHs.[120, 121]

The amount of fluorescence signal between the equivalence ratios is the expected where the flame with the higher soot concentration has a theoretically higher concentration of PAHs and other excitable compounds.[68]

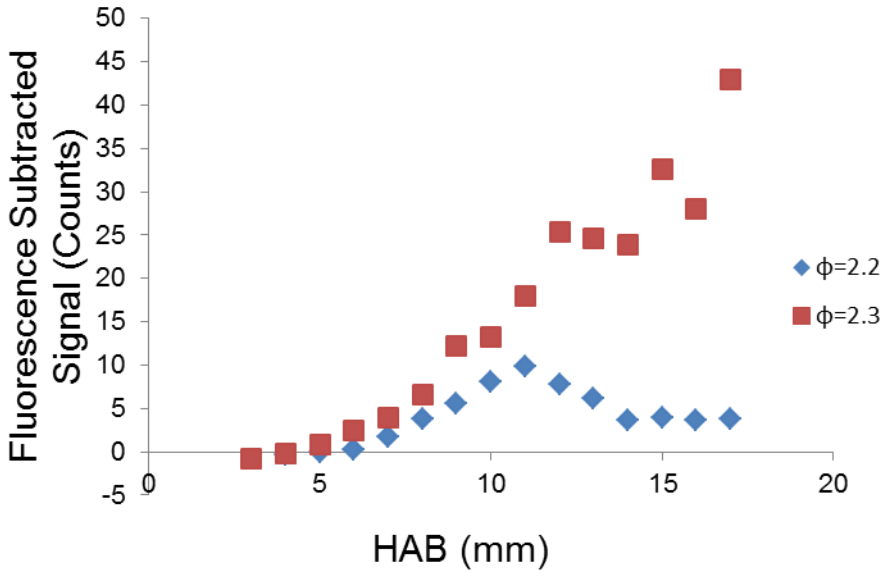

Figure 5-50: Fluorescence Subtracted Signal at 2 different equivalence ratios

The fluorescence subtracted signal could maybe be improved if the signal to noise could be improved. However, because of the constraints of the experiments typical options such as increasing the filter size and shorten the gate length aren't possible. The signal needs to be prompt so therefore the max signal to background can be used. Previous work in the group using a larger equivalence ratio could also help produce a large enough fluorescence signal.[72]

5.7 Discussion of validation and future work

This chapter shows validation when using standard methodology. Beam comparisons to laser sheet comparisons using camera imaging measurements show good agreement when measuring normalised profiles .Though when using the sheet a flat field correction might have to be applied sometimes when required. This correction factor can be different depending on the setup and positioning of the slit on a day to day basis so care must be taken and a calibration image must be taken to achieve a good flat field correction. Overall the methodology can be used in a variety of setups such as changes to filter size, gate time and optical slit size. As long as the same conditions are met for the calibration image these setups can be used to calculate soot volume fractions. The results show the same trend when normalised and gives a good overlapping signal indicating the techniques in use are is reliable.

Extinction measurements show good agreement with standard LII images taken at same equivalence ratio. When comparing signals between experiments care must be taken and typically for experiments a calibration image should be taken to ensure a correct soot concertation to pixel intensity factor can be found. Using LII imaging it is possible to get repeatable and reproducible results and produce an image of soot volume fraction within the flame. The soot volume fraction results are similar to other results from literature and are determined to be reasonable. LII decay time shows good agreement in results between point measurement and imaging measurements meaning that the method used is acceptable so long as the factors involved are taken into consideration. This allows for modelling of particle sizing.

So far, it appears the burner has been characterised well using this LII. It would be advantageous to and maybe to provide more information on the flame such as results from microscopy or Rayleigh scattering.[17] More work could be done to measure incipient soot at lower HABs or in lower equivalence ratios. Some work has already been carried out by using LII followed by TEM as well as SMPS. These techniques while not in-situ can help give information such as particle size distributions and overall morphology.[25]

Using imaging it is possible to subtract signals it is possible to infer fluorescence signal. It was shown that with an increase in equivalence ratio there is an increase in fluorescence signal. This indicates that with larger equivalence ratio there is a larger abundance of PAHs within the flame. It was also seen that there is PAH signal at lower HABs. More work could maybe be done to identify certain compounds and calibrate quantitatively, possibly by using more specific detection filters for species that fluoresce at 532nm laser light. It would be possible to do this if a mix of PAHs was seeded and mixed with the flame. While some of the added known PAH will undergo reactions if a large enough amount of them were added it could be identified by the greater quantities in signal.[72]

Using a higher detection wavelength filter could maybe deliver more fluorescence signal at these lower wavelengths. A spectrometer could be used for both wavelengths to see the difference in signals between detection wavelengths.

Further work could be done and the 3rd Harmonic of the laser could be used as well to help the fluorescence of smaller species. Previous work has shown that using the 283 nm light and comparing it with the 532 nm laser light, there is a difference in signal at different heights caused by the different sizes of PAHs.[40] Additional work could be done in another field to extend exhaust emissions as there has been a lot of work already carried out on exhausts using LII and LIF separately.

6 An investigation of the effects of heat transfer to the stabilisation plate on soot volume fraction in ethylene air premixed laminar flat-flames

6.1 Introduction

Throughout this project it was thought that heat transfer effects caused by the stabilisation plate could cause changes in the temperature of the flame and therefore could change the soot volume fraction. This follows the idea that by changing the stabilisation plate within the flame it would be possible to study soot formation with a range of temperatures without changing the premixed gas composition. It was hypothesized that the temperature of the upper regions of the flame could be influenced by changing the stabilisation plate. A larger amount of heat would be removed from the flame by changing the diameter and thickness of the stabilisation plate, as previously observed in the group. It was visible that the temperatures were different between the burners of different diameter even with same equivalence ratios. This was assumed to have happened because of the different sized stabilisation plates used in each burner causing heat transfer effects therefore it was important to measure the plate temperature between these burners and to investigate the influence of soot volume fraction.[37]

The influence of temperature on soot formation has been well documented to show that at larger temperatures in the flame the lower soot volume fraction. Bohm et at.[122] shows the strong and non-linear dependence of the soot concentration on the flame temperature and Xuan et al.[123] show with modelling that premixed laminar flames, at lower temperatures and with a decrease in oxygen cause the flame to be colder and more soot rich. Bockhorn et al.[124] shows the different types of stabilisation plates used with a premixed ethylene/air flame in a McKenna burner such as a solid plate, a plate with a centre hole and a plate with a stainless steel mesh have different soot volume fractions; however this is down to changes in the flame geometry. Bockhorn et al.[124] has shown that the soot concentration doesn't vary much with the change in heights of stabilisation plate while Axelsson et al. [50] has shown a comparison of decay time thus particle size at different HABs using the stabilisation plates at two different heights. It was seen that at larger heights above burner the plates has an influence on the flame. With the plate at a height of 26 mm the decay becomes longer than the 21 mm stabilisation plate by around HAB of 15 mm. This seemed to be caused by the soot particles becoming larger with the flame temperature influencing the particle size.

Experiments were carried out to investigate the heat transfer effects caused by the stabilisation plate: temperature measurements of 2 different sized stabilisation plates using a thermocouple to see if there is a temperature difference in the plates positioned in the same burner; images showing signal from LII over time; measurements of temperature in 2 different sized burners; comparison of measurements of

LII signal in two different burners. Some modelling of the flame centre line temperature was done using the *Cantera* software at two different equivalence ratios at different boundary condition temperatures which represents the temperature of the stabilisation plate.

6.1.1 Experimental factors

Experimental and processing factors for burner experiments

Table 6-1 shows the experimental factors when using the camera in this investigation. The experiments were typically repeated twice with 100 images recorded for each repeat.

The gate length was set to 20 ns or 50 ns and the gain was set to the maximum. The detection source had a 450nm filter. The fluence was always recorded to be 210 mJ/cm^2.

Table 6-1: Camera experimental parameters

Laser fluence	210 mJ/cm^2
Number of images recorded	2sets of 100
Gate length	20 ns or 50 ns
Intensifier gain setting	99
Camera delay	20 ns to cover Peak Signal
Detection filter	450nm(10 FWHM)

6.2 Heat transfer and flame stability results

6.2.1 Stabilisation plate experiments

Typically the stabilisation plate is used to keep the flow stable.[118] Figure 6-1 shows the flame at an equivalence ratio of 2.3 without a stabilisation plate and Figure 6-2 shows the flame with the stabilisation plate. It is visible from the images that the plate changes the dynamics of the flow as well as the stability with a lot of movement in the flame. It can be seen that the flame is also lifted showing a higher start of the flame from the reaction zone. The flame also becomes narrower with increasing HAB due to the buoyancy and therefore won't be one-dimensional. LII images were taken without the stabilisation plate however because of flame and flow fluctuations the results weren't reproducible. If a shroud co-flow had been used, a more stable image would be recorded and a comparison could be done between the burner with and without the plate.[109]

Langenkamp et al.[125] show experimental and modelling LII and light scattering results in a Mckenna burner without the stabilisation plate but with a co-flow to limit the number of control parameters compared to other studies.

Figure 6-1: Flame @ ϕ = 2.3 with no stabilisation plate

Figure 6-2: Flame @ ϕ = 2.3 with stabilisation plate

To test the effect the stabilisation plate has on temperature an S-thermocouple was used to measure the temperature of the flame. However, by putting the thermocouple straight into the flame it decreased the reliability of the temperature readings due to soot deposition on the probe, as well as intruding on the flame making it difficult to take LII measurements to the corresponding temperature readings. An example of this problem can be seen in Figure 6-3.

Figure 6-3: Burner with lager plate (64 mm diameter) and thermocouple intruding on the flame @ ϕ = 2.2

Therefore a setup like Figure 6-5 was employed to ensure reliable temperature reading with the drilled hole as close to the plate as reasonably practical. The setup is pictured in Figure 6-4. The drilled hole is about 1 mm from the plate; and the diameter of the hole is about 1/4 inch.

Figure 6-4: Burner with large plate(64 mm diameter) with thermocouple inserted into the stabilisation plate @ ϕ = 2.2

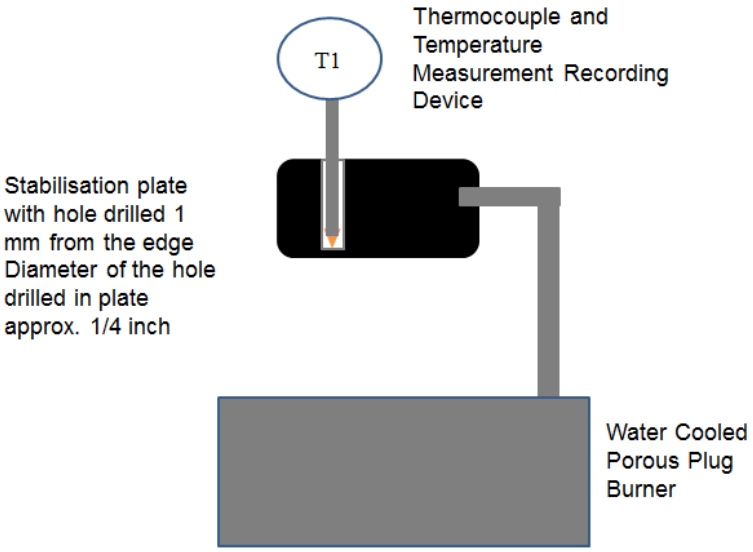

Figure 6-5: Drawing of burner with plate with hole drilled on top

The plates used on these experiments were a 2cm thick and 38mm diameter plate and a 3.5cm thick plate and 64mm diameter plate. These plates were chosen because it was deemed that they would cause a large enough difference for heat transfer but would also have reasonable length and diameter to be used.

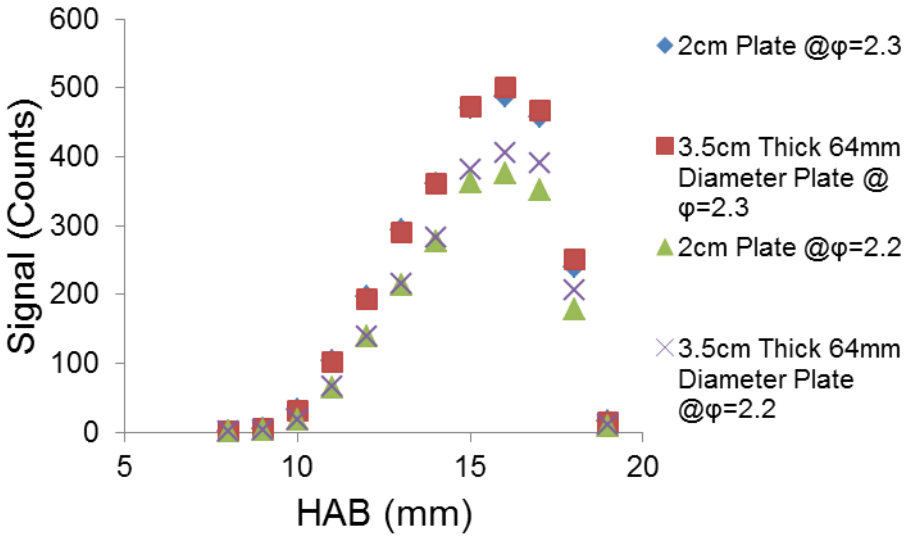

Figure 6-6: Raw LII signals using two different plates ϕ

at different equivalence ratios

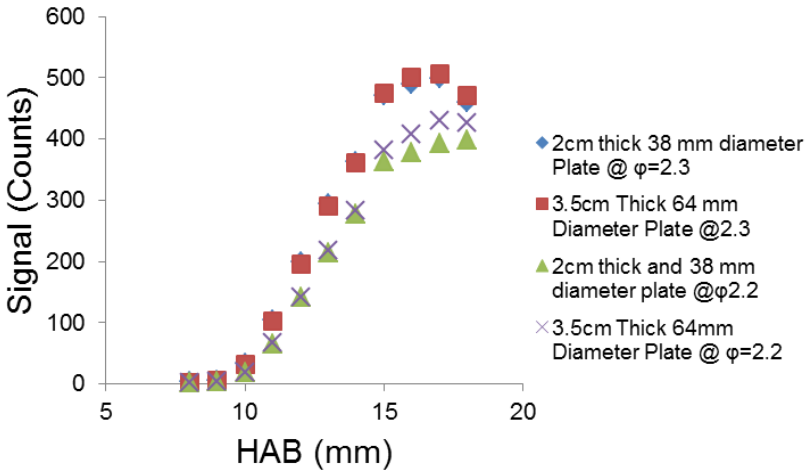

Figure 6-7: Flat field corrected (FFC) LII signals using two different plates at different equivalence ratios

It was thought that a larger plate would act as a larger heat sink because of its larger thermal mass reducing the temperature in the flame. However, this was found not to be the case as when the soot signals were compared there was no real difference between them thus indicating no real difference in soot concentration as seen in Figure 6-6. The raw data signal from the experiment with the flat field corrected signal shown in Figure 6-7. The experiment was carried out at two different equivalence ratios which have discernible difference in soot volume fraction to ensure that the change in soot concentration is caused by the change in equivalence ratio.

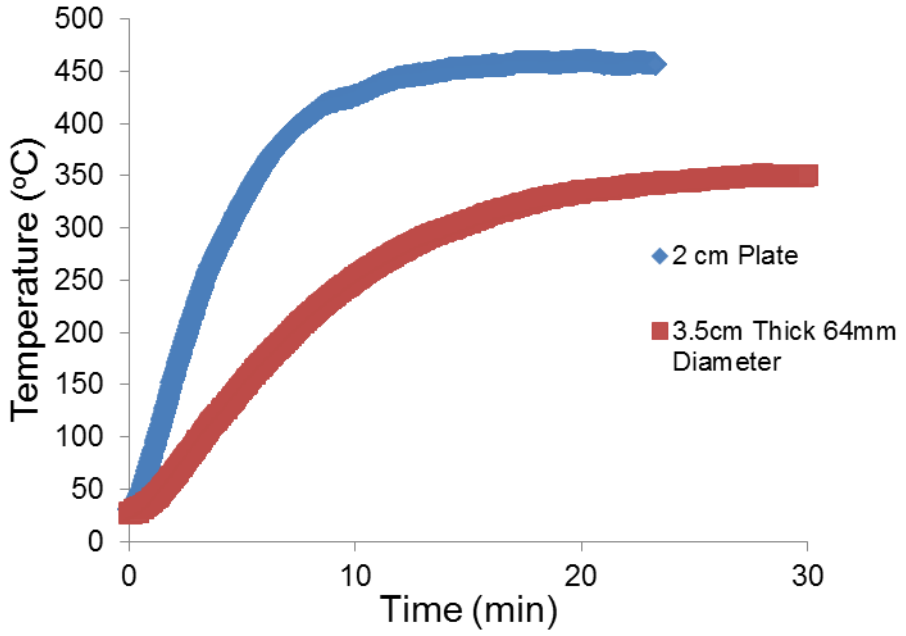

Figure 6-8: Surface temperature of the stabilisation plate over time using two different plates @ϕ =2.3

The temperature results show a difference in temperature of about 100 ^{o}C as seen in Figure 6-8 and Figure 6-9. Also, as expected that as the plate thermal mass decreases the time taken to reach equilibrium decreases. However this corresponds to the results in Figure 6-15 where lower temperatures of the plate at earlier times, and thus lower plate temperature at the time of acquisition doesn't affect the signal. This indicates that there is no real way to control the sooting propensity of the gas by manipulating the stabilisation plate area. This indicates that the temperature at the measured points in the flame doesn't affect the soot concentration. Besides, the comparison between equivalence ratios shows a higher temperature at lower equivalence ratios, as one might expect.

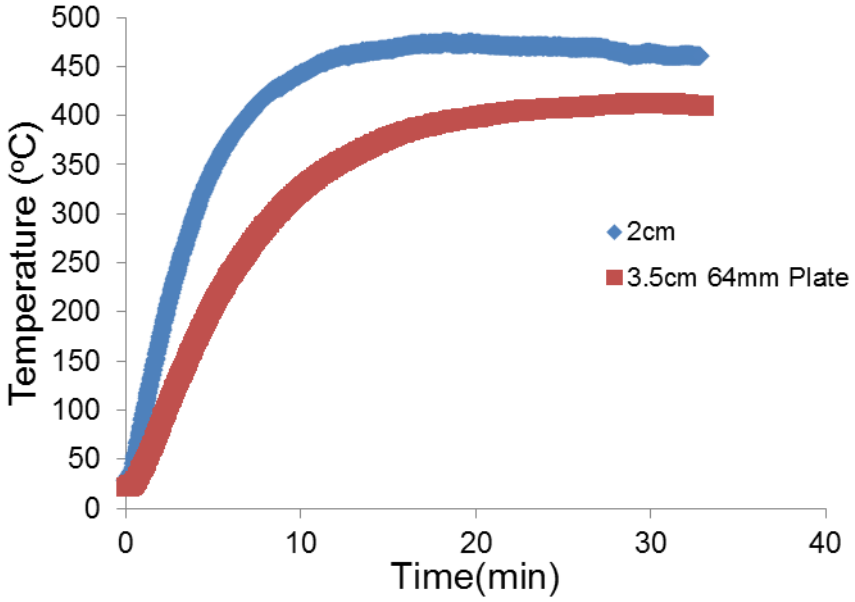

Figure 6-9: Surface temperature of the stabilisation plate vs time using two different plates @ϕ =2.2

6.2.2 Larger burner experiments

A comparison against the larger burner described in the methodology in chapter 4was used to check the difference in the burner temperature.

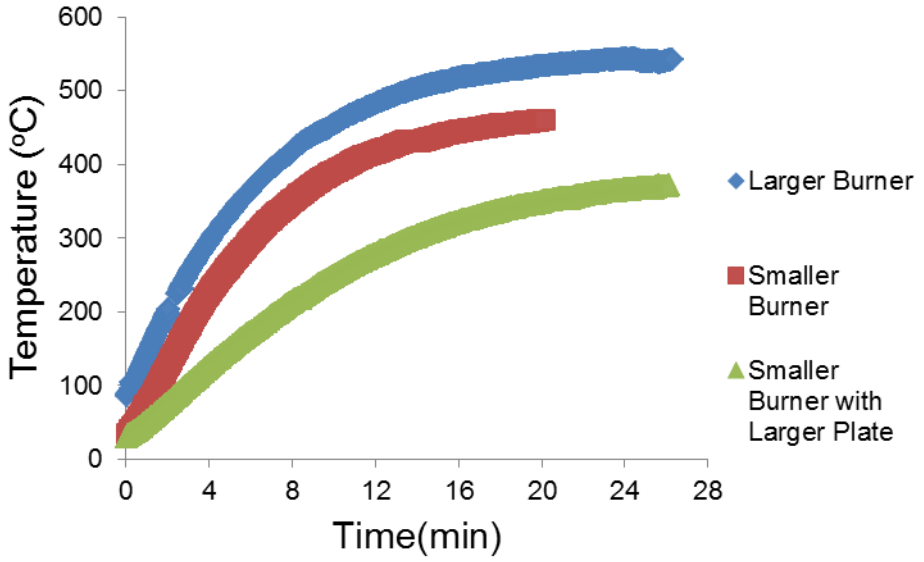

Figure 6-10: Surface temperature of stabilisation plate comparison for different burners @ ϕ =2.2

Figure 6-10 shows a comparison between the larger burner and the smaller porous plug burner while, measuring the temperatures of the 'flame' using the plates and setup as before. Figure 6-11 and Figure 6-12 show the averaged LII results for the larger and smaller burners using their own respective stabilisation plate.

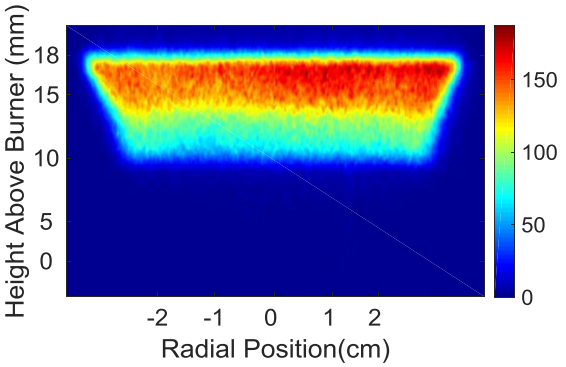

Figure 6-11: Larger burner @ϕ = 2.3

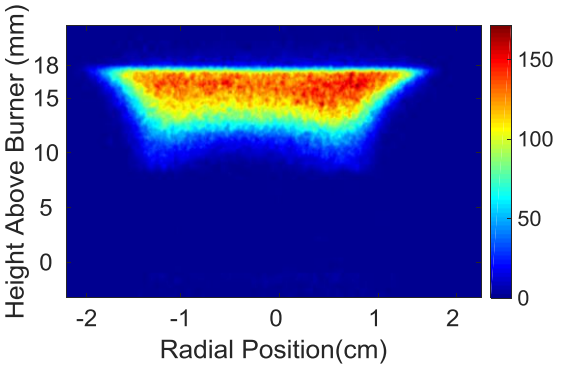

Figure 6-12: Smaller burner @ ϕ = 2.3

Figure 6-13 shows the comparison of the centre line signals between the two burners and Figure 6-14 shows the flat field corrected at the upper ends. They show similarities in the profile as well as empirical signal. This indicates that the soot volume fraction within the flame is similar if not the same. Significant extinction takes place in the larger plate, therefore if any other measurements were to be made in this burner or a similar large burner care has to be taken. For the first half of the burner the signal can be seen to be pretty constant (the laser travels right to left in the image), the signal drops due to extinction caused by the reduced local fluence. Since the fluence is just in the plateau regime the extra path length has reduced the signal. Therefore, it would be recommended to increase the fluence by adding another telescope to decrease the power lost by the expansion of the beam.

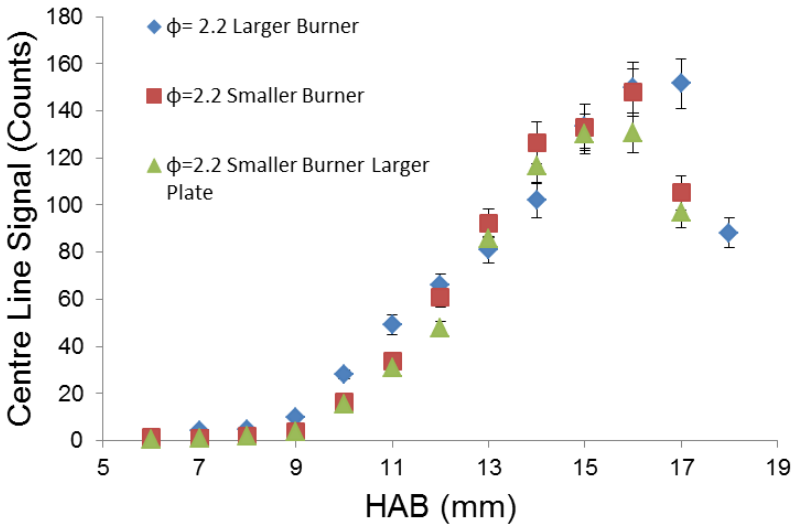

Figure 6-13: Raw LII signal profiles comparisons between 2 different burners ϕ =2.2 @ camera gate 20 ns

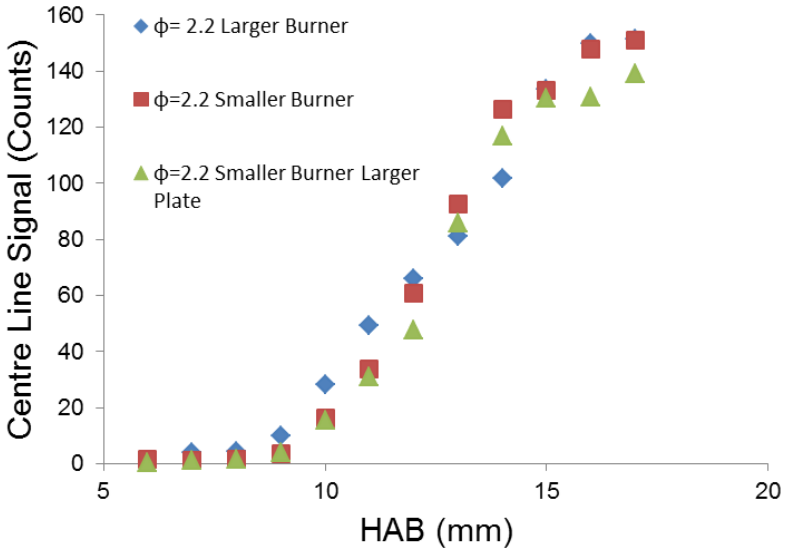

Figure 6-14: Flat field corrected burner comparison @ ϕ = 2.2

6.2.3 Flame stability and the LII signal over burner operating time

To investigate the influence of time on the measurement of soot concentration it is important to measure the LII signal within the flames over time. The same was when taking raw data from using the flame it is important the flame is stable and measurements are consistent. Measurements that show a stable flame include low standard error between shot-to-shot images, no significant changes in soot volume

fraction over time. Previous experiments in the group have shown measurements should be taken during 10 to 25 minutes.

Figure 6-15 shows the LII signal measured by the ICCD camera over time. The results were taken over the 1mm x 1mm from the centre line and the signal was integrated and average. They show that there is no real change in soot volume fraction over time except at 2mins where the flame appears to be more unstable. Therefore it is important to ensure that measurements are typically taken after 2mins. No flat field correction has taken place as to ensure no change in the raw data. The flat field corrected image can be found in Figure 6-16.

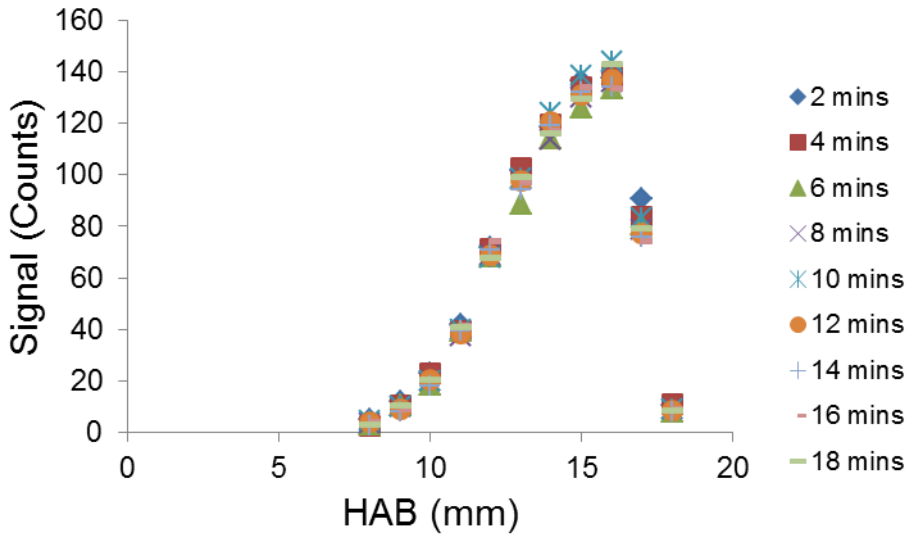

Figure 6-15: Raw LII signal over burner operating time @ ϕ = 2.2

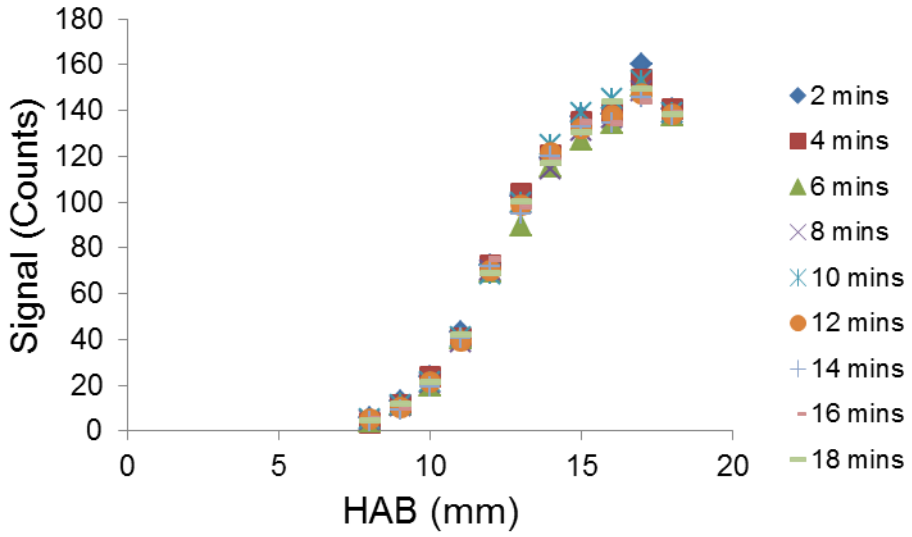

Figure 6-16: Flat-field corrected signal of centre line comparing operating times @ ϕ =2.2

Interestingly these results showed no change in soot volume fraction over flame running time. Shown in Figure 6-9, these different times have different temperatures of stabilisation plates of the burner thus implying differences in temperature of the flame.

For these experiments, there was typically at least a waiting time of 5 mins for the flame to be running and the experiments were finished before 25 mins where it could be visibly seen that the stabilisation plate had soot which effects the flame and may clog the porous plug burner.[72]

It was found that the soot concentration also doesn't change over time in the larger burner as well.

6.3 Modelling

Within the group, the Cantera model was used to model the steady state one-dimensional reacting flows. The code allows for the temperature of the boundary condition to be set, with input of the reactant concentrations. The Cantera model works by modelling flames along a stagnation flow reducing the governing equations to a single dimension. The fluids are assumed to behave as ideal gases and the tangential velocity is assumed to be zero.[126]

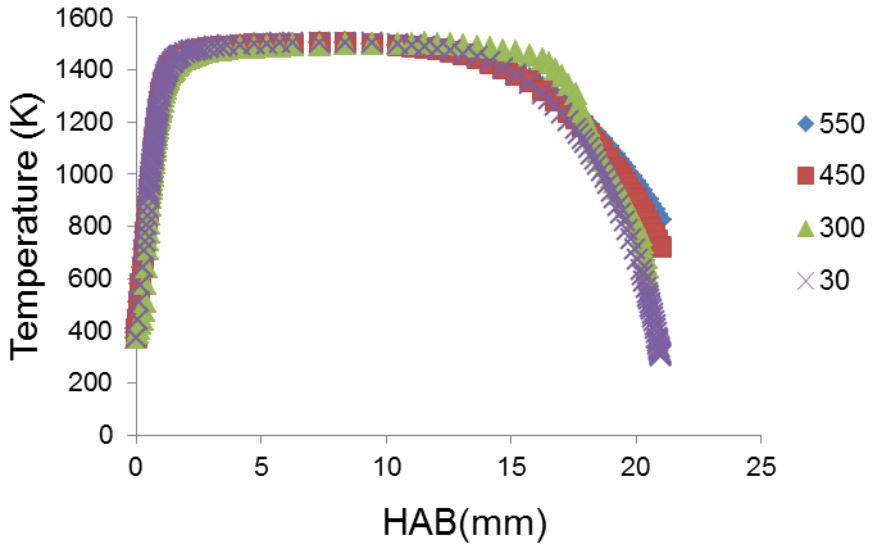

Figure 6-17: Modelled centre line temperatures of different plate temperatures using ABF(Appel-Bockhorn-Frenklach) mechanism @ϕ = 2.3 and mass flux 0.0629 kg/s (550 ^{o}C is the larger plate temperature recorded, 30 ^{o}C is the plate at initial conditions, plate temperatures shown in legend in ^{o}C)

Figure 6-17 shows the results using a model for the chemical kinetics and species production throughout the flame. The results showed the boundary temperature i.e. the temperature of the stabilisation plate does not change up much until around 20 mm HAB. Figure 6-18 shows the results at a different equivalence ratio of 2.2. These results were similar to Figure 6-17 where the temperature has no real effect until closer to the plate. The mass fluxes used here were the same as the experimental mass fluxes.

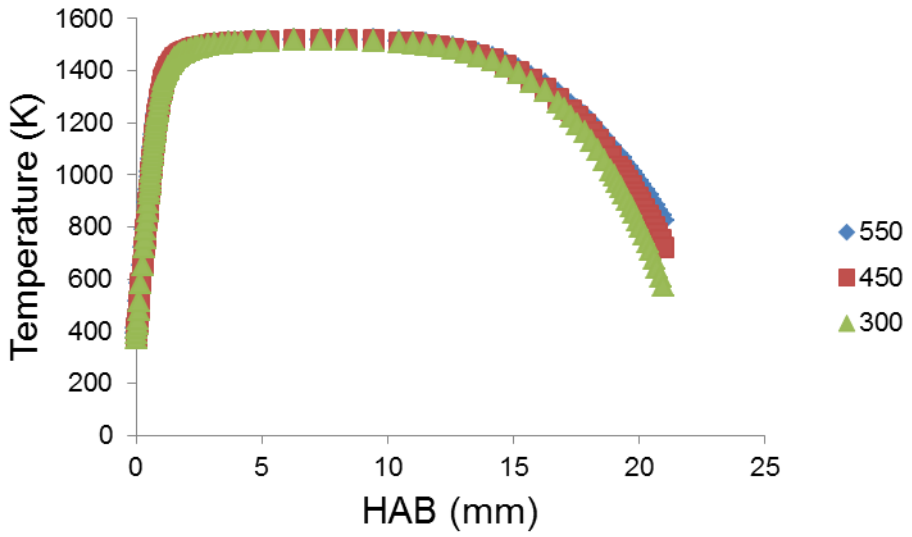

Figure 6-18: Modelled centre line temperatures of different plate temperatures using ABF mechanism @ϕ = 2.2(550 °C is the larger plate temperature recorded, 30 °C is the plate at initial conditions, plate temperatures shown in legend in °C)

An interesting aside is that when the mass flux was lowered, there was a change lower in the flame at around 16 mm as seen in Figure 6-19. Experimentally it seemed unreasonable to test at the low flowrates while keeping the same equivalence ratios because in practice the flame would be difficult to stabilise.

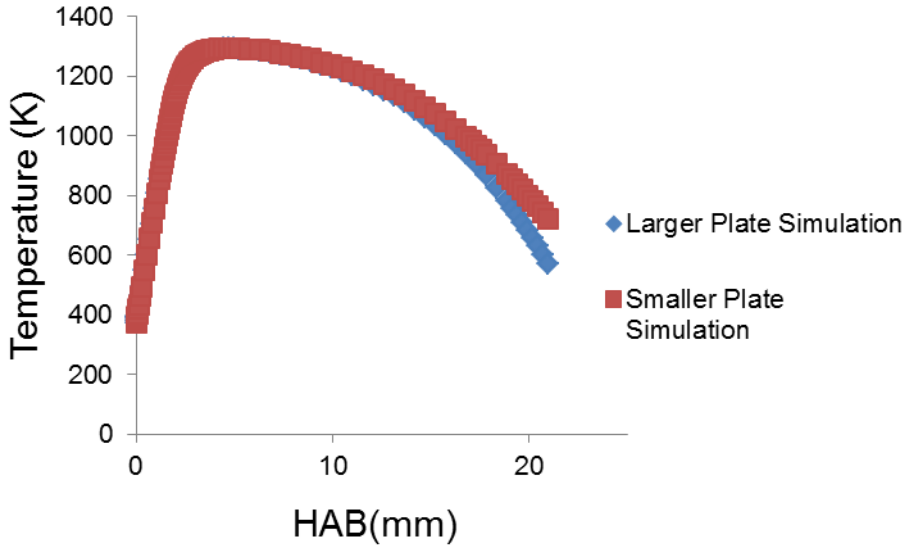

Figure 6-19: Modelled centre line using ABF mechanism at a lower mass flux of 0.167 kg/s (larger plate boundary Temperature=300°C, smaller plate 450 °C) @ϕ =2.3

6.4 Conclusions and future work

Overall the results produced were interesting. Heat transfer effects caused by changing the thermal mass of the stabilisation plate had no noticeable effect on the soot volume fraction within the centre of the flame. The comparison between the same equivalence ratios in 2 different burners provided the same soot volume fraction even though they were at different temperatures. Another interesting point is that there seemed to be no change in soot volume fraction with the amount of time the burner had been running for from recordings up to 25 minutes. The results from these set of experiments were unexpected considering the initial hypothesis, but the overall results were shown to be in agreement. Modelling results have shown that the plate temperature at standard conditions and standard flux have no real effect on the temperature throughout the flame until very near the boundary layer and therefore agrees that there won't be change in the soot volume fraction throughout the LII measurements areas. When the mass flux was reduced though it was found to have an effect on the temperatures at around 16 mm because of the type of burner for these flux rates, this is not feasible to run experimentally.

These experiments show that the time when measurements are taken is not important. Therefore with comparison between group data this is not an issue that needs to be focussed on. The results also stop the redundancy of data collected between groups who used different burner stabilisation plates meaning direct comparisons can take place.

7 Investigation of a long-pulsed fibre laser as an excitation source for LII

7.1 Introduction to long-pulsed and high repetition rate LII

The desire for accurate measurements of soot concentration in exhausts for engine certification standards has led to an increase in the need for methods to accurately measure soot volume fraction. For LII to be effective in industrial test environments it is important that the laser source to be adaptable and easy to insert into a combustion test rig without the need to interfere with the combustion set-up and allow for efficient beam delivery. The G4 long-pulsed fibre laser allows for efficient beam delivery to and there is also safety advantages associated with using a fibre laser in that the beam doesn't have to be mirrored into measurement position. The G4 long-pulsed fibre laser is compact and inexpensive excitation source with the potential for high rep rate measurements.[17,40] Typically the most common LII excitation source is the Nd:YAG laser which has been described as '*bulky, inefficient and the most costly part of an LII system'* [127] and if a methodology can be established the G4 long-pulsed fibre laser may have commercial appeal with these advantages over the Nd:YAG laser.

A previous example of a high rep-rate fibre laser being used, is shown by McCormick et al.[128] ,who demonstrates the proof of principle of for the application of this type of laser in engine exhausts (since current requirements for emission certification require a SAE smoke number[129] this type of laser could facilitate this measurement thereby improving engine measurements).[130] Overall the results shows that LII tended to follow the relative trends of the engine when compared with extractive measurements. These results show the need for an investigation into well- controlled laboratory flames to assess the capabilities and limitations of this laser, which is essential to establish the basis of the technique for measuring the soot volume fraction. With imaging in a smaller laboratory burner it is an advantage that the camera may be physically closer to the measurement allowing better spatial resolution and help the understanding of the signal across the image.

While there has not been much investigation of LII using this type of fibre lasers, there have been some other investigations into high repetition lasers. One set of investigations carried out by Michael et al.[131] showed the effects caused by the gas heating effects when using high pulse energy. This laser was also used to show planar laser induced fluorescence imaging by Slipchenko et al.[132] and shown to monitor low frequency instabilities and high speed fluid dynamics of a lifted methane diffusion flame. A pulsed-burst laser consists of a burst mode Nd:YAG with an incorporated fibre oscillator and diode pumped solid-state amplifier typically producing high pulse energies and high rep rates (15 mJ at 100 kHz). Michael et al.[131] used a standard sooting flame to show the effect of changing the repetition rate on the fluence curve and the effect these have on gas heating. By using a pulse-burst laser to overcome the

problems associated with fluid flame interactions, they showed that the high repetition rate of 100 kHz allowed for better analysis of the fluid-flame interactions in more turbulent flames. Cenker et al.[133] also carried out investigations using high repetition rate detection camera to take images and show the effect of laser induced heating of the bath gas using a standard Nd:YAG laser. Results show that at high fluences above 300 mJ/cm^2 a large region of laser heated volume of the bath gas is heated. Since long-pulsed lasers have a longer pulse over this fluence this effect was neglected for this work, though some checks could be performed to make verify this. Boxx et al.[134] used a kHz-LII solid-state laser in a diesel engine cylinder to show qualitative images of the LII signal uses a high speed CMOS camera.

As well as high-rep rate measurements using solid state Nd:YAG lasers there has been some measurements using long-pulse lasers. Ditaranto et al.[135] used a long-pulsed LII setup (fundamental Nd:YAG laser with some temporal shaping capabilities to change the laser top-hat profiles of duration range 50-1500 ns in a laminar diffusion flame) to show that the measurement of soot volume fraction is not impaired by the use of a range of pulse durations. The difference between the Nd:YAG setup and the fibre laser used in this thesis is the Nd:YAG has the ability to produce high enough laser pulse energy. This allows for spectral filter of a bandpass filter of 488 nm as well as a standard rep rate is used compared to the fibre laser. Results show unexpected LII signal for pulses longer than 100 ns showing a rebound effect of LII signal. A follow up study by Ditaranto et al.[136] with long-pulsed laser induced incandescence using the same fundamental Nd:YAG laser with some temporal shaping capabilities to change the laser top-hat profiles of duration 100 ns, 200 ns and 450 ns in a laminar using the fundamental of a pulsed Nd:YAG laser aimed to reduce the experimental shortcomings of the uncontrolled laser fluence and beam shape which showed two peaks appearing in the temporal LII signals at high fluence with strong fluence dependence and overall results indicate unexpected LII signal behaviour may be physically linked to the laser-soot interaction. Hverven[137] ruled out PAH fluorescence as a phenomena which may cause twin peaks using the discussed setup. It is suggested this is caused by morphological changes in the soot as well as new particles being produced by sublimation. Since the pulse energies are much larger using the Nd:YAG compared to the fibre laser it may seem that from results with the fibre laser do not suffer from this phenomenon. Overall these show the need to produce a reliable methodology using long-pulse fibre laser to allow for soot concentration measurements.

The limitations of using the long-pulsed fibre laser is that while the laser has a typically high average power but lower pulse energy compared to standard Nd:YAG lasers causing the need to focus the beam leading to a Gaussian spatial profile. This means that the beam has different fluences radially across the beam. Another disadvantage is the irregular laser temporal profile making it harder to model.

This chapter shows the results obtained using a long-pulsed fiber laser. The output launch optics shown in Figure 7-1 with comparisons of results produced using conventional a Nd:YAG laser. The aim of this

chapter is to try and produce results that could characterise the flame and show a method of producing a soot volume fraction measurement using this type of excitation source. The results consist of fluence curves, LII images and signal levels plotted as with centre line HAB profiles and radial profile as well as comparison with photomultiplier results and temporal profiles which was measured by the camera by sequentially varying the timing of the camera gate. These results allow for a direct comparison with measurements taken from the Nd: YAG excitation source. These results can help establish this basis of the technique which could maybe be used in more complex flames.

Building from a standard LII heat transfer model, a model of the long-pulsed LII was developed. Past literature shows the need for developing a model that can be adopted from standard LII models. The results showed the effect that long-pulses at high fluences can have on the vapourisation of the soot particle and thus the particle mass and size. Comparisons with time resolved profiles do show considerable difference possibly due to the assumptions being made in the model as well as other components of heat transfer such as annealing not being taken into account which can effect model assumptions such as absorption coefficient can be changed by annealing which is more prevalent when the soot particle is being heated longer.[138, 139]

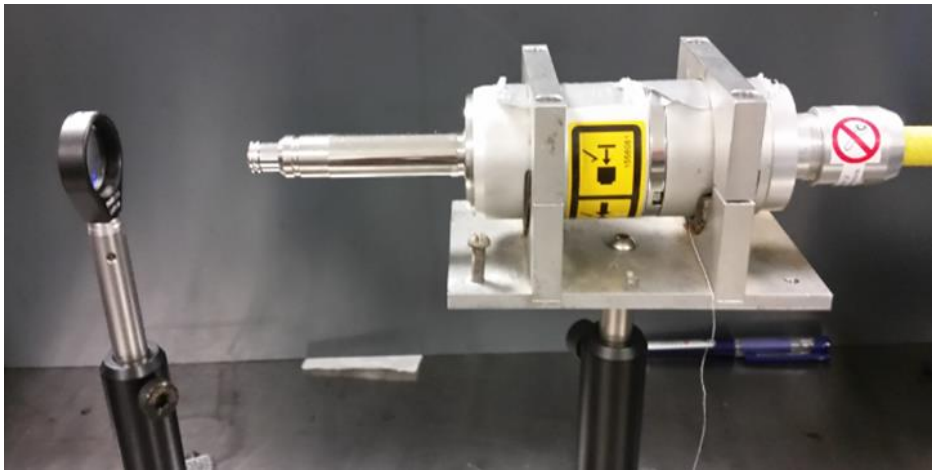

Figure 7-1: Image of long-pulsed fibre laser launch optics and focusing lens

7.2 Long-pulse laser induced incandescence methodology

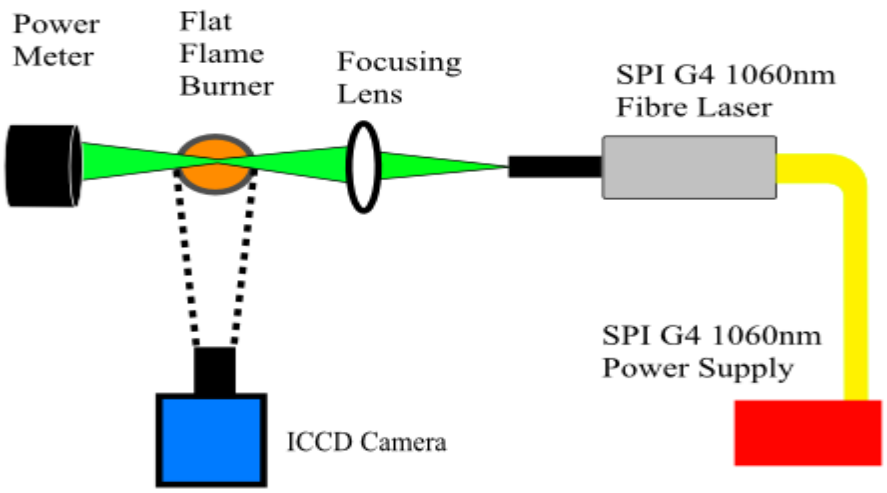

Figure 7-2: Experimental Setup of SPI long-pulsed LII

The set up for using the long-pulsed laser is shown in Figure 7-2. By replacing the Nd:YAG laser with the G4 SPI fiber laser allows for placement without the need for mirrors to align the beam, The focussing lens(*f*=32mm) is used for focussing the divergent beam which focuses to a minimum $1/e^2$ waist size at the centre of the burner. The laser source is commercially available SPI redENEGERY™ G4 1060nm wavelength class 4 fiber laser. The laser source was set to a repetition rate of 30 kHz. This can be changed remotely from a range of 1 kHz and 100 kHz, however for the purpose of these experiments it was kept to a standard rate of 30 kHz so as to compare with McCormick et al[128] as well as it being the optimum repetition rate for producing the highest and most stable power output as found in the appendice in the datasheet for this laser.

Using a Thorlab's dual scanning slit beam profiler (BP209-IR/M)[140], the $1/e^2$ diameter of the laser was measured to be approximately 0.2 mm at the tightly focused centre as seen in the beam sizing profile where the full measured beam profile can be found. The profile was then moved back 1 mm each time to then produce a full spatial profile.

The laser temporal profile was measured by directing weak beam reflections from a microscope slide onto a fast photodiode. The laser pulse shape was found to change slightly with differences in power, so therefore any powers used to measure LII also had to have corresponding pulse shapes however the duration of the laser pulse was approximately 200 ns at all pulse energies tested.

A focusing lens is used in this setup and can be seen that the laser spatial profile is Gaussian. This can cause many problems especially when trying to calculate the fluence across the flame. Experiments were carried out using the flat flame laminar burner previously mentioned so that a comparison between the two different laser types could be produced.

Like previous experiments described in this thesis using an ICCD camera was setup positioned at right angles to the laser beam axis and at a distance from the flame to allow for the best spatial profile. A 50 ns gate was used as it was found that 20 ns didn't produced enough signal whereas with 100ns the background became harder to subtract since the signal to noise ratio became lower. While the laser has a repetition rate of 30 kHz the camera only has a recording rate of approximately 10 Hz. The PTU attached with the camera is able to synchronise the camera and laser to record at the optimum interval. Also to improve the signal to noise ratio no spectral filter was used in front of the camera. This may influence the results by having the signal weighted in favour of different wavelengths in comparison to the previous camera measurements. This also led for the need for the background subtraction to take place during post processing of the raw image.

It is suspected that high fluences may perturb the combustion and the flame causing the gas temperature to increase.[136,131] Most measurements were taken at the power reading 3.29 W(109 mJ pulse energy). De Iulliis et al.[141] showed the effect that a large enough flow rate can reduce the effects caused by repetitive pulsing using a standard laser. It was estimated that the fluence wouldn't be high enough to cause gas heating because of the small measurement area of approximately 200 μs estimating that the speed of the flame is high enough(around 3 m/s) to remove the heated particles before they can influence the gas temperature.

To control the laser such as power, pulse frequency etc., commands were sent from the computer hyperlink to an electrical breakout board connected to the laser. The output power of the laser was controlled by a hyper terminal on the computer. The SI Hyperlink command controlled the current in the laser which determines the output power. It was seen that the power was linearly proportional to drive current as seen in Figure 7-3 and it was shown that the power of the laser was very reproducible to this command showing the close control of output power without the need for a polariser.

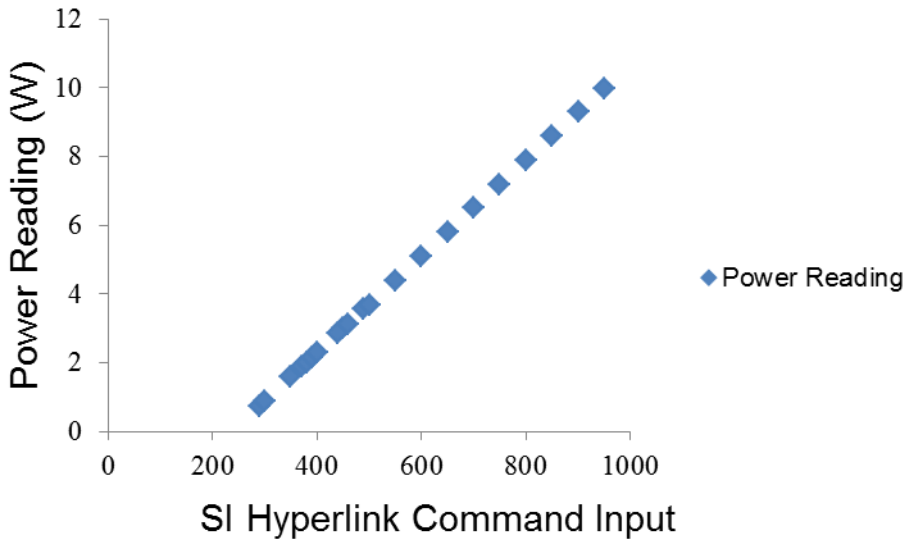

Figure 7-3: Computer Command Input to Power at a rep rate of 30 kHz

The beam is terminated using a thermophile power meter to measure the power output as well as reduce any scattered light in the laboratory.

7.2.1 Experimental factors and settings

Table 7-1 shows the factors and inputs which were used for the experiments using the camera. For the signal to noise ratio of the camera results no filter was used and a 50 ns gate would have to be used. Most results were a combination of three experimental repeats of 100 recorded images. The camera was at a fixed distance of 30 cm away from the centre of the burner.

Table 7-1: Typical Camera Settings for LPLII Experiments

Number of Images	300
Intensifier Gain Setting	99
Gate length	50 ns
Optical Filter	None
Laser wavelength	1060 nm

Table 7-2 shows the factors which were used for the experiments using the PMT. The gain was set to 1000 and a Schott Cut on Filter was used to help reduce the signal to noise ratio. The PMT results were two experimental repeats with 256 averages on the oscilloscope. The number of averages was increased, so as to reduce the noise on the oscilloscope as compared with typical LII there is lower signal and a higher gain setting which causes more random noise.

Table 7-2: Typical PMT settings for LPLII experiments

Number of averages	256
Optical Filter	Blue Schott Low pass Filter
Gain	1000 V

7.3 Long-pulsed laser induced incandescence experimental results

7.3.1 Long-pulse laser shape profile

The laser spatial profile is important for long-pulse LII measurements since unlike standard LII measurements where the shape is typically and preferably uniform, the profile for this long-pulse laser is Gaussian meaning that the fluence changes across the measurement area. Figure 7-4 shows the beam diameter after the focussing lens; the minimum diameter thickness ($1/e^2$) is 178 µm. The reason the $1/e^2$ width was chosen as it is a widely accepted way of measuring laser beam diameters as it is better practice than to just use the FWHM as it states more of the laser output. It is the distance between the two points on the power intensity chart that are $1/e^2$ of the maximum value. Any fluence value stated will calculated using the $1/e^2$ area, particularly at the focal point.

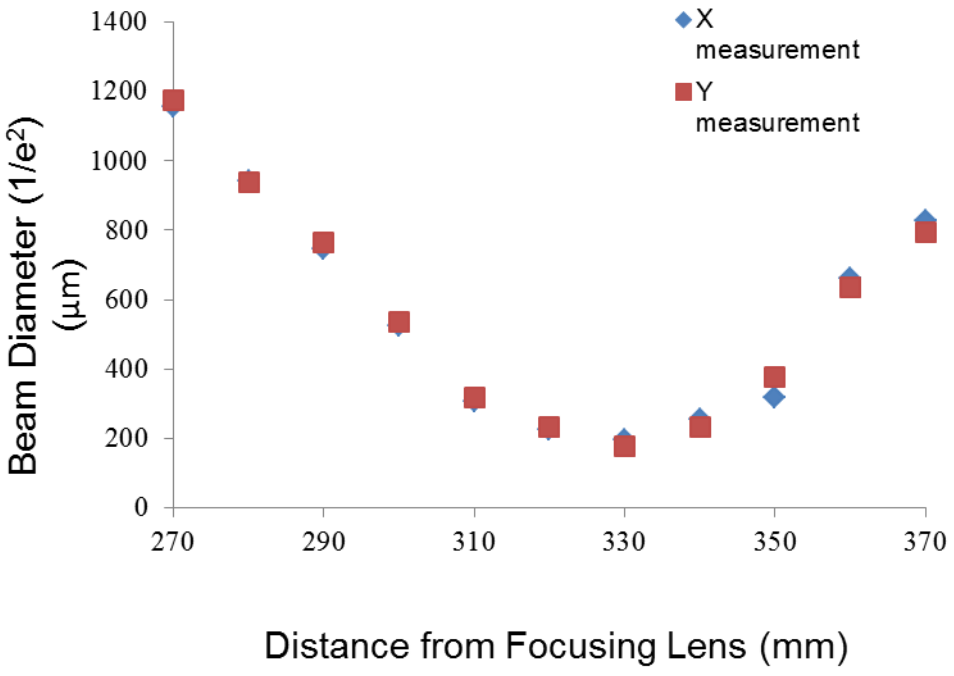

Figure 7-4: Beam Shape after being focussed(focal point occurring 330 mm after the lens) Measured in two planes x and y

This was taken at pulse energy of 0.09 mJ and it is known that the profile doesn't change in shape with the increase in power measured by weak reflection to the beam profiler. The measurement was taken at this power since higher powers may have damaged the beam profiler.

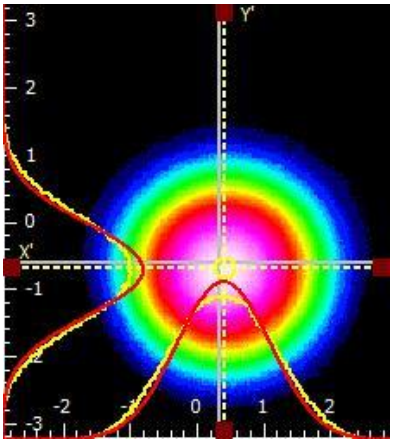

Figure 7-5: Profile of long-pulsed laser at focussed waist. Measured using beam profiler (1 unit in the scale equates to 100 µm) The yellow lines show the measured intensity whereas the red lines show the fit

Figure 7-5 shows the profile of the beam measured at the centre of the focussed beam. It shows the beam to be fairly Gaussian and circular. This is useful to know especially when comparison with modelling. The beam profile was measured using a beam profiler which was also used to measure the waist size to be determined. The measured values were used for measuring the beam diameters not the fitted function.

Further confirmation that the measurement beam was found to be Gaussian was the measurement of LII signal profiles at the centre line signal at individual points as seen Figure 7-5. By taking a point just below the measurement beam in the centre line and MATLAB can then translate up the beam and integrate the signal over the horizontal position of 0.4 mm. The resultant signal across the beam is shown to be Gaussian and MATLAB can fit a Gaussian function *gauss2* (a two term Gaussian model, which is a fit based off a Gaussian and linear profile allowing for a background signal subtraction). The fit is shown to fit well showing that the beam is very Gaussian.

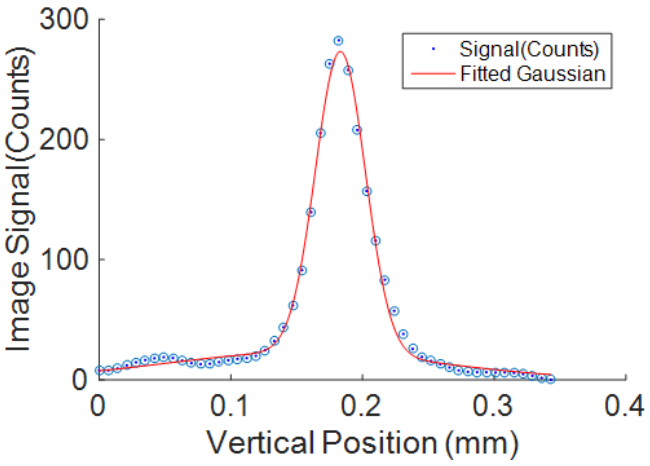

Figure 7-6: Example signal across the centre line in a ϕ =2.2 flame

7.3.2 Long-pulse laser temporal profile

Standard LII uses a laser which typically has a Gaussian temporal profile with a FWHM of 6-9ns and because of the short times when modelling the laser temporal profile was have less of an effect on the whole LII signal when changed, however with long-pulse the pulses being longer and different shape may cause the LII signal out to change dramatically therefore its important measure the temporal profile. The laser pulse shape was found using a Silicon fast photodiode. As seen in Figure 7-7, the pulse is around 30 times larger than what is used in conventional LII, an example shown in previous parts of this thesis such as chapter 5. The laser pulse shape changes with change in power output from the laser in a seemingly random manner, it does seem that the results are repeatable so this means that when measuring LII signal images it is important to measure the pulse shape saying it has no real uniform shape. Care has to be taken when using the laser at specific powers as this may have an effect on the signal due to the pulse shape of the laser.

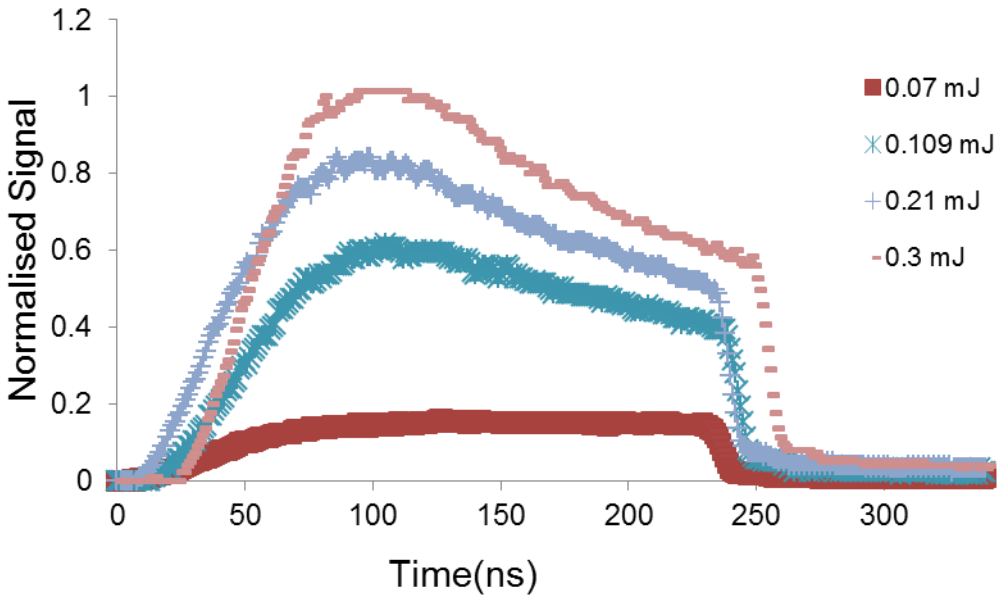

Figure 7-7: Laser pulse shape at a range of different pulse energies normalised to the largest signal

7.4 Long-pulse laser images

For images the values chosen was the mean over a specified area. It was assumed that no extinction takes place across the flame since none could be measured at these equivalence ratios and therefore assumed ineligible. This assumption then allows for the fluence to be found locally at different points within the beam by dividing the pulse energy by the $1/e^2$ beam waist area.

7.4.1 Camera images at different fluences

Figure 7-8 to Figure 7-11 show examples images of average images at ϕ =2.2 at different pulse energies. At the lower powers it can be seen that the background emission of the flame may place a significant part in image it is only when the pulse energy is above 109 mJ that the background correction becomes relatively much lower than the beam. If there was a way a filter was put in used with the camera without drastically changing the signal to noise ratio this may help the improve the image quality at lower fluences as seen in Figure 7-8 as it could allow for some of the background flame radiation.

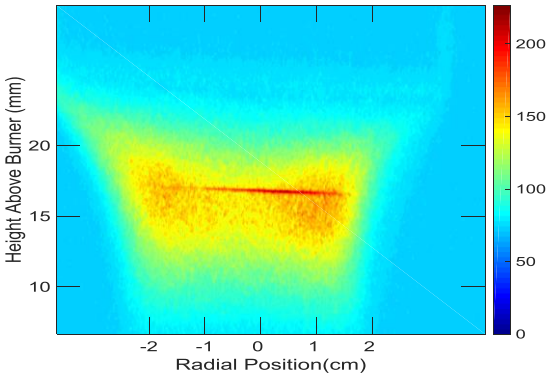

Figure 7-8: Image of LPLII at 0.03 mJ @ϕ = 2.2 and camera gate of 50 ns

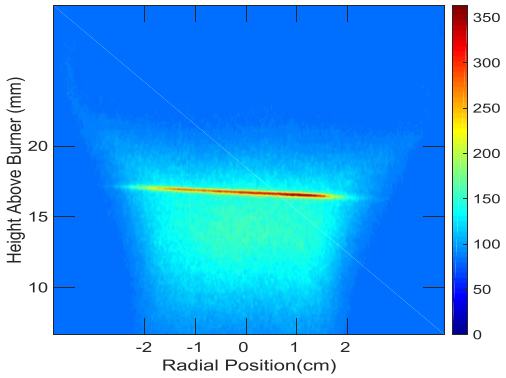

Figure 7-9: Image of LPLII at 0.05 mJ @ϕ = 2.2 and camera gate of 50 ns

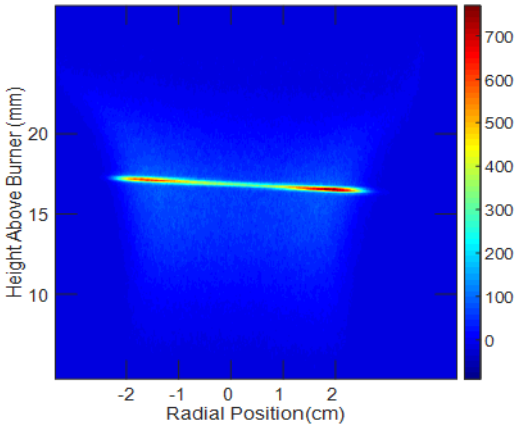

Figure 7-10: Image of LPLII at 0.17 mJ @ϕ = 2.2 and camera gate of 50 ns

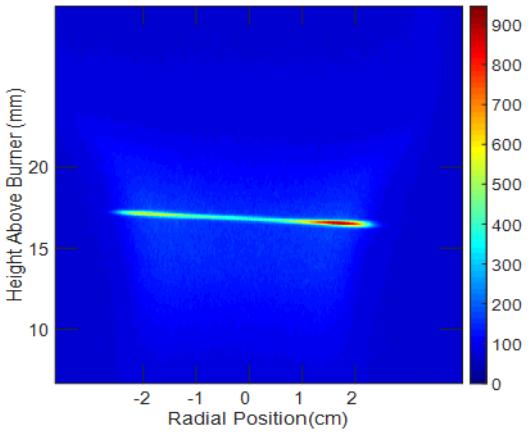

Figure 7-11: LPLII at 0.22 mJ @ϕ = 2.2 and camera gate of 50 ns

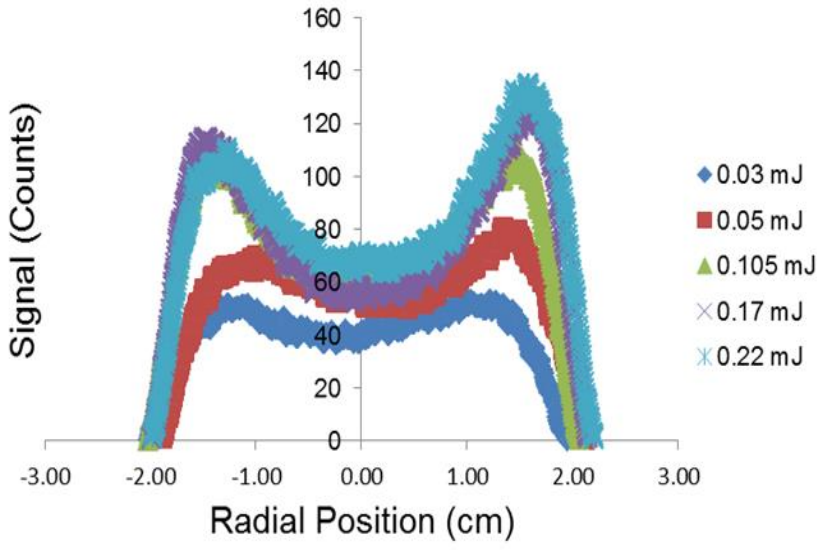

Figure 7-12: Radial Profile at different pulse energies, showing the change in profile with increase of local fluence

Figure 7-12 shows the radial profile at different pulse energies. It shows that at lower heights the profile is more uniform because fluence in the centre hasn't plateau yet. With comparison between the different pulse energy profiles it can be seen that the centre lime signal still rises but then only slightly rises with the increase in pulse energy, it can be seen that the edges increase between the images until it reaches a point where the signal starts to plateau this is a good indication of what is expected to happen. The data was found by as discussed in the previous section integrating across 1 mm of the beam to ensure all the signal is collected for the radial profile.

It can be seen that there is a slight incline of the laser beam probably because of the optical lens used. The images give an exaggerated impression of this effect. It can be seen that this is not too much of a problem since it is approximate incline of 0.08 mm from one peak at one side to the peak signal at the other side as seen an example in Figure 7-13.

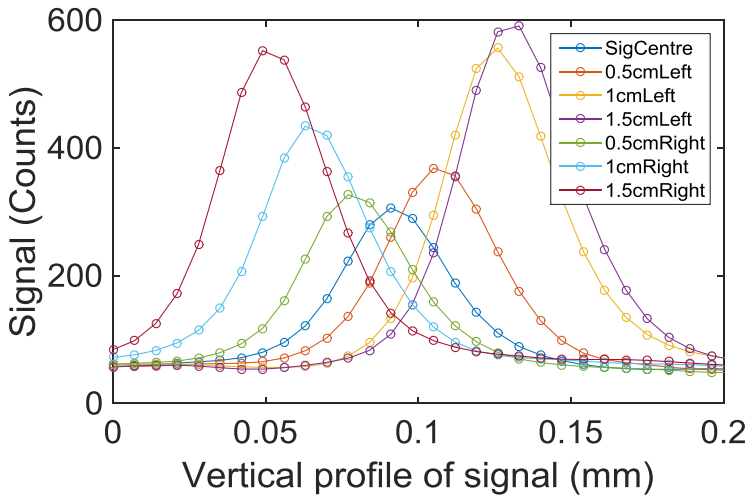

Figure 7-13: Vertical profile of LII signal across the beam (the zero level of the height scale is arbitrary)

7.5 Long-pulse laser fluence measurements

It is important to know the fluence curve, to understand the relationship between LII signals and the laser energy density. To simplify these results the fluence was calculated using the power measured by the power meter and the area of the waist measured using the beam profiler. The signals temporal shape changes with pulse energy though beam shape does not. Since with long-pulsed LII the laser temporal profile slightly changes with the pulse energy it means that peak signal will occur at different time for different pulse energy as seen in Figure 7-7. This makes taking a fluence curve by changing the power difficult. For camera fluence measurements it was deemed that the best way to find a fluence curve was to measure the fluence across the burner profile then the signal which has been corrected for cross sectional area, this can then be used to produce a fluence curve. This fluence curve can then be used to correct the radial profile, in cases where the radial uniformity cannot be assumed.

7.5.1 Fluence curve measured by camera and radial profile with correction

Figure 7-14 shows the variation of fluence across the burner when the pulse energy is 0.105 mJ. The fluence is calculated by using the $1/e^2$ diameter to calculate the cross sectional area. Unlike the temporal profile of the laser the laser spatial profile is known not to change over changes in the output pulse energy.

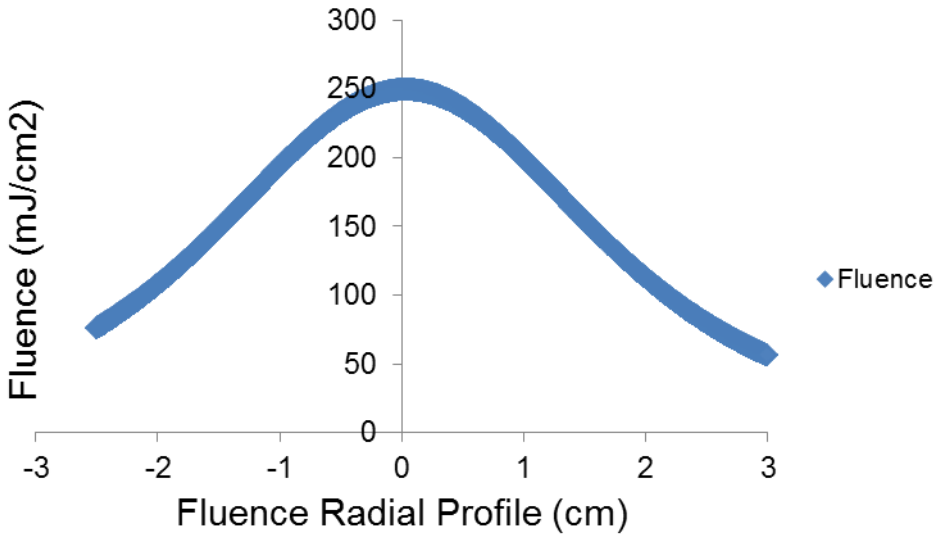

Figure 7-14: Fluence calculated across the burner measured at pulse energy of 105 mJ.

Figure 7-15 shows the fluence curve when the signal is corrected for the cross sectional area. The correction is done by dividing by the cross sectional area which is measured by the beam profiler and the focus being at the centre of the burner and then normalising the signal from the LII image. This was

done at a HAB of 16 mm where the profile is known to be uniform The fluence is taken at radial positions where soot volume fraction is known from other measurements at HAB of 16 mm. The results show the trend that is expected for a Gaussian profile where the signal levels off but still increases slightly with increasing fluence due to the contribution of the wings of the beam profile.

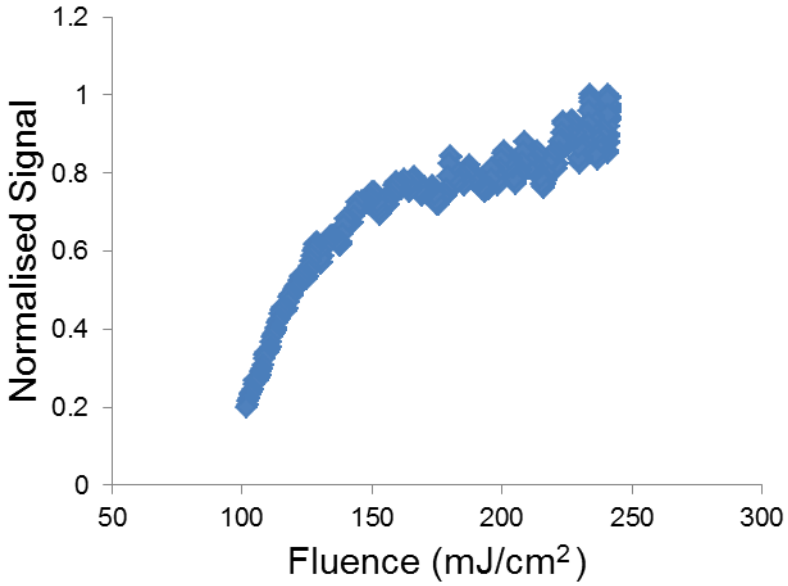

Figure 7-15: Fluence Curve with area corrected signal at for overall pulse energy of 105 mJ in ϕ = 2.2 Flame @HAB=16 mm

Figure 7-16 shows the correction for half the radial profile in an ϕ = 2.2 flame. The correction was made by multiplying the signal that was corrected for the measurement area with the fluence curve normalised signal. The profile is slightly uniform at 0 cm outwards till about 1 cm as what is expected in the central part of the flame. The profile only shows half the radial profile just now as the correction in made easier when just considering the half of the radial profile. This profile is close to what is expected with it being near-uniform though it can be seen that this is caused by random variation. Another way to check would be to use the PMT and measure across the laser using a translation stage.

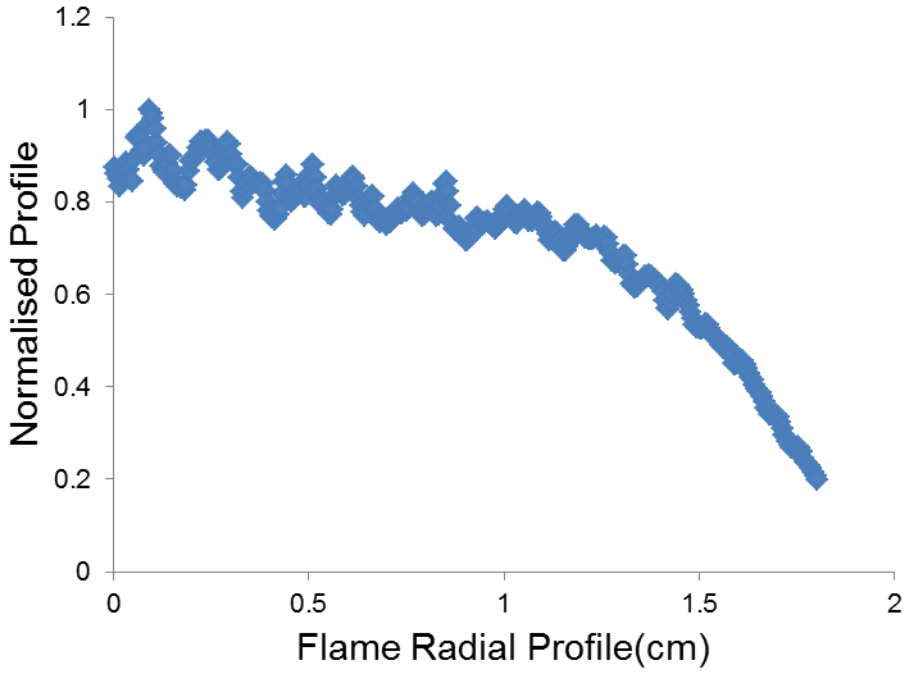

Figure 7-16: Corrected ½ Radial profile for overall pulse energy of 105 mJ in ϕ = 2.2 Flame @HAB=16 mm

7.5.2 PMT fluence curve

The LII fluence curve can be seen to be different depending on the measurement device and the way the signal is collected. This is most likely due to the gated nature of the camera. Figure 7-17 show results of the peak signal as well as the signal integrated over 50 ns. The difference between the fluence curves between camera and PMT is because of some of the same factors where the time where the peak of the LII signal changes and the camera has a fixed gate position discussed in the methodology chapter as well as because of the different filters and spectral responses of the detection equipment. These results show a similar trend to the fluence curve produced by Ditaranto et al[135] who uses long pulses showing a steady rise followed by a slight levelling off and then a rise in signal again. This is also similar to what is shown by Hverven.[137] These results show the importance of measuring using the same detection method. As expected the 'plateau' occurs earlier with the integrated camera signal whereas the peak signal form the PMT show a levelling off but still an increase in signal with fluence. Since the fluence curve using the PMT measures the peak signal the change in the temporal profile doesn't change the measurement.

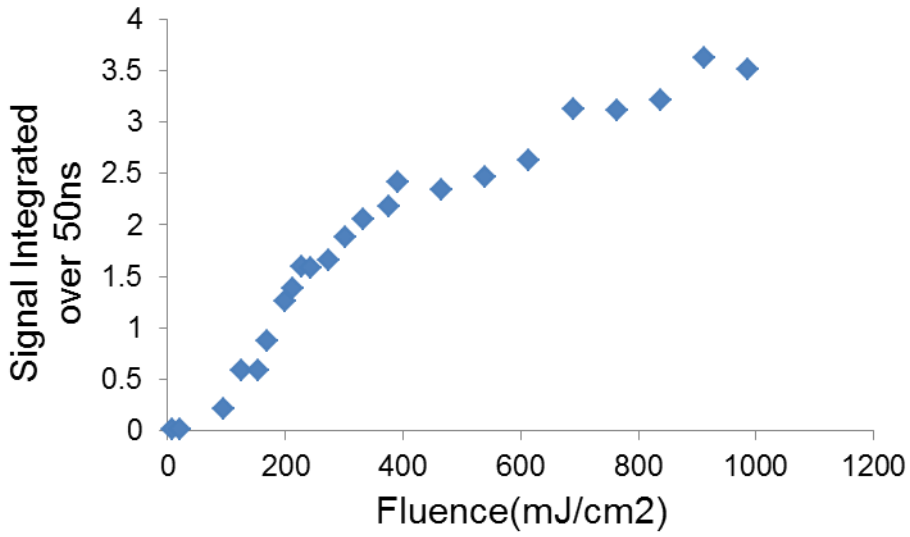

Figure 7-17: Fluence curve of PMT signal integrated over 50ns at Centre Line @ ϕ = 2.2

Model and PMT fluence curve comparison

Figure 7-18 shows the difference between a modelled long-pulsed LII fluence curve and a measured PMT fluence curve. The peak signal was used for both fluence curves. The model carries quite a few assumptions such as absorption coefficient, density as well as particle size of 30 nm. It shows a similar trend, this could maybe be improved with more averages in experiments. The fit could also be improved between the two curves.

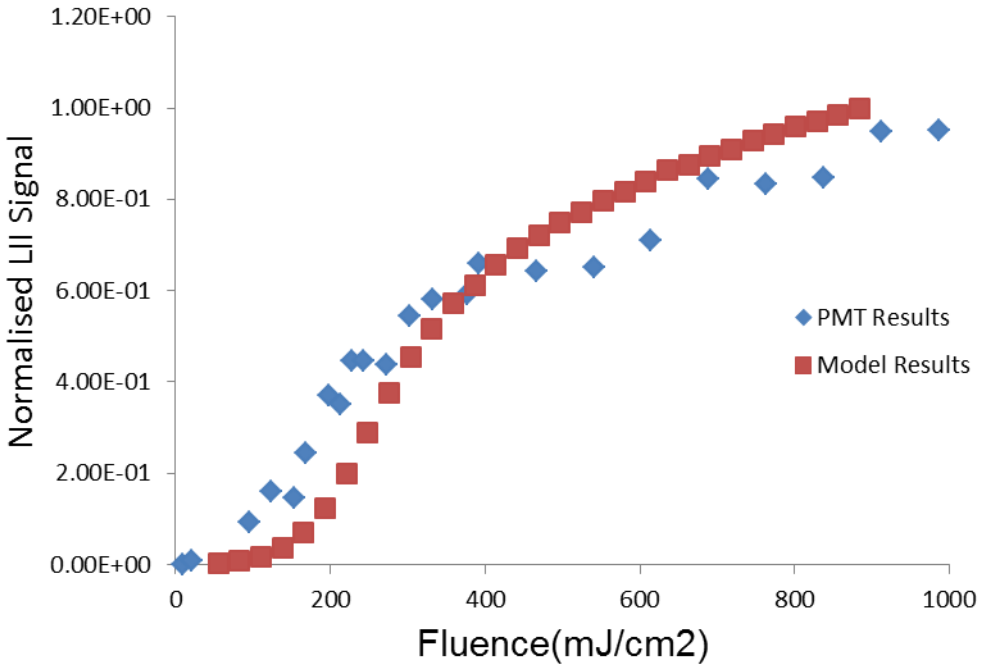

Figure 7-18: Comparison between PMT and model peak fluence curve

Overall there is a way to overcome the gaussian beam problem for signal interpretation. More work could be done further to investigate how to improve the signal interpretation however shown is a way of working to overcome this issue.

7.6 LII images at different HABs for different equivalence ratios

To produce a quantitative signal from the images, mean signals were recorded over a specific area of 1 mm. This area was the same for all measurements. For measurements of the HAB signal, results were taken at pulse energy of 0.109 mJ. These results allowed the centre line to enter the plateau region without having too much emphasis on sublimation of the particles and by validating with the model which is discussed further on in this chapter.

7.6.1 Centre line signal HAB comparisons for long-pulse detection measurements and LII excitation measurements

Figure 7-19 shows the centre line signal collected using the camera. The results show similarities as to what is expected with the profile rising steadily until it plateaus off. The signal for soot starts at around 9-10 mm. Similar to Nd:YAG results however it seems that signal to noise ratio at the lower heights may affect where the signal can be seen.

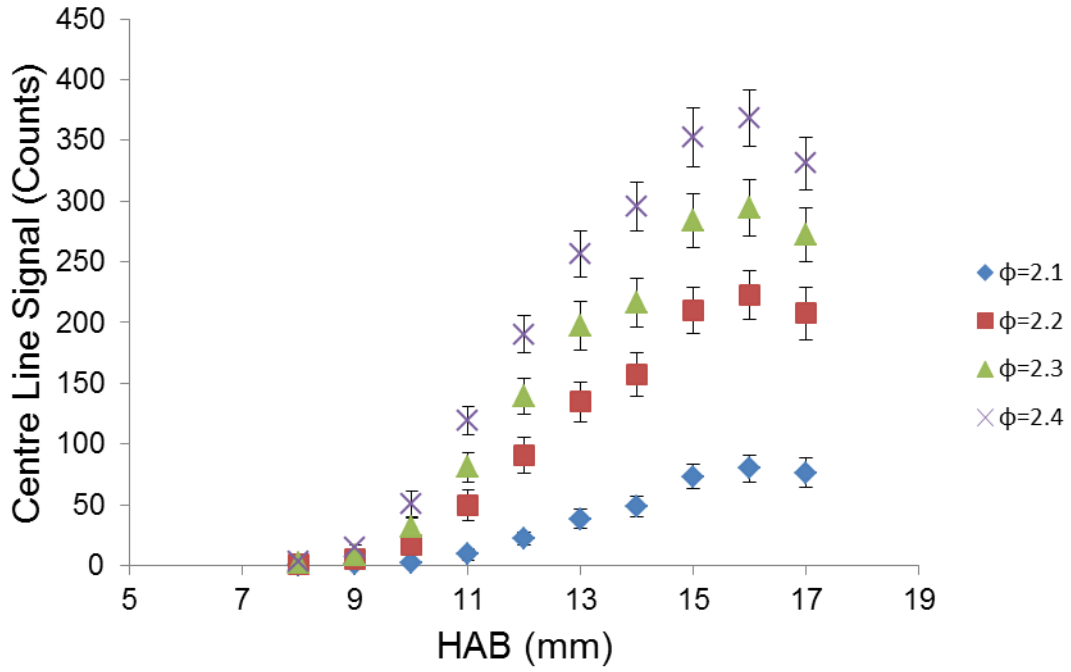

Figure 7-19: Centre line profile of HABs at different equivalence ratios using LP-LII at 0.109 mJ at camera gate of 50 ns

Time resolved point measurements were recorded as seen in Figure 7-20 using a Schott long pass filter as mentioned previously, to help increase the signal to noise ratio, and results show a good comparison

to the camera HAB profiles. The overall signal could then be fitted with a smooth fit as the signal to noise was larger without it. The ability to try and get a decay time from the PMT signal also proved to be difficult due to the shape of the signal over time. The peak signal was then used for comparison for centre line HAB measurements as seen in Figure 7-21.

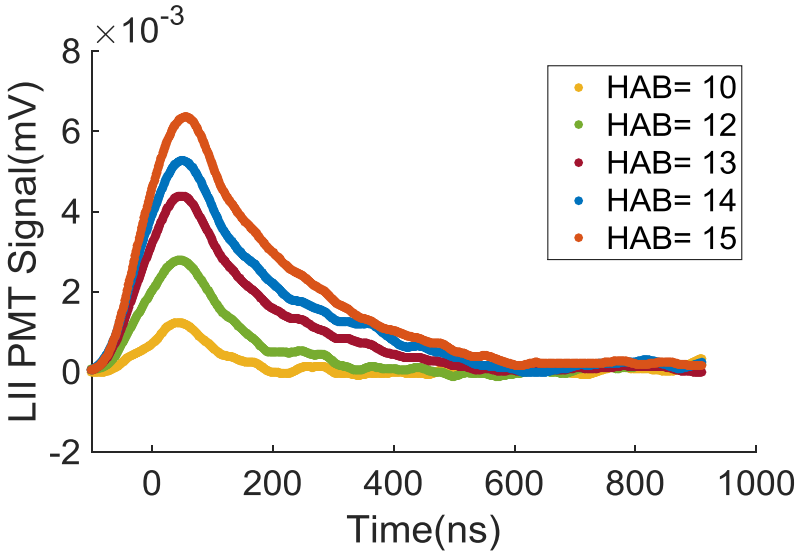

Figure 7-20: PMT results @ ϕ = 2.4 for different HABs

Figure 7-21 shows the comparison between the cameras with a 50 ns gate, long-pulsed LII centre line signal and PMT measured long-pulse centre line signal measured at the same laser pulse energy at 109 mJ/ pulse. Comparing PMT measurements and camera measurements gives confidence that it doesn't matter what detection setup is used to measure the soot volume fraction the answer will be the same.

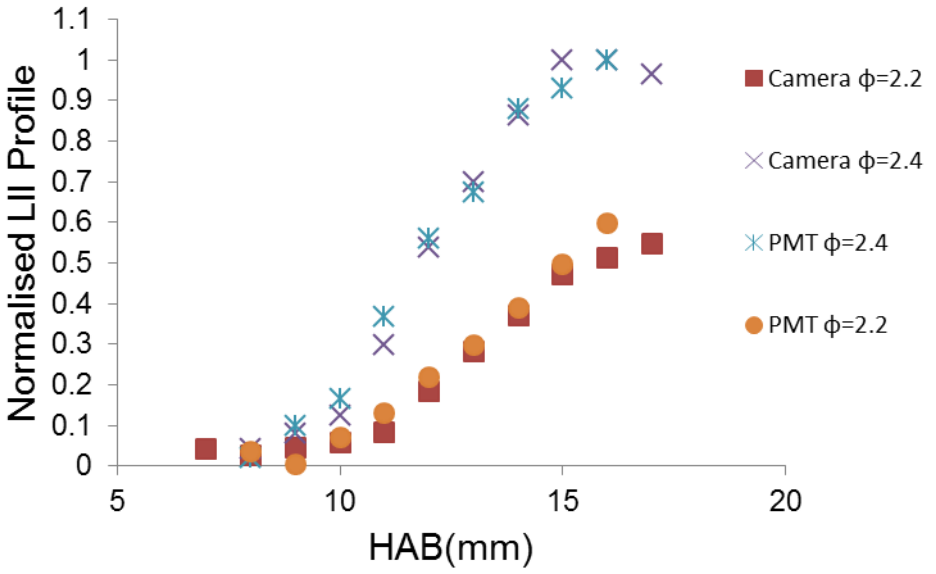

Figure 7-21: Long-pulsed Laser Imaging and PMT measurements comparisons with HAB centre line measurements

Figure 7-22 shows the comparison for the standard LII Nd:YAG laser excitation source measurement and the long-pulse excitation source centre line signals. For the normalisation the Nd:YAG results were divided by the largest number for the signal collected by the camera. Results show good agreement indicating that a calibration can be achieved and an absolute soot volume fraction can be done. However at the lower heights for the lower equivalence ratios the long pulse laser becomes overestimated due to the background subtraction not being larger enough due to the signal to background becoming much lower.

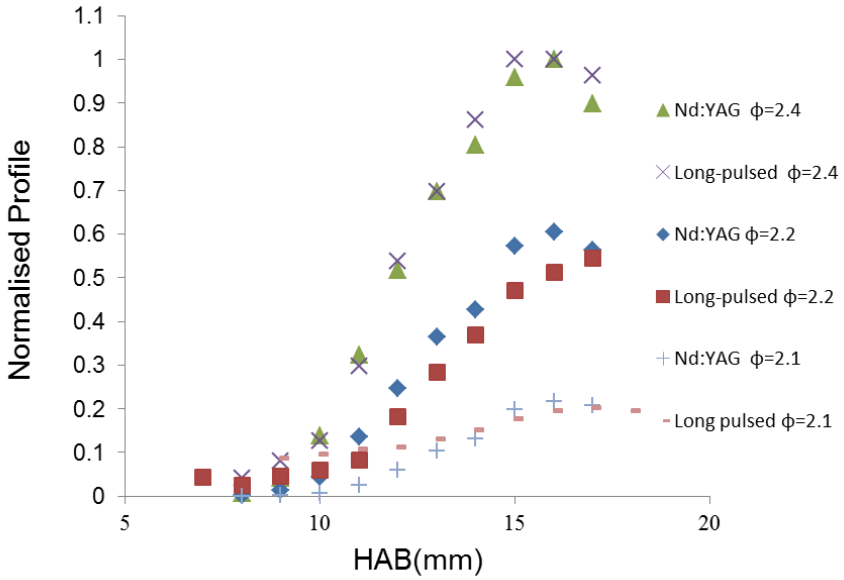

Figure 7-22: Long-pulsed laser centre line HAB comparison with Nd:YAG results

7.6.2 Long-pulsed LII temporally resolved image profile

Figure 7-23 shows the temporal profile measured in an ϕ= 2.2 flame. This indicates that the technique is able to be adapted to give an imaging temporal profile.[128] Care does have to be taken with background subtraction to ensure the starting and finishing points are correct. This is a point which could be improved through the use of filters.

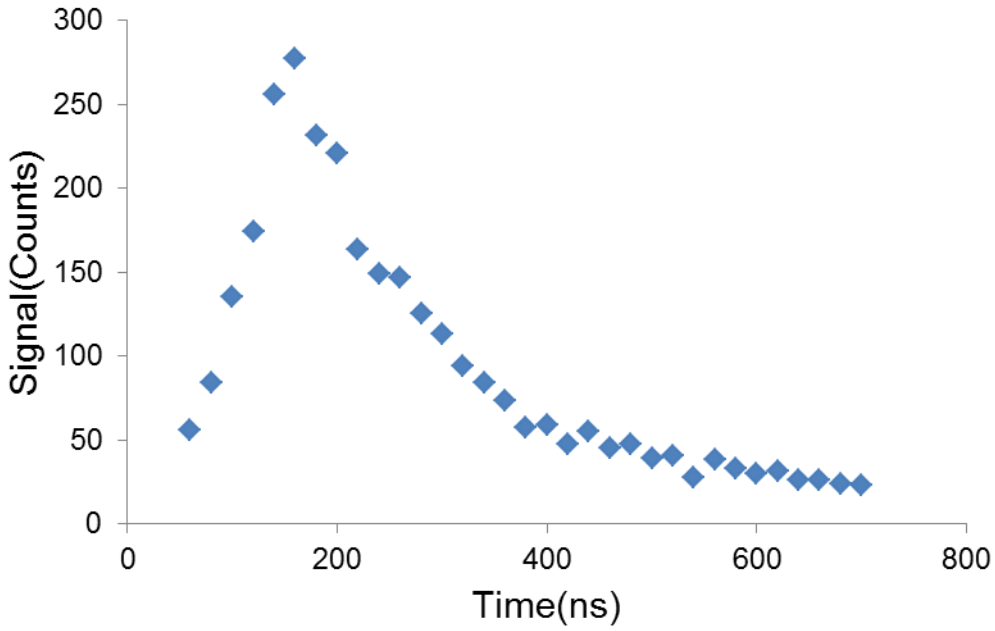

Figure 7-23: LP-LII temporal profile measured with camera @ ϕ = 2.2 @ 109 mJ

7.7 Long-pulse LII modelling

For modelling long-pulsed LII there has to be differences in the code to account for differences in the experimental setup. This is the temporal laser profile, laser spatial profile and detection efficiency at multiple wavelengths.

7.7.1 Laser temporal profile modelling

When considering LII modelling one key area in which long-pulse LII differs from short pulse LII is the laser temporal profile. As previously mentioned, the laser profile can vary significantly due to the laser power and pulse length. By creating a laser profile model that is dependent on both of these factors, the accuracy of the model will be significantly increased. Another method that could be used to represent the laser profile more accurately is to import experimental data, and model the data as a function which can then be implemented in the model.

The temporal profile was changed for long-pulsed LII compared to the standard model by implementing the pulse recorded on the photodiode from experiments. The data for the laser from the experiment is read into the model, the model then accounts for differences in time steps etc. by making a fit of the curve. The fit of the curve can then be normalised so the area is equal to one under the graph. This is done by finding the integral of the fit read in and normalising the profile. Fit the curve has shown to produce an artefact from the data of some ringing but overall this shouldn't influence the results produced.

7.7.2 Laser spatial profile modelling

When modelling LPLII it is important to account for the spatial profile. The long-pulse LII follows a Gaussian profile which needs to be accounted for unlike the standard LII which uses a top-hat profile.[81,109]

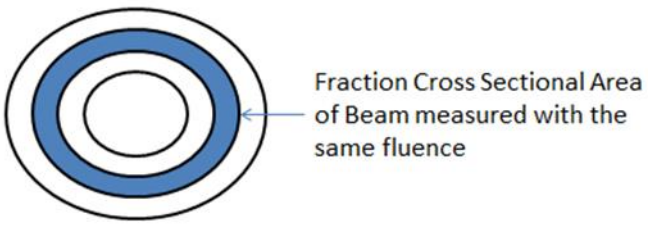

Figure 7-24: Cross section of the beam measured

The profile is accounted for by knowing the width of the laser beam. A power can be inputted and then a FOR loop rub a sequence of radial positions in the beam, a fluence can be calculated for each increment as seen in Figure 7-24. The signal for this fluence can be produced and multiplied by a factor

which accounts for the annulus of the Gaussian profile at each position within the beam. The fluence for the area of the segment of the Gaussian profile follows the Gaussian distribution as seen in Bladh et al [56]:

$$F(r) = \frac{P}{f}\frac{2}{\pi\, r_L^2}\ \exp\left(-\frac{r^2}{\omega_2^2}\right) \qquad \textbf{Equation 7-1}$$

Where

F(r) is the local laser fluence at position r in the beam (mJ/cm^2)

P is the average Laser power (W)

f is the pulse frequency (Hz)

r_L is the laser radius. (m)

This gives the laser fluence however a correction has to be applied to the signal for the annulus of the beam:

$$\propto = \frac{\pi\, r(x+1) - r(x)\,)^2}{\pi\, r_L^2} \qquad \textbf{Equation 7-2}$$

Where:

$\propto$ is the fraction of the area of the annulus

7.7.3 Spectral detector efficiency

Since in the long-pulsed LII experiments there was no filter used on the camera meaning that different wavelengths collected will have different collection efficiencies due to the detection medium therefore a way of modelling this effect has to be developed. This was done by reading in a recording of the detection efficiencies from provider's manual as seen in Figure 7-25. The detection efficiencies read into the model, can be interpolated with a set of wavelengths that want to be used. The model can then produce a signal at each wavelength stated, which has been multiplied by the collection efficiency factor. The model has therefore calculated a spectrum of the LII signal weighted for detection efficiency at each radial position in the beam at for each time step. Figure 7-25 shows the detector efficiency for the camera which is used in this model.[67]

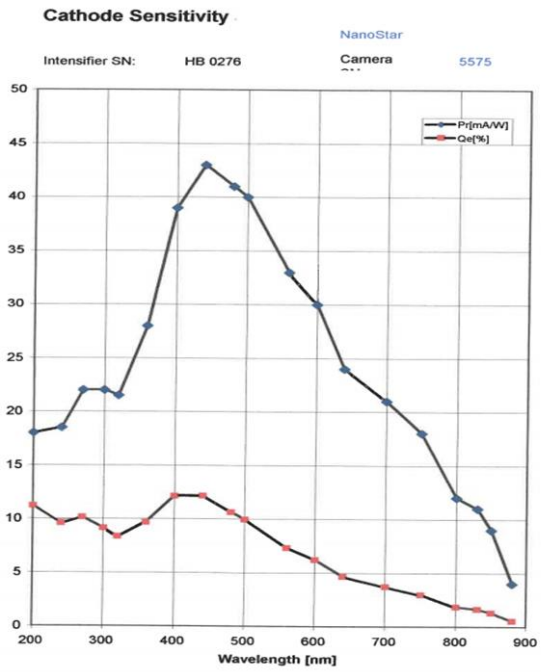

Figure 7-25: Camera collection efficiency adapted from the Nanostar Lavision Manual[67]

7.7.4 Long-pulsed LII modelling overall results

Figure 7-26 shows the model temperature over time results at different range of pulse energies. The results show as expected that the larger fluences the temperature is larger and at the highest pulse energy of 0.22 mJ shows a prolonged time at the maximum temperature. The assumptions used in the model similar to the ones that are used previously. Some assumptions used in the model include:

- Initial Particle Diameter = 30 nm
- Gas Temperature = 1700 K
- Initial Density = 2200 kg/m^3
- Absorption Function=0.36

Modelling measurements at different fluences

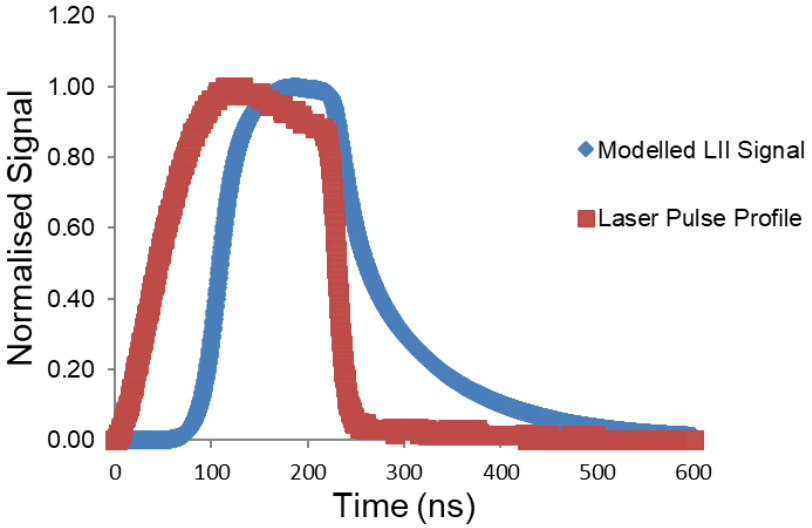

Figure 7-26: Modelled LII profile at pulse energy of 0.22 mJ (fluence 680 mJ/cm^2)

Figure 7-26 shows the modelled LII profile along with the Laser pulse profile measured experimentally and included in the model. It shows where the peak signal is compared to the laser temporal profile. It can be seen that the laser pulse spends a considerable time over the modelled peak LII signal showing that the soot particle is being heated over a long time.

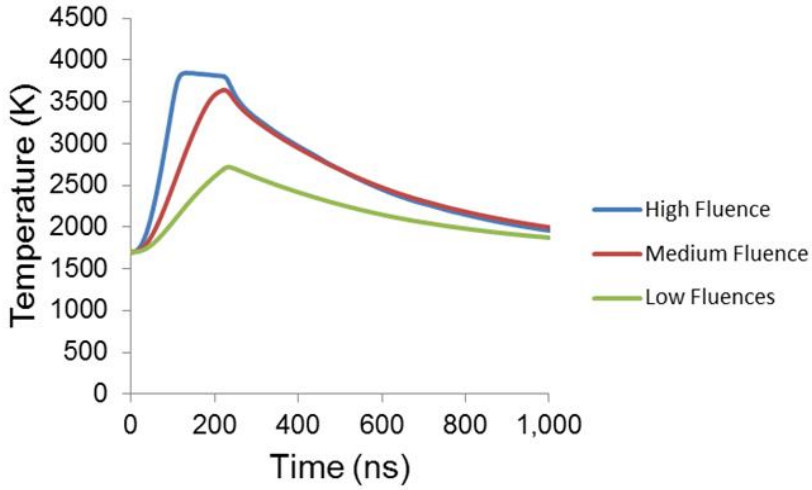

Figure 7-27: Modelling temperature of soot vs time comparisons at different range of fluences. Fluences range from 680 mJ/cm^2 for the high fluence, 290 mJ/cm^2 for the medium fluence and 145 for the mJ/cm^2 for the low fluence.

Figure 7-27 shows the modelled temperature for the LII model at 3 different fluences. The results show an extended time the particle spends at peak temperature. The peak temperature shows a temperature which is consistent to typical LII modelling.

Figure 7-28 and Figure 7-29 shows results of the model at the largest fluence modelled which has a pulse energy of 0.22 mJ. Figure 7-28 shows the heat transfer components rate of energy changed involved in the model. It can be seen that absorption and vaporisation have a very large effect on the model which was also affect the mass and diameter greatly.

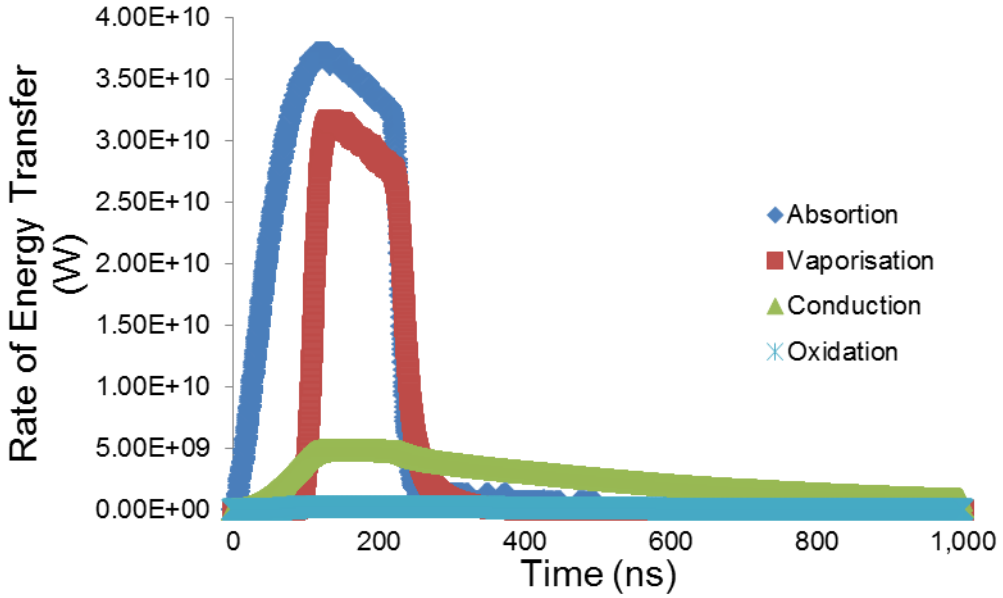

Figure 7-28: The contribution of different heat transfer components rate of energy change over time for pulse energy of 0.22 mJ

Figure 7-29 shows the change in the mass of the particle over time which corresponds to the heat transfer components showing the large effect vapourisation has.

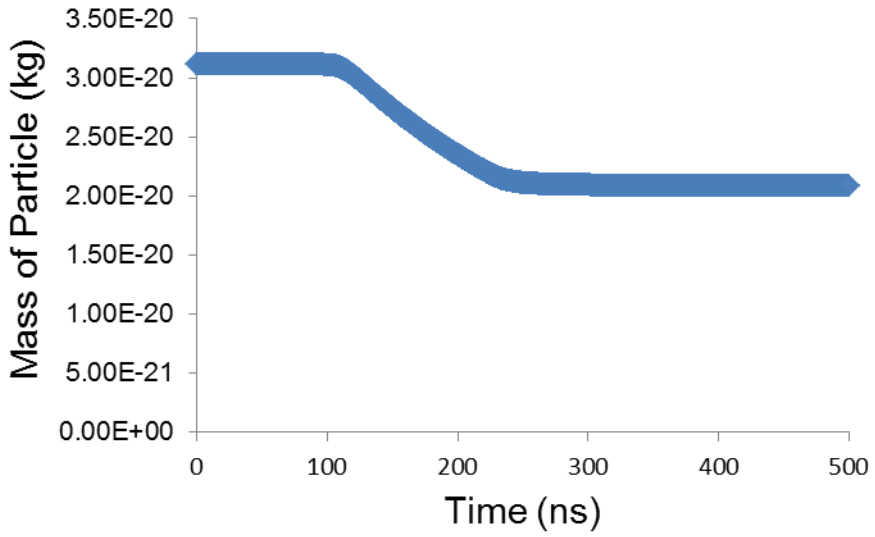

Figure 7-29: Mass of particle over time at the pulse energy of 0.22 mJ(fluence 680 mJ/cm^2)

Figure 7-30 and Figure 7-31 shows the results of the model at 0.109 mJ. Figure 7-30 shows the heat transfer components energy transfer; it shows that the effects of the absorption and vaporisation have less of an effect compared to the larger fluence.

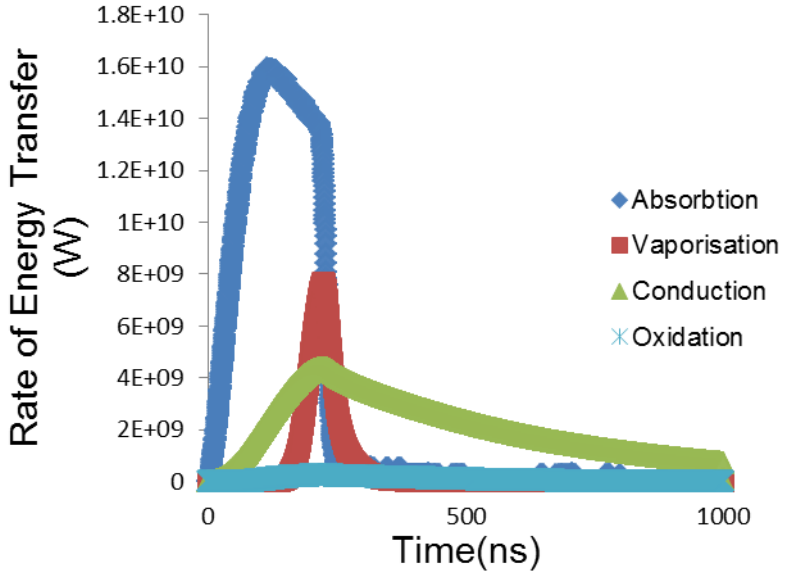

Figure 7-30: The contribution of heat transfer components at the pulse energy of 0.109 mJ (fluence 290 mJ/cm^2)

This can also be seen in Figure 7-31 which shows the change in mass of the particle is very small compared to Figure 7-29 which has a larger fluence. These results show indication that the model is working in ways that it is supposed to. Oxidation as a heat and mass transfer mechanism was included

as it was thought that the longer laser pulses may have an effect however it can be seen that the effect is relatively small. [83]

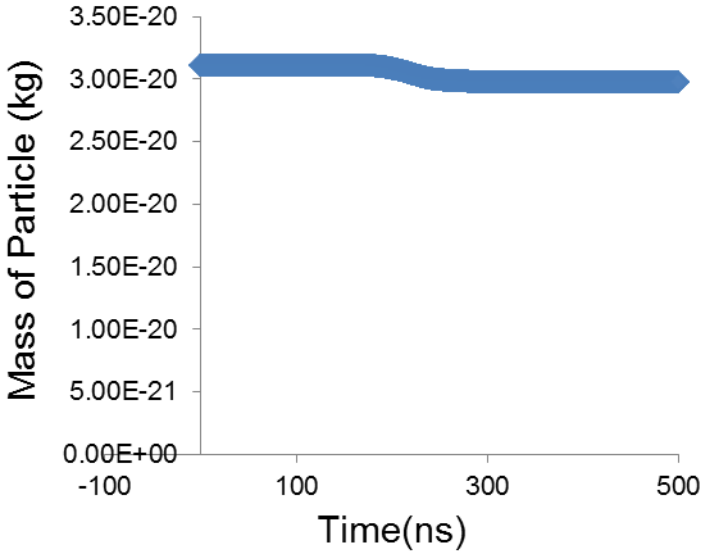

Figure 7-31: Mass of particle over time at the pulse energy of 0.109 mJ (fluence 290 mJ/cm^2)

7.7.5 Model comparison

Figure 7-32 shows a comparison between the camera measurement and the modelled signal. It shows a difference between the modelled signals. The modelled signal has many assumptions associated which may cause the difference between the signals. The modelling conditions are the same as shown in chapter 3 with E(m)=0.36 and the particle diameter of 30 nm and at a pulse energy of 0.109 mJ. The model may not include all the components that affect the signal such as annealing. Annealing has been stated to effect signal by changing properties of the soot particle especially if the soot particle has spent a longer time at higher temperatures, this shows the need for maybe further development in the model.[133,139]

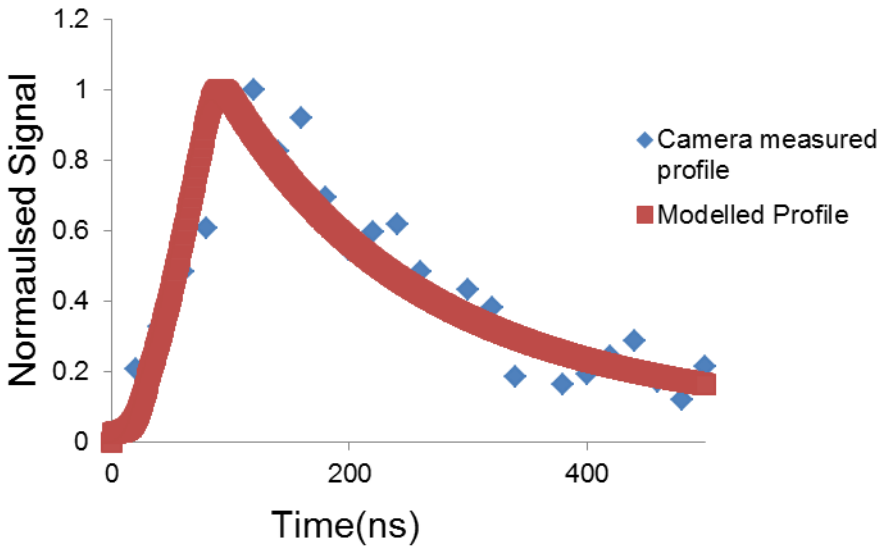

Figure 7-32: Time resolved camera comparison with modelled signal

Overall it seems that the long-pulse modelling behaves as expected with relation to changes in pulse energy. Trying to get a fit with the temporal profile is difficult because of the unknown factors therefore more work must be done to try and get the best fit between the model and experimental results.

7.8 Conclusions and future work

In-situ LII has been demonstrated using high power, long-pulsed fibre laser to measure soot volume fraction within a flat flame burner. Results with averaged LII images have been processed and shown to give comparable profiles to the benchmark data measured by short-pulse LII shown in the thesis in a previous chapter. The radial profile shows somewhat agreement with what is expected with it producing a uniform profile; however by assuming no absorption across the flame the fluence and difference in beam width this can seemingly be accounted for it does lead to some noise in the result. There was a correction for the fluence and the beam width which seemingly provides a similar radial profile across the burner, showing that a correction is possible to use in variety of circumstances.

Overall results show good agreement with Nd:YAG excited LII HAB profiles for different equivalence ratios, reliable fluence curves, reliable temporal profile results. Modelling shows promising results with steps being taken into the broadband detection, longer temporal profile and the change in radius of the beam being different to the standard models typically used in LII modelling. With some further development such as developing an annealing component in the model, it could produce results that give us more detail into the effects of long-pulsed heating on the soot particles.

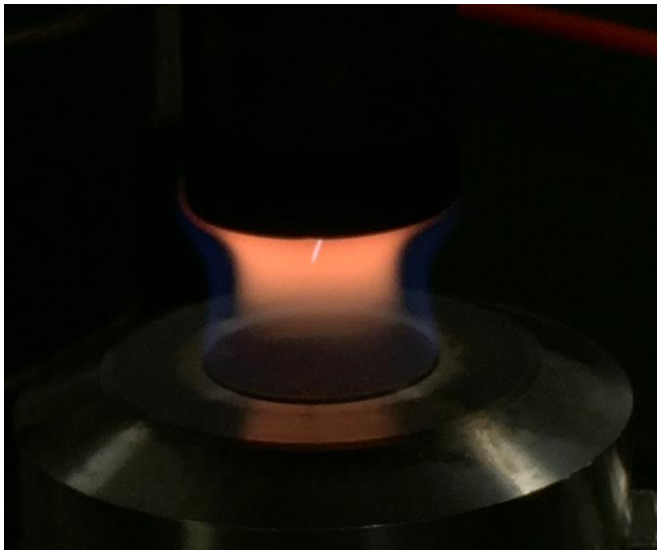

Figure 7-33: Image showing visible LPLII using mobile phone camera

The laser could be tested in more complex or turbulent flames such as the biofuel burner or aero engine to see if it can give results similar to modelling in these complex flames. Using filters could also allow for 2-colour LII to be carried out using this laser source. One way of improving the long-pulsed Laser LII set up and technique would be to also use with a filter to reduce flame background radiation as this will help be able to produce a more reliable images as help simplify complex modelling. Another

investigation would be into the effect the laser at high pulses has on the surrounding gas temperature, as well as changing the pulse frequency to see how that affects the surrounding gas temperature. Thus the LIIsignal.[128,142]

8 Laser induced incandescence imaging in diffusion flames of liquid fuels relevant to biomass combustion

8.1 Introduction to biomass combustion and use of representative pure liquid fuels for experimental investigation

8.1.1 Introduction and background

The requirement for sustainable energy generation has led to an increase in the utilisation of biofuels sources in combustion. There has been a global drive to finding bio-based alternative fuels to partially replace fossil fuels. It is important to investigate the formation of pollutants from using these alternative fuels, particularly the formation of aromatic hydrocarbons and soot.

Tran et al. [89] measured soot volume fraction of different biofuel blends in a diesel fuel using LII, in a wick diffusion. They showed that the smoke point increases in height with blends containing larger biofuel content, showing the comparison with LII images. The smoke point is a way of measuring sooting propensity, and it is measured by the maximum flame height before the flame emits a visible track of smoke. Measurements using this type of burner were performed to study biodiesel blending and sooting propensity. As the biofuel percentage is increased in the fuel the LII signal decreased. Extinction was used to calibrate the LII signal to find the soot volume fractions.[89] Soot volume fraction in these types of flames and fuels can vary from 1 ppm to 300 ppm depending on a wide range of burner configurations and fuel types. Tolomelli et al.[143] also showed similar results to Tran el al.[89] showing biofuel blends but with no calibration to soot concentration. Salamanca et al. [144] hypothesised that when ethanol is added to the fuel there is a reduction in coagulation efficiency or a slowdown in the mechanism of nanoparticle formation and growth. They showed how ethanol additives can have on the effect of particle size distributions in ethylene premixed flames. Jozsa et al.[145] demonstrated the chemiluminescence of a rapeseed oil flame in a laminar premixing flame, with a large peak at 554 nm in the spectra belonging to the C_2^* radical compared to standard diesel measurements. The results from these sources show the importance of knowing the method of soot formation. These sources also show the potential of the widespread use of biofuels to be used as a fuel source such as in the transport industry and if these fuels can be used to help limit the use of fossil fuels there is more interest in using liquid and solid biomass fuels.

With the increased interest in using alternative fuels such as wood/cellulosic fuels the number of investigations into low-temperature biofuel combustion has also been increasing. Venkataraman et al.[146] have stated that using low temperature biofuel combustion can result in more production of PAH compared to the higher temperature industrial combustion. Therefore, if the formation of PAHs rises,

this will lead to a rise in the soot concentration which could be interesting to measure. Biomass from wood is one form of biofuel source. Wood and cellulose compounds are complex fuels so there is a need to first analyse simplest compounds involved in the combustion of wood to better understand the underlying mechanisms of pollutant formation. Typically wood when heated undergoes pyrolysis which frees organic gases and leaves behind the charcoal.[147,148] Since up to 85% of the mass and 60% of the heating value from wood is contained in the vapours produced by pyrolysis, therefore it is important to try to mimic the conditions faced when burning these products.[149,150,151]

Wilson et al.[150] used Eugenol, Furfural and n-Decane in a wick burner (similar used in this project) and used aerosol time-of-flight mass spectrometer (ATOFMS) for the study of soot formation. Experimentally produced results revealed the mass spectra of the products of burning these biofuels.. There was accompanying computational combustion modelling. The model takes into account the different pathways of soot production for different flames as seen in Figure 8-1. Since there is a difference in the PAH formation routes it would be interesting to see if the sooting propensity that may be influenced by this. CPD (cyclopentadienyl dimerization) is a mechanism involving the reaction of cyclopentadienyl radicals, which generates naphthalene and indene to then produce soot through further HACA mechanisms.

Atiku et al.[149] studied the products from the fuels eugenol, furfural, n-decane and anisole, used throughout this section of the project. They also compared the combustion products using TEM and showed the mechanisms of soot formation for certain fuels. LII point measurements were recorded in this study and for better understanding of the soot concentration and soot distribution it was decided that imaging could be used to better understand these flames.

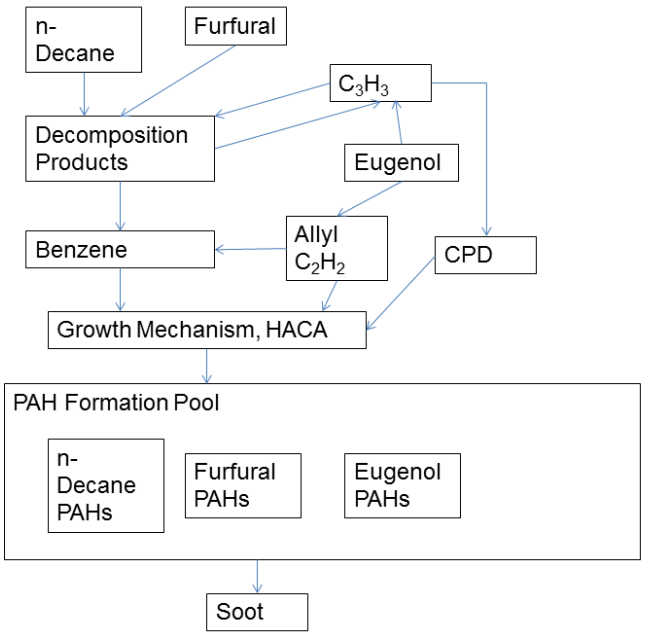

Figure 8-1: Diagram showing the PAH formation pathway in the three flames (adapted from Wilson et al.[150])

This chapter investigates these biofuels (Furfural, Eugenol, Anisole and a conventional hydrocarbon *n*-Decane for comparison), using a wick diffusion flame burner, to represent components that are devolatilised as pyrolysis products during combustion of wood. Previous work in Atiku et al.[149] have used point measurements to measure the soot volume fraction and the radial profile for each of these fuels, it was thought for more precise results imaging would be a better method to understand the soot distribution within these flames. By calibrating with a flat flame burner a spatially-resolved, two dimensional maps of soot volume fraction were found for each fuel as well as this is a time resolved profile can be produced. The images were either averaged or they were single shot(one image recorded). It was found that using single shot images showed the flame structure more accurately as it wasn't suppressed due to averaging. Preliminary investigations into the fluorescence signal generated using 532 nm excitation were performed.

8.2 Biofuel burner experimental procedure

The biofuel setup is similar to methodology used in earlier previous chapters of this thesis with the main exception that the flat flame burner has been replaced by the biofuel wick diffusion flame as seen in Figure 8-2. The four fuels used were >98% pure from Fischer Scientific. LII measurements were carried out using 1064 or 532 nm excitation wavelength. The same optics as previously discussed in the methodology chapter was used with a 1 mm wide slit being employed since the diameter of the biofuel flames is smaller. This allows for a trade-off between the spatial resolution of the burner and signal level since the signal level is large enough.

For experiments in which two wavelengths were to be used a 532 nm notch filter was used in addition to the bandpass filter. This was used so that no scattering from the 532nm light can affect the signal produced by the image intensifier. No notch filter was needed at 1064 nm since the image intensifier is not sensitive to that wavelength. Signal levels were sufficient to allow for single-shot imaging of soot volume fraction in these flames, with favourable spatial resolution.

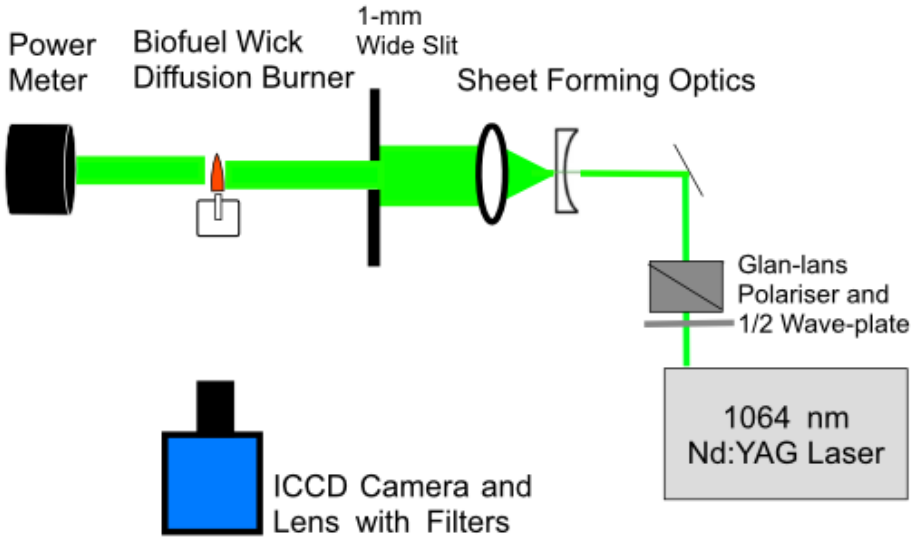

Figure 8-2: Biofuel burner wick experiment

The wick burner used here does however result in problems with repeatability and inability to produce precisely symmetrical flames. Using a constant wick height length of 7 mm and a wick diameter of 2 mm, however helps to ensure reasonably reproducible behaviour. [89] [149]

The type of flame used was a laminar diffusion flame.[16] As discussed previously this is where the fuel and the oxidiser meet by diffusion. The flame's heat vapourises the liquid fuel which then diffuses to the reaction zone. Soot particles are formed in the fuel rich regions of the flame then transported to the lean regions and in the oxygen containing ambient surroundings there is some combustion of the soot particles.

The results shown in the next sections are direct averages and no image has been omitted. It would be possible to process the data to exclude any flames showing significant movement however it will be shown that this wasn't necessary to obtain representative averages. A 3x3 median filter has been applied to all images. Most images don't have a flat field correction applied since it was deemed to be not needed when the calibration image is compared.

Some information on the fuels can be found in Table 8-1. This gives an indication of the sooting propensity and some other factors that the change in fuel.

Table 8-1: Combustion properties of the fuels. Found by measuring the physical burner properties. These were found in Atiku et al.[149]

Fuel	Bp, ^{o}C	Smoke Point, mm	Mass Burning Rate, mg/s	Emission, mg soot /g fuel	C/H Ratio
n-Decane	174.1	27	5.4	0.18	0.45
Furfural	161.7	16	4.8	27	1.25
Anisole	154	11	4.7	17.1	0.88
Eugenol	254	6.5	1.4	132.2	0.83

8.3 Soot profiles of different biofuel flames

The first step to characterise the fuels is to measure the soot volume fraction. Single shot and averaged images were recorded to show the effect that averaging can have on the soot volume fraction due to any movements within the flame. These results were taken using 1064 nm excitation wavelength, with a single image shown or an average of 50 images using a 1 mm wide slit and the fluence is 210 mJ/cm^2. It is assumed negligible extinction takes place across this flame however that probably isn't the case due to the high soot volume fraction even with the compensation of a smaller flame front. The prompt LII signal gives a good indication of soot volume fraction since the fluence is in the plateau region.

One source of error in soot volume fraction sizing could be the difference in soot properties such as the absorption function, when comparing soot produced in the biofuel burner compared to extinction measurements in the flat flame premixed porous plug burner. However because the soot is being measured is mature it is assumed that there will not be too much of a change in the absorption function compared to the calibration soot properties.

8.3.1 Single shot images of biofuels

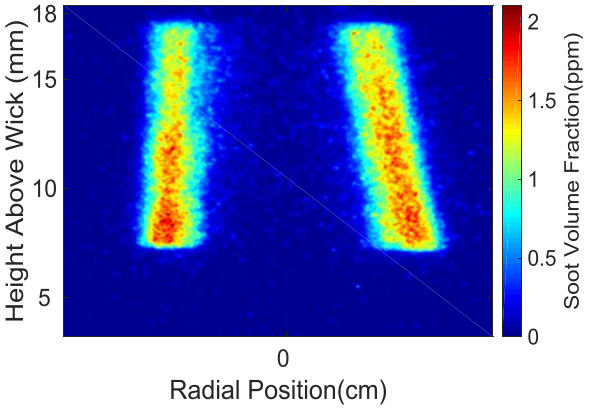

Figure 8-3:Single shot image of anisole soot volume fraction

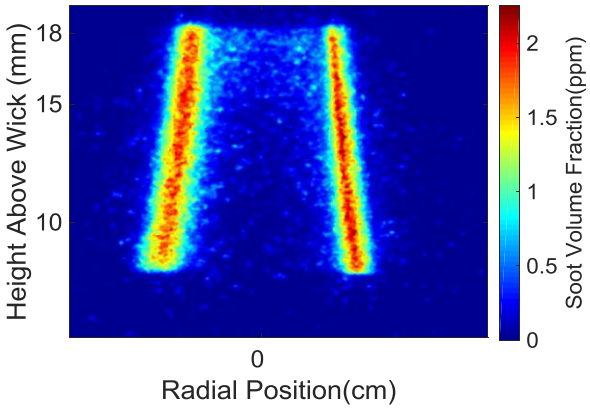

Figure 8-4: Single shot image of furfural soot volume fraction

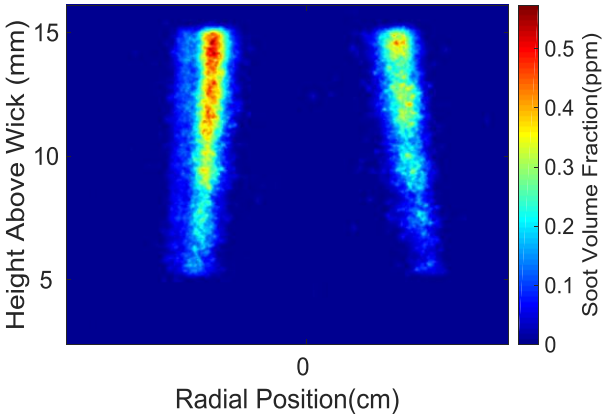

Figure 8-5: Single shot image of n-decane soot volume fraction

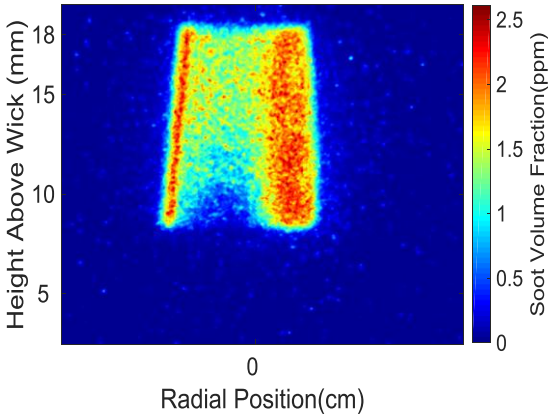

Figure 8-6: Single shot image of eugenol soot volume fraction

Comparing the single shot images as seen in Figure 8-3 to Figure 8-6, it can be seen that that eugenol has the largest soot volume fraction throughout the flame. This was expected as saw even by eye the amount of black smoke emitted by the eugenol flame compared to the other flames. Thin flame fronts are observed from Figure 8-3 to Figure 8-5 which could be useful when comparing with averaged images which can remove spatial precision due to flame movement. It was deemed that flat field corrections weren't needed for these images since the calibration flat field image should no need for it.

Figure 8-7 to Figure 8-10 shows the single-shot radial profiles across the burner at different HABs. It can be seen that all the HABs for each fuel have similar radial profile of soot volume fraction apart from n-Decane where there does seem to be a rise in soot concentration with HAB.

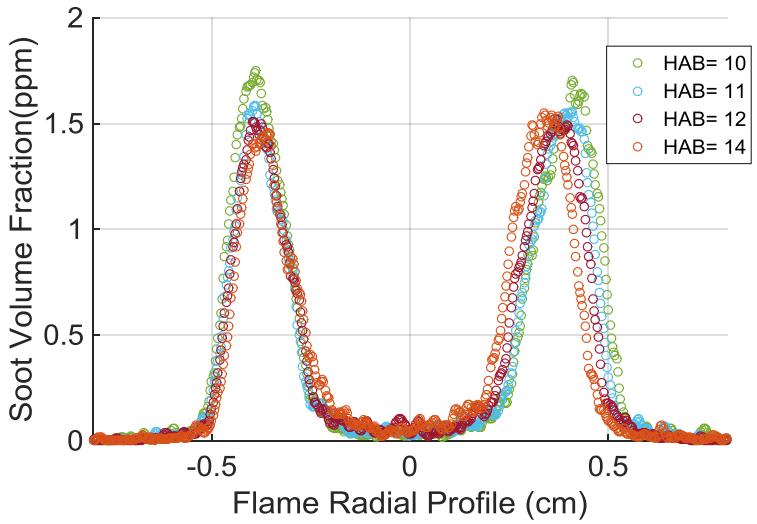

Figure 8-7: Single shot radial profile of soot volume fraction for anisole at different HABs

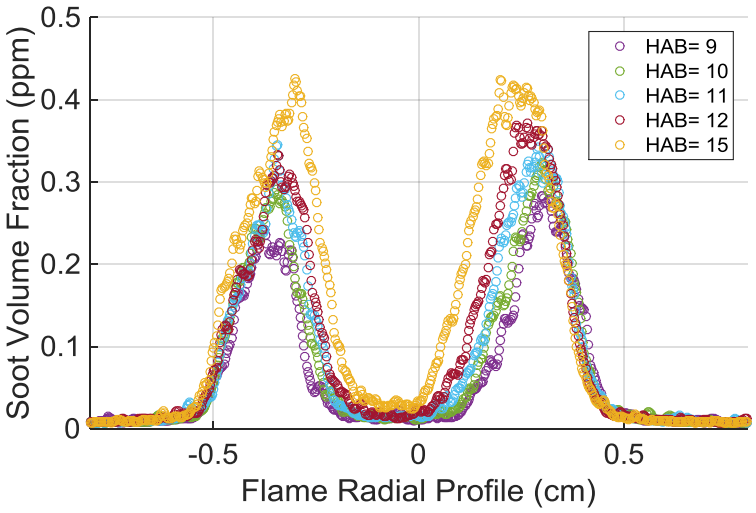

Figure 8-8: Single shot radial profile of soot volume fraction for n-decane at different HABs

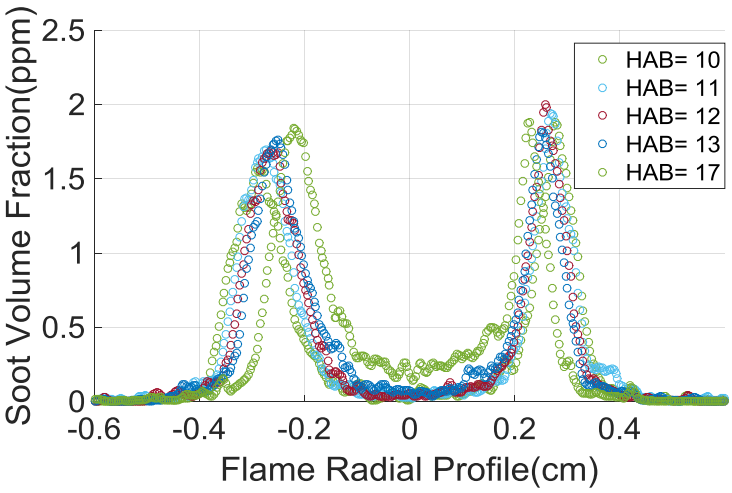

Figure 8-9:Single shot radial profile of soot volume fraction for furfural at different HABs

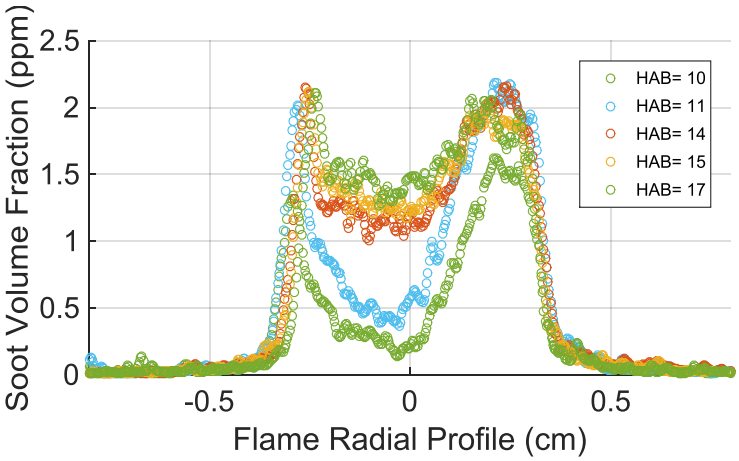

Figure 8-10:Single shot radial profile of soot volume fraction for eugenol at different HABs

Figure 8-10 shows the radial soot volume fraction profile of eugenol. It can be seen compared to the other soot volume fraction profiles to be noisier. This is due to the nature of eugenol which cause the flame to burn out fast and make the flame unstable to even measure single shot.

8.3.2 50 averaged biofuel images

This section shows the soot volume fraction profiles of the different fuels used previously except instead of single-shot images being shown an average of 50 images are shown.

Anisole

Figure 8-11 and Figure 8-12 show a different image because the sheet is at different HAB with Figure 8-12 lower down than Figure 8-11. The soot concentration is similar however there is as there is one lower as seen in Figure 8-13 because of the movement within the flame and it can be seen that the flame

front is slightly larger than Figure 8-14. When comparing with single shot image in Figure 8-3 it can be seen that there is effects of suppression by averaging of the images. One advantage of using imaging allows for the validation of the average image.

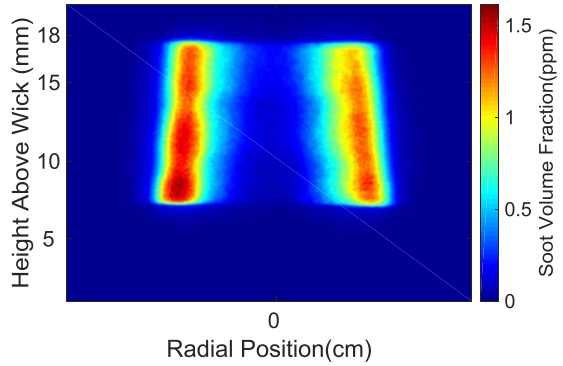

Figure 8-11: Anisole image soot volume fraction averaged over 50 images

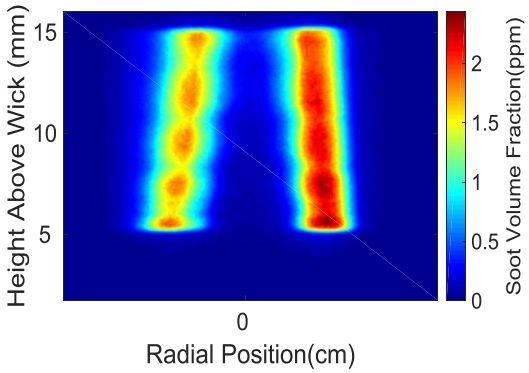

Figure 8-12: Repeated Anisole averaged soot volume fraction Image

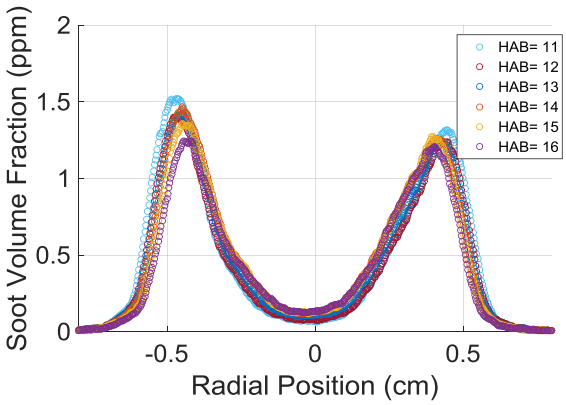

Figure 8-13: Average radial profile of Anisole soot volume fraction at different HABs

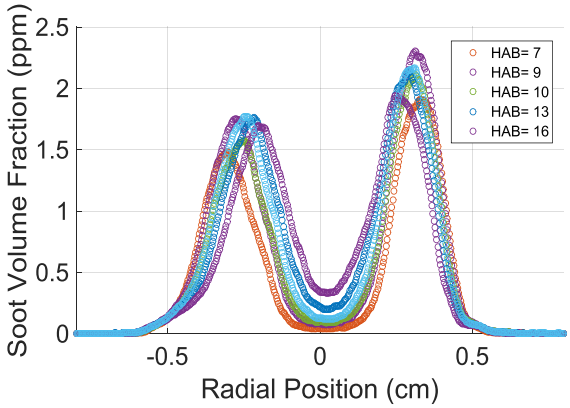

Figure 8-14: Radial profile of repeated Anisole soot volume fraction at different HABs

Furfural

Figure 8-15 and Figure 8-16 show two different images for Furfural. Like the previous shown images the soot volume fractions are similar but with the radial profiles slightly different because of flame movements. This shows that the soot volume fraction is relatively reproducible however the averaging supresses the overall soot volume fraction. Figure 8-17 and Figure 8-18 show two different radial profiles measured from the biofuel image. Again when comparing with the single shot images show the suppression by averaging.

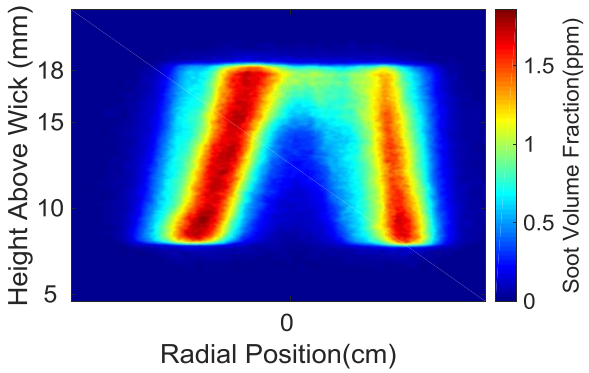

Figure 8-15: Furfural soot volume fraction averaged over 50 images

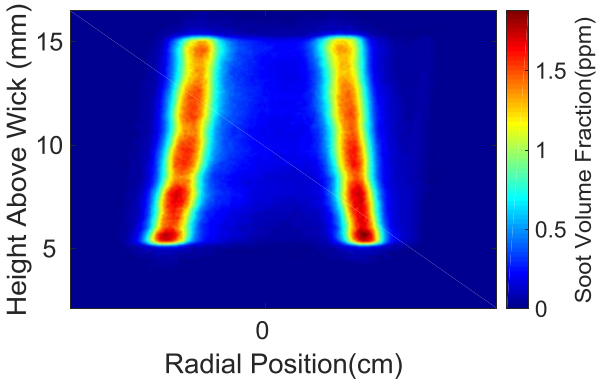

Figure 8-16: Repeated Furfural soot volume Fraction averaged over 50 images

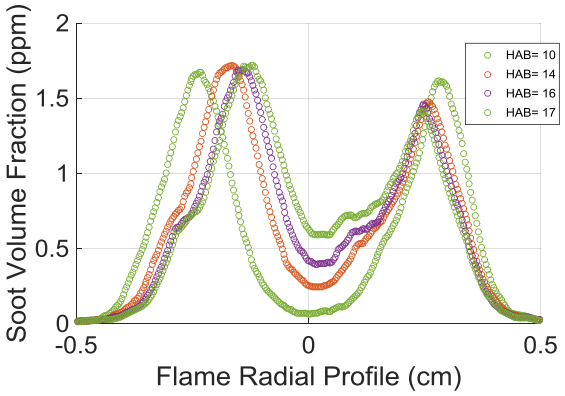

Figure 8-17: Average radial profile for Furfural soot volume fraction at different HABs over 50 images

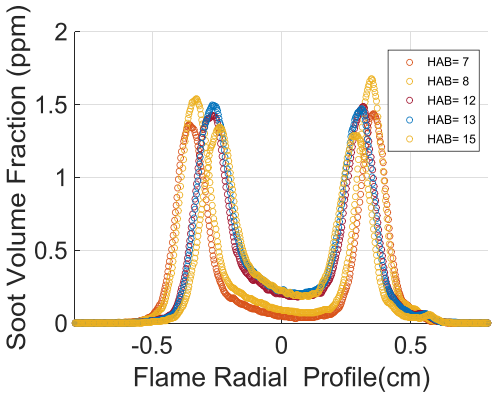

Figure 8-18: Repeated average radial profile for Furfural soot volume fraction at different HABs over 50 images

n-decane

Figure 8-19 and Figure 8-20 show two different average images for n-Decane. Both images show similar profiles and soot volume fraction. Figure 8-21 and Figure 8-22 show the corresponding radial profiles. Again they are similar to the single shot profiles except the flame front loses resolution by the effects of suppression by averaging. Unlike the other biofuels n-Decane seems to show a larger soot volume fraction higher up in the flame unlike the uniform profile with height shown by the other biofuels.

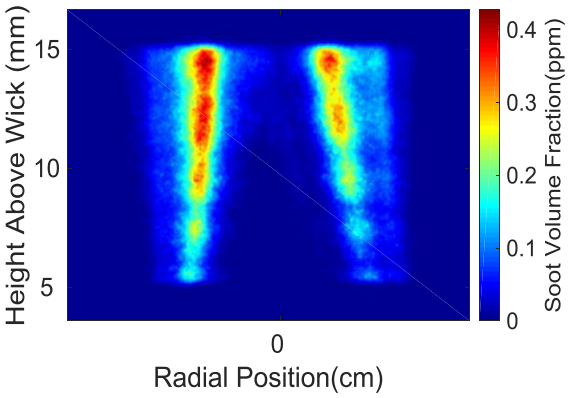

Figure 8-19: n-Decane soot volume fraction averaged of 50 images

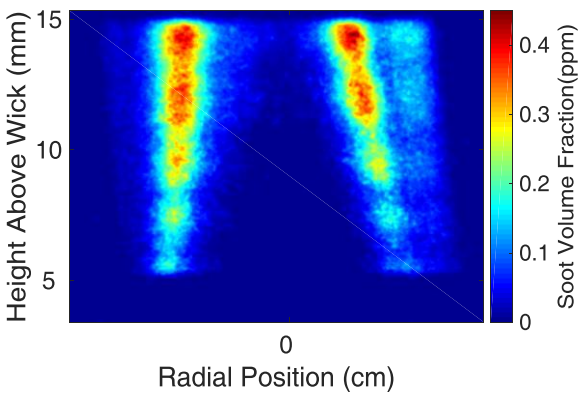

Figure 8-20: Repeated n-Decane soot volume fraction averaged over 50 images

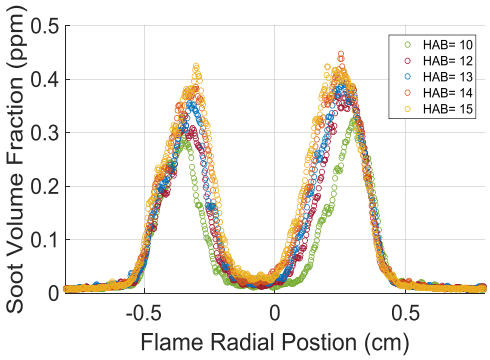

Figure 8-21: Average Radial Profile of Soot volume fraction of n-Decane at different HABs over 50 images

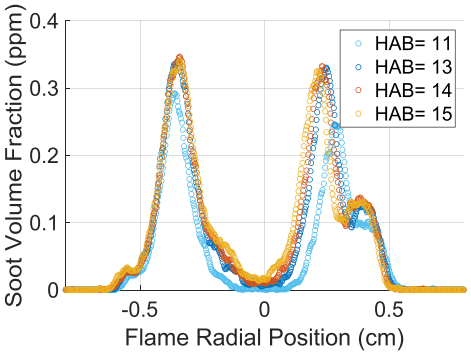

Figure 8-22:Radial Profile of Repeated n-Decane Soot Volume Fraction in ppm at different HABs over 50 images

Eugenol

Figure 8-23 shows the averaged image for Eugenol with a corresponding radial profile image in Figure 8-24. It can be seen that like single shot images the overall profile is unreliable. The soot volume fraction is also underestimated probably because of this fluctuations and movements within the flame.

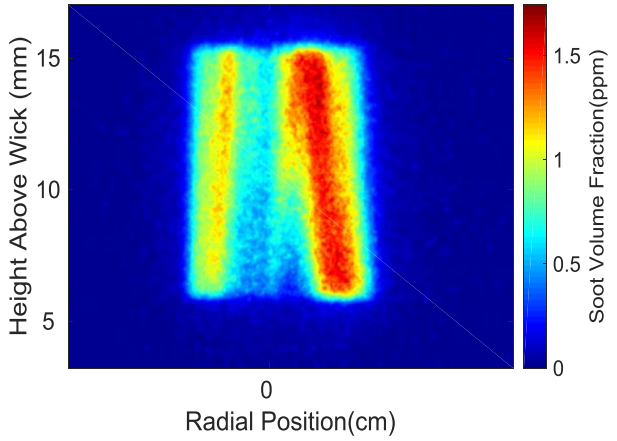

Figure 8-23: Eugenol Soot Volume Fraction Averaged over 50 images

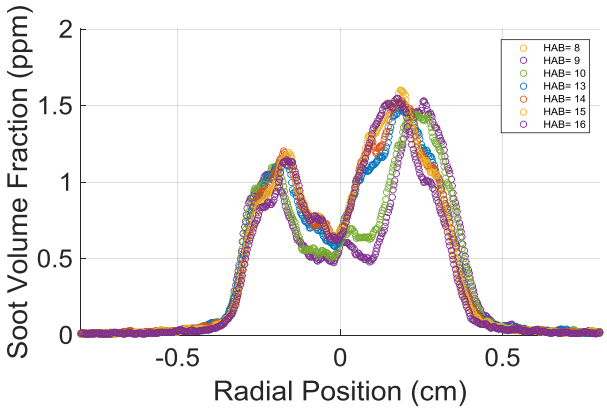

Figure 8-24:Radial Profile for Eugenol soot volume fraction at different HABs over 50 images

8.3.3 Biofuel soot volume fraction discussion

Imaging results show that anisole has the highest soot volume fraction followed by eugenol, furfural and n-decane which has a considerably lower soot volume fraction. The difference in the soot volume fraction from Eugenol and Furfural has been put down to the aromatic nature and concentration of soot particles. [150] By looking at the flames it is possible to see that eugenol should be the most sooting since it produces a large amount of black and gain one of the problems however with eugenol has more flickering and movement of the flame more so than the other flames possibly because of the soot deposition onto the wick because of this it is expected that eugenol should have a larger soot volume fraction. The high soot volume fraction produced an audible photoacoustic signal consistent with the soot volume fraction.

Figure 8-25 to Figure 8-28 show the groups LII using point measurements measured as stated in Atiku et al.[149] Point measurements were measured using the PMT and the burner was on a translation stage and moved to measure at each radial position. The results by the point measurements are taken at an

excitation wavelength of 1064 nm and using a beam of 1 mm diameter with a top-hat profile. These measurements were taken at 10 mm above the wick at different radial positions. They were averaged on the oscilloscope of 64 averages.

Overall results show some similarities to the camera measurements when comparing soot concentrations however the point measurements show an underestimation of the soot volume fraction as expected due to suppression by averaging and the probability of movement within the flame. Camera results show that n-decane has a peak soot volume fraction of around 3 times lower than the other flames which is also consistent with the point measurement results.[149] PMT results show different radial profiles and this is because of the effects of averaging as well as the limitations of the experiments where the flame has to be moved and the radial profile is measured at different times. Radial profiles between the point and camera measurements are quite different probably due to the PMT results not being able to gather the radial profile simultaneously and therefore when the translation stage is moved with the burner on it to move the flame into the correct measurement position; it may affect the stability of the flame.

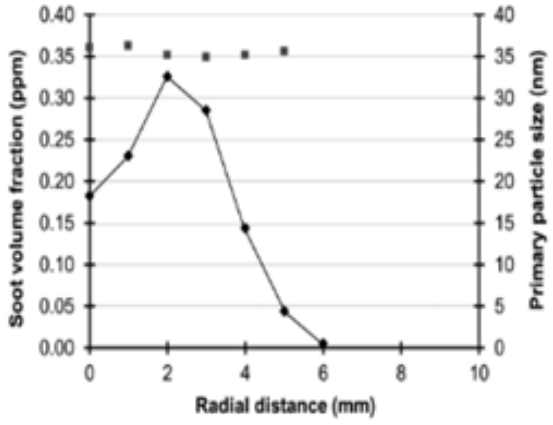

Figure 8-25: Point measurements of n-decane soot volume fraction(diamonds) and particle sizes (squares) [149]

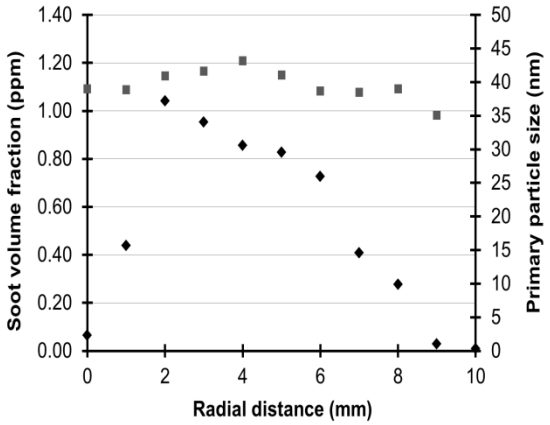

Figure 8-26: : Point measurements of anisole soot volume fraction(diamonds) and particle sizes (squares) [149]

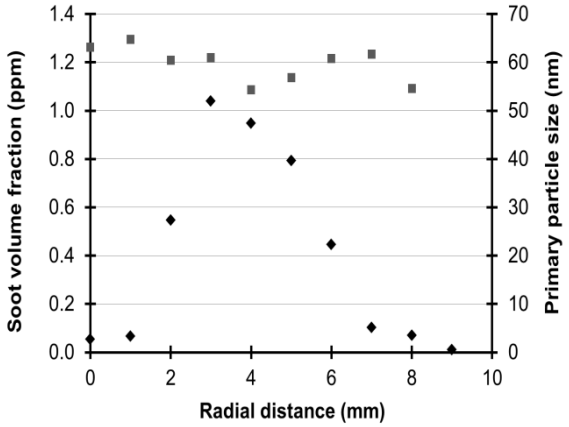

Figure 8-27: : Point measurements of furfural soot volume fraction(diamonds) and particle sizes (squares)[149]

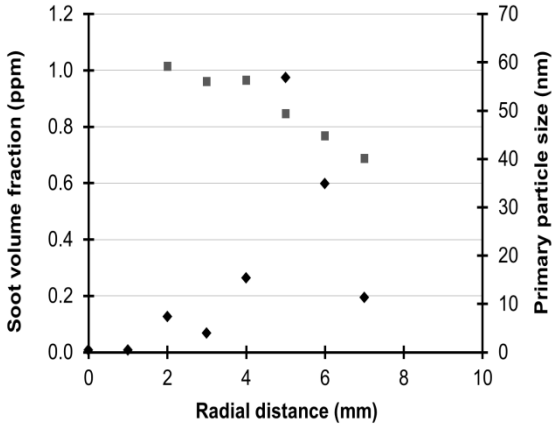

Figure 8-28: : Point measurements of eugenol soot volume fraction(diamonds) and particle sizes (squares) [149]

8.4 Temporal profiles of the biofuels

Temporally resolved imaging results were taken using 1064 nm excitation wavelength. These were acquired by recording image sets sequentially at a range of intensifier gate timings. They are an average of 50 images using the same methodology discussed in the methodology chapter. Since the flame front area is smaller the smaller 1 mm slit is used and the fluence 210 mJ/cm^2. The maximum signal for each height was found for each biofuel and recorded to give the time resolved profiles. The decay times are found the same way decay times are typically found for LII signal with an exponential decay fit after 120 ns when the soot particle is in the conduction regime. Figure 8-29 to Figure 8-32 show these temporal profiles measured by the camera and Table 3-1 shows the decay times associated with the graphs.

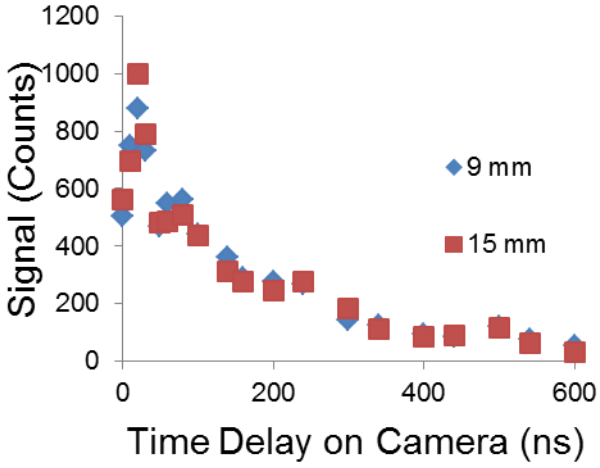

Figure 8-29: Time resolved of averaged anisole

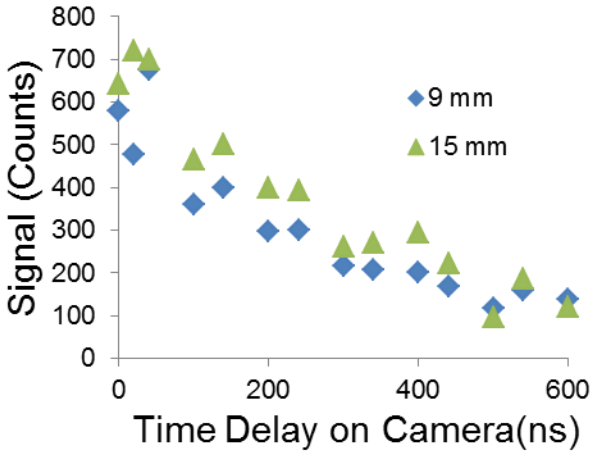

Figure 8-30: Time resolved profile of eugenol

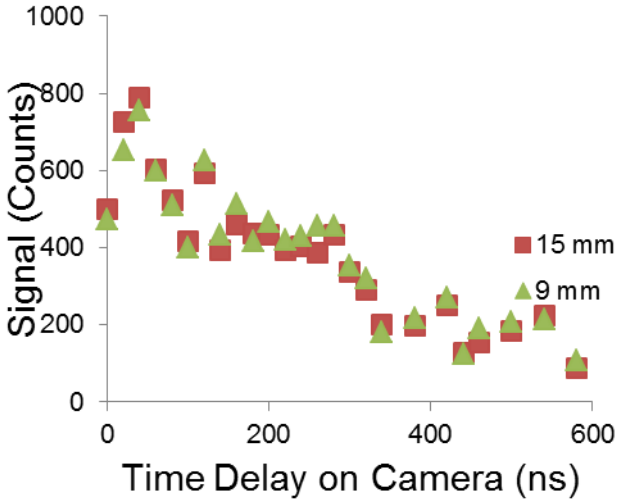

Figure 8-31: Time resolved profile of furfural

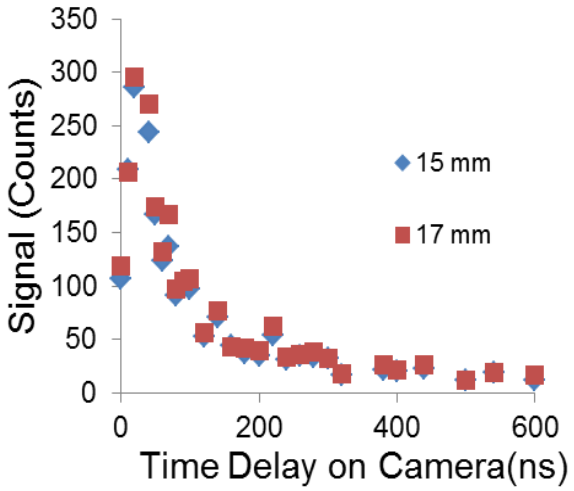

Figure 8-32: Time resolved profiles of n-decane

Table 8-2: Table of fuel decay times at HABs of 9 and 15 mm

Fuel	HAB (mm)	Decay Time (ns)
Anisole	9	256
	15	222
Eugenol	9	323
	15	312
Furfural	9	304
	15	322
n-Decane	15	232
	17	294

8.4.1 Overall temporal profiles discussion

Table 8-3 shows the decay time comparison between the PMT and the camera decay time results.

Table 8-3: Decay Time Comparisons between camera results at HAB of 9 mm and PMT measurements

Fuel	Camera decay time (ns)	PMT decay time (ns)
Anisole	256	477
Eugenol	323	812
Furfural	304	952
n-Decane	232	337

The produced particle sizes can be seen in Table 8-4. The particle sizes were calculated by taking into account of the porous plug decay times of 105 ns where the particle size is assumed to be 25 nm. Modelling the decay time shows this is a reasonable particle size to use when comparing with the porous plug burner decay time however this is just an estimate because it does rely on multiple assumptions used stated in the modelling chapter. Since the particle size related to surface area the particle size can be assumed through extrapolation assuming a square law. The 25 ns are multiplied by the square root of the camera biofuel decay time divided by the porous plug burner 105 ns decay time. This was done as this was the way the particle size was described in Atiku et al.[149]

The decay time results could be improved by more selective image gathering removing outliers caused by movement of the flame. The decay time results reliability also could be improved by using a fit of the time resolved profile reducing the influence of any outliers. The results may also be influenced by aggregation within the flame which can drastically change the properties of the particle sizing if there are large aggregates formed. Bladh et al.[152] showed that neglecting to consider for aggregation with identical decay rates in modelling but not in experimental results as well as the model being able to replicate the trends from LII experiments but with large differences in the signal decay rate in every case studied.

These results are also only for the maximum signal for each set of images read into the code, the results could be improved by having the code read and produce a time resolved profile at each radial distance from the centre.

Table 8-4: Particle size from the camera compared to the PMT particle size. The particle sizes have been calculated through the calibration of a 'known' reference particle size and its decay time and extrapolating.

Fuel	Camera modelled particle size (nm)	PMT particle size (nm)
Anisole	39	41
Eugenol	44	56
Furfural	42	65
n-Decane	36	36

The particle sizes are reasonable; they are larger as expected than particles produced in the premixed porous plug burner which is as expected since larger soot volume fraction etc. They are also reasonable compared to literature sizes however the PMT sizes for Eugenol and Furfural are quite a bit larger than the camera sizing measurements.

From the time resolved profiles of Eugenol and Furfural in Figure 8-30 and Figure 8-31, it can be seen that the temporal profiles differ from the other fuels. It seems like they don't reach the same temperature since the position of the peak signal occurred at different points to anisole and n-decane. It was thought that it might be because of larger particle sizes however as shown in the earlier modelling chapter that this isn't the case therefore it could be due to different physical properties of the soot produced by the fuels such as absorption coefficient, density and thermal conductivity. This gives scope to investigate the morphological properties of the soot produced. Dastanpour et al.[153] showed the variation of optical properties of soot of particle mass using a variety of measurements that show that light absorption and scattering properties do change with mass. Stated is that the soot aggregate size is correlated with primary particle size and could affect the properties of soot.[153] Figure 8-1 does show that the soot of these flames is produced by different pathways and this may affect the soot properties therefore this does give the hypothesis some credibility.

8.5 LIF from LII subtraction

Further investigations into the measurements of PAH in these types of fuels would be interesting because Wilson et al.[150] states the concentration of soot particles and the aromatic species is a large difference between the final soot product from furfural and eugenol. Furfural tends to follow the HACA route because of initial decomposition to suitable species that can follow this path while eugenol undergoes side-chain cracking, followed by conventional phenol decomposition reactions, and also decomposition and reaction via cyclopentadiene.[150] Unlike Schoemaecker et al.[68] and Bouvier et al.[154] who were able to show the position of the PAH fluorescence in a co-flow non-premixed ethylene flame and show a superimposed image of fluorescence and incandescence within the flame because the flame is stable, it proved to be an issue using the biofuel burner because the flame moves around which then makes the position of PAH signal to be uncertain.

The main problems with trying to infer LIF is how precise the images have to overlap. The wick burner has to be placed in the same position as well as the laser sheet and fluence. The wick has to be moved and cleaned within runs and this makes the prospect of moving to the exact same position difficult. There would have changes to the experimental setup for this to work such as shielding for the burner to make the flame more stable as well as way of ensuring the sheet is positioned precisely in the same position between the two different wavelengths with respect with the burner too.

8.6 Conclusions and future work using biofuel burner

Results using LII imaging methods showed the advantage of using imaging in these types of flames when compared to other detection methods such as point measurements. The results gave an insight into soot formation for different fuels within the burner. Presented results showed that a way of overcoming problems often associated with point measurements of these flames. With point measurements movements within the flame cannot be discriminated against, therefore this leads to a larger uncertainty in the soot volume fraction. Time resolved profiles are promising and show a decay which was expected for an LII curve. For time resolved profiles, fitting a smoother curve to the data could lead to a reduction in error of the decay times and thus particle sizes. They show similar trend in particle sizes when compared to point measurements. The best method for combined particle sizing and soot concentration measurements could be to use the PMT and camera at the same time to image the same point in the image. This may allow for the flame movement to be tracked but could also validate the precision of the LII signal.

More investigations into the combustion of these fuels could be improved if the burner was more stable therefore there could be maybe some changes made to the burner to ensure this. This would help the investigations using different excitation wavelengths and measure the fluorescence. Other investigations could be done using UV excitation wavelength revealing more about the type of fluorescing particles produced in this type of flame. Another reason why imaging is a better source of detection is the ability to see where fluorescence.

Measurements could also be used in conjunction with probe technique studies of the soot within the flame. This would be interesting to compare with the morphology and the type of soot produced from the flat flame burner which was used for extinction. This could give us more detail into the modelling of the soot for things such as soot polydispersity and aggregation of the soot particles. The LII of the fuels can be seen by eye at points. This could allow for another measurement device such as a regular CCD camera to be used to gather more information on the flame such as radical emission.[146]

With imaging poor images can may be removed as outliers as well as giving a spatial profile of the soot volume fraction. Further work could be done to the data to improve the quality of the results such as spatial compensation of single shot images.

9 Overall thesis summary, outlook and references

9.1 Conclusions

The work presented here is aimed firstly to assess the method of Laser Induced Incandescence and imaging in a flat flame burner. Results showed detailed comparisons to accurately characterise the flat flame burner. Centre line HAB profiles and radial profiles show agreement when comparing with beam and point measurements.

The LII images generated validate the methodology for different applications. Similar methodologies in literature show results with comparable soot volume fractions. The technique was then adapted and by using the subtraction of signal from 2 different wavelengths was used to infer fluorescence from PAHs in the premixed flat flame burner. This work has shown the ability to use the different excitation wavelengths of 1064 and 532 nm to obtain imaging information about fluorescing PAHs in a flat flame burner.

Interesting work presented was the changing of the flame temperature using the stabilisation plate to show no change of soot volume fraction at relatively high heights above the burner. The temperature was measured between two different sized burners to show the same soot concentration at the same equivalence ratios. These results help stop the risk of having redundant data due to different stabilisation plate setups as well as different measurements of operating times.

The use of a produced LII heat transfer model is shown to produce results very similar to other researchers such as Hoffman et al.[41] and with some additional components such as oxidation and gated signals show results that follow the expected trends. Modelling is a big area of interest within the LII community and efforts have been made to ensure collaboration between groups and their modelling results.

A different standard excitation source was used in the form of a long-pulsed fibre laser. The results show the applicability and uncertainty in measuring the soot volume fraction using the long-pulsed fibre laser. Centre line HAB profiles show agreement with 2 different measuring techniques. It was shown that point measurements in the centre of the flame agreed with the camera measurement, and with fluence correction across the beam in the flame, a radial profile could be produced. Modelling long-pulsed laser incandescence shows promising results shows differences expected with different fluences. Differences between a standard model and the long-pulse model include the spectral dependence and laser temporal and spatial profiles.

Using the imaging technique developed it was possible to measure the soot concentration in biofuels measured in a biofuel wick diffusion burner. Using imaging can help overcome some of the difficulties

associated with using point measurements in this type of flame such as the flame instability and simultaneous measurement of the flame structure with the soot volume fraction. Time resolved measurements show some similar trends to point measurement results, and that the standard hydrocarbon fuel ,n-decane has a lower primary particle size compared to the biofuels.

9.2 Future work

This work has showed the possibility to use different excitation wavelengths of 1064 and 532 nm to obtain imaging information about fluorescing PAHs. This could be used to develop further information such as changing the detection wavelength, by using a 283 nm wavelength or using a spectrometer to identify the different species. This method developed may also be applied to further combustion studies with reference to exhaust emissions. Using this method in the biofuel wick burner was showed to be a problem because of the type of flame and movement of the flame. Future work could be finding a way to burn the biofuels used in a more stable environment to help the flame from flickering. Another point to look into is the type of soot produced in this type of flame either through probe methods or another optical method. Since the soot concentration is calculated from a calibration in a flat flame burner it would be interesting to see how similar the mature soot in the flat flame burner matches the soot produced in the wick diffusion flame. By knowing this it could help improve modelling results and give a more precise primary particle size estimate.

Further work could be done to investigate using long-pulsed laser for LII, as previously shown to be a method for producing a calibrated soot volume fraction measurement however more work could lead to better modelling and further investigation could test a way to find a better signal to noise ratio. For future references long-pulsed laser could be used and tested in larger combustion rigs. This is because for example in larger test rigs there could be a larger effect of beam steering.

For the biofuel experiments it would be interesting if there was a way to ensure more stability in the flames either by manipulating the burner or limiting the amount of air gradients during measurement this could allow for better LII subtraction experiments.

9.3 References

1. Agency for Natural Resources and Energy. *Key World Energy statistics*. *IEA International Energy Agency* (2017). doi:10.1017/CBO9781107415324.004

2. U.S. Energy Information Amministration. *EIA International Enegry Outlook 2017*. (2017). doi:www.eia.gov/forecasts/ieo/pdf/0484(2016).pdf

3. BP Energy Economics. 2018 BP Energy Outlook 2018 BP Energy Outlook. 125 (2018).

4. LSE & Npower, R. *Energy and the Economy: The 2030 Outlook for UK Businesses. A Report Commissioned by RWE npower*. (2012).

5. *Updated Energy and Emissions Projections 2017*. (2018).

6. Institute, P. S. *World Energy Scenarios: Composing energy futures to 2050*. *World Energy Scenarios: Composing energy futures to 2050* **32**, (2006).

7. AQEG. *Particulate Matter in the UK: Summary*. *Environmental Health* **4**, (2005).

8. Medina, S. *Summary report of the Aphekom project 2008-2011*. (2012).

9. Highwood, E. J. & Kinnersley, R. P. When smoke gets in our eyes: The multiple impacts of atmospheric black carbon on climate, air quality and health. *Environ. Int.* **32**, 560–566 (2006).

10. Air Quality Expert Group. *Fine Particulate Matter in the United Kingdom*. *http://uk-air.defra.gov.uk/assets/documents/reports/cat11/1212141150_AQEG_Fine_Particulate_Matter_in_the_UK.pdf* (2012).

11. A.C.Eckbreth. *Laser Diagnostics For Combustion Temperature and Species*. (Abacus Press, 1988).

12. Johansson, O. Cracking the code to soot formation — scientists unlock mystery to help reduce hazardous emissions. *Phys.org* 1–4 (2018).

13. Kohse-Höinghaus, K. & Jeffries, J. . *Applied Combustion Diagnostics*. (Taylor and Francis, 2002).

14. Mansurov, Z. A. Soot Formation in Combustion Processes (Review). **41**, 727–744 (2005).

15. Campbell, M. F. *et al.* A small porous-plug burner for studies of combustion chemistry and soot formation. *Rev. Sci. Instrum.* **88**, (2017).

16. J.Warnatz, U.Maas, R. W. D., Warnatz, J., Mass, U. & Dibble, R. W. *Combustion: Physical and*

Chemical Fundamentals, Modelling and Simulation, Experiments, Pollutant Formation. *Springer* (Springer, 2006).

17. Michelsen, H. A. Probing soot formation , chemical and physical evolution , and oxidation : A review of in situ diagnostic techniques and needs. *Proc. Combust. Inst.* **000**, 1–19 (2016).

18. Desgroux, P., Mercier, X. & Thomson, K. A. Study of the formation of soot and its precursors in flames using optical diagnostics. *Proc. Combust. Inst.* **34**, 1713–1738 (2013).

19. Cain, J., Laskin, A., Kholghy, M. R., Thomson, M. J. & Wang, H. Molecular characterization of organic content of soot along the centerline of a coflow diffusion flame. *Phys. Chem. Chem. Phys.* **16**, 25862–25875 (2014).

20. Russo, C., Tregrossi, A. & Ciajolo, A. Dehydrogenation and growth of soot in premixed flames. *Proc. Combust. Inst.* **35**, 1803–1809 (2015).

21. Frenklach, M. Reaction mechanism of soot formation in flames. *Phys. Chem. Chem. Phys.* **4**, 2028–2037 (2002).

22. Indarto, A., Giordana, A., Ghigo, G., Maranzana, A. & Tonachini, G. Polycyclic aromatic hydrocarbon formation mechanism in the "particle phase". A theoretical study. *Phys. Chem. Chem. Phys.* **12**, 9429–9440 (2010).

23. Davis, S. G., Joshi, A. V., Wang, H. & Egolfopoulos, F. An optimized kinetic model of H_2/CO combustion. *Proc. Combust. Inst.* **30**, 1283–1291 (2005).

24. Bladh, H. *et al.* Probing the smallest soot particles in low-sooting premixed flames using laser-induced incandescence. *Proc. Combust. Inst.* **35**, 1843–1850 (2015).

25. Betrancourt, C. *et al.* Investigation of the size of the incandescent incipient soot particles in premixed sooting and nucleation flames of n-butane using LII, HIM, and 1 nm-SMPS. *Aerosol Sci. Technol.* **51**, 916–935 (2017).

26. Maricq, M. M. Examining the relationship between black carbon and soot in flames and engine exhaust. *Aerosol Sci. Technol.* **48**, 620–629 (2014).

27. Vander Wal, R. L. A TEM Methodology for the Study of Soot Particle Structure. *Combust. Sci. Technol.* **126**, 333–351 (1997).

28. Vander Wal, R. L. Soot precursor carbonization: Visualization using LIF and LII and comparison using bright and dark field TEM. *Combust. Flame* **112**, 607–616 (1998).

29. Wang, S. C. & Flagan, R. C. Scanning electrical mobility spectrometer. *Aerosol Sci. Technol.*

13, 230–240 (1990).

30. Krüger, V. *et al.* Comparison of laser-induced incandescence method with scanning mobility particle sizer technique: the influence of probe sampling and laser heating on soot particle size distribution. *Meas. Sci. Technol.* **16**, 1477–1486 (2005).

31. Hwang, S. M. *et al.* Application of optical diagnostics techniques to a laboratory-scale turbulent pulverized coal flame. *Energy and Fuels* **19**, 382–392 (2005).

32. J. Reimann, S.A. Kuhlmann, S. W. 2D aggregate sizing by combining laser-induced incandescence (LII) and elastic light scattering (ELS). *Appl. Phys. B* **96**, 538–592 (2009).

33. Lee, K., Han, Y., Lee, W., Chung, J. & Lee, C. Quantitative measurements of soot particles in a laminar diffusion flame using a LII/LIS technique. *Meas. Sci. Technol.* **16**, 519–528 (2005).

34. Taylor, P., Sorensen, C. M. & Sorensen, C. M. *Light Scattering by Fractal Aggregates : A Review Light Scattering by Fractal Aggregates : A Review*. **6826**, (2010).

35. Quay, B., Lee, T., Ni, T. & Santoro, R. J. Spatially Resolved Measurements of Soot Volume Fraction Using Laser-Induced Incandescence. **392**, 384–392 (1994).

36. Atkins, P. & Paula, J. de. *Atkins' Physical Chemistry*. (2006).

37. Humphries, G. S. *et al.* A simple photoacoustic method for the in situ study of soot distribution in flames. *Appl. Phys. B* **119**, 709–715 (2015).

38. Mansmann, R. *et al.* LIISim: a modular signal processing toolbox for laser-induced incandescence measurements. *Appl. Phys. B Lasers Opt.* **124**, 1–20 (2018).

39. Hofmann, M., Bessler, W. G., Schulz, C. & Jander, H. Laser-induced incandescence for soot diagnostics at high pressures. (2003).

40. Michelsen, H. A., Schulz, C., Smallwood, G. J. & Will, S. Laser-induced incandescence: Particulate diagnostics for combustion, atmospheric, and industrial applications. *Prog. Energy Combust. Sci.* **51**, 2–48 (2015).

41. Hofmann, M., Kock, B. F. & Schulz, C. A web-based interface for modeling laser-induced incandescence (LIISim). *CEUR Workshop Proc.* **211**, 26 (2007).

42. Schraml, S., Dankers, S., Bader, K., Will, S. & Leipertz, A. Soot Temperature Measurements and Implications for Time-Resolved Laser-Induced Incandescence (TIRE-LII). *Combust. Flame* **2180**, 439–450 (2000).

43. Michelsen, H. a. *et al.* Modeling laser-induced incandescence of soot: a summary and comparison of LII models. *Appl. Phys. B* **87**, 503–521 (2007).

44. Roy, R. G. Modelling Laser Induced Incandescence. (University of Strathclyde, 2014).

45. Goulay, F., Schrader, P. E., Nemes, L., Dansson, M. & Michelsen, H. Photochemical interferences for laser-induced incandescence of flame-generated soot. *Proc. Combust. Inst.* **32**, 963–970 (2009).

46. Vander Wal, R. L. Laser-induced incandescence: detection issues. *Appl. Opt.* **35**, 6548–6559 (1996).

47. Wal, R. L. Vander, Ticich, T. M. & Stephens, a. B. Can soot primary particle size be determined using laser-induced incandescence? *Combust. Flame* **2180**, 0–5 (1999).

48. Liu, F., Daun, K. J. J., Snelling, D. R. R. & Smallwood, G. J. J. Heat conduction from a spherical nano-particle: status of modeling heat conduction in laser-induced incandescence. *Appl. Phys. B* **83**, 355–382 (2006).

49. Maffi, S., De Iuliis, S., Cignoli, F. & Zizak, G. Investigation on thermal accommodation coefficient and soot absorption function with two-color Tire-LII technique in rich premixed flames. *Appl. Phys. B Lasers Opt.* **104**, 357–366 (2011).

50. Axelsson, B., Collin, R. & Bengtsson, P. E. Laser-induced incandescence for soot particle size measurements in premixed flat flames. *Appl. Opt.* **39**, 3683–3690 (2000).

51. Schulz, C. *et al.* Laser-induced incandescence: recent trends and current questions. *Appl. Phys. B* **83**, 333–354 (2006).

52. Krishnan, S. S., Lin, K.-C. & Faeth, G. M. Extinction and Scattering Properties of Soot Emitted From Buoyant Turbulent Diffusion Flames. *J. Heat Transfer* **123**, 331 (2001).

53. Bengtsson, P.-E. & Therssen, E. Determination of key parameters for LII. in *8th Int. Workshop on LII* (2018).

54. López-Yglesias, X., Schrader, P. E. & Michelsen, H. Soot maturity and absorption cross sections. *J. Aerosol Sci.* **75**, 43–64 (2014).

55. Michelsen, H. A., Witze, P. O., Kayes, D. & Hochgreb, S. Time-resolved laser-induced incandescence of soot: the influence of experimental factors and microphysical mechanisms. *Appl. Opt.* **42**, 5577 (2003).

56. Bladh, H. & Bengtsson, P.-E. Characteristics of laser-induced incandescence from soot in

studies of a time-dependent heat- and mass-transfer model. *Appl. Phys. B Lasers Opt.* **78**, 241–248 (2004).

57. Zerbs, J. *et al.* The influence of wavelength in extinction measurements and beam steering in laser-induced incandescence measurements in sooting flames. *Appl. Phys. B* **96**, 683–694 (2009).

58. Axelsson, B., Collin, R. & Bengtsson, P. E. Laser-induced incandescence for soot particle size and volume fraction measurements using on-line extinction calibration. **372**, 367–372 (2001).

59. Hadef, R., Geigle, K. P., Meier, W. & Aigner, M. Soot characterization with laser-induced incandescence applied to a laminar premixed ethylene–air flame. *Int. J. Therm. Sci.* **49**, 1457–1467 (2010).

60. Wal, R. L. Vander & Weiland, K. J. Laser Induced Incandescence: Development and Characterization towards a measurement of soot volume fraction. **452**, 445–452 (1994).

61. Cignoli, F., De Iuliis, S., Manta, V. & Zizak, G. Two-dimensional two-wavelength emission technique for soot diagnostics. *Appl. Opt.* **40**, 5370 (2001).

62. De Iuliis, S., Migliorini, F., Cignoli, F. & Zizak, G. 2D soot volume fraction imaging in an ethylene diffusion flame by two-color laser-induced incandescence (2C-LII) technique and comparison with results from other optical diagnostics. *Proc. Combust. Inst.* **31**, 869 (2007).

63. Bladh, H., Johnsson, J., Olofsson, N.-E., Bohlin, a. & Bengtsson, P.-E. Optical soot characterization using two-color laser-induced incandescence (2C-LII) in the soot growth region of a premixed flat flame. *Proc. Combust. Inst.* **33**, 641–648 (2011).

64. de Risi, A., Naccarato, F. & Potenza, M. Two-dimensional measurements of primary soot diameter in diffusion flames by two-dimensional time resolved laser induced incandescence. *IET Sci. Meas. Technol.* **8**, 107–115 (2014).

65. Iuliis, S. De, Cignoli, F. & Zizak, G. Two-color laser-induced incandescence (2C-LII) technique for absolute soot volume fraction measurements in flame. **i**, (2005).

66. Stanford Computer Optics, I. The optical performance of an ultra high speed ICCD camera. (2013). Available at: http://www.stanfordcomputeroptics.com/technology/optical-resolution.html. (Accessed: 19th February 2015)

67. LaVision. NanoStar Camera Manual. in *Product-Manual for DaVis 8.1* (2012).

68. Moreau, C. S., Therssen, E., Mercier, X., Pauwels, J. F. & Desgroux, P. Two-color laser-induced

incandescence and cavity ring-down spectroscopy for sensitive and quantitative imaging of soot and PAHs in flames. *Appl. Phys. B Lasers Opt.* **78**, 485–492 (2004).

69. Bladh, H. *et al.* Experimental and theoretical comparison of spatially resolved laser-induced incandescence signals in a sooting flame. in *Combustion, European Published, Meeting Meeting, European Combustion* (2016).

70. Sun, Z. W. W., Gu, D. H. H., Nathan, G. J. J., Alwahabi, Z. T. T. & Dally, B. B. B. Single-shot, time-resolved planar laser-induced incandescence (TiRe-LII) for soot primary particle sizing in flames. *Proc. Combust. Inst.* **35**, 3673–3680 (2015).

71. Tian, B., Zhang, C., Gao, Y. & Hochgreb, S. Planar 2-color time-resolved laser-induced incandescence measurements of soot in a diffusion flame. *Aerosol Sci. Technol.* **51**, 1345–1353 (2017).

72. Dunn, J. Investigation of Premixed Sooting Flames by Combined Laser Induced Incandescence and Laser Induced Fluorescence. (University of Strathclyde, 2014).

73. Daily, J. W. Laser induced fluorescence spectroscopy in flames. *Prog. Energy Combust. Sci.* **23**, 133–199 (1997).

74. Jonsson, M., Ehn, A., Christensen, M., Aldén, M. & Bood, J. Simultaneous one-dimensional fluorescence lifetime measurements of OH and CO in premixed flames. *Appl. Phys. B Lasers Opt.* **115**, 35–43 (2014).

75. Grisch, F. & Orain, M. Role of Planar Laser-Induced Fluorescence in Combustion Research. *AersospaceLab* 1–14 (2009).

76. Vander Wal, R. L. Investigation of soot precursor carbonization using laser-induced fluorescence and laser-induced incandescence. *Combust. Flame* **110**, 281–284 (1997).

77. Smyth, K. C., Shaddix, C. R. & Everest, D. A. Aspects of soot dynamics as revealed by measurements of broadband fluorescence and flame luminosity in flickering diffusion flames. *Combust. Flame* **111**, 185–207 (1997).

78. Shaddix, C. R., Wang, H., Oefelein, J. C. & Pickett, L. M. *Predicting the Effects of Fuel Composition and Flame Structure on Soot Generation in Turbulent Non-Premixed Flames*. (2011).

79. Meyer, T. R., Roy, S., Belovich, V. M., Corporan, E. & Gord, J. R. Simultaneous planar laser-induced incandescence, OH planar laser-induced fluorescence, and droplet Mie scattering in swirl-stabilized spray flames. *Appl. Opt.* **44**, 445–454 (2005).

80. Oh, C. & Sorensen, C. M. Light scattering study of fractal cluster aggregation near the free molecular regime. *J. Aerosol Sci.* **28**, 937–957 (1997).

81. Bladh, H. On the Use of Laser-Induced Incandescence for Soot Diagnostics: From Theoretical Aspects to Applications in Engines. (University of Lund, 2007).

82. Smallwood, G; Snelling, D; Liu, F; Gulder, O. L. Clouds over soot evaporation : errors in modeling laser-induced incandescence of soot. *J. Heat Transfer* **123,** 814–818 (2001).

83. Michelsen, H. a. Understanding and predicting the temporal response of laser-induced incandescence from carbonaceous particles. *J. Chem. Phys.* **118**, 7012 (2003).

84. Lehre, T., Suntz, R. & Bockhorn, H. Time-resolved two-color LII: size distributions of nano-particles from gas-to-particle synthesis. *Proc. Combust. Inst.* **30**, 2585–2593 (2005).

85. Michelsen, H. a. *et al.* Modeling laser-induced incandescence of soot: enthalpy changes during sublimation, conduction, and oxidation. *Appl. Phys. B* **93**, 645–656 (2008).

86. Strickland-Constable, R. F. Part played by surface oxides in the oxidation of carbon. *Trans. Faraday Soc.* **34**, 1074–1080 (1938).

87. Leipertz, A. & Dankers, S. Characterization of Nano-Particles Using Laser-Induced Incandescence. **20**, (2003).

88. Lisanti, J., Cenker, E. & Roberts, W. L. Comprehensive Laser-induced Incandescence (LII) modeling for soot particle sizing. *Proc. Eur. Combust. Meet.* 1–5 (2015).

89. Tran, M. K., Dunn-Rankin, D. & Pham, T. K. Characterizing sooting propensity in biofuel–diesel flames. *Combust. Flame* **159**, 2181–2191 (2012).

90. Clara, S. *Operation and Maintenance Manual for Surelite Lasers*. (2002).

91. Thorlabs. *PDF10x Operation Manual*. (2012).

92. Desgroux, P. & Black, J. D. Soot volume fraction measurements in aero- engine exhausts using extinction-calibrated backward laser-induced incandescence. *Appl. Phys. B* **4**, (2009).

93. Tsurikov, M. S. *et al.* Laser-based investigation of soot formation in laminar premixed flames at atmospheric and elevated pressures. *Combust. Sci. Technol.* **177**, 1835–1862 (2005).

94. Hebert, D., Coppalle, A. & Talbaut, M. 2D soot concentration and burning rate of a vertical PMMA slab using Laser-Induced Incandescence. *Proc. Combust. Inst.* **34**, 2575–2582 (2013).

95. Photonics, H. *Hamamatsu Photomultiplier Tube Datasheet*. (1994).

96. Mass, M. S. & Meters, F. *Precision Gas Flow Meter Operating Manual*.

97. Burns, I. ., Hult, J., Hartung, G. & Kaminski, C. . A thermometry technique based on atomic lineshapes using diode laser LIF in flames. *Proc. Combust. Inst.* **31**, 775–782 (2007).

98. Adelaide, U. of. Laminar Premixed Flames: Target Flames. *Internation Sooting Flame (ISF) workshop* **1**, 12–13

99. Hossiain, M. M. *et al.* Study on direct flame solid oxide fuel cell using flat burner and ethylene flame. *ECS Trans.* **68**, 1989–1999 (2015).

100. Solomon, Chris ; Breckon, T. *Fundamentals of Digital Image Processing: A Practical Approach with Examples In Matlab*. (Wiley Blackwell, 2011).

101. Attaway, S. *MATLAB: A Practical Introduction To Programming And Problem Solving*. (Butterworth-Heinemann, 2013).

102. Oijen, J. a. Van, de Goey, L. P. . & Roekaerts, D. *International Combustion Institute Winter School Lecture Notes*. **1**, (2016).

103. Frederickson, K., Kearney, S. P. & Grasser, T. W. Laser-induced incandescence measurements of soot in turbulent pool fires. *Appl. Opt.* **50**, A49-59 (2011).

104. Sommer, R. & Leipertz, A. Application of laser-induced incandescence to suspended carbon black particles. *Opt. Lett.* **32**, 1947 (2007).

105. Leipertz, A. & Sommer, R. Characterization of carbonaceous particles by time-resolved laser-induced incandescence. (2004).

106. Bejaoui, S., Lemaire, R., Desgroux, P. & Therssen, E. Experimental study of the E(m, λ)/E(m, 1064) ratio as a function of wavelength, fuel type, height above the burner and temperature. *Appl. Phys. B* **116**, 313–323 (2013).

107. Desgroux, P. *et al.* Soot volume fraction measurement in low-pressure methane flames by combining laser-induced incandescence and cavity ring-down spectroscopy: Effect of pressure on soot formation. *Combust. Flame* **155**, 289–301 (2008).

108. Olofsson, N.-E., Johnsson, J., Bladh, H. & Bengtsson, P.-E. Soot sublimation studies in a premixed flat flame using laser-induced incandescence (LII) and elastic light scattering (ELS). *Appl. Phys. B* **112**, 333–342 (2013).

109. Olofsson, N. Laser-Induced Incandescence and Complementary Diagnostics for Flame Soot Characterization. (Lund University, 2015).

110. Ni, T., Pinson, J. A., Gupta, S. & Santoro, R. J. Two-dimensional imaging of soot volume fraction by the use of laser-induced incandescence. **34**, 7083–7091 (1995).

111. Boufflers, D., Betrancourt, C., Bakali, A. El, Mercier, X. & Desgroux, P. Laser induced incandescence investigation of radial soot distribution in atmospheric premixed sooting flames. *Proc. Eur. Combust. Meet.* 1–5 (2015).

112. Liu, F., Thomson, K. a. & Smallwood, G. J. Numerical investigation of the effect of signal trapping on soot measurements using LII in laminar coflow diffusion flames. *Appl. Phys. B* **96**, 671–682 (2009).

113. Inal, F. & Senkan, S. M. Effects of equivalence ratio on species and soot concentrations in premixed n-heptane flames. *Combust. Flame* **131**, 16–28 (2002).

114. Tran, L. S., Glaude, P. A., Réactions, L. & Grandville, N. An experimental study of the structure of laminar premixed flames of ethanol / methane / oxygen / argon. **49**, 11–18 (2013).

115. Desgroux, P. *et al.* Comparative study of the soot formation process in a "nucleation" and a "sooting" low pressure premixed methane flame. *Combust. Flame* **184**, 153–166 (2017).

116. Stirn, R. *et al.* Comparison of particle size measurements with laser-induced incandescence, mass spectroscopy, and scanning mobility particle sizing in a laminar premixed ethylene-air flame. *Combust. Sci. Technol.* **181**, 329–349 (2009).

117. Hadef, R., Geigle, K. P., Zerbs, J., Sawchuk, R. a. & Snelling, D. R. The concept of 2D gated imaging for particle sizing in a laminar. *Appl. Phys. B* **112**, 395–408 (2013).

118. Migliorini, F., De Iuliis, S., Cignoli, F. & Zizak, G. How 'flat' is the rich premixed flame produced by your McKenna burner? *Combust. Flame* **153**, 384–393 (2008).

119. Cléon, G., Amodeo, T., Faccinetto, a. & Desgroux, P. Laser induced incandescence determination of the ratio of the soot absorption functions at 532 nm and 1064 nm in the nucleation zone of a low pressure premixed sooting flame. *Appl. Phys. B* **104**, 297–305 (2011).

120. Wartel, M., Pauwels, J. F., Desgroux, P. & Mercier, X. Quantitative measurement of naphthalene in low-pressure flames by Jet-Cooled Laser-Induced Fluorescence. *Appl. Phys. B Lasers Opt.* **100**, 933–943 (2010).

121. Manta, V., Cignoli, F., Iuliis, S. De & Zizak, G. 2-D Soot Diagnostic with a Two-Color Emission Technique. in *Open Meeting on Combustion, XXIII Event of the Italian Section of The Combustion Institute* **1**, 6–9 (2000).

122. H. Bohm, D. Hesse, H. Jander, B. L. & J. Pieter, H. GG. Wagner, M. W. The Influence of pressure and temperature on soot formation in premixed flames. in *Twenty-Second Symposium (International) on Combustion* 403–411 (1988).

123. Xuan, Y. & Blanquart, G. Two-dimensional flow effects on soot formation in laminar premixed flames. *Combust. Flame* **166**, 113–124 (2016).

124. Bockhorn, H., D'Anna, A., Sarofim, A. F. & Wang, H. *Combustion Generated Fine Carbonaceous Particles: Proceedings of an International Workshop held in Villa Orlandi, Anacapri, May*. (KIT Scientific Publishing, 2007).

125. Langenkamp, P. N., Van Oijen, J. A., Levinsky, H. B. & Mokhov, A. V. Growth of Soot Volume Fraction and Aggregate Size in 1D Premixed C2H4/Air Flames Studied by Laser-Induced Incandescence and Angle-Dependent Light Scattering. *J. Combust.* **2018**, (2018).

126. Kee, R., Coltrin, M. & Glasborg, P. *Chemically reacting flow: theory and practice*. (John Wiley & Sons, Inc., 2003).

127. Black, J. D. Longer laser pulses for practical LII. *CEUR Workshop Proc.* **211**, 13 (2006).

128. McCormick, D., Black, J. D., Feng, Y., Nilsson, J. & Ozanyan, K. B. High-sensitivity in situ soot particle sensing in an aero-engine exhaust plume using long-pulsed fiber-laser-induced incandescence. *IEEE Sens. J.* **16**, 2674–2682 (2016).

129. SAE ARP1179 Rev. D. *Aircraft Gas Turbine Engine Exhaust Smoke Measurement*. (2011).

130. Black, J. D., Delhay, J., Johnson, M. P., Desgroux, P. & Johnson, M. P. In-Situ Laser-Induced Incandescence of Soot in Large Civil Aeroengine Exhausts. *26th AIAA Aerodyn. Meas. Technol. Gr. Test. Conf.* (2008). doi:10.2514/6.2008-4265

131. Michael, J. B., Venkateswaran, P., Shaddix, C. R. & Meyer, T. R. Effects of repetitive pulsing on multi-kHz planar laser-induced incandescence imaging in laminar and turbulent flames. *Appl. Opt.* **54**, 3331 (2015).

132. Slipchenko, M. N. *et al.* Quasi-continuous burst-mode laser for high-speed planar imaging. *Opt. Lett.* **37**, 1346 (2012).

133. Cenker, E., Bennett, A. & Roberts, W. L. Investigations of the long-term effects of LII on soot and bath gas. *Aerosol Sci. Technol.* **51**, 1354–1367 (2017).

134. Boxx, I. G., Heinold, O. & Geigle, K. P. Laser‐induced incandescence measurements in a fired diesel engine at 3 kHz. *Exp. Fluids* **56**, 1–10 (2015).

135. Ditaranto, M., Meraner, C., Haugen, N. E. L. & Saanum, I. Influence of long pulse duration on time-resolved laser-induced incandescence. *Appl. Phys. B Lasers Opt.* **112**, 359–367 (2013).

136. Ditaranto, M. & Hverven, S. Behaviour of laser induced incandescence signal with long laser pulse duration and high fluence.

137. Hverven, S. M. Laser Induced Incandescence with Long Pulse Duration. (2013).

138. Saffaripour, M., Geigle, K. P., Snelling, D. R., Smallwood, G. J. & Thomson, K. A. Influence of rapid laser heating on the optical properties of in-flame soot. *Appl. Phys. B Lasers Opt.* **119**, 621–642 (2015).

139. Cenker, E. & Roberts, W. L. Quantitative effects of rapid heating on soot particle sizing through analysis of two-pulse LII. *36th Int. Symp. Combust.* **123**, 1–10 (2016).

140. Beam, T. & Software, B. A. M2MS-BP209 Operation Manual. (2018).

141. De Iuliis, S., Cignoli, F., Maffi, S. & Zizak, G. Influence of the cumulative effects of multiple laser pulses on laser-induced incandescence signals from soot. *Appl. Phys. B Lasers Opt.* **104**, 321–330 (2011).

142. Wright, P. *et al.* Progress towards non-intrusive optical measurement of gas turbine exhaust species distributions. *IEEE Aerosp. Conf. Proc.* **2015-June**, (2015).

143. Tollomelli, L., Barreta, L. G., Lacava, P. T. & Carinhana Jr, D. Study of the Influence of Biodiesel in Soot Emissions of Diesel Laminar Diffusion Flames. *J. Braz. Chem. Soc.* **28**, 1384–1388 (2017).

144. Salamanca, M., Sirignano, M., Commodo, M., Minutolo, P. & D'Anna, A. The effect of ethanol on the particle size distributions in ethylene premixed flames. *Exp. Therm. Fluid Sci.* **43**, 71–75 (2012).

145. Józsa, V. & Kun-Balog, A. Spectroscopic analysis of crude rapeseed oil flame. *Fuel Process. Technol.* **139**, 61–66 (2015).

146. Venkataraman, C., Negi, G., Brata Sardar, S. & Rastogi, R. Size distributions of polycyclic aromatic hydrocarbons in aerosol emissions from biofuel combustion. *J. Aerosol Sci.* **33**, 503–518 (2002).

147. Curkeet, R. Wood Combustion Basics. in *EPA Workshop* 1–36 (2011).

148. Jahirul, M. I., Rasul, M. G., Chowdhury, A. A. & Ashwath, N. Biofuels production through biomass pyrolysis- A technological review. *Energies* **5**, 4952–5001 (2012).

149. Atiku, F. A. *et al.* Some Aspects of the Mechanism of Formation of Smoke from the Combustion of Wood. *Energy & Fuels* **31**, 1935–1944 (2017).

150. Wilson, J. M. *et al.* Soot Formation from the Combustion of Biomass Pyrolysis Products and a Hydrocarbon Fuel, n -Decane: An Aerosol Time Of Flight Mass Spectrometer (ATOFMS) Study. *Energy & Fuels* **27**, 1668–1678 (2013).

151. Klippel, N., Nussbaumer, T. & Hess, A. Particle Emissions from Residential Wood and biodiesel. (Umea University, 2016).

152. Bladh, H. *et al.* Influence of soot particle aggregation on time-resolved laser-induced incandescence signals. *Appl. Phys. B* **104**, 331–341 (2011).

153. Dastanpour, R., Momenimovahed, A., Thomson, K., Olfert, J. & Rogak, S. Variation of the optical properties of soot as a function of particle mass. *Carbon N. Y.* **124**, 201–211 (2017).

154. Bouvier, Y., Mihesan, C., Ziskind, M., Therssen, E. & Focsa, C. Molecular species adsorbed on soot particles issued from low sooting methane and acetylene laminar flames : A laser-based experiment. **31**, 841–849 (2007).

9.4 Appendices

9.4.1 Data sheets and equipment technical information

Hamatasu R636-10 photomultiplier[95]

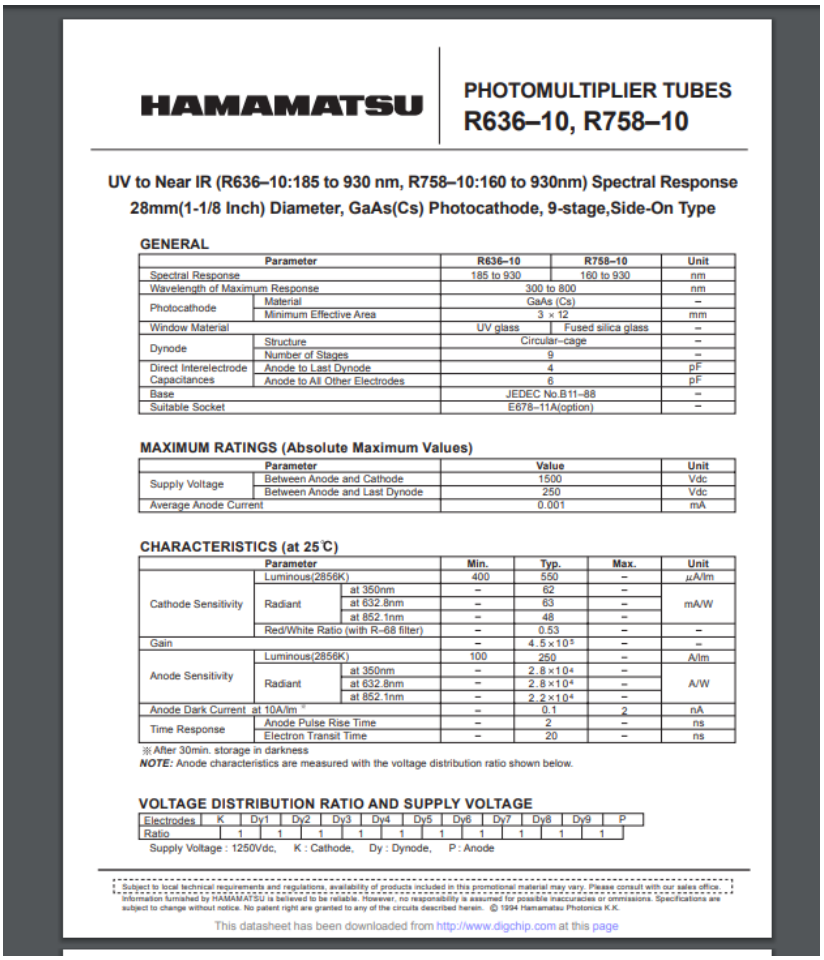

HAMAMATSU

PHOTOMULTIPLIER TUBES
R636–10, R758–10

UV to Near IR (R636–10:185 to 930 nm, R758–10:160 to 930nm) Spectral Response
28mm(1-1/8 Inch) Diameter, GaAs(Cs) Photocathode, 9-stage,Side-On Type

GENERAL

Parameter		R636–10	R758–10	Unit
Spectral Response		185 to 930	160 to 930	nm
Wavelength of Maximum Response		300 to 800		nm
Photocathode	Material	GaAs (Cs)		–
	Minimum Effective Area	3 × 12		mm
Window Material		UV glass	Fused silica glass	–
Dynode	Structure	Circular–cage		–
	Number of Stages	9		–
Direct Interelectrode Capacitances	Anode to Last Dynode	4		pF
	Anode to All Other Electrodes	6		pF
Base		JEDEC No.B11–88		–
Suitable Socket		E678–11A(option)		–

MAXIMUM RATINGS (Absolute Maximum Values)

Parameter		Value	Unit
Supply Voltage	Between Anode and Cathode	1500	Vdc
	Between Anode and Last Dynode	250	Vdc
Average Anode Current		0.001	mA

CHARACTERISTICS (at 25°C)

Parameter			Min.	Typ.	Max.	Unit
Cathode Sensitivity	Luminous(2856K)		400	550	–	μA/lm
	Radiant	at 350nm	–	62	–	mA/W
		at 632.8nm	–	63	–	
		at 852.1nm	–	48	–	
	Red/White Ratio (with R–68 filter)		–	0.53	–	–
Gain			–	4.5×10^5	–	–
Anode Sensitivity	Luminous(2856K)		100	250	–	A/lm
	Radiant	at 350nm	–	2.8×10^4	–	A/W
		at 632.8nm	–	2.8×10^4	–	
		at 852.1nm	–	2.2×10^4	–	
Anode Dark Current after 30min. storage ※			–	0.1	2	nA
Time Response	Anode Pulse Rise Time		–	2	–	ns
	Electron Transit Time		–	20	–	ns

※ After 30min. storage in darkness
NOTE: Anode characteristics are measured with the voltage distribution ratio shown below.

VOLTAGE DISTRIBUTION RATIO AND SUPPLY VOLTAGE

Electrodes	K	Dy1	Dy2	Dy3	Dy4	Dy5	Dy6	Dy7	Dy8	Dy9	P
Ratio	1	1	1	1	1	1	1	1	1	1	1

Supply Voltage : 1250Vdc, K : Cathode, Dy : Dynode, P : Anode

PHOTOMULTIPLIER TUBES R636–10, R758–10

Figure 1: Typical Spectral Response

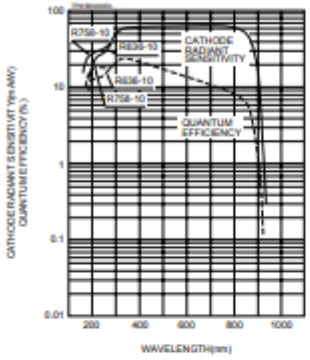

Figure 2: Typical Anode Sensitivity and Typical Gain

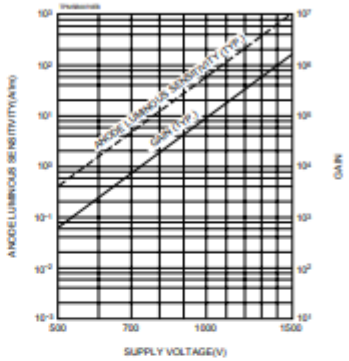

Figure 3: Dimensional Outline and Basing Diagram (Unit : mm)

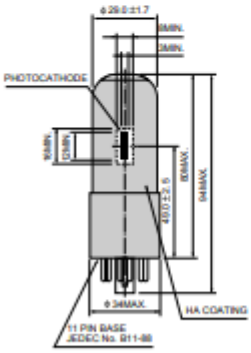

Socket
(E678 – 11A)

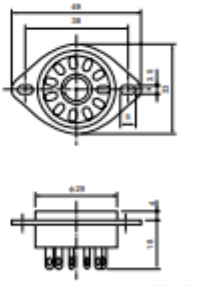

HAMAMATSU

HAMAMATSU PHOTONICS K.K., Electron Tube Center
314-5, Shimokanzo, Toyooka-village, Iwata-gun, Shizuoka-ken, 438-0193, Japan, Telephone: (81)539/62-5248, Fax: (81)539/62-2205

TPMS1016E03
JUN. 1994

Thorlabs Fast Si Photodiode PDF10[91]

Specification	PDF10A	PDF10C
Detector Material	Silicon	InGaAs / PIN
Detector Wavelength Range	320 - 1100nm	800 - 1700nm
Max. Responsivity	typ. 0.6A/W @ 960nm	typ. 1.0A/W @ 1550nm
Detector Active Area	1.1 x 1.1mm²	∅ 0.5mm
Transimpedance Gain	1 x 10^{12} V/A ±10%	1 x 10^{11} V/A ±10%
Max. Conversion Gain	0.6 x 10^{12} V/W ±10%	1 x 10^{11} V/W ±10%
Output Bandwidth (-3dB)	DC - 20Hz	DC - 25Hz
Rise/Fall Time (10% -90%)	22ms	19ms
CW Saturation Power	16pW	100pW
Max. Input Power (photodiode damage threshold))	10mW	
Minimum NEP (DC to 3dB bandwidth)	1.4fW/√Hz	7.5fW/√Hz
Integrated Noise (DC to 3dB bandwidth)	6.5 fW_{RMS}	35 fW_{RMS}
Overall output voltage noise, typ.	6.5 mV_{RMS}	3.5 mV_{RMS}
Electrical Output, Impedance	BNC, 200Ω	
Maximum Output Voltage	10V	
DC-Offset Electrical Output	< ±150mV	
Size	53.4 x 43.2 x 21 mm³	
Power Supply	±12V, 250 mA	

All technical data are valid at 23 ± 5°C and 45 ± 15% rel. humidity (non condensing)

5.1.1 PDF10A

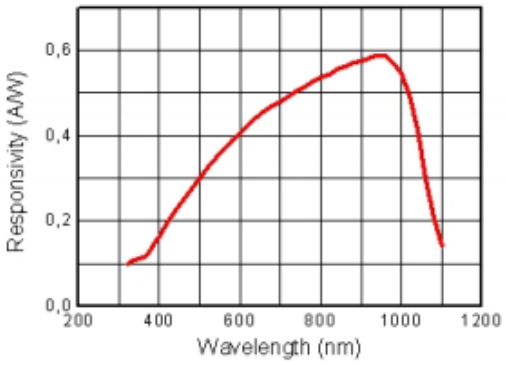

PDF10A Detector Responsivity

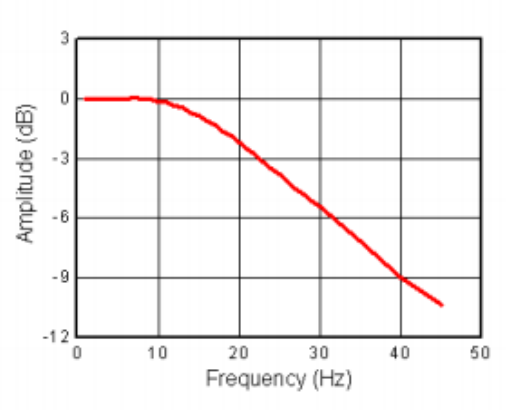

PDF10A output frequency response

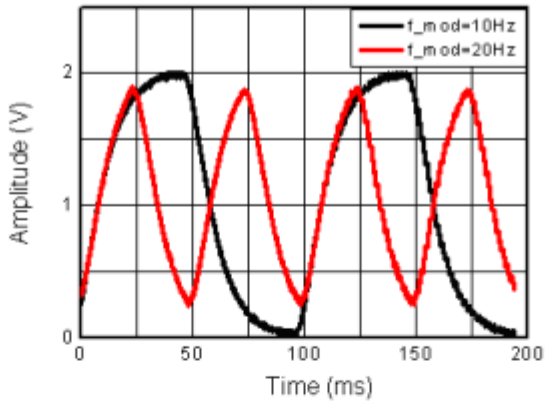

PDF10A output time response

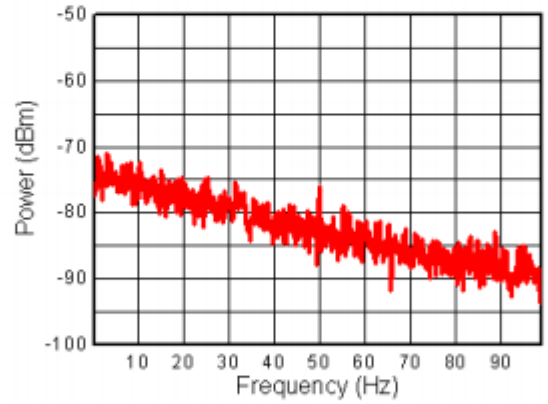

PDF10A spectral noise

Surelite Continuum II Nd:YAG laser[90]

Section 7: Specifications

DESCRIPTION	I-10	I-20	II-20	III-10
Repetition Rate (Hz)	10	20	10	10
Energy (mJ)				
1,064 nm	450	420	650	800
532 nm	200	160	300	425
355 nm	60/100 (1)	50/100 (1)	100/160 (1)	225
266 nm	60	45	80	100
Pulsewidth (2) (nsec)				
1,064 nm	5-7	5-7	5-7	4-6
532 nm	4-6	4-6	4-6	3-5
355 nm	4-6	4-6	4-6	3-5
266 nm	4-6	4-6	4-6	3-5
Linewidth (cm^{-1})				
No options	1.0	1.0	1.0	1.0
Line (3)	0.2	0.2	0.2	N/A
Divergence (4) (mrads)	0.6	0.6	0.6	0.6
Rod Diameter (mm)	6	6	7	9
Beam Pointing Stability (µrads)	100	100	100	100
Jitter (5) (± ns)	0.5	0.5	0.5	0.5
Energy Stability (6) (± %)				
1,064 nm	2.5	2.5	2.5	2.5
532 nm	3.5	3.5	3.5	3.5
355 nm	4.0	4.0	4.0	4.0
266 nm	7	7	7	7
Power Drift (7) (± %)				
1,064 nm	3.0	3.0	3.0	3.0
532 nm	5.0	5.0	6.0	5.0
355 nm	5.0	5.0	6.0	5.0
266 nm	8.0	8.0	8.0	8.0
Beam Spatial Profile (fit to Gaussian) (8)				
Near Field (<1 m)	0.70	0.70	0.70	0.70
Far Field (∞)	0.95	0.95	0.95	0.95
Max Deviation from Fitted Gaussian (9) (± %)				
Near Field (<1 m)	30	30	30	30

SPI G4 Fibre laser- Z type

Product selection parameters

Wavelength	1060nm																
Beam quality options [1]	**S Type**					**Z Type**								**L Type**	**H Type**		
M²	<1.3		<1.2	<1.3	<1.2	<1.6								1.6 - 2.0	2.5 - 3.5		
Rated average power (W)	20	20	20	50	50	20	20	30	50	50	70	70	100	20	40	70	
PulseTune Functionality[2]	HS	EP	EP	HS	EP	RM	EP	RM	RM	EP	RM	EP	EP	HS	HS	HS	
Beam delivery cable length (m)	2		0	2	0	3	3	3	3	3	3	3/5	3	3	3/5	3/5	
Beam delivery optic / connector	ILOC												HE-ILLK	ILOC			
Pulse parameters																	
Max peak power (kW)*	>7		>20	>10	>20	>10							>8	>12	>20		
Max pulse energy (mJ) *	>0.7					>1								>0.8	>1.25		
Pulse repetition frequency range (kHz)	1-1000		1 - 2000	1-1000	1- 2000	1-500	1-1000	1-500		1-1000	1-500			1-1000			
PulseTune waveforms	25	40		25	40	2	40	2		38	2	37	32		25		
Pulse duration range (ns)	10-240	3-500		10-240	3-500	26-250	3-500	26-250		6-500	26-250	9-500	12-500	10-220	10-250		
CW mode with modulation	Yes					No	Yes	No		Yes	No			Yes			
Modulation range in CW (kHz)	1-100					N/A	1-100	N/A		1-100	N/A			1-100			
Output power stability %p-p*	<5																
Cooling options																	
Air cooled or Water cooled	Air												Water	Air			
Electrical																	
Power supply voltage (V)	24																
Power supply current (A)	<10			<16		<10		<16			<20			<10		<20	
Mechanical																	
Weight (kg)	10		13.5	10	13.5	10					13			10		13	
Laser module length (mm)	347		421	347	421	347					377		400	347		377	
Laser module width (mm)	201		205	201	205	201						249		201		249	
Laser module height (mm)	95		110	95	110	95							63	95			
Environmental																	
Ambient temperature range (°C)	0-45		10-45	0-42	10-45	0-45			0-40				15-35	0-45		0-40	
Relative humidity	5-95% RH (non-codensing).																

* As measured at rated average power, waveform 0, max pulse energy and over full operating temperature range.

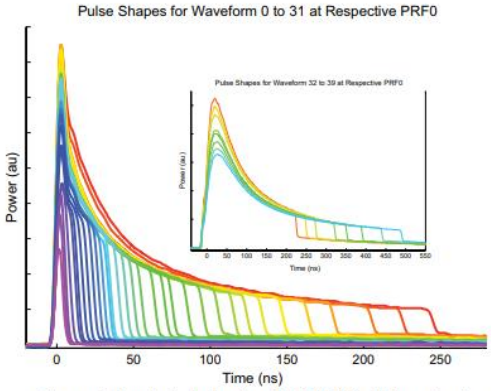

The graph shows typical pulses from the 20W EP- S with the option to select from 40 PulseTune Waveform.

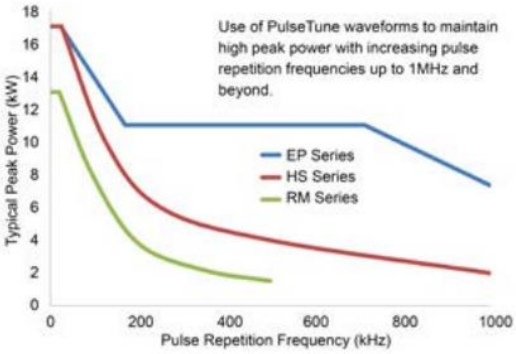

Thorlab's dual scanning slit beam profiler (BP209-IR/M),[140]

11.1 Technical Data Beam Profiler

Model	BP209-VIS BP209-VIS/M	BP209-IR BP209-IR/M	BP209-IR2 BP209-IR2/M
Wavelength Range	200 - 1100 nm	900 - 1700 nm	900 - 2700 nm
Detector Type	Si, UV enhanced	InGaAs	Extended InGaAs
Aperture Diameter	9 mm		
Scan Method	Scanning Slits, Knife Edge		
Slit Size	5 µm and 25 µm		
Minimum Beam Diameter	2.5 µm		
Maximum Beam Diameter	9 mm [1]		
Sampling Resolution	0.12 to 1.24 µm (Depending on Scan Rate)		
Scan Rate	2.0 to 20.0 s^{-1} (Continuously Variable)		
Optical Power Range	1 µW to 10 W (Depending on Beam Diameter and Model)		
Amplifier Bandwidth	16 to 1000 kHz in 11 steps (@ -1dB)		
Sample Frequency	0.2872 to 2.0 MHz		
Dynamic Range	78 dB (Amplifier Switchable)		
Photodiode Bias Voltage	0 / -1.5 V (Switchable)		0 V
Signal Digitization	15 bit		
Head Dimensions	Ø 79.5 mm x 60 mm (Including Rotation Mount)		
Minimum Pulse Rate	10 Hz [2]		
Software			
Displayed Parameters and Features	X-Y-Profile, Centroid Position, Peak Position, Pseudo 3D Profile, Beam Width Clip Level / Second Moment (4σ), Gaussian Fit Applicable, Colored Pass/Fail Test		
Compliance with Standards	ISO 11146 (Beam Widths, Divergence Angle and Beam Propagation Factor)		
General System Requirements	Windows® 7 or later, USB 2.0 High Speed Port		
M² Analysis System			
Compatible M² Options	M2MS M² Measurement Systems		
Compliance with Standards	ISO 11146		
Measured Parameters [3]	M², Waist Width, Waist Position, Rayleigh Length, Divergence, Beam Pointing, Waist Asymmetry, Astigmatism		
General			
Operating Temperature	+5 ... +35 °C		
Storage Temperature	-40 ... +70 °C		
Warm-up time for rated accuracy	15 min		

[1] BP209-VIS; BP209-IR: Beam diameter error <10% at Ø9 mm
BP209-IR2: Beam diameter error <20% at Ø9 mm for beam divergence <5°
[2] 300 kHz using M² Option
[3] using M² Option

All technical data are valid at 23 ± 5°C and 45 ± 15% rel. humidity

11.2 Technical Data M2MS-BP209

Item #	M2MS-BP209VIS-AL	M2MS-BP209VIS-AL/M	M2MS-BP209VIS	M2MS-BP209VIS/M
Beam Profiler	BP209-VIS	BP209-VIS/M	BP209-VIS	BP209-VIS/M
Wavelength Range	250 - 600 nm		400 - 1100 nm	
Beam Diameter Range	20 µm - 9 mm (at Beam Profiler Input Aperture)			
Power Range	1 µW to 10 W, Depending on Beam Diameter			
Translation Stage	DDSM100/M			
Travel Range	100mm			
Velocity (Max)	500 mm/s			
Effective Translation Range	200 mm, -100 mm to +100 mm from Focal Point			
Lens Focal Length	250 mm			
Optical Axis Height	70 mm (without additional feet)			
M^2 Measurement Range	1.0 - No Upper Limit			
Typical M^2 Accuracy	±5 %, Depending on Optics and Alignment			
Accepted Beam Diameter for 5% Uncertainty	20 µm - 4.5 mm (at Beam Profiler Input Aperture)			
Minimum Detectable Divergence Angle	<0.1 mrad			
Applicable Light Sources	CW and Pulsed Sources ≥300 kHz			
Typical Measurement Time	15 - 30 s, Depending on Beam Shape and Settings			
General				
Size	300 mm x 175 mm x 130mm			
Weight	4.6kg			

Coherent PM10V1 thermophile power meter

Name	PM10V1	PM30V1
Calibration Uncertainty (%)	1	1
Max Power (W)	10	30
Calibration Wavelength (nm)	514	514
Dimensions (mm)	Ø 63 x 36	Ø 101 x 56
Wavelength Range (µm)	0.25 - 3	0.25 - 3
Power Resolution (W)	0.001	0.01
RoHS Compliant	Yes	Yes
Part Number	1098338	1098429